Quasi 3-D Modeling of Nearshore Hydrodynamics

by

A. R. van Dongeren

and

Ib A. Svendsen

RESEARCH REPORT NO. CACR-97-04

August, 1997

Center for Applied Coastal Research
Ocean Engineering Laboratory
University of Delaware
Newark, DE 19716

TABLE OF CONTENTS

LIST OF FIGURES

LIST OF TABLES

ABSTRACT

In this thesis a depth-integrated, shortwave-averaged nearshore circulation model, called SHORECIRC, is developed, which includes the current-current and current-wave interactions over depth. This model belongs to the class of quasi-3D models, which combine the effect of the vertical structure with the simplicity of 2DH models. The present model uses semi-analytical solutions for the 3D current profiles in combination with a numerical solution of the depth-integrated 2D horizontal equations. The goal of this model is to gain an enhanced prediction and analysis capability for nearshore circulation on any bathymetry and under any hydrodynamical condition.

The current-current, current-wave induced dispersion mechanism has previously been found to significantly augment the lateral turbulent mixing in the case of a steady, uniform longshore current on a straight coast. In this thesis, the generalized quasi 3-D continuity and momentum equations governing nearshore circulation are presented. These equations are based on the complete Reynolds equations with as few additional assumptions as possible.

The numerical modeling of these governing equations is described in Chapter 3. Special emphasis is placed on the development of accurate boundary conditions, which are essential to the performance of a numerical model. For the artificial ("seaward") boundaries we develop an absorbing-generating boundary

condition based on the Method of Characteristics, which is capable of generating waves at a boundary while simultaneously absorbing any outgoing progressive wave with a mimimum of reflection. This boundary condition's reflection errors are shown in a number of formal tests.

At the shoreline a relatively simple inundation-storage boundary condition is developed. It is compared for the case of one-dimensional run-up to the analytical solution by Carrier & Greenspan (1958) and for the case of two-dimensional run-up of a solitary wave on a concave beach to numerical solutions by Zelt (1986) and Özkan-Haller & Kirby (1997).

In the last two chapters the model is applied to a number of specific cases involving infragravity waves and longshore currents. It is emphasized that the use of the SHORECIRC model is not limited to these cases, but has been developed so that it can be used for general bathymetries and hydrodynamical conditions.

In Chapter 4, the generation of infragravity waves forced by normally-incident wave groups (also called "surf beat") is analyzed. It turns out that the generation process can be characterized by three external parameters: the relative slope steepness S_Δ, the mean short-wave breakpoint location $\frac{h_b}{h_s}$ and the breaking mechanism κ. It is shown that a variation of the above-mentioned parameters results in a variation in the ratio of outgoing to incoming wave energy. The value of this "reflection coefficient" R can be interpreted as an integral measure of the net transfer of energy to the infragravity waves as a result of shoaling and breaking of the short-wave groups and their interaction with the long waves.

In Chapter 5, the SHORECIRC model is applied to the start-up of a longshore current and to infragravity waves forced by obliquely-incident wave groups. In both cases it is shown that the quasi 3-D terms have a significant effect on the

results and represent terms in the momentum equations that can be at least of the same order as the terms corresponding to the nonlinear shallow water equations.

The cross-shore component of the IG wave particle profiles shows a significant depth variation. The depth variation of the longshore component is seemingly slight, but nonetheless essential to the existence of dispersive mixing.

The magnitude of the quasi 3-D coefficients as a function of time and cross-shore distance is also analyzed. It is found that the (time-varying) forcing has a large effect on the size of these terms. The magnitude of these coefficients is also compared to the approximate values under the simplifying assumption of depth-invariant velocity profiles below trough, which will be shown to cause significant underpredictions.

The analysis of the quasi 3-D contributions to the momentum equations shows that a number of these terms can be neglected in the cases shown in this thesis. However, the assessment of the relative magnitude of these terms should be performed for each individual case. For particularly complicated cases it is advisable to retain all terms in the equations, since they may be significant locally in space and time.

ACKNOWLEDGMENTS

This work has been sponsored by NOAA Office of Sea Grant, Department of Commerce, under Award No. NA 56 RG 0147 (Project No. R/OE-17) and the U.S. Army Research Office, University Research Initiative under Contract No. DAAL03-92-G-0116.

Dr. H.A. Schäffer is gratefully acknowledged for providing his computer code of the analytical infragravity wave solutions.

Chapter 1

INTRODUCTION

1.1 Nearshore Circulation

Nearshore circulation can be defined as the current and long wave pattern induced by short-wave motion, wind and tides in the vicinity of the shore. Especially the first aspect, the shoaling, breaking and refraction of short waves, can generate steady and unsteady currents and low frequency (infragravity) waves. These so-called nearshore phenomena, although hardly detectable when one looks out over the ocean from the shore, are suspected to have a profound influence on coastal processes such as beach erosion.

It is therefore important to be able to understand, predict and analyze these hydrodynamical processes to be able to predict, plan and manage the evolution of the coast. Since these processes are very complex, existing analytical solutions and simplified numerical models do not suffice anymore.

In order to gain an enhanced prediction and analysis capability, a model called SHORECIRC has been developed within the framework of the Seagrant program. SHORECIRC is based on the complete Reynolds equations with as few additional assumptions as possible and can be used to analyze nearshore circulation on any nearshore bathymetry and under any hydrodynamical condition. In

this thesis special emphasis is placed on infragravity waves and their generation, since these waves dominate the motion in the nearshore region.

1.2 Objective of the Project

This research effort is part of a long-term project by Dr. I.A. Svendsen and co-authors, which began in 1989. The preceding publications are listed in the next section. The major objectives of this work are:

1. To develop a quasi three-dimensional model for the generation of time-varying currents and infragravity waves in the nearshore region.

2. To validate the model against a known analytical solution for the simplified case of infragravity waves generated by simple wave groups incident on a plane beach.

3. To analyze the mechanisms for the generation of infragravity waves inside the surf zone. This includes the role of free and bound long waves in association with time-varying breaking points and short-wave groupiness inside the surf zone.

4. To analyze the importance of the dispersive mixing in shaping the generation and propagation of infragravity waves. This includes analysis of how infragravity waves are influenced by the 3D structure of their horizontal velocity distributions.

5. To analyze which physical effects in the governing equations can be neglected in order to simplify and therefore economize the modeling efforts.

1.3 Overview of Previous Work

In this section an overview of relevant previous work is presented. Since research initially focused on distinct phenomena of nearshore circulation, this chapter is organized to give an account of the progress on each topic. For a more thorough review, we refer to Svendsen & Putrevu (1996). Additional references on specific topics will be given in the chapters where they are addressed.

1.3.1 Longshore Currents

The analysis of nearshore circulation has been under continuing development since the early sixties when the concept of wave radiation stress was developed by Longuet-Higgins & Stewart (1962, 1964). Bowen (1969a), Thornton (1970) and Longuet-Higgins (1970) used that concept to physically explain phenomena such as the longshore current and its shape. These early investigations found that the lateral mixing required to match model results and longshore current distribution data needed to be at least one order of magnitude larger than the turbulent mixing. For early discussions on this topic, see Inman *et al.* (1971), Bowen and Inman (1974) and Battjes (1975).

Putrevu & Svendsen (1992) and Svendsen & Putrevu (1994a) found that current-current and wave-current interactions due to the nonuniformities of the current over depth cause a momentum dispersion mechanism, which is analogous to the dispersion of pollutants in shear flow (Taylor, 1954; Elder, 1959; Fisher, 1978) and increases lateral mixing on a plane beach by an order of magnitude relative to the vertical eddy viscosity. This means that the horizontal (or lateral) eddy viscosity parameter does not need to be artificially adjusted to force agreement with data. Indeed, their calculations agreed well with Visser's (1984) data,

which were taken on a plane laboratory beach.

A remaining problem, which has been studied intensively, is the longshore current distribution on barred beaches. Various models (Baum & Basco, 1986; Thornton & Guza, 1986; Larson & Kraus, 1991; Smith *et al.*, 1993; Church & Thornton, 1993 among others) show a distinct double peak in the longshore current profile over a barred beach due to the fact that the wave breaks over the bar, reforms and breaks again on the beach face. This process causes two regions of radiation shear stress forcing, which drive the current. This finding is in conflict with field data, such as Allender *et al.* (1978) and the DELILAH experiments, which show a single peak in the trough behind the bar. The analytical model by Dalrymple (1978), the numerical model results by Sancho *et al.* (1995) and field analysis by Reniers *et al.* (1995) indicate that longshore variations of the bathymetry can induce longshore pressure gradients, which in turn can shift the maximum longshore current from the top of the bar to the trough.

1.3.2 2-DH Coastal Circulation

Nearshore phenomena such as the current circulation over periodically longshore varying bottom topographies (Noda *et al.*, 1974; Ebersole & Dalrymple, 1980 and others) and in closed basins with in principle arbitrary bathymetries (Wu & Liu, 1985; Wind & Vreugdenhil, 1986) have been studied using two-dimensional horizontal (2D-H) models. These models describe the depth-mean current and surface elevation and are based on the turbulence-averaged, depth-integrated, time-averaged Navier-Stokes equations. Some models assume steady state while some are time-dependent. Since the averaging is done over the short-wave period, the effect of the short-wave motion is replaced by the radiation stress and the shortwave-induced volume flux, which force the long wave and current motion.

These quantities cannot be determined by the wave-averaged equations themselves and have to be supplied to the model through a so-called "short-wave driver". The bottom boundary layer effect is replaced by a wave-averaged bottom shear stress, which in itself is modeled as a function of the depth-averaged velocity. The turbulent shear stresses are represented by an eddy viscosity model, which closes the equations.

These types of models have also been used to study the generation of rip currents (e.g., Noda, 1974). Rip currents are strong jet-like flows in the seaward direction. Ample field evidence of these features exists (Inman *et al.*, 1971; Dalrymple & Lozano, 1978 to mention two). A number of theoretical mechanisms that can induce these flows are mentioned in Bowen (1969b), Dalrymple (1978) and Tang & Dalrymple (1988).

1.3.3 Vertical Structure of Currents and IG-waves

The vertical structure of currents and in particular the cross-shore circulation or undertow has been another topic of research. Two-dimensional vertical (2D-V) models, which can resolve the vertical distribution, have been used by various authors (Dyhr-Nielsen & Sörensen, 1970; Börekçi, 1982; Svendsen, 1984b; Dally & Dean, 1984, 1986; Stive & Wind, 1986; Svendsen *et al.*, 1987; Svendsen & Hansen, 1988; Okayasu *et al.*, 1988 and Deigaard & Fredsøe, 1989). Most models assume steady state and assume longshore uniformity, which reduces the equations considerably.

In essence, the steady cross-shore circulation current (or undertow), meaning wave-induced volume flux and the return flow, is a result of the balance between the pressure gradient, which acts uniformly over depth, the short-wave forcing, which is not uniform over depth, and the turbulent shear stresses. This

inequilibrium along the vertical axis drives the flow. The turbulent shear stresses are usually represented by an eddy viscosity model. This results in a cross-shore momentum equation, which is of second order in the depth coordinate z, which requires two boundary conditions to close the problem. The usual choices are a bottom boundary condition (i.e., the expression of the bottom shear stress in terms of the bottom velocity) and the specification of either cross-shore conservation of mass or a shear stress at the short-wave trough or mean water level.

Putrevu & Svendsen (1993, 1995) extended the analysis to include time-varying forcing and presented local solutions for the vertical structure of the velocity profiles in infragravity (IG) waves, both inside and outside the surf zone for the case of surfbeat. They found that the local short-wave forcing causes a substantial vertical variation of these profiles, while in the absence of such forcing the profiles are relatively depth-invariant.

1.3.4 Quasi 3-D Circulation

Quasi-3D models were developed to combine the effect of the vertical structure with the simplicity of 2DH circulation models, which were described in the two previous subsections. In an approach by De Vriend & Stive (1987) and Stive & De Vriend (1987), the current is split into primary and secondary flow profiles based on the assumption that the primary velocity profiles are the same in the cross-shore and longshore direction. In a different approach, Svendsen & Lorenz (1989) determined the vertically-varying longshore and cross-shore currents separately under the assumption of weak dependence. They found that the total vertical current profile has a spiral shape, see Fig. 1.1, with profiles that are very different in the cross-shore and longshore direction.

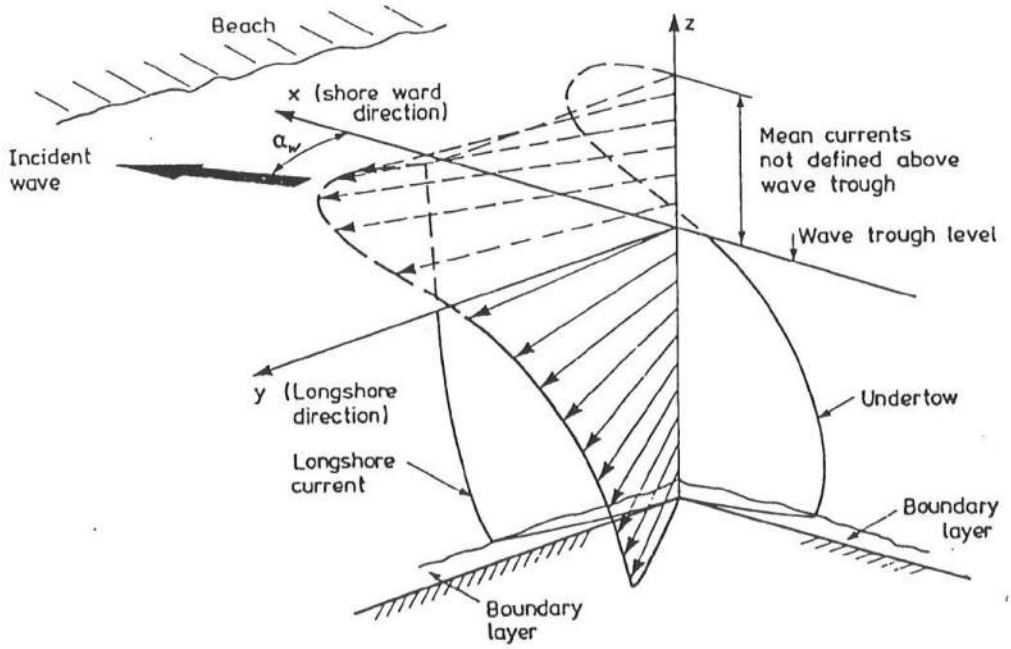

Figure 1.1: Three-dimensional structure of the current velocities in the surf zone (from Svendsen & Lorenz, 1989).

Svendsen & Putrevu (1990) formulated a steady state 3D nearshore circulation model using analytical solutions for the 3D current profiles in combination with a numerical solution of the depth-integrated 2D horizontal equations for a long straight coast. Sánchez-Arcilla *et al.* (1990, 1992) presented a similar concept. They split the current velocity into a depth-invariant component and a component with a vertical variation with zero mean flow integrated over the central layer. Putrevu & Svendsen (1992) and Svendsen & Putrevu (1994a) recognized that the current-current and current-wave interactions neglected in previous investigations induce a non-linear dispersion mechanism, which significantly augments the lateral turbulent mixing and explains the difference in magnitude between the vertical and horizontal mixing.

The time-dependent version of this model was presented in Van Dongeren

et al. (1994) for the special case of longshore uniformity in both the bathymetric and hydrodynamical conditions. The generalized quasi 3-D model is presented in this thesis.

1.3.5 Other Time-dependent Models

For completeness we mention a different class of models, which resolve the instantaneous state of motion, such as models based on the nonlinear shallow water equations or on the Boussinesq-equations.

Contributions to the former category include nonlinear shallow water models developed by Peregrine and co-authors (e.g., Hibberd & Peregrine, 1979; Packwood & Peregrine, 1980; Packwood, 1983) and Kobayashi and co-authors (e.g., Kobayashi *et al.*, 1989; Kobayashi & Wurjanto, 1992). Boussinesq-models for breaking waves have been developed by Karambas *et al.* (1990), Brocchini *et al.* (1992), Schäffer *et al.* (1992,1993) and Madsen *et al.* (1994) among others. Since in that approach the governing equations are not averaged over the short-wave period, these models are able to represent both short and long waves simultaneously, which can be an advantage. This, however, also makes them more computer-intensive and therefore expensive. These types of models are an alternative to the types described in the previous sections.

1.4 Outline of Present Work

In the next chapter, the short-wave averaged, depth-integrated governing equations are derived. Then, the local time-averaged (in other words, non depth-integrated) equations are derived, the solution of which yield expressions of the

depth variations of the currents. These will be used to transform the current-current and current-wave integrals in the governing equations into expressions which are dependent only on depth-averaged quantities. This procedure yields the set of general quasi 3-D equations of horizontal momentum and continuity, which can be solved numerically by finite differences in time and space with semi-analytical expressions for the effect of the current distribution along the vertical. As a check to their validity, these general equations are reduced to the previously derived equations in the case of a long straight (or cylindrical) coast. Also presented in Chapter 2 are the energy equations for the short and the long waves.

In Chapter 3, the numerical method and the boundary conditions are described. The method's stability and accuracy are checked and the truncation errors and their effect are investigated.

For our modeling purposes it was necessary to develop boundary conditions at the open boundaries and at the moving shoreline. To that end, a so-called absorbing-generating boundary condition for the seaward (or open) side of the model is derived, which allows the propagation of outgoing long waves through the boundary with a minimum of reflection while specifying an incoming long wave. This boundary condition is tested for accuracy and reflection errors in a number of formal tests.

A two-dimensional shoreline boundary condition based on the inundation-drainage procedure is derived and tested for accuracy against a classical analytical solutions for the case of a long straight coast and against two numerical solutions for the case of a concave beach.

In Chapter 4, infragravity waves forced by normally-incident wave groups (also called "surf beat") are investigated. First, results from the linearized version

of the model are compared to a linear analytical solution and the nonlinear model results are compared to laboratory data. The generation of these infragravity waves by the transfer of energy from the short waves is analyzed in both the linear and nonlinear versions of the model. Special attention is paid to the role of incoming free and bound long waves in association with time-varying breaking points as a function of the short-wave and bathymétrical parameters.

Chapter 5 addresses the importance of the dispersive mixing terms in the governing equations. First, the start-up of a longshore current under steady state forcing and the associated long and cross shore time scales are discussed. Then, two-dimensional infragravity waves forced by obliquely incident wave groups are shown. As in Chapter 4, the linearized model results are compared to an analytical solution. Next, the effect of the nonlinear terms corresponding to the nonlinear shallow water equations and the effect of the quasi 3-D terms is shown. Finally, the magnitude of the quasi 3-D terms is shown relative to the other terms in the momentum equation as a function of the cross-shore coordinate.

In Chapter 6, we will summarize the present work, draw conclusions and list recommendations for future work.

Chapter 2

DERIVATION OF THE GOVERNING EQUATIONS

In this chapter the governing equations of the SHORECIRC model are described. In the first section, the depth-integrated, time-averaged governing equations are derived. The complete derivation of the continuity equation is given while only the procedure of the derivation of the momentum equations is described. We refer to Putrevu & Svendsen (1991) for a more elaborate derivation.

In Section 2.2, the local, time-averaged momentum equations (sometimes called "velocity profile"or "undertow equations") are solved with the appropriate boundary conditions. The derivation in this thesis is the time-steady version of the more general one by Putrevu & Svendsen (1997).

The solutions to the local equations are then used in Section 2.3 to convert the advective current-current and current-wave interaction terms in the depth-integrated governing equations into terms that are functions of the depth-integrated quantities and that reveal the momentum-dispersive effect or quasi 3-D effect that these interaction terms represent.

The quasi 3-D terms are expressed in Section 2.4 in terms of polynomials for the (quasi) steady state.

In Section 2.5, the governing equations are shown to reduce to the special case of a long straight beach of Svendsen & Putrevu (1994a).

Finally, in Section 2.6 the energy equations for the short-wave and long-wave motion are given as derived originally by Phillips (1977) with modifications by Schäffer (1993). The energy equation for the short waves can be used as a short-wave driver while the equation for the long waves will be used in Chapter 4 as an analytical tool to study the generation of infragravity waves.

2.1 Time-averaged, Depth-integrated Equations

The time-averaged, depth-integrated equations of conservation of mass and momentum are derived for non-uniform currents over depth. This is a more general form than those given by Phillips (1977) and Mei (1983) but the procedure is essentially the same.

2.1.1 Conservation of Mass

The continuity equation reads

$$\frac{\partial u_\alpha}{\partial x_\alpha} + \frac{\partial w}{\partial z} = 0 \tag{2.1}$$

where u_α is the total velocity of long and short waves and w is the vertical velocity. α is the index notation indicating the horizontal x, y directions. z is the vertical coordinate, defined from the still water level (SWL) up, as is shown in the definition sketch of Fig. 2.1.

Integrating this equation from the bottom at $z = -h_o$ to the instantaneous surface at $z = \zeta$ gives

$$\int_{-h_o}^{\zeta} \frac{\partial u_\alpha}{\partial x_\alpha}\, dz + w(\zeta) - w(-h_o) = 0 \tag{2.2}$$

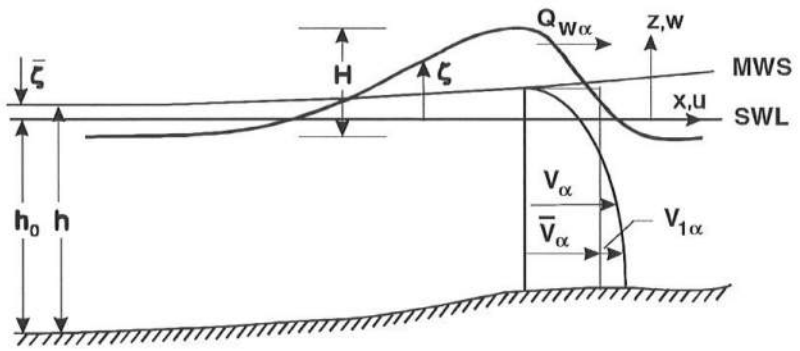

Figure 2.1: Definition sketch.

We can apply the Leibniz rule to the first term, which yields

$$\int_{-h_o}^{\zeta} \frac{\partial u_\alpha}{\partial x_\alpha}\, dz = \frac{\partial}{\partial x_\alpha}\int_{-h_o}^{\zeta} u_\alpha\, dz - \frac{\partial \zeta}{\partial x_\alpha} u_\alpha(\zeta) + \frac{\partial(-h_o)}{\partial x_\alpha} u_\alpha(-h_o) \tag{2.3}$$

Substituting (2.3), the bottom boundary condition (BBC)

$$w(-h_o) + u_\alpha \frac{\partial h_o}{\partial x_\alpha} = 0 \tag{2.4}$$

and the kinematic free surface boundary condition (KFSBC)

$$w(\zeta) - u_\alpha \frac{\partial \zeta}{\partial x_\alpha} = \frac{\partial \zeta}{\partial t} \tag{2.5}$$

into (2.2) yields the depth-integrated continuity equation

$$\frac{\partial \zeta}{\partial t} + \frac{\partial Q_\alpha}{\partial x_\alpha} = 0 \tag{2.6}$$

In (2.6) we have defined

$$Q_\alpha \equiv \int_{-h_o}^{\zeta} u_\alpha\, dz \tag{2.7}$$

Next this equation will be shortwave-averaged or time-averaged, i.e., averaged over the period of the short waves

$$\frac{\partial \overline{\zeta}}{\partial t} + \frac{\partial \bar{Q}_\alpha}{\partial x_\alpha} = 0 \tag{2.8}$$

where the overbar is defined as

$$\overline{\cdot} = \frac{1}{T}\int_0^T \cdot \, dt \tag{2.9}$$

The effect of the time-averaging can be made more visible by splitting the total velocity into three parts: the current (or long-wave) component V_α, the short-wave component $u_{w\alpha}$ and the turbulent component u'_α or

$$u_\alpha = V_\alpha + u_{w\alpha} + u'_\alpha \tag{2.10}$$

After turbulent (ensemble) averaging, which implies $\widehat{u'_\alpha} = 0$, we have

$$\widehat{u_\alpha} = \widehat{V_\alpha} + \widehat{u_{w\alpha}} \tag{2.11}$$

where the overbraces denote turbulent averaging. Dropping them for convenience, the velocities are shortwave-averaged, where we define

$$\overline{u_{w\alpha}} = 0 \quad \text{below trough} \tag{2.12}$$

so that the time- and turbulent-averaged (2.7) becomes

$$\bar{Q}_\alpha = \int_{-h_o}^{\bar{\zeta}} V_\alpha \, dz + \overline{\int_{\zeta_t}^{\zeta} u_{w\alpha} \, dz} \tag{2.13}$$

where ζ_t denotes the trough level. Defining the wave-induced volume flux,

$$Q_{w\alpha} \equiv \overline{\int_{\zeta_t}^{\zeta} u_{w\alpha} \, dz} \tag{2.14}$$

Eq. (2.13) becomes

$$\bar{Q}_\alpha = \int_{-h_o}^{\bar{\zeta}} V_\alpha \, dz + Q_{w\alpha} \tag{2.15}$$

Substituting (2.15) into (2.8) yields the result

$$\frac{\partial \overline{\zeta}}{\partial t} + \frac{\partial}{\partial x_\alpha}\left(\int_{-h_o}^{\bar{\zeta}} V_\alpha \, dz + Q_{w\alpha}\right) = 0 \tag{2.16}$$

which is the depth-integrated, time-averaged continuity equation.

2.1.2 Conservation of Momentum

In this subsection, an outline is given of the derivation of the depth-integrated, time-averaged momentum equations. A more complete derivation for the case of depth-varying currents is given by Putrevu & Svendsen (1991), which is the extension of the procedure given by Phillips (1977) and Mei (1983). In the following we largely follow the derivation given by Svendsen & Putrevu (1996).

The governing equations are derived from the Reynolds equations of horizontal momentum, which read, in index notation

$$\frac{\partial u_\beta}{\partial t} + \frac{\partial u_\alpha u_\beta}{\partial x_\alpha} + \frac{\partial u_\beta w}{\partial z} = -\frac{1}{\rho}\delta_{\alpha\beta}\frac{\partial p}{\partial x_\alpha} + \frac{1}{\rho}\left(\frac{\partial \tau_{\alpha\beta}}{\partial x_\alpha} + \frac{\partial \tau_{z\beta}}{\partial z}\right) \tag{2.17}$$

where ρ is the density, p is the instantaneous pressure, $\delta_{\alpha\beta}$ is the Kronecker delta. The turbulent (or Reynolds) shear stresses $\tau_{\alpha\beta}$ are defined as

$$\tau_{\alpha\beta} \equiv -\rho \overbrace{u'_\alpha u'_\beta} \tag{2.18}$$

We have assumed that the viscous stresses are negligible in a turbulent environment.

These equations are integrated term by term over depth from the bottom at $z = -h_o$ to the instantaneous surface at $z = \zeta$. The partial derivatives and the integrals are then interchanged using the Leibniz rule, which yields a number of boundary terms. Most of these boundary terms can be eliminated using the KFSBC and the BBC, while others can be replaced by surface and bottom shear stresses. After performing these steps and applying a time-averaging, Eq. (2.17) can be written as

$$\frac{\partial}{\partial t}\overline{\int_{-h_o}^{\zeta} u_\beta \, dz} + \frac{\partial}{\partial x_\alpha}\overline{\int_{-h_o}^{\zeta} u_\alpha u_\beta \, dz} = \frac{1}{\rho}\overline{p(-h_o)}\frac{\partial h_o}{\partial x_\beta}$$

$$-\frac{1}{\rho}\frac{\partial}{\partial x_\alpha}\left(\overline{\int_{-h_o}^{\zeta} p\,\delta_{\alpha\beta} - \tau_{\alpha\beta}\, dz}\right) + \frac{\tau_\beta^S}{\rho} - \frac{\tau_\beta^B}{\rho} \tag{2.19}$$

where τ_β^S is the surface shear stress, τ_β^B is the bottom shear stress.

The pressure at the bottom can be eliminated using the vertical component of the Reynolds equations of momentum

$$\frac{\partial w}{\partial t} + \frac{\partial u_\alpha w}{\partial x_\alpha} + \frac{\partial w^2}{\partial z} = -\frac{1}{\rho}\frac{\partial p}{\partial z} - g + \frac{1}{\rho}\left(\frac{\partial \tau_{\alpha z}}{\partial x_\alpha} + \frac{\partial \tau_{zz}}{\partial z}\right) \tag{2.20}$$

which is also integrated from the bottom to the free surface. Then the Leibniz rule is applied and the boundary terms are eliminated. After time-averaging and some rearranging this leads to

$$\overline{p(-h_o)} = \rho\, g\,(h_o + \bar{\zeta}) + \frac{\partial}{\partial x_\alpha}\left(\overline{\int_{-h_o}^{\zeta} \rho\, u_\alpha\, w - \tau_{\alpha z} dz}\right) \simeq \rho\, g\,(h_o + \bar{\zeta}) \tag{2.21}$$

where the second term on the right hand side of the equality is small under the assumption that the vertical Reynolds shear stresses are small, so that the pressure at the bottom is essentially hydrostatic.

We substitute (2.21) into (2.19), which gives

$$\begin{aligned}
&\frac{\partial}{\partial t}\overline{\int_{-h_o}^{\zeta} u_\beta\, dz} + \frac{\partial}{\partial x_\alpha}\overline{\int_{-h_o}^{\zeta} u_\alpha u_\beta\, dz} = -g\,(h_o + \bar{\zeta})\frac{\partial \bar{\zeta}}{\partial x_\beta} \\
&-\frac{1}{\rho}\frac{\partial}{\partial x_\alpha}\left[\overline{\int_{-h_o}^{\zeta} p\,\delta_{\alpha\beta}\, dz} - \delta_{\alpha\beta}\frac{1}{2}\rho\, g\, h^2\right] + \frac{1}{\rho}\frac{\partial}{\partial x_\alpha}\overline{\int_{-h_o}^{\zeta} \tau_{\alpha\beta}\, dz} \\
&+\frac{\tau_\beta^S}{\rho} - \frac{\tau_\beta^B}{\rho}
\end{aligned} \tag{2.22}$$

where $h = h_o + \bar{\zeta}$. We time-average (2.7) so that

$$\bar{Q}_\beta \equiv \overline{\int_{-h_o}^{\zeta} u_\beta\, dz} \tag{2.23}$$

and expand the total velocity in the advective acceleration term into a current part and a short-wave part, as in (2.11), so that we can write that term as

$$\overline{\int_{-h_o}^{\zeta} u_\alpha u_\beta\, dz} = \overline{\int_{-h_o}^{\zeta} (V_\alpha + u_{w\alpha})\,(V_\beta + u_{w\beta})\, dz} =$$

$$\int_{-h_o}^{\bar{\zeta}} V_\alpha V_\beta \, dz + \overline{\int_{-h_o}^{\zeta} u_{w\alpha} \, u_{w\beta} \, dz} + \overline{\int_{\zeta_t}^{\zeta} (u_{w\alpha} V_\beta + u_{w\beta} V_\alpha) \, dz} \quad (2.24)$$

These equations can be used to rewrite (2.22) as

$$\frac{\partial \bar{Q}_\beta}{\partial t} + \frac{\partial}{\partial x_\alpha} \int_{-h_o}^{\bar{\zeta}} V_\alpha V_\beta \, dz + \frac{\partial}{\partial x_\alpha} \overline{\int_{\zeta_t}^{\zeta} (u_{w\alpha} V_\beta + u_{w\beta} V_\alpha) \, dz} =$$

$$- g (h_o + \zeta) \frac{\partial \bar{\zeta}}{\partial x_\beta} - \frac{1}{\rho} \frac{\partial}{\partial x_\alpha} \left[\overline{\int_{-h_o}^{\zeta} (p \, \delta_{\alpha\beta} + u_{w\alpha} \, u_{w\beta}) \, dz} - \delta_{\alpha\beta} \frac{1}{2} \rho \, g \, h^2 \right] +$$

$$\frac{1}{\rho} \frac{\partial}{\partial x_\alpha} \overline{\int_{-h_o}^{\zeta} \tau_{\alpha\beta} \, dz} + \frac{\tau_\beta^S}{\rho} - \frac{\tau_\beta^B}{\rho} \quad (2.25)$$

The term in the square brackets on the right-hand side (RHS) is identified as the radiation stress (the momentum flux due to the short waves) which can be written as

$$S_{\alpha\beta} \equiv \overline{\int_{-h_o}^{\zeta} (p \, \delta_{\alpha\beta} + \rho \, u_{w\alpha} \, u_{w\beta}) \, dz} - \delta_{\alpha\beta} \frac{1}{2} \rho \, g \, h^2 \quad (2.26)$$

This definition is symbolically similar to Mei (1983), who uses a different definition of $u_{w\alpha}$, however. He requires $\overline{\int_{-h_o}^{\zeta} u_{w\alpha} \, dz} = 0$ where in the present derivation we use the definition (2.12). With (2.26), (2.25) becomes

$$\frac{\partial \bar{Q}_\beta}{\partial t} + \frac{\partial}{\partial x_\alpha} \int_{-h_o}^{\bar{\zeta}} V_\alpha V_\beta \, dz + \frac{\partial}{\partial x_\alpha} \overline{\int_{\zeta_t}^{\zeta} (u_{w\alpha} V_\beta + u_{w\beta} V_\alpha) \, dz} =$$

$$- g (h_o + \zeta) \frac{\partial \bar{\zeta}}{\partial x_\beta} - \frac{1}{\rho} \frac{\partial}{\partial x_\alpha} \left[S_{\alpha\beta} - \overline{\int_{-h_o}^{\zeta} \tau_{\alpha\beta} \, dz} \right] + \frac{\tau_\beta^S}{\rho} - \frac{\tau_\beta^B}{\rho} \quad (2.27)$$

It is convenient to split the current velocity in a depth-invariant and a depth-varying part as

$$V_\alpha = \tilde{V}_\alpha + V_{1\alpha}(z) \quad (2.28)$$

where we choose $\tilde{V}_\alpha$ such that

$$\tilde{V}_\alpha \equiv \frac{1}{h} \overline{\int_{-h_o}^{\zeta} u_\alpha \, dz} = \frac{\bar{Q}_\alpha}{h} \quad (2.29)$$

By (2.15) this implies that

$$\int_{-h_o}^{\bar{\zeta}} V_{1\alpha}\, dz \;=\; -Q_{w\alpha} \tag{2.30}$$

Substituting (2.28) into (2.27) yields the "final" form of the horizontal momentum equations

$$\begin{aligned}
&\frac{\partial \bar{Q}_\beta}{\partial t} + \frac{\partial}{\partial x_\alpha}\left(\frac{\bar{Q}_\alpha \bar{Q}_\beta}{h}\right) + \frac{\partial}{\partial x_\alpha}\int_{-h_o}^{\bar{\zeta}} V_{1\alpha}\, V_{1\beta}\, dz + \\
&\frac{\partial}{\partial x_\alpha}\overline{\int_{\zeta_t}^{\zeta} (\, u_{w\alpha}\, V_{1\beta} \,+\, u_{w\beta}\, V_{1\alpha})\, dz} \;=\; -\, g\,(h_o + \zeta)\frac{\partial \bar{\zeta}}{\partial x_\beta} \\
&-\frac{1}{\rho}\frac{\partial}{\partial x_\alpha}\left[S_{\alpha\beta} - \overline{\int_{-h_o}^{\zeta} \tau_{\alpha\beta}\, dz}\right] + \frac{\tau_\beta^S}{\rho} - \frac{\tau_\beta^B}{\rho}
\end{aligned} \tag{2.31}$$

We can solve these equations if we know the variation over depth of the currents, which are the third and fourth terms on the left-hand side. In the next section, these terms are analyzed and rewritten in terms of the depth-integrated variables.

2.2 Local, Time-averaged Equations

The variation over depth of the currents can be determined by solving the local shortwave-averaged equations, which are not integrated over depth. In this section and the next we will follow the derivation of Putrevu & Svendsen (1997).

Starting with the horizontal Reynolds equations, we introduce a split between currents and short-wave velocities (2.11)

$$u_\alpha \;=\; V_\alpha \,+\, u_{w\alpha} \tag{2.32}$$

and average over the short-wave period to yield

$$\frac{\partial V_\beta}{\partial t} + \frac{\partial V_\alpha V_\beta}{\partial x_\alpha} + \frac{\partial V_\beta W}{\partial z} + \frac{\partial \overline{u_{w\alpha} u_{w\beta}}}{\partial x_\alpha} + \frac{\partial \overline{u_{w\beta} w_w}}{\partial z} =$$

$$-\frac{1}{\rho}\delta_{\alpha\beta}\frac{\partial p}{\partial x_\alpha} + \frac{1}{\rho}\left(\frac{\partial \tau_{\alpha\beta}}{\partial x_\alpha} + \frac{\partial \tau_{z\beta}}{\partial z}\right) \tag{2.33}$$

(Svendsen & Lorenz, 1989). The vertical momentum equation can be integrated over depth to yield

$$\begin{aligned} \bar{p} &= \rho\, g\,(\bar{\zeta} - z) - \rho\overline{w_w^2} + \tau_{zz} + \frac{\partial}{\partial x_\alpha}\overline{\int_z^\zeta (\rho\, u_\alpha\, w - \tau_{\alpha z})\, dz} \\ &\simeq \rho\, g\,(\bar{\zeta} - z) - \rho\overline{w_w^2} \end{aligned} \tag{2.34}$$

The turbulent shear stresses may be expressed as (e.g., Rodi, 1980)

$$\tau_{\alpha\beta} = \mu\left(\frac{\partial V_\alpha}{\partial x_\beta} + \frac{\partial V_\beta}{\partial x_\alpha}\right) \tag{2.35}$$

and

$$\tau_{z\beta} = \mu\frac{\partial V_\beta}{\partial z} \tag{2.36}$$

where $\mu = \rho\,\nu_t$ is the dynamic viscosity and ν_t is the turbulent eddy viscosity. Introducing these expressions into (2.33) yields

$$\frac{\partial V_\beta}{\partial t} + \frac{\partial V_\alpha V_\beta}{\partial x_\alpha} + \frac{\partial V_\beta W}{\partial z} + \frac{\partial}{\partial x_\alpha}\left(\overline{u_{w\alpha}u_{w\beta}} - \overline{w_w^2}\right) + \frac{\partial \overline{u_{w\beta}w_w}}{\partial z} =$$

$$-g\,\frac{\partial \bar{\zeta}}{\partial x_\beta} + \frac{\partial}{\partial x_\alpha}\left(\nu_t\left(\frac{\partial V_\alpha}{\partial x_\beta} + \frac{\partial V_\beta}{\partial x_\alpha}\right)\right) + \frac{\partial}{\partial z}\left(\nu_t\frac{\partial V_\beta}{\partial z}\right) \tag{2.37}$$

Using (2.28) and the continuity equation, we can rewrite (2.37) as

$$\frac{\partial}{\partial z}\left(\nu_t\frac{\partial V_{1\beta}}{\partial z}\right) = \beta_\beta + \frac{\partial \tilde{V}_\beta}{\partial t} + \frac{\partial V_{1\beta}}{\partial t} + \left(\tilde{V}_\alpha + V_{1\alpha}\right)\frac{\partial(\tilde{V}_\beta + V_{1\beta})}{\partial x_\alpha} +$$

$$W\frac{\partial V_{1\beta}}{\partial z} + g\,\frac{\partial \bar{\zeta}}{\partial x_\beta} \tag{2.38}$$

where

$$\beta_\beta = \frac{\partial}{\partial x_\alpha}\left(\overline{u_{w\alpha}u_{w\beta}} - \overline{w_w^2}\right) + \frac{\partial \overline{u_{w\beta}w_w}}{\partial z} - \frac{\partial}{\partial x_\alpha}\left(\nu_t\left(\frac{\partial V_\alpha}{\partial x_\beta} + \frac{\partial V_\beta}{\partial x_\alpha}\right)\right) \tag{2.39}$$

which is Putrevu & Svendsen's Eq. (8) without neglecting the $\overline{w_w^2}$ and turbulence contributions. The fourth term on the RHS of (2.38) can be approximated by

$$\left(\tilde{V}_\alpha + V_{1\alpha}\right) \frac{\partial(\tilde{V}_\beta + V_{1\beta})}{\partial x_\alpha} \simeq \tilde{V}_\alpha \frac{\partial \tilde{V}_\beta}{\partial x_\alpha} + \tilde{V}_\alpha \frac{\partial V_{1\beta}}{\partial x_\alpha} + V_{1\alpha} \frac{\partial \tilde{V}_\beta}{\partial x_\alpha} \tag{2.40}$$

where we have used that in most practical case we have $V_{1\beta} \ll \tilde{V}_\beta$. Defining

$$\frac{d}{dt} \equiv \frac{\partial}{\partial t} + \tilde{V}_\alpha \frac{\partial}{\partial x_\alpha} \tag{2.41}$$

we can write (2.38) as

$$\begin{aligned} \frac{\partial V_{1\beta}}{\partial t} - \frac{\partial}{\partial z}\left(\nu_t \frac{\partial V_{1\beta}}{\partial z}\right) &= -\beta_\beta - \left(\frac{d\tilde{V}_\beta}{dt} + g\,\frac{\partial \bar{\zeta}}{\partial x_\beta}\right) \\ &\quad - V_{1\alpha}\frac{\partial \tilde{V}_\beta}{\partial x_\alpha} - \tilde{V}_\alpha \frac{\partial V_{1\beta}}{\partial x_\alpha} - W\frac{\partial V_{1\beta}}{\partial z} \end{aligned} \tag{2.42}$$

Lastly, we can eliminate the term in parentheses on the right-hand side by substituting from the depth-integrated equation for the leading-order terms, which reads

$$\frac{d\tilde{V}_\beta}{dt} + g\,\frac{\partial \bar{\zeta}}{\partial x_\beta} = -\frac{1}{\rho\, h}\frac{\partial}{\partial x_\alpha}\left(S_{\alpha\beta} - \overline{\int_{-h_o}^{\zeta} \tau_{\alpha\beta}\, dz}\right) + \frac{\tau_\beta^S - \tau_\beta^B}{\rho\, h} \tag{2.43}$$

Eq. (2.42) then becomes

$$\begin{aligned} \frac{\partial V_{1\beta}}{\partial t} - \frac{\partial}{\partial z}\left(\nu_t \frac{\partial V_{1\beta}}{\partial z}\right) &= -\beta_\beta + \frac{1}{\rho\, h}\frac{\partial}{\partial x_\alpha}\left(S_{\alpha\beta} - \overline{\int_{-h_o}^{\zeta} \tau_{\alpha\beta}\, dz}\right) - \frac{\tau_\beta^S - \tau_\beta^B}{\rho\, h} \\ &\quad - V_{1\alpha}\frac{\partial \tilde{V}_\beta}{\partial x_\alpha} - \tilde{V}_\alpha \frac{\partial V_{1\beta}}{\partial x_\alpha} - W\frac{\partial V_{1\beta}}{\partial z} \end{aligned} \tag{2.44}$$

To solve for the vertical profiles, we split the depth-varying current velocity into two parts

$$V_{1\beta} = V_{1\beta}^{(0)} + V_{1\beta}^{(1)} \tag{2.45}$$

where the first part is primarily the (slowly time-varying) component generated by the local external forcing while the second part is generated by the advective terms in (2.44). In this derivation, we will assume that the first component is much larger than the second one,

$$V_{1\beta}^{(1)} \ll V_{1\beta}^{(0)} \tag{2.46}$$

which implies that the local external forcing is dominant and provides the primary generation.

Splitting (2.44) in this way we have for $V_{1\beta}^{(0)}$

$$\frac{\partial V_{1\beta}^{(0)}}{\partial t} - \frac{\partial}{\partial z}\left(\nu_t \frac{\partial V_{1\beta}^{(0)}}{\partial z}\right) = -f_\beta \tag{2.47}$$

where the local external forcing is

$$f_\beta = \beta_\beta - \frac{1}{\rho\, h}\frac{\partial}{\partial x_\alpha}\left(S_{\alpha\beta} - \overline{\int_{-h_o}^{\zeta} \tau_{\alpha\beta}\, dz}\right) + \frac{\tau_\beta^S - \tau_\beta^B}{\rho\, h} \tag{2.48}$$

with two boundary conditions

$$\frac{\partial V_{1\beta}^{(0)}}{\partial z} = \frac{\tau_\beta^B}{\rho\, \nu_t} \qquad \text{at} \qquad z = -h_o \tag{2.49}$$

which assumes a slip velocity and an associated stress, and

$$\int_{-h_o}^{\bar{\zeta}} V_{1\beta}^{(0)}\, dz = -Q_{w\beta} \tag{2.50}$$

If we assume that the time scale of the motion is large, we can neglect the local acceleration term on the left-hand side of (2.47). This can be seen if we non-dimensionalize the left-hand side of this equation using

$$t = T\, t' \qquad z = h_b\, z' \qquad \nu_t = h_b \sqrt{g\, h_b}\, \nu_t' \qquad V_{1\beta}^{(0)} = c_b\, V_{1\beta}^{\prime(0)} \tag{2.51}$$

where T is a typical time scale of the motion, and h_b and c_b are the depth and celerity at breaking, respectively. The non-dimensionalized left-hand side then becomes

$$\frac{c_b}{T}\frac{\partial V_{1\beta}^{\prime(0)}}{\partial t} - \frac{c_b\, h_b \sqrt{g\, h_b}}{h_b^2}\frac{\partial}{\partial z'}\left(\nu_t' \frac{\partial V_{1\beta}^{\prime(0)}}{\partial z'}\right) \tag{2.52}$$

This implies that the acceleration is small if the parameter

$$\frac{1}{T}\sqrt{\frac{h_b}{g}} \ll 1 \tag{2.53}$$

Integrating (2.47) for the steady state with the two boundary conditions yields

$$V_{1\beta}^{(0)} = \frac{f_\beta}{\nu_t}\left(\frac{z^2}{2} - \frac{h^2}{6}\right) + \frac{\tau_\beta^B}{\rho\,\nu_t}\left(z - \frac{h}{2}\right) - \frac{Q_{w\beta}}{h} \tag{2.54}$$

Notice that the velocity $V_{1\beta}^{(0)}$ is now written in terms of the (known) short-wave forcing and the bottom friction. Putrevu & Svendsen (1997) show that this expression is the first approximation to the time-dependent solution of (2.47).

From the remainder of (2.44), we have the equation for $V_{1\beta}^{(1)}$, which reads

$$\frac{\partial V_{1\beta}^{(1)}}{\partial t} - \frac{\partial}{\partial z}\left(\nu_t \frac{\partial V_{1\beta}^{(1)}}{\partial z}\right) = -F_\beta \tag{2.55}$$

where

$$F_\beta = V_{1\alpha}^{(0)}\frac{\partial \tilde{V}_\beta}{\partial x_\alpha} + \tilde{V}_\alpha \frac{\partial V_{1\beta}^{(0)}}{\partial x_\alpha} + W\frac{\partial V_{1\beta}^{(0)}}{\partial z} \tag{2.56}$$

The boundary conditions that need to be satisfied are

$$\frac{\partial V_{1\beta}^{(1)}}{\partial z} = 0 \qquad \text{at} \qquad z = -h_o$$

$$\int_{-h_o}^{\bar{\zeta}} V_{1\beta}^{(1)}\,dz = 0$$

Integrating this equation for the steady state and substituting the boundary condition yields

$$V_{1\beta}^{(1)} = V_{1\beta}^{(1)}(\bar{\zeta}) - \int_z^{\bar{\zeta}} \frac{1}{\nu_t}\int_{-h_o}^{z} F_\beta\,dz\,dz \tag{2.57}$$

This result means that the depth variation of $V_{1\beta}^{(1)}$ is known in terms of variables in the depth-integrated equations ($\tilde{V}_\alpha$), the short-wave forcing (through $V_{1\beta}^{(0)}$) and the value of $V_{1\beta}^{(1)}$ at the mean surface elevation. This expression will be used in the next section to transform the nonlinear integrals in (2.31).

2.3 Calculation of Current-current and Current-wave Interaction Terms

In this section, results from the previous section are used to transform the nonlinear integrals in (2.31) in such a way that they can be expressed in terms of the variables in the depth-integrated equations and the known short-wave forcing.

First we split the depth-varying part of the velocity into

$$V_{1\alpha} = V_{1\alpha}^{(0)} + V_{1\alpha}^{(1)} \tag{2.58}$$

as (2.45). The nonlinear integrals in (2.31) can then be expanded to read

$$\begin{aligned} I &= \int_{-h_o}^{\bar{\zeta}} V_{1\alpha} V_{1\beta}\, dz + \overline{\int_{\zeta_t}^{\zeta} u_{w\alpha} V_{1\beta} + u_{w\beta} V_{1\alpha}\, dz} \\ &\approx \int_{-h_o}^{\bar{\zeta}} V_{1\alpha} V_{1\beta}\, dz + V_{1\beta}(\bar{\zeta}) \overline{\int_{\zeta_t}^{\zeta} u_{w\alpha}\, dz} + V_{1\alpha}(\bar{\zeta}) \overline{\int_{\zeta_t}^{\zeta} u_{w\beta}\, dz} \\ &= \int_{-h_o}^{\bar{\zeta}} V_{1\alpha}^{(0)} V_{1\beta}^{(0)}\, dz + \int_{-h_o}^{\bar{\zeta}} V_{1\alpha}^{(0)} V_{1\beta}^{(1)}\, dz + \int_{-h_o}^{\bar{\zeta}} V_{1\beta}^{(0)} V_{1\alpha}^{(1)}\, dz \\ &\quad + \int_{-h_o}^{\bar{\zeta}} V_{1\alpha}^{(1)} V_{1\beta}^{(1)}\, dz + V_{1\beta}(\bar{\zeta}) \overline{\int_{\zeta_t}^{\zeta} u_{w\alpha}\, dz} + V_{1\alpha}(\bar{\zeta}) \overline{\int_{\zeta_t}^{\zeta} u_{w\beta}\, dz} \end{aligned} \tag{2.59}$$

We can neglect the fourth term on the RHS because of the smallness of the $V_{1\alpha}^{(1)}$ term. Using the definition (2.14) and substituting the solution for $V_{1\alpha}^{(1)}$ from (2.57), we have

$$\begin{aligned} I &= \int_{-h_o}^{\bar{\zeta}} V_{1\alpha}^{(0)} V_{1\beta}^{(0)}\, dz + \int_{-h_o}^{\bar{\zeta}} V_{1\alpha}^{(0)} \left(V_{1\beta}^{(1)}(\bar{\zeta}) - \int_z^{\bar{\zeta}} \frac{1}{\nu_t} \int_{-h_o}^{z} F_\beta\, dz\, dz \right) dz \\ &\quad + \int_{-h_o}^{\bar{\zeta}} V_{1\beta}^{(0)} \left(V_{1\alpha}^{(1)}(\bar{\zeta}) - \int_z^{\bar{\zeta}} \frac{1}{\nu_t} \int_{-h_o}^{z} F_\alpha\, dz\, dz \right) dz \\ &\quad + V_{1\beta}(\bar{\zeta})\, Q_{w\alpha} + V_{1\alpha}(\bar{\zeta})\, Q_{w\beta} \end{aligned} \tag{2.60}$$

This can be expanded as

$$I = \int_{-h_o}^{\bar{\zeta}} V_{1\alpha}^{(0)} V_{1\beta}^{(0)}\, dz - \int_{-h_o}^{\bar{\zeta}} V_{1\alpha}^{(0)} \int_z^{\bar{\zeta}} \frac{1}{\nu_t} \int_{-h_o}^{z} F_\beta\, dz\, dz\, dz +$$

$$- \int_{-h_o}^{\bar{\zeta}} V_{1\beta}^{(0)} \int_z^{\bar{\zeta}} \frac{1}{\nu_t} \int_{-h_o}^{z} F_\alpha\, dz\, dz\, dz$$

$$+ V_{1\beta}(\bar{\zeta})\, Q_{w\alpha} - V_{1\beta}^{(1)}(\bar{\zeta})\, Q_{w\alpha} + V_{1\alpha}(\bar{\zeta})\, Q_{w\beta} - V_{1\alpha}^{(1)}(\bar{\zeta})\, Q_{w\beta} \quad (2.61)$$

where (2.50) was used. Using the expansion (2.58) for $V_{1\alpha}$ this gives

$$I = \int_{-h_o}^{\bar{\zeta}} V_{1\alpha}^{(0)} V_{1\beta}^{(0)}\, dz - \int_{-h_o}^{\bar{\zeta}} V_{1\alpha}^{(0)} \int_z^{\bar{\zeta}} \frac{1}{\nu_t} \int_{-h_o}^{z} F_\beta\, dz\, dz\, dz$$

$$- \int_{-h_o}^{\bar{\zeta}} V_{1\beta}^{(0)} \int_z^{\bar{\zeta}} \frac{1}{\nu_t} \int_{-h_o}^{z} F_\alpha\, dz\, dz\, dz$$

$$+ V_{1\beta}^{(0)}(\bar{\zeta})\, Q_{w\alpha} + V_{1\alpha}^{(0)}(\bar{\zeta})\, Q_{w\beta} \quad (2.62)$$

We define the coefficient

$$D_{\alpha\gamma} \equiv \frac{1}{h} \int_{-h_o}^{\bar{\zeta}} V_{1\alpha}^{(0)} \int_z^{\bar{\zeta}} \frac{1}{\nu_t} \int_{-h_o}^{z} V_{1\gamma}^{(0)}\, (dz)^3 \quad (2.63)$$

which has a momentum-dispersive effect as will be shown later. Furthermore, we define

$$G_{1\alpha\beta\gamma} \equiv \int_{-h_o}^{\bar{\zeta}} V_{1\alpha}^{(0)} \int_z^{\bar{\zeta}} \frac{1}{\nu_t} \left(\frac{\partial}{\partial x_\gamma} \int_{-h_o}^{z} V_{1\beta}^{(0)}\, dz - V_{1\beta}^{(0)} \frac{\partial h_o}{\partial x_\gamma} \right) (dz)^2 \quad (2.64)$$

$$G_{2\alpha\beta} \equiv - \int_{-h_o}^{\bar{\zeta}} V_{1\alpha}^{(0)} \int_z^{\bar{\zeta}} \frac{1}{\nu_t} V_{1\beta}^{(0)}\, (h_o + z)\, (dz)^2 \quad (2.65)$$

and

$$M_{\alpha\beta} \equiv \int_{-h_o}^{\bar{\zeta}} V_{1\alpha}^{(0)} V_{1\beta}^{(0)}\, dz + V_{1\alpha}^{(0)}(\bar{\zeta})\, Q_{w\beta} + V_{1\beta}^{(0)}(\bar{\zeta})\, Q_{w\alpha} \quad (2.66)$$

so that (2.62) can be rewritten as

$$I = M_{\alpha\beta} - h\left(D_{\alpha\gamma}\frac{\partial \tilde{V}_\beta}{\partial x_\gamma} + D_{\beta\gamma}\frac{\partial \tilde{V}_\alpha}{\partial x_\gamma} + 2\,D_{\alpha\beta}\frac{\partial \tilde{V}_\gamma}{\partial x_\gamma}\right)$$

$$- \left(G_{1\alpha\beta\gamma} + G_{1\beta\alpha\gamma}\right)\tilde{V}_\gamma - \left(G_{2\alpha\beta} + G_{2\beta\alpha}\right)\frac{\partial \tilde{V}_\gamma}{\partial x_\gamma} \qquad (2.67)$$

The derivation of (2.67) from (2.62) is rather lengthy and is detailed in Appendix A.

With (2.67), (2.31) then becomes

$$\frac{\partial \bar{Q}_\beta}{\partial t} + \frac{\partial}{\partial x_\alpha}\left(\tilde{V}_\alpha \tilde{V}_\beta\, h + M_{\alpha\beta}\right)$$

$$-\frac{\partial}{\partial x_\alpha}\left[h\left(D_{\beta\gamma}\frac{\partial \tilde{V}_\alpha}{\partial x_\gamma} + D_{\alpha\gamma}\frac{\partial \tilde{V}_\beta}{\partial x_\gamma} + 2\,D_{\alpha\beta}\frac{\partial \tilde{V}_\gamma}{\partial x_\gamma}\right)\right]$$

$$-\frac{\partial}{\partial x_\alpha}\left[\left(G_{1\alpha\beta\gamma} + G_{1\beta\alpha\gamma}\right)\tilde{V}_\gamma\right] - \frac{\partial}{\partial x_\alpha}\left[\left(G_{2\alpha\beta} + G_{2\beta\alpha}\right)\frac{\partial \tilde{V}_\gamma}{\partial x_\gamma}\right]$$

$$= -g\,h\frac{\partial \bar{\zeta}}{\partial x_\beta} - \frac{1}{\rho}\frac{\partial}{\partial x_\alpha}\left(S_{\alpha\beta} - \overline{\int_{-h_o}^{\zeta} \tau_{\alpha\beta}\,dz}\right) + \frac{\tau_\beta^S - \tau_\beta^B}{\rho} \qquad (2.68)$$

Notice that we have the following correspondence between the present notation and the notation in Putrevu & Svendsen (1997)'s Eqs. (27) - (30)

$$A_{\alpha\beta\delta}|_{P\&S97} = -G_{1\alpha\beta\gamma} - G_{1\beta\alpha\gamma} \qquad (2.69)$$

$$B_{\alpha\beta}|_{P\&S97} = 2\,D_{\alpha\beta} + \frac{1}{h}\left(G_{2\alpha\beta} + G_{2\beta\alpha}\right) \qquad (2.70)$$

This means that (2.68) can alternatively be rewritten as

$$\frac{\partial \bar{Q}_\beta}{\partial t} + \frac{\partial}{\partial x_\alpha}\left(\tilde{V}_\alpha \tilde{V}_\beta\, h + M_{\alpha\beta}\right)$$

$$-\frac{\partial}{\partial x_\alpha}\left[h\left(D_{\beta\gamma}\frac{\partial \tilde{V}_\alpha}{\partial x_\gamma} + D_{\alpha\gamma}\frac{\partial \tilde{V}_\beta}{\partial x_\gamma} + B_{\alpha\beta}\frac{\partial \tilde{V}_\gamma}{\partial x_\gamma}\right)\right] + \frac{\partial}{\partial x_\alpha}\left[A_{\alpha\beta\gamma}\,\tilde{V}_\gamma\right]$$

$$= -g\,h\frac{\partial \bar{\zeta}}{\partial x_\beta} - \frac{1}{\rho}\frac{\partial}{\partial x_\alpha}\left(S_{\alpha\beta} - \overline{\int_{-h_o}^{\zeta}\tau_{\alpha\beta}\,dz}\right) + \frac{\tau_\beta^S - \tau_\beta^B}{\rho} \tag{2.71}$$

Eqs. (2.8) and (2.68) (or (2.71)) are the quasi 3-D equations. It is important to note here that all the terms in (2.68) including the D and G terms are functions of either the depth-averaged quantities or the $V_{1\alpha}^{(0)}$ velocities, which we can determine by using (2.47) or (2.54). In this form, the governing equations can readily be coded in a numerical model, which solves the two-dimensional horizontal equations numerically while using the semi-analytical solution of (2.47) or (2.54) to represent the effect of the depth-varying currents (or IG waves).

For reference, we will expand (2.71) in x and y. The cross-shore momentum equation then reads

$$\frac{\partial \bar{Q}_x}{\partial t} + \frac{\partial}{\partial x}\left(\tilde{U}^2\,h + M_{xx}\right) + \frac{\partial}{\partial y}\left(\tilde{U}\,\tilde{V}\,h + M_{xy}\right)$$

$$-\frac{\partial}{\partial x}\left[h\left((2\,D_{xx} + B_{xx})\frac{\partial \tilde{U}}{\partial x} + 2\,D_{xy}\frac{\partial \tilde{U}}{\partial y} + B_{xx}\frac{\partial \tilde{V}}{\partial y}\right)\right]$$

$$-\frac{\partial}{\partial y}\left[h\left((D_{xy} + B_{xy})\frac{\partial \tilde{U}}{\partial x} + D_{yy}\frac{\partial \tilde{U}}{\partial y} + D_{xx}\frac{\partial \tilde{V}}{\partial x} + (D_{xy} + B_{xy})\frac{\partial \tilde{V}}{\partial y}\right)\right]$$

$$+\frac{\partial}{\partial x}\left[A_{xxx}\,\tilde{U} + A_{xxy}\,\tilde{V}\right] + \frac{\partial}{\partial y}\left[A_{xyx}\,\tilde{U} + A_{xyy}\,\tilde{V}\right]$$

$$= -g\,h\frac{\partial \bar{\zeta}}{\partial x} - \frac{1}{\rho}\left(\frac{\partial S_{xx}}{\partial x} + \frac{\partial S_{xy}}{\partial y}\right) + \frac{1}{\rho}\left(\frac{\partial}{\partial x}\overline{\int_{-h_o}^{\zeta}\tau_{xx}\,dz} + \frac{\partial}{\partial y}\overline{\int_{-h_o}^{\zeta}\tau_{xy}\,dz}\right)$$

$$+\frac{\tau_x^S - \tau_x^B}{\rho} \tag{2.72}$$

For the longshore momentum equation we get

$$\frac{\partial \bar{Q}_y}{\partial t} + \frac{\partial}{\partial x}\left(\tilde{U}\,\tilde{V}\,h + M_{xy}\right) + \frac{\partial}{\partial y}\left(\tilde{V}^2\,h + M_{yy}\right)$$

$$-\frac{\partial}{\partial x}\left[h\left((D_{xy} + B_{xy})\frac{\partial \tilde{U}}{\partial x} + D_{yy}\frac{\partial \tilde{U}}{\partial y} + (D_{xx}\frac{\partial \tilde{V}}{\partial x} + (D_{xy} + B_{xy})\frac{\partial \tilde{V}}{\partial y}\right)\right]$$

$$-\frac{\partial}{\partial y}\left[h\left(B_{yy}\frac{\partial \tilde{U}}{\partial x} + 2\,D_{xy}\frac{\partial \tilde{V}}{\partial x} + (2\,D_{yy} + B_{yy})\frac{\partial \tilde{V}}{\partial y}\right)\right]$$

$$+\frac{\partial}{\partial x}\left[A_{xyx}\,\tilde{U} + A_{xyy}\,\tilde{V}\right] + \frac{\partial}{\partial y}\left[A_{yyx}\,\tilde{U} + A_{yyy}\,\tilde{V}\right]$$

$$= -g\,h\frac{\partial \bar{\zeta}}{\partial y} - \frac{1}{\rho}\left(\frac{\partial S_{xy}}{\partial x} + \frac{\partial S_{yy}}{\partial y}\right) + \frac{1}{\rho}\left(\frac{\partial}{\partial x}\overline{\int_{-h_o}^{\zeta}\tau_{xy}\,dz} + \frac{\partial}{\partial y}\overline{\int_{-h_o}^{\zeta}\tau_{yy}\,dz}\right)$$

$$+\frac{\tau_y^S - \tau_y^B}{\rho} \tag{2.73}$$

2.4 Calculation of the Quasi 3-D Terms in the (Quasi) Steady State

In the quasi steady state (i.e., when the local acceleration is small), we can determine the current profiles of $V_{1\beta}^{(0)}$ by integrating (2.47) twice and applying the boundary conditions to yield (2.54). We can rewrite this equation using a transformation of the vertical coordinate z to a new coordinate ξ, so that

$$\xi = z + h_o \tag{2.74}$$

which means that $\xi = 0$ at the local bottom and $\xi = h = h_o + \bar{\zeta}$ at the mean surface elevation. Eq. (2.54) then becomes

$$V_{1\beta}^{(0)} = \frac{f_\beta}{2\,\nu_t}\xi^2 + \frac{\tau_\beta^B}{\rho\,\nu_t}\xi - \left(\frac{f_\beta}{6\,\nu_t}h^2 + \frac{\tau_\beta^B}{\rho\,\nu_t}\frac{h}{2} + \frac{Q_{w\beta}}{h}\right) \tag{2.75}$$

For simplicity we can write this as

$$V_{1\beta}^{(0)} = b_1\,\xi^2 + b_2\,\xi + b_3 \tag{2.76}$$

where

$$b_1 = \frac{f_\beta}{2\,\nu_t} \tag{2.77}$$

$$b_2 = \frac{\tau_\beta^B}{\rho\,\nu_t} \tag{2.78}$$

$$b_3 = -\left(\frac{b_1}{3}\,h^2 + b_2\,\frac{h}{2} + \frac{Q_{w\beta}}{h}\right) \tag{2.79}$$

Equivalently we can write

$$V_{1\alpha}^{(0)} = a_1\,\xi^2 + a_2\,\xi + a_3 \tag{2.80}$$

where a_1, a_2 and a_3 have the equivalent definitions for direction α.

Using (2.76) and (2.80) we can express the coefficients (2.63)-(2.66) in terms of known variables and parameters. After some manipulations the dispersion coefficient (2.63) can be rewritten as

$$\begin{aligned} D_{\alpha\beta} = \frac{1}{\nu_t}\Bigg(& a_1\,b_1\,\frac{h^6}{63} + (a_1\,b_2 + a_2\,b_1)\,\frac{h^5}{36} \\ & + (a_1\,b_3 + \frac{3}{4}\,a_2\,b_2 + a_3\,b_1)\,\frac{h^4}{15} \\ & + (a_2\,b_3 + a_3\,b_2)\,\frac{h^3}{8} + a_3\,b_3\,\frac{h^2}{3}\Bigg) \end{aligned} \tag{2.81}$$

Notice that the result is symmetrical in a and b or, in other words, in direction.

We can write (2.66) as

$$\begin{aligned} M_{\alpha\beta} = & \; a_1\,b_1\,\frac{h^5}{5} + (a_1\,b_2 + a_2\,b_1)\,\frac{h^4}{4} \\ & + (a_1\,b_3 + a_2\,b_2 + a_3\,b_1)\,\frac{h^3}{3} + (a_2\,b_3 + a_3\,b_2)\,\frac{h^2}{2} + a_3\,b_3\,h \end{aligned}$$

$$+(a_1\,h^2\,+\,a_2\,h\,+\,a_3)\,Q_{w\beta}\,+\,(b_1\,h^2\,+\,b_2\,h\,+\,b_3)\,Q_{w\alpha} \qquad (2.82)$$

which is also directionally symmetrical.

Eq. (2.69) can be expressed as

$$\begin{aligned} A_{\alpha\beta\gamma} \;=\; -\frac{1}{\nu_t}\Bigg[& \frac{\partial a_1\,b_1}{\partial x_\gamma}\,\frac{h^7}{63} + \left(\frac{\partial a_1\,b_2}{\partial x_\gamma} + \frac{\partial a_2\,b_1}{\partial x_\gamma}\right)\frac{h^6}{36} + \\ & \left(\frac{\partial a_1\,b_3}{\partial x_\gamma} + \frac{\partial a_3\,b_1}{\partial x_\gamma}\right)\frac{h^5}{15} + \frac{\partial a_2\,b_2}{\partial x_\gamma}\,\frac{h^5}{20} + \\ & \left(\frac{\partial a_2\,b_3}{\partial x_\gamma} + \frac{\partial a_3\,b_2}{\partial x_\gamma}\right)\frac{h^4}{8} + \frac{\partial a_3\,b_3}{\partial x_\gamma}\,\frac{h^3}{3}\Bigg] \end{aligned} \qquad (2.83)$$

This expression is symmetrical in the first two indices.

Finally, Eq. (2.70) becomes

$$\begin{aligned} B_{\alpha\beta} \;=\; -\frac{h^3}{\nu_t}\Bigg[& \frac{4}{63}\,a_1\,b_1\,h^3 + (a_1\,b_2\,+\,a_2\,b_1)\,\frac{h^2}{12} + a_2\,b_2\,\frac{h}{10} + \\ & \frac{2}{15}\,(a_1\,b_3\,+\,a_3\,b_1)\,h\,+\,\frac{1}{8}\,(a_2\,b_3\,+\,a_3\,b_2)\Bigg] \end{aligned} \qquad (2.84)$$

which is also symmetrical. The (partial) symmetry of the terms allows us to calculate less coefficients, which will make the numerical model more efficient. These expressions will be used to calculate the quasi 3-D terms in Chapter 5.

2.5 Reduction of the Equations on a Cylindrical Beach

Svendsen & Putrevu (1994a) [SP94] presented the quasi 3-D equations for the special case of a cylindrical (longshore uniform) beach with longshore uniform, steady forcing. In this section, we will show that the general formula (2.68) for the y-momentum equation is consistent with SP94's results.

We first substitute (2.67) back into (2.68)

$$\frac{\partial \bar{Q}_\beta}{\partial t} - \frac{\partial}{\partial x_\alpha}\left(\int_{-h_o}^{\bar{\zeta}} V_{1\alpha}^{(0)} \int_z^{\bar{\zeta}} \frac{1}{\nu_t}\int_{-h_o}^{z} F_\beta\,(dz)^3 + \int_{-h_o}^{\bar{\zeta}} V_{1\beta}^{(0)} \int_z^{\bar{\zeta}} \frac{1}{\nu_t}\int_{-h_o}^{z} F_\alpha\,(dz)^3\right)$$

$$+\frac{\partial}{\partial x_\alpha}\left(\tilde{V}_\alpha\,\tilde{V}_\beta\,h + \int_{-h_o}^{\bar{\zeta}} V_{1\alpha}^{(0)}\,V_{1\beta}^{(0)}\,dz + V_{1\alpha}^{(0)}(\bar{\zeta})\,Q_{w\beta} + V_{1\beta}^{(0)}(\bar{\zeta})\,Q_{w\alpha}\right)$$

$$= -\,g\,h\,\frac{\partial \bar{\zeta}}{\partial x_\beta} - \frac{1}{\rho}\frac{\partial}{\partial x_\alpha}\left(S_{\alpha\beta} - \overline{\int_{-h_o}^{\zeta} \tau_{\alpha\beta}\,dz}\right) + \frac{\tau_\beta^S - \tau_\beta^B}{\rho} \tag{2.85}$$

Under the assumption of steady, longshore uniform conditions without wind forcing, we can reduce the y-component of (2.85) to

$$-\frac{d}{d\,x}\left(\int_{-h_o}^{\bar{\zeta}} U_1^{(0)} \int_z^{\bar{\zeta}} \frac{1}{\nu_t}\int_{-h_o}^{z} F_y\,(dz)^3 + \int_{-h_o}^{\bar{\zeta}} V_1^{(0)} \int_z^{\bar{\zeta}} \frac{1}{\nu_t}\int_{-h_o}^{z} F_x\,(dz)^3\right)$$

$$+\frac{d}{d\,x}\left(\int_{-h_o}^{\bar{\zeta}} U_1^{(0)}\,V_1^{(0)}\,dz + U_1^{(0)}(\bar{\zeta})\,Q_{wy} + V_1^{(0)}(\bar{\zeta})\,Q_{wx}\right)$$

$$= -\frac{1}{\rho}\frac{d}{d\,x}\left(S_{xy} - \overline{\int_{-h_o}^{\zeta} \tau_{xy}\,dz}\right) - \frac{\tau_y^B}{\rho} \tag{2.86}$$

where under longshore uniform conditions $\tilde{U} \equiv 0$. Substituting from (2.57)

$$\int_z^{\bar{\zeta}} \frac{1}{\nu_t}\int_{-h_o}^{z} F_\beta\,dz\,dz = V_{1\beta}^{(1)}(\bar{\zeta}) - V_{1\beta}^{(1)} \tag{2.87}$$

(2.86) becomes

$$-\frac{d}{d\,x}\left(\int_{-h_o}^{\bar{\zeta}} U_1^{(0)}(V_1^{(1)}(\bar{\zeta}) - V_1^{(1)})\,dz + \int_{-h_o}^{\bar{\zeta}} V_1^{(0)}(U_1^{(1)}(\bar{\zeta}) - U_1^{(1)})\,dz\right)$$

$$+\frac{d}{d\,x}\left(\int_{-h_o}^{\bar{\zeta}} U_1^{(0)}\,V_1^{(0)}\,dz + U_1^{(0)}(\bar{\zeta})\,Q_{wy} + V_1^{(0)}(\bar{\zeta})\,Q_{wx}\right)$$

$$= -\frac{1}{\rho}\frac{d}{d\,x}\left(S_{xy} - \overline{\int_{-h_o}^{\zeta} \tau_{xy}\,dz}\right) - \frac{\tau_y^B}{\rho} \tag{2.88}$$

We arrange and add back in the neglected term of (2.59), which gives

$$\frac{d}{d\,x}\left(\int_{-h_o}^{\bar{\zeta}} U_1^{(0)}\,V_1^{(0)} + U_1^{(0)}\,V_1^{(1)} + V_1^{(0)}\,U_1^{(1)} + U_1^{(1)}\,V_1^{(1)}\,dz\right) +$$

$$\frac{d}{d\,x}\left(\int_{-h_o}^{\bar{\zeta}} (-V_1^{(1)}(\bar{\zeta})\,U_1^{(0)} - U_1^{(1)}(\bar{\zeta})\,V_1^{(0)})\,dz + U_1^{(0)}(\bar{\zeta})\,Q_{wy} + V_1^{(0)}(\bar{\zeta})\,Q_{wx}\right)$$

$$= -\frac{1}{\rho}\frac{d}{d\,x}\left(S_{xy} - \overline{\int_{-h_o}^{\zeta} \tau_{xy}\,dz}\right) - \frac{\tau_y^B}{\rho} \tag{2.89}$$

We undo the split in the current velocities, (2.58), use (2.50) and the definition (2.14), so that (2.6) can be rewritten as

$$\frac{d}{d\,x}\left(\int_{-h_o}^{\bar{\zeta}} U_1\,V_1\,dz + U_1(\bar{\zeta})\,\overline{\int_{\zeta_t}^{\zeta} v_w\,dz} + V_1(\bar{\zeta})\,\overline{\int_{\zeta_t}^{\zeta} u_w\,dz}\right)$$

$$= -\frac{1}{\rho}\frac{d}{d\,x}\left(S_{xy} - \overline{\int_{-h_o}^{\zeta} \tau_{xy}\,dz}\right) - \frac{\tau_y^B}{\rho} \tag{2.90}$$

This can be approximated (as was done in SP94 in their Eq. (2.9)) to

$$\frac{d}{d\,x}\left(\overline{\int_{-h_o}^{\bar{\zeta}} U_1\,V_1 + U_1\,v_w + V_1\,u_w\,dz}\right) =$$

$$-\frac{1}{\rho}\frac{d}{d\,x}\left(S_{xy} - \overline{\int_{-h_o}^{\zeta} \tau_{xy}\,dz}\right) - \frac{\tau_y^B}{\rho} \tag{2.91}$$

which is their Eq. (2.8). From there, their derivation can be followed to yield the quasi 3-D y-momentum equation in the case of a cylindrical coast Q.E.D.

This result means that the present quasi 3-D equations reduce to the previously found result for the special case of longshore uniformity.

2.6 Energy Equations

In this section the energy equations for the total motion, the short-wave motion and the long-wave motion are given in the present notation. They are

essentially the equations given in Phillips (1977) with some modifications as derived by Schäffer (1993). The energy equation of the short waves can be used as a wave driver if the wave pattern is known. This equation is applied in Chapter 4.4. The energy equation of the long waves will be used in Chapter 4 as a tool for the analysis of the transfer of energy.

The energy equation for the total motion can be written as

$$\frac{\partial}{\partial t}\left(E + \frac{1}{2}\rho g \bar{\zeta}^2 + \frac{1}{2}\rho\left(\frac{\bar{Q}_\alpha^2}{h} - \frac{Q_{w\alpha}^2}{h}\right)\right) +$$

$$\frac{\partial}{\partial x_\alpha}\left(E_{f\alpha} + \tilde{V}_\alpha E + \tilde{V}_\beta S'_{\alpha\beta} + \right.$$

$$\left.\rho \bar{Q}_\alpha\left[\frac{1}{2}\left(\frac{\bar{Q}_\beta}{h}\right)^2 - \frac{1}{2}\left(\frac{Q_{w\beta}}{h}\right)^2 + g\bar{\zeta}\right]\right) - \mathcal{D} = 0 \qquad (2.92)$$

where $\mathcal{D}$ is the total dissipation. E is the energy density in the short waves

$$E = \overline{\int_{-h_o}^{\zeta} \frac{1}{2}\rho\left(u_{w\alpha}^2 + w^2\right) dz} + \frac{1}{2}\rho g \overline{\eta^2} \qquad (2.93)$$

where w is the vertical short-wave induced velocity and η is the surface elevation above the mean water level (as opposed to SWL). $E_{f\alpha}$ is the energy flux in the short waves

$$E_{f\alpha} \equiv \overline{\int_{-h_o}^{\zeta} u_{w\alpha}\left(p\,\delta_{\alpha\beta} + \rho g z - \rho g \bar{\zeta} + \frac{1}{2}\rho\left(u_{w\beta}^2 + w^2\right)\right) dz} \qquad (2.94)$$

In order to be consistent with Phillips (1977), his definition of the radiation stress is used

$$S'_{\alpha\beta} \equiv \overline{\int_{-h_o}^{\zeta} (p\,\delta_{\alpha\beta} + \rho\, u_{w\alpha}\, u_{w\beta})\, dz} - \delta_{\alpha\beta}\frac{1}{2}\rho g h^2 - \rho\frac{Q_{w\alpha} Q_{w\beta}}{h} \qquad (2.95)$$

The governing equation for the short waves can then be written as

$$\frac{\partial}{\partial t}\left(E - \frac{1}{2}\rho\frac{Q_{w\alpha}^2}{h}\right) + \frac{\partial}{\partial x_\alpha}\left(E_{f\alpha} + \tilde{V}_\alpha E - \frac{1}{2}\bar{Q}_\alpha\left(\frac{Q_{w\beta}}{h}\right)^2\right) +$$

$$S'_{\alpha\beta}\frac{\partial \tilde{V}_\beta}{\partial x_\alpha} - \frac{Q_{w\beta}}{h}\frac{\partial S'_{\alpha\beta}}{\partial x_\alpha} - \mathcal{D} - \tilde{V}_\alpha \tau_{b\alpha} = 0 \tag{2.96}$$

This equation can in principle be used as a time-dependent short-wave driver to calculate the wave heights (and hence the wave-induced volume flux and the radiation stresses) in the domain if the wave pattern is already known.

The energy equation for the long waves (or currents) reads

$$\frac{\partial}{\partial t}\left(\frac{1}{2}\rho\left(g\bar{\zeta}^2 + \frac{\bar{Q}_\alpha^2}{h}\right)\right) + \frac{\partial}{\partial x_\alpha}\left(\frac{1}{2}\rho\bar{Q}_\alpha\left(\frac{\bar{Q}_\beta}{h}\right)^2 + \rho g\bar{\zeta}\bar{Q}_\alpha\right) +$$

$$\frac{\bar{Q}_\alpha}{h}\frac{\partial S'_{\alpha\beta}}{\partial x_\beta} + \tilde{V}_\alpha \tau_{b\alpha} = 0 \tag{2.97}$$

This equation (in the present or linearized form) is used in Chapter 4 and 5 as a tool of the analysis of the transfer of energy from the short waves to the long (infragravity) waves. Eqs. (2.96) and (2.97) are complementary, which means that their sum is the energy equation of the total motion (2.92).

Chapter 3

NUMERICAL MODEL AND BOUNDARY CONDITIONS

In this chapter the numerical model SHORECIRC, which solves the governing equations of Chapter 2, is described. First, the numerical method is presented and checked for stability and accuracy, which gives insight into the nature of the leading error inherent in the scheme.

In Sections 3.2 and 3.3 the boundary conditions of the nearshore model domain are described in detail. Fig. 3.1 shows a typical domain (in this case the bathymetry of the U.S. Corps of Engineers' Field Research Facility at Duck, NC on October 10, 1990), which can be used in the SHORECIRC model.

An important part of this thesis is the development of accurate boundary conditions at the "open" boundaries and at the moving shoreline. In Section 3.2 an absorbing-generating boundary condition is developed at the "open" boundaries. Its accuracy is measured on the basis of an analysis of the reflection error. The shoreline boundary condition, which is based on an inundation/drainage procedure, is described in Section 3.3. The performance of this condition is measured against a well-known analytical solution for longshore uniform run-up and against two highly accurate numerical solutions for the case of two-dimensional run-up on a concave beach.

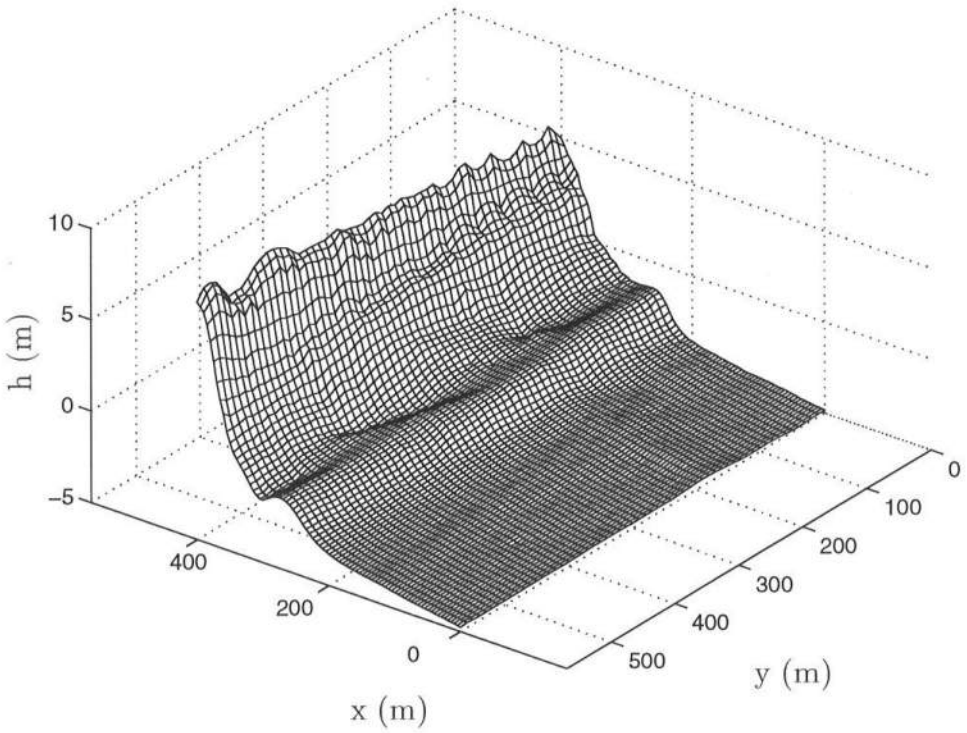

Figure 3.1: Typical bathymetry at the U.S. Corps of Engineers' Field Research Facility at Duck, NC taken on October 10, 1990.

3.1 Numerical Scheme

The governing equations (2.8) and (2.71) will be solved using a finite difference scheme on a fixed spatial grid. An explicit second-order Adams-Bashforth predictor scheme and a third-order Adams-Moulton corrector time-stepping scheme (Atkinson, 1978, p. 388) with $O(\Delta t^3)$ overall accuracy (when applied to ODE's) is used. The advantage of this type of scheme is that it is explicit and easy to code but the disadvantage is that the stability range is limited and that all calculations have to be done twice per time step.

Eqs. (2.8) and (2.71) are rewritten so that only the local acceleration

appears on the left-hand side, or

$$\frac{\partial \bar{\zeta}}{\partial t} = N \tag{3.1}$$

$$\frac{\partial \bar{Q}_\beta}{\partial t} = M_\beta \tag{3.2}$$

where N and M_β are the right-hand sides of the continuity and momentum equations, respectively.

The second-order Adams-Bashforth predictor step then reads

$$\bar{\zeta}_i^* = \bar{\zeta}_i^n + \frac{\Delta t}{2}\left(3\,N_i^n - N_i^{n-1}\right) + O(\Delta t^2) \tag{3.3}$$

$$\bar{Q}_{\beta i}^* = \bar{Q}_{\beta i}^n + \frac{\Delta t}{2}\left(3\,M_{\beta i}^n - M_{\beta i}^{n-1}\right) + O(\Delta t^2) \tag{3.4}$$

where subscript i indicates the spatial index, while superscripts $*$, n and $n+1$ denote the time-level at the predictor step, at $t = t^n$ and $t = t^{n-1}$, respectively.

The third-order Adams-Moulton corrector step reads

$$\bar{\zeta}_i^{n+1} = \bar{\zeta}_i^n + \frac{\Delta t}{12}\left(5\,N_i^* + 8\,N_i^n - N_i^{n-1}\right) + O(\Delta t^3) \tag{3.5}$$

$$\bar{Q}_{\beta i}^{n+1} = \bar{Q}_{\beta i}^n + \frac{\Delta t}{12}\left(5\,M_{\beta i}^* + 8\,M_{\beta i}^n - M_{\beta i}^{n-1}\right) + O(\Delta t^3) \tag{3.6}$$

The advantage of this method is that it is explicit while maintaining a high accuracy in Δt. As will be shown in Chapter 3.1.2., the overall method has an accuracy of $O(\Delta t^3, \Delta x^2, \Delta x^2 \Delta t, \Delta y^2, \Delta y^2 \Delta t)$.

The right-hand sides of the equations contain spatial derivatives, which are solved using a central difference scheme of $O(\Delta x^2)$ in the interior of the domain. At the boundary points we will apply a 3-point scheme of the same order.

3.1.1 Stability

The stability of this scheme can be determined by performing a Von Neumann (or Fourier) stability analysis (e.g., Twizell, 1984) on the linearized set of equations, which reads

$$\begin{aligned}
\frac{\partial \zeta}{\partial t} &= -\frac{\partial Q_x}{\partial x} - \frac{\partial Q_y}{\partial y} \\
\frac{\partial Q_x}{\partial t} &= -g\, h_o \frac{\partial \zeta}{\partial x} + F_x \qquad (3.7) \\
\frac{\partial Q_y}{\partial t} &= -g\, h_o \frac{\partial \zeta}{\partial y} + F_y
\end{aligned}$$

where F_x and F_y represent the forcing, which in the present model is not solved by an additional equation (such as the energy equation) but is known analytically or through a wave driver. As will be seen below, these forcing terms do not enter the amplification matrix and are not important in the stability analysis. Notice that in this and further equations we will drop the overbar.

In the predictor step the set (3.7) reads

$$\begin{aligned}
\frac{\zeta^*_{i,j} - \zeta^n_{i,j}}{\Delta t} &= -\frac{1}{2}\left(3\left(\frac{Q^n_{i+1,j} - Q^n_{i-1,j}}{2\,\Delta x}\right) - \left(\frac{Q^{n-1}_{i+1,j} - Q^{n-1}_{i-1,j}}{2\,\Delta x}\right)\right. \\
&\quad \left. + 3\left(\frac{P^n_{i,j+1} - P^n_{i,j-1}}{2\,\Delta y}\right) - \left(\frac{P^{n-1}_{i,j+1} - P^{n-1}_{i,j-1}}{2\,\Delta y}\right)\right) \\
\frac{Q^*_{i,j} - Q^n_{i,j}}{\Delta t} &= -\frac{g\, h_o}{2}\left(3\left(\frac{\zeta^n_{i+1,j} - \zeta^n_{i-1,j}}{2\,\Delta x}\right) - \left(\frac{\zeta^{n-1}_{i+1,j} - \zeta^{n-1}_{i-1,j}}{2\,\Delta x}\right)\right) \qquad (3.8) \\
&\quad + F_x \\
\frac{P^*_{i,j} - P^n_{i,j}}{\Delta t} &= -\frac{g\, h_o}{2}\left(3\left(\frac{\zeta^n_{i,j+1} - \zeta^n_{i,j-1}}{2\,\Delta y}\right) - \left(\frac{\zeta^{n-1}_{i,j+1} - \zeta^{n-1}_{i,j-1}}{2\,\Delta y}\right)\right) + F_y
\end{aligned}$$

where the superscripts indicate the time-level. ζ^n is the value of the surface elevation at $t = t^n$ and the predictor level is indicated by the *. We have used the short-hand notation Q for Q_x and P for Q_y. The subscripts indicate the node in the spatial domain.

The corrector step reads

$$\begin{aligned}
\frac{\zeta_{i,j}^{n+1} - \zeta_{i,j}^{n}}{\Delta t} &= -\frac{1}{12}\left(5\left(\frac{Q_{i+1,j}^{*} - Q_{i-1,j}^{*}}{2\,\Delta x}\right) + 8\left(\frac{Q_{i+1,j}^{n} - Q_{i-1,j}^{n}}{2\,\Delta x}\right)\right. \\
&\quad - \left(\frac{Q_{i+1,j}^{n-1} - Q_{i-1,j}^{n-1}}{2\,\Delta x}\right) + 5\left(\frac{P_{i,j+1}^{*} - P_{i,j-1}^{*}}{2\,\Delta y}\right) \\
&\quad \left. + 8\left(\frac{P_{i,j+1}^{n} - P_{i,j-1}^{n}}{2\,\Delta y}\right) - \left(\frac{P_{i,j+1}^{n-1} - P_{i,j-1}^{n-1}}{2\,\Delta y}\right)\right) \\
\frac{Q_{i,j}^{n+1} - Q_{i,j}^{n}}{\Delta t} &= -\frac{g\,h_o}{12}\left(5\left(\frac{\zeta_{i+1,j}^{*} - \zeta_{i-1,j}^{*}}{2\,\Delta x}\right) + 8\left(\frac{\zeta_{i+1,j}^{n} - \zeta_{i-1,j}^{n}}{2\,\Delta x}\right)\right. \\
&\quad \left. - \left(\frac{\zeta_{i+1,j}^{n-1} - \zeta_{i-1,j}^{n-1}}{2\,\Delta x}\right)\right) + F_x \qquad (3.9) \\
\frac{P_{i,j}^{n+1} - P_{i,j}^{n}}{\Delta t} &= -\frac{g\,h_o}{12}\left(5\left(\frac{\zeta_{i,j+1}^{*} - \zeta_{i,j-1}^{*}}{2\,\Delta y}\right) + 8\left(\frac{\zeta_{i,j+1}^{n} - \zeta_{i,j-1}^{n}}{2\,\Delta y}\right)\right. \\
&\quad \left. - \left(\frac{\zeta_{i,j+1}^{n-1} - \zeta_{i,j-1}^{n-1}}{2\,\Delta y}\right)\right) + F_y
\end{aligned}$$

In the following we will analyze the stability of this predictor-corrector scheme following the procedure of Twizell (1984), which was also used by Wei (1997). We will restrict ourselves in this analysis to the 1-DH equations for reasons of clarity and brevity in the notation. The method itself is applicable to the sets of 2-DH finite-differenced equations (3.8) and (3.9).

The stability range of the overall scheme can be found by substituting (3.8)

into (3.9), which in the case of one-dimensional flow yields the following combined set of finite-difference equations

$$\begin{aligned}
\zeta_i^{n+1} &= \zeta_i^n - \frac{\Delta t}{24\,\Delta x}\left(5\left(Q_{i+1}^n - \frac{g\,h_o\,\Delta t}{4\,\Delta x}\left[3\,\zeta_{i+2}^n - 3\,\zeta_i^n - \zeta_{i+2}^{n-1} + \zeta_i^{n-1}\right]\right)\right. \\
&\quad -5\left(Q_{i-1}^n - \frac{g\,h_o\,\Delta t}{4\,\Delta x}\left[3\,\zeta_i^n - 3\,\zeta_{i-2}^n - \zeta_i^{n-1} + \zeta_{i-2}^{n-1}\right]\right) \\
&\quad \left.+8\left(Q_{i+1}^n - Q_{i-1}^n\right) - \left(Q_{i+1}^{n-1} - Q_{i-1}^{n-1}\right)\right) \qquad (3.10)
\end{aligned}$$

$$\begin{aligned}
Q_i^{n+1} &= Q_i^n - \frac{g\,h_o\,\Delta t}{24\,\Delta x}\left(5\left(\zeta_{i+1}^n - \frac{\Delta t}{4\,\Delta x}\left[3\,Q_{i+2}^n - 3\,Q_i^n - Q_{i+2}^{n-1} + Q_i^{n-1}\right]\right)\right. \\
&\quad -5\left(\zeta_{i-1}^n - \frac{\Delta t}{4\,\Delta x}\left[3\,Q_i^n - 3\,Q_{i-2}^n - Q_i^{n-1} + Q_{i-2}^{n-1}\right]\right) \\
&\quad \left.+8\left(\zeta_{i+1}^n - \zeta_{i-1}^n\right) - \left(\zeta_{i+1}^{n-1} - \zeta_{i-1}^{n-1}\right)\right) + F_x \qquad (3.11)
\end{aligned}$$

In the Von Neumann stability analysis the numerical solution is split into an exact solution to the finite difference equation and an error term as

$$\begin{aligned}
\zeta &= \zeta^e + \eta \\
Q &= Q^e + q
\end{aligned} \qquad (3.12)$$

where ζ^e and Q^e are the exact solutions, and η and q are the error terms. By definition, the exact solutions must satisfy (3.10) and (3.11) identically and those two equations therefore reduce to a set of finite difference equations in η and q, respectively. These error terms can be represented as a Fourier series

$$\eta_i^n = \sum_{m=1}^{\infty} \eta_o \, e^{i\,(k_m\, x_i \,-\, n\,\omega_m\,\Delta t)}$$

$$q_i^n = \sum_{m=1}^{\infty} q_o \, e^{i\,(k_m\, x_i \,-\, n\,\omega_m\,\Delta t)} \tag{3.13}$$

and the question addressed is whether such errors grow or decay in time. To answer this question we consider one particular mode m, substitute that mode into (3.10), and define the parameter

$$r = \nu \, \sin k\Delta x \tag{3.14}$$

where ν is the Courant number

$$\nu = c_o \frac{\Delta t}{\Delta x} \tag{3.15}$$

and $c_o = \sqrt{g\,h_o}$. After some rearranging we get from (3.10)

$$\eta_i^{n+1} = \eta_i^n \left(1 - \frac{5}{8} r^2\right) + q_i^n \left(-\frac{13}{12}\, i\, \frac{r}{c_o}\right)$$

$$+ \eta_i^{n-1} \left(\frac{5}{24} r^2\right) + q_i^{n-1} \left(\frac{1}{12}\, i\, \frac{r}{c_o}\right) \tag{3.16}$$

where $i = \sqrt{-1}$ (when it is not used as a subscript) and where we have used the trigonometric identities

$$\sin k\Delta x = \frac{e^{i\,k\Delta x} - e^{-i\,k\Delta x}}{2\,i} \tag{3.17}$$

and

$$\cos k\Delta x = \frac{e^{i\,k\Delta x} + e^{-i\,k\Delta x}}{2} \tag{3.18}$$

in the derivation.

In a similar way we find by substitution of (3.13) into the x-momentum equation (3.11)

$$q_i^{n+1} = \eta_i^n \left(-\frac{13}{12}\, i\, c_o\, r\right) + q_i^n \left(1 - \frac{5}{8}\, r^2\right)$$

$$+ \eta_i^{n-1} \left(\frac{1}{12}\, i\, c_o\, r\right) + q_i^{n-1} \left(\frac{5}{24}\, r^2\right) + F_x \tag{3.19}$$

To determine the stability, we combine (3.16) and (3.19) into a single matrix equation

$$\mathbf{Z}^{n+1} = \mathbf{A}\, \mathbf{Z}^n + \mathbf{F} \tag{3.20}$$

where

$$\mathbf{Z}^{n+1} = [\, \eta^{n+1}\,,\, q^{n+1}\,,\, \eta^n\,,\, q^n\,]^T \tag{3.21}$$

$$\mathbf{Z}^n = [\, \eta^n\,,\, q^n\,,\, \eta^{n-1}\,,\, q^{n-1}\,]^T \tag{3.22}$$

and

$$\mathbf{F} = [\, 0\,,\, F_x\,,\, 0\,,\, 0\,]^T \tag{3.23}$$

The amplification matrix $\mathbf{A}$ then reads from (3.16) and (3.19)

$$\mathbf{A} = \begin{pmatrix} 1 - \frac{5}{8}\, r^2 & -\frac{13}{12}\, i\, \frac{r}{c_o} & \frac{5}{24}\, r^2 & \frac{1}{12}\, i\, \frac{r}{c_o} \\ -\frac{13}{12}\, i\, c_o\, r & 1 - \frac{5}{8}\, r^2 & \frac{1}{12}\, i\, c_o\, r & \frac{5}{24}\, r^2 \\ 1 & 0 & 0 & 0 \\ 0 & 1 & 0 & 0 \end{pmatrix} \tag{3.24}$$

The matrix $\mathbf{A}$ can be diagonalized as

$$\mathbf{A} = \lambda_p\, \mathbf{I} \tag{3.25}$$

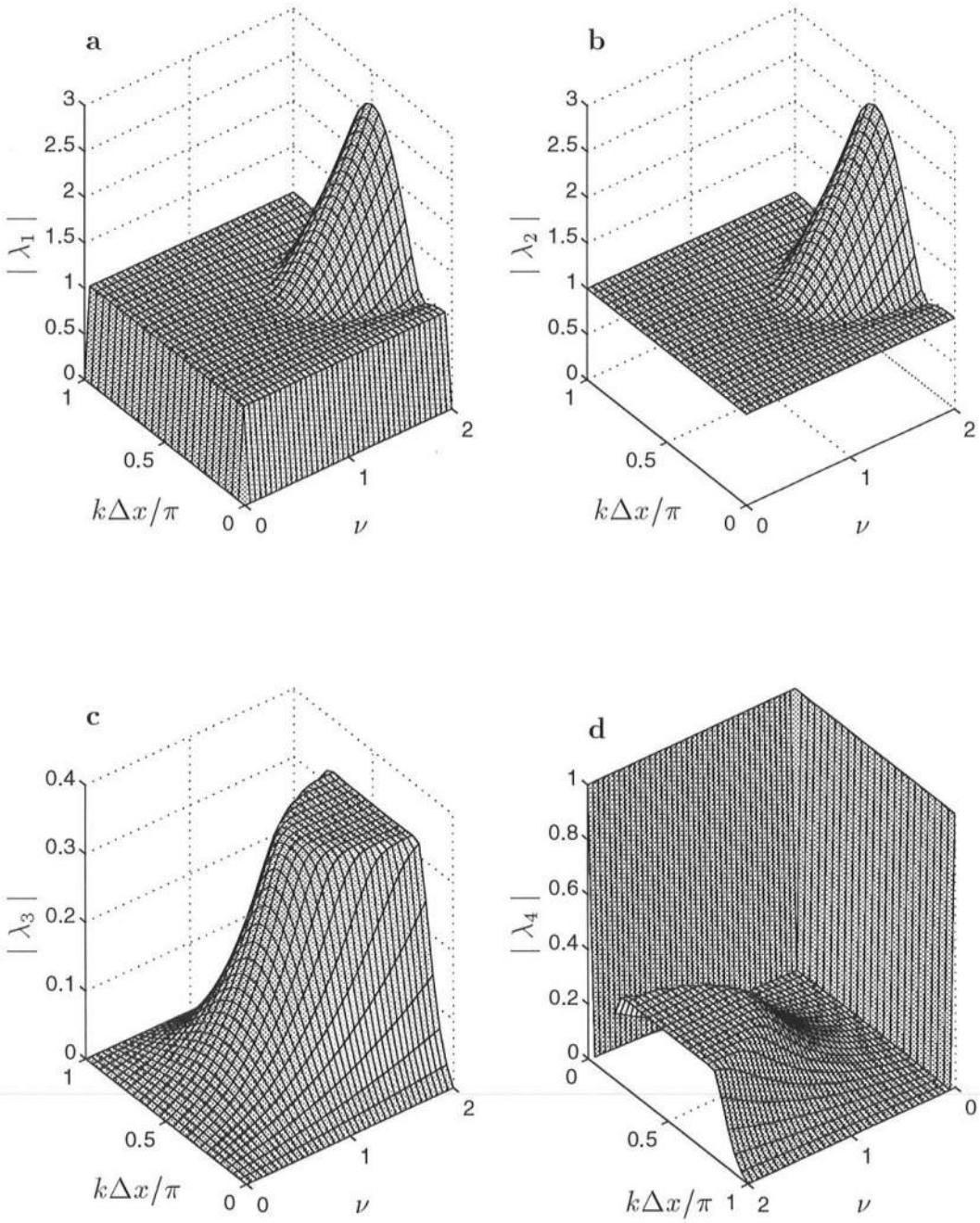

Figure 3.2: Variation of the absolute eigenvalues $|\lambda_p|$ versus the Courant number ν and the wave number $k\Delta x$: (a) $|\lambda_1|$; (b) $|\lambda_2|$; (c) $|\lambda_3|$; (d) $|\lambda_4|$.

where λ_p $(p = 1, 2, 3, 4)$ is a vector containing the four eigenvalues of $\mathbf{A}$. For a given c_o, these eigenvalues are a function of r, which itself depends on the Courant number ν and the wave number $k\Delta x$.

For the error vector $\mathbf{Z}$ to remain bounded after successive applications of (3.20) (i.e., in the process of time-stepping), we then have to require that the norm of $\mathbf{A}$ satisfy the limit

$$\| \mathbf{A} \| \leq 1 \tag{3.26}$$

and by (3.25) that the absolute value of all eigenvalues also satisfy

$$|\lambda_p| \leq 1 \tag{3.27}$$

If the error vector remains bounded, or in other words, does not grow in time, the method is stable. Conversely, we would also like the first two eigenvalues (which are related to η^n and q^n) to be not much less than unity, because that would imply numerical dissipation (Anderson *et al.*, 1984).

The eigenvalues of matrix $\mathbf{A}$ are determined numerically for Courant numbers ranging from $0 \leq \nu \leq 2$ and for wave numbers ranging from $0 \leq k\Delta x \leq \pi$. Fig. 3.2 shows the variation of the four eigenvalues as a function of ν and $k\Delta x$. It can be seen that only the first two eigenvalues can exceed the stability limit (3.27) for this range of parameter values. Notice that Fig. 3.2d is rotated 180^o relative to the other figures.

The second eigenvalue λ_2 is the most critical, since its values are closest to unity. For this eigenvalue, Fig. 3.3 shows cross-sections of Fig. 3.2b for $k\Delta x = 0, \pi/6, \pi/3, \pi/2$. The last value is recognized as the most unstable wave number and is shown to limit the stability range of this scheme to $\nu \leq 1.2$.

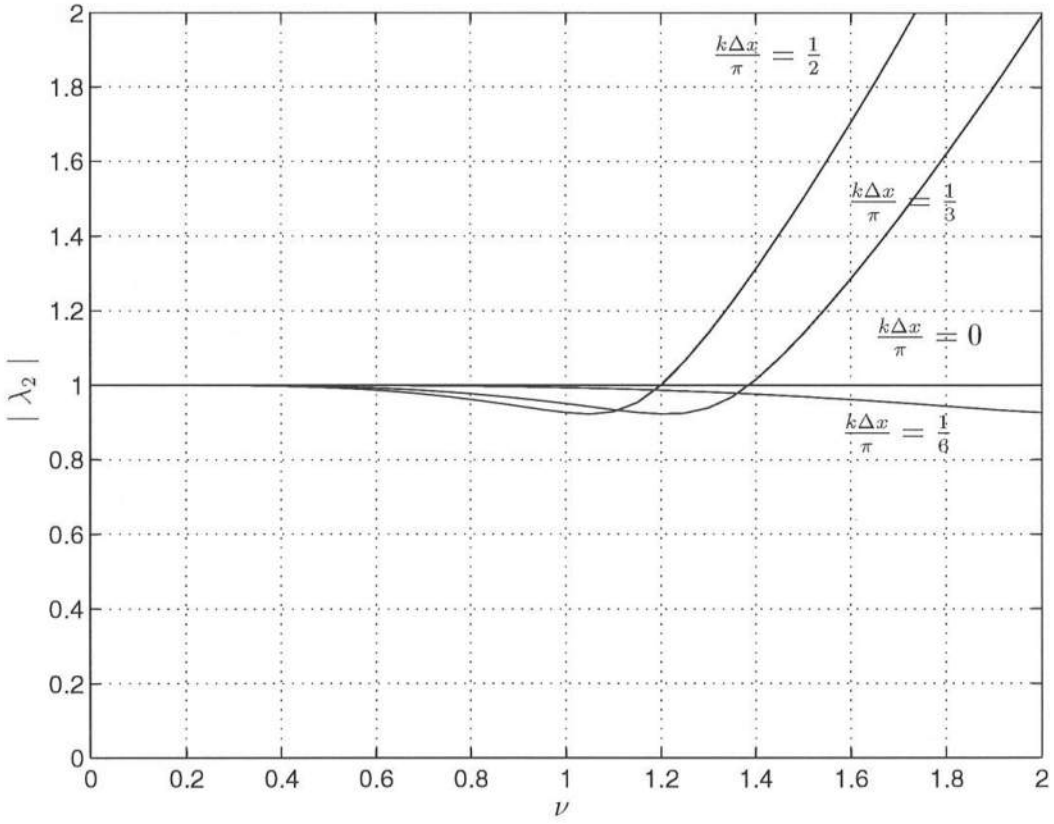

Figure 3.3: Variation of the absolute eigenvalue $|\lambda_2|$ versus the Courant number ν for $k\,\Delta x/\pi = 0, \frac{1}{6}, \frac{1}{3}, \frac{1}{2}$.

Notice that a stability analysis on the 2-DH equations would have introduced the wave number $l\,\Delta y$ in the y-direction. This would have made the analysis more complicated and the graphical representation less clear but would not have changed the general conclusions about the stability range of the scheme.

It is important to emphasize here that the Von Neumann analysis is performed on the linear equations and that these limits do not necessarily apply to the nonlinear case, which is in general more stringent. In our case it has been found through practical experiments with the scheme that in the two-dimensional

case a Courant limit of

$$\nu = c_o \frac{\Delta t}{\Delta x} \leq 0.7 \tag{3.28}$$

gives accurate and stable numerical results.

3.1.2 Accuracy

In this section we will investigate the accuracy of the scheme. This is useful since it will give an indication of the nature of the truncation errors made in the finite difference scheme. We follow the procedure as outlined in Anderson *et al.* (1984).

To check the accuracy we first linearize the system (which implies that we assume that the nonlinear terms are small) and write the set of governing linearized equations (3.7) in matrix form as

$$\frac{\partial}{\partial t}\begin{bmatrix} Q_x \\ Q_y \\ \zeta \end{bmatrix} = -\begin{bmatrix} 0 & 0 & g\,h_o \\ 0 & 0 & 0 \\ 1 & 0 & 0 \end{bmatrix}\frac{\partial}{\partial x}\begin{bmatrix} Q_x \\ Q_y \\ \zeta \end{bmatrix} - \begin{bmatrix} 0 & 0 & 0 \\ 0 & 0 & g\,h_o \\ 0 & 1 & 0 \end{bmatrix}\frac{\partial}{\partial y}\begin{bmatrix} Q_x \\ Q_y \\ \zeta \end{bmatrix} + \begin{bmatrix} F_x \\ F_y \\ 0 \end{bmatrix} \tag{3.29}$$

If we define

$$\mathbf{E} = \begin{bmatrix} Q_x \\ Q_y \\ \zeta \end{bmatrix} \tag{3.30}$$

we can write the system (3.29) as

$$\frac{\partial \mathbf{E}}{\partial t} = -\mathbf{A}\frac{\partial \mathbf{E}}{\partial x} - \mathbf{B}\frac{\partial \mathbf{E}}{\partial y} + \mathbf{F} \tag{3.31}$$

where $\mathbf{A}$, $\mathbf{B}$ and $\mathbf{F}$ correspond to the matrices in (3.29). In the following analysis of the accuracy, the forcing matrix $\mathbf{F}$ will not influence the results since it is known either analytically or through an external wave driver. We will omit this term in the following, which does not imply that the term itself is small.

The finite-differenced system (3.31) reads in the predictor step

$$\begin{aligned}\frac{\mathbf{E}^*_{i,j} - \mathbf{E}^n_{i,j}}{\Delta t} &= -\frac{3}{2}\mathbf{A}\left(\frac{\mathbf{E}^n_{i+1,j} - \mathbf{E}^n_{i-1,j}}{2\Delta x}\right) + \frac{1}{2}\mathbf{A}\left(\frac{\mathbf{E}^{n-1}_{i+1,j} - \mathbf{E}^{n-1}_{i-1,j}}{2\Delta x}\right) \\ &- \frac{3}{2}\mathbf{B}\left(\frac{\mathbf{E}^n_{i,j+1} - \mathbf{E}^n_{i,j-1}}{2\Delta y}\right) + \frac{1}{2}\mathbf{B}\left(\frac{\mathbf{E}^{n-1}_{i,j+1} - \mathbf{E}^{n-1}_{i,j-1}}{2\Delta y}\right) \quad (3.32)\end{aligned}$$

where the subscripts $_i$ and $_j$ represent the indices in the x and y directions, respectively.

To check the accuracy of this step we can substitute Taylor expansions about the point (i, j, n) into the finite-difference equation (3.32) to find the lowest order truncation error, which defines the accuracy of the scheme. Using the shorthand notation

$$\frac{\partial \mathbf{E}}{\partial t} = \mathbf{E}_t \qquad \frac{\partial \mathbf{E}}{\partial x} = \mathbf{E}_x \qquad \frac{\partial \mathbf{E}}{\partial y} = \mathbf{E}_y \quad (3.33)$$

we can write the Taylor series as (where for convenience we will omit the subscripts i, j, n on the right-hand side)

$$\mathbf{E}^*_{i,j} = \mathbf{E}^n_{i,j} + \Delta t\,\mathbf{E}_t + \frac{\Delta t^2}{2}\mathbf{E}_{tt} + \frac{\Delta t^3}{6}\mathbf{E}_{ttt} + O(\Delta t)^4 \quad (3.34)$$

$$\mathbf{E}^n_{i+1,j} - \mathbf{E}^n_{i-1,j} = 2\Delta x\,\mathbf{E}_x + \frac{\Delta x^3}{3}\mathbf{E}_{xxx} + O(\Delta x)^4 \quad (3.35)$$

$$\mathbf{E}^n_{i,j+1} - \mathbf{E}^n_{i,j-1} = 2\Delta y\,\mathbf{E}_y + \frac{\Delta y^3}{3}\mathbf{E}_{yyy} + O(\Delta y)^4 \quad (3.36)$$

$$\mathbf{E}^{n-1}_{i+1,j} - \mathbf{E}^{n-1}_{i-1,j} = 2\,\Delta x \left(\mathbf{E}_x - \Delta t\,\mathbf{E}_{xt} + \frac{\Delta t^2}{2}\,\mathbf{E}_{xtt} \right) + \frac{\Delta x^3}{3}\,\mathbf{E}_{xxx}$$

$$+ O(\Delta x \Delta t^3, \Delta x^3 \Delta t, \Delta x^4) \tag{3.37}$$

$$\mathbf{E}^{n-1}_{i,j+1} - \mathbf{E}^{n-1}_{i,j-1} = 2\,\Delta y \left(\mathbf{E}_y - \Delta t\,\mathbf{E}_{yt} + \frac{\Delta t^2}{2}\,\mathbf{E}_{ytt} \right) + \frac{\Delta y^3}{3}\,\mathbf{E}_{yyy}$$

$$+ O(\Delta y \Delta t^3, \Delta y^3 \Delta t, \Delta y^4) \tag{3.38}$$

After substitution of these series into (3.32) and some rearranging we get

$$\mathbf{E}_t + \mathbf{A}\,\mathbf{E}_x + \mathbf{B}\,\mathbf{E}_y = -\frac{\Delta t}{2}\left(\mathbf{E}_{tt} + \mathbf{A}\,\mathbf{E}_{xt} + \mathbf{B}\,\mathbf{E}_{yt}\right) - \frac{\Delta t^2}{6}\mathbf{E}_{ttt}$$

$$- \mathbf{A}\,\frac{\Delta x^2}{6}\,\mathbf{E}_{xxx} - \mathbf{B}\,\frac{\Delta y^2}{6}\,\mathbf{E}_{yyy} + \frac{\Delta t^2}{4}\,\mathbf{A}\,\mathbf{E}_{xtt} + \frac{\Delta t^2}{4}\,\mathbf{B}\,\mathbf{E}_{ytt}$$

$$+ O(\Delta t^3, \Delta x^3, \Delta y^3, \Delta x^2 \Delta t, \Delta y^2 \Delta t) \tag{3.39}$$

where we have put the original PDE on the left-hand side and the truncation errors on the right-hand side. Notice that, because the right-hand side of the original set of equations (3.29) contains spatial derivatives, we obtain mixed truncation errors in (3.39). The leading truncation errors contain Δt terms, which means that halving the time step does not increase the accuracy by a factor 8 (through the Δt^3 term) but by a factor 2 only. The Δt term is multiplied by Δx^2 and Δy^2, so its effect depends on the spatial resolution.

Next, we will replace the time-derivatives in the truncation error by spatial derivatives by taking derivatives of the finite difference equation (3.39) and resubstituting into (3.39). As a result we will find the modified equation (Anderson *et al*, 1984).

First, we take the time-derivative of (3.39) and multiply by $-\frac{\Delta t}{2}$ where we keep terms only to the order of the truncation

$$-\frac{\Delta t}{2}\left(\mathbf{E}_{tt} + \mathbf{A}\,\mathbf{E}_{xt} + \mathbf{B}\,\mathbf{E}_{yt}\right) = \frac{\Delta t^2}{4}\left(\mathbf{E}_{ttt} + \mathbf{A}\,\mathbf{E}_{xtt} + \mathbf{B}\,\mathbf{E}_{ytt}\right)$$

$$+ O(\Delta t^3, \Delta x^3, \Delta y^3, \Delta x^2\Delta t, \Delta y^2\Delta t) \tag{3.40}$$

Substituting this result into (3.39) yields

$$\mathbf{E}_t + \mathbf{A}\,\mathbf{E}_x + \mathbf{B}\,\mathbf{E}_y = \frac{\Delta t^2}{2}\left(\mathbf{E}_{ttt} + \mathbf{A}\,\mathbf{E}_{xtt} + \mathbf{B}\,\mathbf{E}_{ytt}\right) - \frac{5}{12}\Delta t^2\,\mathbf{E}_{ttt}$$

$$- \mathbf{A}\,\frac{\Delta x^2}{6}\,\mathbf{E}_{xxx} - \mathbf{B}\,\frac{\Delta y^2}{6}\,\mathbf{E}_{yyy} + O(\Delta t^3, \Delta x^3, \Delta y^3, \Delta x^2\Delta t, \Delta y^2\Delta t) \tag{3.41}$$

Next, we take a double time-derivative of (3.39) and multiply by $\frac{\Delta t^2}{2}$, which yields

$$\frac{\Delta t^2}{2}\left(\mathbf{E}_{ttt} + \mathbf{A}\,\mathbf{E}_{xtt} + \mathbf{B}\,\mathbf{E}_{ytt}\right) = O(\Delta t^3, \Delta x^3, \Delta y^3, \Delta x^2\Delta t, \Delta y^2\Delta t) \tag{3.42}$$

Substituting this into (3.41) eliminates the first term on the right-hand side to the leading order in the truncation, so (3.41) becomes

$$\mathbf{E}_t + \mathbf{A}\,\mathbf{E}_x + \mathbf{B}\,\mathbf{E}_y = -\frac{5}{12}\Delta t^2\,\mathbf{E}_{ttt} - \mathbf{A}\,\frac{\Delta x^2}{6}\,\mathbf{E}_{xxx} - \mathbf{B}\,\frac{\Delta y^2}{6}\,\mathbf{E}_{yyy}$$

$$+ O(\Delta t^3, \Delta x^3, \Delta y^3, \Delta x^2\Delta t, \Delta y^2\Delta t) \tag{3.43}$$

Finally, we can eliminate the remaining $\mathbf{E}_{ttt}$-term in (3.43) by taking a double time-derivative of (3.39) and adding a combination of mixed derivatives in x and y so that after some manipulation we have

$$\mathbf{E}_{ttt} = -\mathbf{A}^3\,\mathbf{E}_{xxx} - 3\,\mathbf{A}^2\,\mathbf{B}\,\mathbf{E}_{xxy} - 3\,\mathbf{A}\,\mathbf{B}^2\,\mathbf{E}_{xyy} - \mathbf{B}^3\,\mathbf{E}_{yyy}$$

$$+ O(\Delta t^3, \Delta x^3, \Delta y^3, \Delta x^2\Delta t, \Delta y^2\Delta t) \tag{3.44}$$

Substituting this result into (3.43) yields the *modified equation*

$$\mathbf{E}_t + \mathbf{A}\,\mathbf{E}_x + \mathbf{B}\,\mathbf{E}_y = \frac{\mathbf{A}}{6}\left(\frac{5}{2}\,\mathbf{A}^2\Delta t^2 - \Delta x^2\right)\mathbf{E}_{xxx} +$$

$$\frac{\mathbf{B}}{6}\left(\frac{5}{2}\,\mathbf{B}^2\Delta t^2 - \Delta y^2\right)\mathbf{E}_{yyy} + \frac{5}{4}\Delta t^2\left(\mathbf{A}^2\,\mathbf{B}\,\mathbf{E}_{xxy} + \mathbf{A}\,\mathbf{B}^2\,\mathbf{E}_{xyy}\right) +$$

$$+ O(\Delta t^3, \Delta x^3, \Delta y^3, \Delta x^2\Delta t, \Delta y^2\Delta t) \tag{3.45}$$

The terms on the right-hand side in (3.45) represent the finite-differenced, leading-order errors of the numerical scheme. Hence the leading-order truncation errors in the numerical scheme have the same effect as if we were actually solving (3.45) exactly. We see that these terms are proportional to $O(\Delta t^2, \Delta x^2, \Delta x^2\Delta t, \Delta y^2, \Delta y^2\Delta t)$ and that the leading order is a third derivative, which causes dispersive errors.

The same procedure can also be applied to the corrector step, which finally can be written as

$$\mathbf{E}_t + \mathbf{A}\,\mathbf{E}_x + \mathbf{B}\,\mathbf{E}_y = -\frac{\mathbf{A}}{6}\Delta x^2\,\mathbf{E}_{xxx} +$$

$$-\frac{\mathbf{B}}{6}\Delta y^2\,\mathbf{E}_{yyy} + O(\Delta t^3, \Delta x^3, \Delta y^3, \Delta x^2\Delta t, \Delta y^2\Delta t) \tag{3.46}$$

This equation shows that the corrector step is accurate to $O(\Delta t^3, \Delta x^2, \Delta x^2\Delta t, \Delta y^2, \Delta y^2\Delta t)$. This apparent mismatch of the accuracy in both steps is due to the fact that the values of $\mathbf{E}$ calculated in the predictor step are premultiplied by a factor Δt in the corrector step which makes the steps consistent (Atkinson, 1978). This is the reason why it is consistent to use a combination of a second-order Adams-Bashforth and a third-order Adams-Moulton time-stepping scheme.

The leading-order errors in both steps are third derivatives, which cause dispersive errors, i.e., wave components of different wave length or period will propagate at different speeds.

From this analysis we can also see that the finite difference scheme is consistent because the scheme approaches the original set of PDE's when $\Delta x, \Delta y, \Delta t \rightarrow 0$.

3.2 Absorbing-Generating Boundary Condition

In this section, an absorbing-generating boundary condition is derived for the 2D-horizontal nonlinear shallow water equations using the Method of Characteristics. It assumes local superposition of the incoming and outgoing long waves at the boundary and uses a relationship between the flux and surface elevation of the waves. This boundary condition allows the outgoing waves to leave the computational domain through the boundaries with a minimum of reflection while specifying incoming waves at the same boundaries. The boundary condition's absorbing properties are tested for both linear and nonlinear waves for a range of amplitudes and of angles of incidence. Its performance is compared to the classical Sommerfeld radiation condition for the linear case and is shown to cause significantly less reflection errors, especially for oblique angles. Also, a case of simultaneous absorption and generation of waves at the same boundary is analyzed where it is shown that the errors are of the same order as for the case of absorption only. Finally, the boundary condition is extended to include known currents.

This section has been published as Van Dongeren & Svendsen (1997).

3.2.1 Introduction

When analyzing nearshore problems using numerical models it is usually necessary to limit the computations to a small region around the area of immediate interest. This implies introducing artificial boundaries for the computational region that form the interface to the exterior, which is either not modeled or modeled in a simplified way. Thus one of the most important problems in developing time-dependent shallow water models is the specification of accurate boundary conditions along these artificial boundaries because, after long enough time, the performance of these conditions will dominate the model results in the entire computational domain.

These time-dependent models essentially solve approximations to the equations of motion (conservation of mass and momentum) by integration in time of certain dependent variables, typically surface elevation and horizontal velocities. The boundary conditions are required to provide a similar upgrading in time of the same variables along the boundaries.

In developing the nearshore circulation model SHORECIRC (Van Dongeren *et al.*, 1994, 1995), which is capable of describing a number of phenomena (such as edge-waves, surfbeat, longshore currents, shear waves, etc.), we encountered exactly this problem. For our purposes it was necessary to develop boundary conditions on the artificial boundaries that are able to generate a specified long wave and simultaneously absorb outgoing waves, i.e., an absorbing-generating boundary condition.

Most of the existing literature on the topic of artificial boundaries is concerned with absorbing (sometimes called *radiating*, *non-reflective* or *open*) boundary conditions specifically derived for the wave equation or the shallow water

equations. For a thorough review of this subject, we refer to Givoli (1991).

In one of the most frequently quoted papers, Engquist & Majda (1977) [E&M] developed a perfectly absorbing boundary condition which is nonlocal in space and time. This means that the complete time history along the entire boundary is required in order to update the variables at any point along the boundary in time. Because this is very impractical for any numerical application, E&M derived local approximations to the general solution of increasing order of accuracy. The approximations are centered around chosen angles of incidence θ_n between the boundary normal and the direction of the outgoing waves. Higdon (1986, 1987) derived a general form of this radiation condition and showed that it can be written as

$$\left(\frac{\partial}{\partial t} + \frac{c_o}{\cos\theta_n}\frac{\partial}{\partial x}\right)^n u = 0 \tag{3.47}$$

where n is the order of accuracy and c_o is the linear phase speed. This expression gives the best absorption when the angle of the outgoing wave to the normal is θ_n. For $\theta_n = 0^o$ the equation reduces to E&M's boundary condition, which only absorbs normally incident waves optimally. To the first order of the approximation ($n = 1$), the E&M boundary condition further reduces to the Sommerfeld radiation condition (Sommerfeld, 1964)

$$\left(\frac{\partial}{\partial t} + c_o\frac{\partial}{\partial x}\right) u = 0 \tag{3.48}$$

which essentially states that the outgoing wave is propagating in the positive direction without change of form. Eq. (3.47) was also found independently by Keys (1985) and is an improvement over the boundary condition developed by E&M because the reflection coefficient can be greatly reduced if the angle of incidence θ_n is known in advance. This might be the case for some types of problems (e.g., waves radiating from a source inside the computational domain), but not for the more general models we are considering here.

Another disadvantage of this type of boundary condition is that the solution to the problem is assumed to have a certain form. Broeze & Van Daalen (1992) did not make that assumption and derived a boundary condition from the local energy flux in the normal direction to the boundary using the variational principle and showed improved accuracy in a panel method.

Unfortunately, these boundary conditions are only capable of absorbing waves and (except for Broeze & Van Daalen) only address the linear problem. Hibberd (1977) considered the more general problem of simultaneously generating and absorbing waves in one horizontal direction and derived a boundary condition for the nonlinear shallow water equations (NSW) where the outgoing wave is calculated using the Method of Characteristics while an incoming Riemann variable associated with an incident uniform bore is specified. On a similar basis, Verboom *et al.* (1981) gave more general expressions for weakly-reflective boundary conditions based on the specification of incoming Riemann variables. Verboom & Slob (1984) derived two orders of approximation of this type of boundary condition and calculated reflection coefficients which were of the order of a few percent. However, the applications in the last two papers deal only with situations where no incoming wave is specified and the boundary condition reduces to the case of absorption only.

In the case of simultaneous absorption and reflection, it is not possible to specify the incoming Riemann variable since it is a function of the unknown surface elevation and velocity. Instead, considering the problem in one horizontal direction, Kobayashi *et al.* (1987) used the outgoing characteristic and substituted a linear long wave relationship between the velocity and the surface elevation to solve for the outgoing wave. They did not report on the accuracy of the boundary condition. The present work gives an extension of this boundary condition to the

general case of two horizontal dimensions and expands the condition to a higher order of approximation.

The outline of this section is as follows. In Subsection 3.2.2 we discuss the formulation of the problem. In Subsection 3.2.3 the boundary condition is derived from the fundamental equations for two orders of the approximation. In Subsection 3.2.4 the reflection properties of both versions are investigated for the case of absorption only and compared to the classical Sommerfeld radiation condition for the linear case. In Subsection 3.2.5 the boundary condition is further tested for the case of simultaneous generation and absorption at the same boundary. We will conclude this section with a Discussion and Conclusions.

3.2.2 Formulation of the Problem

The boundary conditions we specify along the artificial ocean-side boundaries must guarantee a unique and well-posed solution to the differential equations. As may also be inferred from the literature review given above, this is not a straightforward problem, and it appears that to some extent waves and currents need to be addressed separately.

From the outset one would expect that the idea of emulating the effects of a large ocean in a computation that only covers a small region of that ocean imposes some limitations on what can actually be represented in the model, and this is true. More importantly, however, it also requires a clarification of which physical mechanisms we should actually try to describe along those boundaries.

Our requirements can be formulated by stating that the boundary conditions need to satisfy two criteria:

1. The region outside the computational domain can influence the motion inside only through the incident (long) waves and through the currents along the boundaries. Thus we must assume that we know and can specify those currents and incident waves.

2. (Long) waves propagating out of the computational region must be allowed to propagate freely through the open ocean-side boundaries with minimal reflection.

It turns out that whereas outgoing waves can be separated from the total signal and absorbed at the artificial boundaries, this is not the case for currents. The distribution of the currents is essentially an elliptic problem. (This becomes apparent if we combine the governing equations of continuity and momentum into the two-dimensional wave equation. In the case of (quasi)-steady currents, this equation reduces to the elliptic Laplace equation.) Therefore, the currents, or their derivatives, have to be specified along the entire boundary to uniquely specify the problem. This also implies, however, that in the general case extensive information is needed about the currents outside the domain in order to be able to specify the currents along the computational boundary.

Finally, it raises the question of how to distinguish between waves and time-varying currents. A closer inspection of this problem suggests that this is a matter of the time scale of the variations relative to the time it takes for a disturbance to propagate across the computational domain.

Thus the boundary conditions must be able to generate a specified long wave and simultaneously absorb outgoing waves, in the presence of known currents and ideally without much additional computational effort. For simplicity, we limit the applications in the present work to the case of incident long waves without

currents, although in the Discussion we will derive the results for the case including currents.

3.2.3 Derivation of the Boundary Condition

The governing equations of the SHORECIRC model are the depth-integrated, short-wave-averaged continuity and momentum equations with short-wave-induced forcing (Van Dongeren *et al.*, 1994; Svendsen & Putrevu, 1996), which were derived in Chapter 2. If we place the open boundaries carefully we can achieve weak local forcing near these boundaries. This means that the dominating terms in the continuity and momentum equations near those boundaries are the terms corresponding to the nonlinear shallow water (NSW) equations, which in matrix form read

$$\frac{\partial}{\partial t}\begin{bmatrix} \bar{u}' \\ \bar{v}' \\ h \end{bmatrix} + \begin{bmatrix} \bar{u}' & 0 & g \\ 0 & \bar{u}' & 0 \\ h & 0 & \bar{u}' \end{bmatrix} \frac{\partial}{\partial x'}\begin{bmatrix} \bar{u}' \\ \bar{v}' \\ h \end{bmatrix} + \begin{bmatrix} \bar{v}' & 0 & 0 \\ 0 & \bar{v}' & g \\ 0 & h & \bar{v}' \end{bmatrix} \frac{\partial}{\partial y'}\begin{bmatrix} \bar{u}' \\ \bar{v}' \\ h \end{bmatrix} = \begin{bmatrix} g\frac{\partial h_o}{\partial x'} + f_x \\ g\frac{\partial h_o}{\partial y'} + f_y \\ 0 \end{bmatrix} \tag{3.49}$$

where h is the total water depth $h = h_o + \bar{\zeta}$, h_o is the still water depth and $\bar{\zeta}$ is the shortwave-averaged surface elevation. $\bar{u}'$ and $\bar{v}'$ are the depth averaged and shortwave-averaged velocities in the x' and y' directions, respectively. See Fig. 3.4 for a definition sketch of the wave properties and Fig. 3.5a for the coordinate system. It may be worth emphasizing that since we are considering the general case of short-wave motion with arbitrary time variation, the shortwave-averaged $\bar{\zeta}$ and $\bar{u}', \bar{v}'$ represent surface elevation and the depth-averaged part of the particle motion, respectively, in the infragravity wave motion. Usually $\bar{\zeta}$ will also include a

steady set-down or set-up component. f represents all the local forcing terms for the motion, which comprises the radiation stress gradients, the current-current and current-wave integrals (originating from the non-uniform variation of the velocities over depth) and the bottom and wind shear stresses. These effects are included in the original SHORECIRC equations.

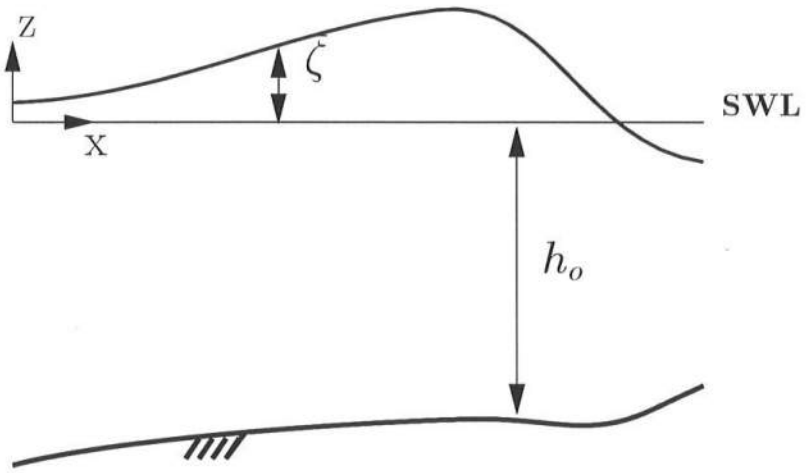

Figure 3.4: Definition sketch.

In the general case of arbitrary angle ϑ between the boundary at a point and the coordinate axes, we can follow the procedure outlined in Abbott (1979). Thus we can write (3.49) in the form

$$\mathbf{w}_t + \mathbf{A}\,\mathbf{w}_{x'} + \mathbf{B}\,\mathbf{w}_{y'} = \mathbf{C} \tag{3.50}$$

where

$$\mathbf{w} = \begin{bmatrix} \bar{u}' \\ \bar{v}' \\ h \end{bmatrix} \tag{3.51}$$

and the matrices **A**, **B** and **C** correspond to the matrices in (3.49), respectively. We can determine the eigenvalues for this system from the determinant of the linear combination of the matrices **A** and **B** or

$$| \cos\vartheta \, \mathbf{A} + \sin\vartheta \, \mathbf{B} - \lambda_n \, \mathbf{I} | = 0 \tag{3.52}$$

where ϑ is the angle between the normal to the boundary and the x'-axis as identified by Verboom *et al.* (1981) (see Fig.3.5a), **I** is the identity matrix and λ_n are the eigenvalues. The eigenvalues thus found are

$$\lambda_1 = \quad \bar{u}' \cos\vartheta + \bar{v}' \sin\vartheta \tag{3.53}$$

$$\lambda_2 = \quad \bar{u}' \cos\vartheta + \bar{v}' \sin\vartheta + \sqrt{g\,h} \tag{3.54}$$

$$\lambda_3 = \quad \bar{u}' \cos\vartheta + \bar{v}' \sin\vartheta - \sqrt{g\,h} \tag{3.55}$$

From these eigenvalues we can construct the eigenvector matrix **P** of the determinant (3.52)

$$\mathbf{P} = \begin{pmatrix} \cos\vartheta & \cos\vartheta & \sin\vartheta \\ \sin\vartheta & \sin\vartheta & -\cos\vartheta \\ \sqrt{\frac{h}{g}} & -\sqrt{\frac{h}{g}} & 0 \end{pmatrix} \tag{3.56}$$

Premultiplying the system of equations (3.50) with $\mathbf{P^{-1}}$ and adding in $\mathbf{I} = \mathbf{P}\,\mathbf{P^{-1}}$ yields

$$\mathbf{P^{-1}}\mathbf{w}_t + (\mathbf{P^{-1}}\mathbf{A}\,\mathbf{P})\,\mathbf{P^{-1}}\mathbf{w}_{x'} + (\mathbf{P^{-1}}\mathbf{B}\,\mathbf{P})\,\mathbf{P^{-1}}\mathbf{w}_{y'} = \mathbf{P^{-1}}\mathbf{C} \tag{3.57}$$

where the terms between parentheses are the diagonalized matrices. System (3.57) represents the governing equations in characteristic form as derived by Verboom *et al.* (1981), their Eq. (11.7), which is valid for an arbitrary angle ϑ between the coordinate axes and the model boundary. (Note that the eigenvectors in their Eq. (11.5) contain a typographical error and are therefore not identical to (3.56).)

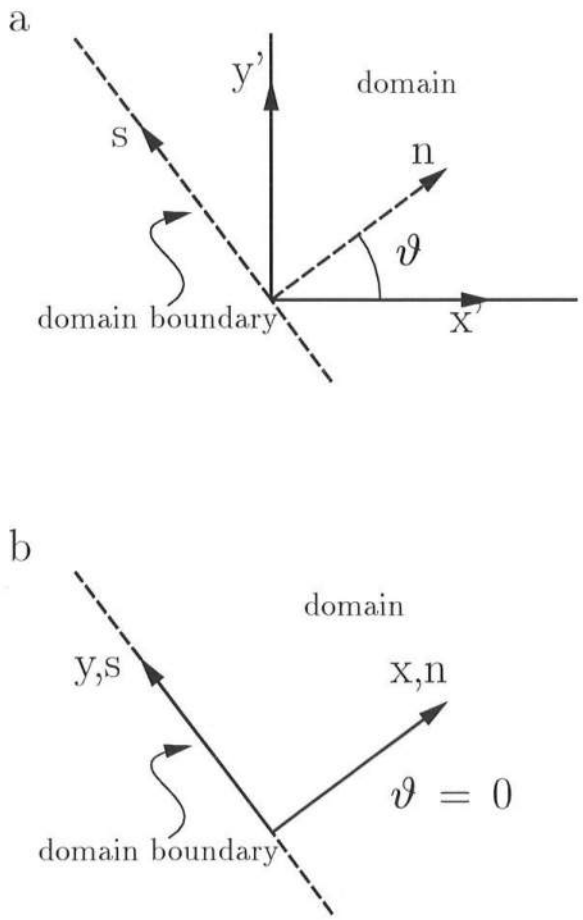

Figure 3.5: Coordinate system (a) for arbitrary angle ϑ between domain boundary and x-axis; (b) for $\vartheta = 0$.

However, the derivation becomes easier to follow if we define the coordinate system in such a way that the x-axis is normally inward to the seaward boundary of our rectangular domain, which sets $\vartheta = 0$; see Fig. 3.5b. The equations in characteristic form (3.57) then simplify to

$$\frac{\partial \beta^-}{\partial t} = -(\bar{u} - c)\frac{\partial \beta^-}{\partial x} - \bar{v}\frac{\partial \beta^-}{\partial y} + c\frac{\partial \bar{v}}{\partial y} + g\frac{\partial h_o}{\partial x} + F_{\beta-} \tag{3.58}$$

$$\frac{\partial \beta^+}{\partial t} = -(\bar{u} + c)\frac{\partial \beta^+}{\partial x} - \bar{v}\frac{\partial \beta^+}{\partial y} - c\frac{\partial \bar{v}}{\partial y} + g\frac{\partial h_o}{\partial x} + F_{\beta+} \tag{3.59}$$

$$\frac{\partial \gamma}{\partial t} = -\bar{u}\frac{\partial \gamma}{\partial x} - \bar{v}\frac{\partial \gamma}{\partial y} - g\frac{\partial \bar{\zeta}}{\partial y} + F_\gamma \tag{3.60}$$

In (3.58) the Riemann-variable β^- is defined as

$$\beta^- = \bar{u} - 2\,c = \frac{Q_x}{(h_o + \bar{\zeta})} - 2\sqrt{g\,(h_o + \bar{\zeta})} \tag{3.61}$$

where Q_x is the total flux in the x direction and $\bar{u}$ is the depth averaged velocity. The Riemann-variable of (3.59) is similarly defined as $\beta^+ = \bar{u} + 2c$. It turns out that the γ-equation is the y-momentum equation itself which has the Riemann-variable

$$\gamma = \bar{v} = \frac{Q_y}{(h_o + \bar{\zeta})} \tag{3.62}$$

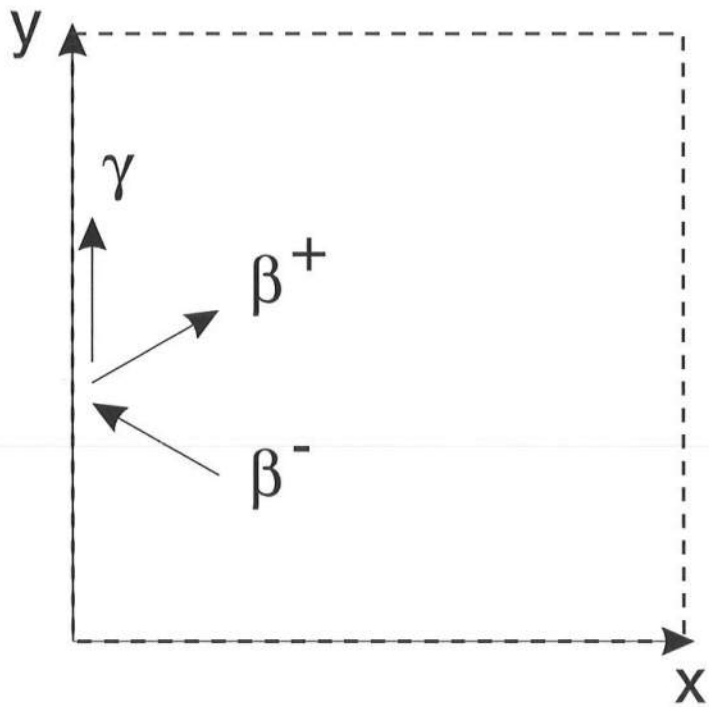

Figure 3.6: Definition sketch of the characteristics.

The definition sketch in Fig. 3.6 shows that β^+ propagates along a characteristic in the positive x direction, β^- in the negative x direction and γ in the y direction. The forcing terms $F_{\beta+}$, $F_{\beta-}$ and F_γ originate from the f-terms in (3.49). These terms imply that β^+, β^- and γ vary along their characteristics and hence are variables rather than invariants.

During the computation we will at time step n know the value of $\bar{\zeta}^n$ and (Q_x^n, Q_y^n) at interior as well as boundary points. The incoming wave motion is specified along the boundaries through specification of $(Q_{x,i}, Q_{y,i})$, which represent the x and y components of the flux of the incident wave. The numerical integration of (3.49) will then provide the values of the total $\bar{\zeta}, Q_x, Q_y$ for interior points in the domain at time step $n+1$, and the problem is to determine the equivalent total values along the boundaries at $n+1$. In this process we also determine the parameters of the outgoing wave.

In the following, the absorbing-generating boundary conditions for two different orders of the expansion are derived for the $x = 0$ boundary. These boundary conditions can be generalized to boundaries with a normal at an arbitrary angle to the coordinate axes. Since the boundary conditions are local, a generalized form can be developed, which applies to any overall shape of the boundary. This is omitted here for brevity. In Subsection 3.2.4 we do, however, implement the equivalent boundary conditions on all sides of the rectangular domain.

Assuming linear superposition of the incoming wave (subscripted i in the following) and the outgoing wave (subscripted r), we can write

$$Q_x = Q_{x,i} + Q_{x,r} \tag{3.63}$$

$$\bar{\zeta} = \bar{\zeta}_i + \bar{\zeta}_r \tag{3.64}$$

Without further approximation the outgoing Riemann-variable (3.61) can then be

rewritten as

$$\frac{\beta^-}{c_o} = \frac{Q_{x,i}}{c_o h_o}\left(1+\frac{\bar{\zeta}_i+\bar{\zeta}_r}{h_o}\right)^{-1} + \frac{Q_{x,r}}{c_o h_o}\left(1+\frac{\bar{\zeta}_i+\bar{\zeta}_r}{h_o}\right)^{-1} - 2\sqrt{1+\frac{\bar{\zeta}_i+\bar{\zeta}_r}{h_o}} \tag{3.65}$$

where

$$c_o = \sqrt{g h_o} \tag{3.66}$$

At this point we introduce the assumption that the total volume flux in the direction of the wave propagation is related to the surface elevation by the equation

$$Q = c_a(\bar{\zeta} - \bar{\bar{\zeta}}) + \bar{\bar{Q}} \tag{3.67}$$

where c_a is the celerity of the wave seen from a fixed coordinate system and $c_a\,\bar{\zeta}$ represents the volume flux in the oscillatory part of the motion. $\bar{\bar{Q}}$ is the net volume flux, which consists of the nonlinear volume flux, Q_w, in the infragravity waves and the "current". $\bar{\bar{\zeta}}$ is the average over the infragravity wave period of the infragravity wave surface elevation $\bar{\zeta}$. It has been shown (see Svendsen (1974) or Svendsen & Justesen (1984) for two different derivations) that this relationship, which is purely kinematical, is exact for plane progressive waves of constant form, no matter what height or nature. Thus the use of this relationship here only implies that assumption for the incoming and outgoing wave motion in the neighborhood of the boundary in question. (Svendsen & Justesen (1984) found that even for waves deforming rapidly towards breaking, the error from using this relationship was less than 5%). For reference, the derivation of this relationship following Svendsen (1974) is repeated in Appendix B.

For simplicity we assume in the following that $\bar{\bar{\zeta}}$ as well as $\bar{\bar{Q}}$ are zero. Then, again using linear superposition, Eq. (3.67) for the x-components of the incoming and outgoing waves can be written as

$$Q_{x,i} = c\,\bar{\zeta}_i \cos\theta_i \tag{3.68}$$

$$Q_{x,r} = -c\,\bar{\zeta}_r \cos\theta_r \tag{3.69}$$

where θ_i and θ_r are defined as the angles between the normal to the boundary and the incoming and outgoing waves in the range $[-\frac{\pi}{2}, \frac{\pi}{2}]$, respectively. Eq. (3.65) then becomes

$$\begin{aligned}\frac{\beta^-}{c_o} &= \frac{Q_{x,i}}{c_o h_o}\left(1 + \frac{Q_{x,i}}{h_o c\cos\theta_i} - \frac{Q_{x,r}}{h_o c\cos\theta_r}\right)^{-1} \\ &+ \frac{Q_{x,r}}{c_o h_o}\left(1 + \frac{Q_{x,i}}{h_o c\cos\theta_i} - \frac{Q_{x,r}}{h_o c\cos\theta_r}\right)^{-1} \\ &- 2\left(1 + \frac{Q_{x,i}}{h_o c\cos\theta_i} - \frac{Q_{x,r}}{h_o c\cos\theta_r}\right)^{\frac{1}{2}}\end{aligned} \tag{3.70}$$

Here we can expect that $Q_x/h_o c_o \ll 1$, in which case an explicit result for $Q_{x,r}$ can be developed as follows. If we expand this expression to first order with respect to $Q_x/h_o c_o$ we get

$$c_3 = c_1\,Q'_{x,i} + b_1\,Q'_{x,r} + O\left(\frac{Q_x}{c_o h_o}\right)^2 \tag{3.71}$$

where for convenience we have defined

$$Q'_{x,i} \equiv \frac{Q_{x,i}}{c_o\,h_o} \tag{3.72}$$

$$Q'_{x,r} \equiv \frac{Q_{x,r}}{c_o\,h_o} \tag{3.73}$$

$$b_1 \equiv \frac{(\cos\theta_r + 1)}{\cos\theta_r} \tag{3.74}$$

$$c_1 \equiv \frac{(\cos\theta_i - 1)}{\cos\theta_i} \tag{3.75}$$

$$c_3 \equiv \frac{\beta^-}{c_o} + 2 \tag{3.76}$$

Solving with respect to $Q'_{x,r}$ yields

$$Q'_{x,r} = \frac{1}{b_1}\left(c_3 - c_1\,Q'_{x,i}\right) + O\left(\frac{Q_x}{c_o h_o}\right)^2 \tag{3.77}$$

It turns out, however, that for larger amplitude waves this expansion (3.77) is one of the most significant error sources. It is therefore useful to carry the expansion of (3.70) to second order, which yields a quadratic equation in $Q'_{x,r}$

$$c_3 = c_1 Q'_{x,i} + b_1 Q'_{x,r} + c_2 Q'^2_{x,i} + a Q'^2_{x,r} + b_2 Q'_{x,r} Q'_{x,i} + O\left(\frac{Q_x}{c_o h_o}\right)^3 \quad (3.78)$$

where

$$a \equiv \frac{\frac{3}{4} + \cos\theta_r}{\cos^2\theta_r} \quad (3.79)$$

$$b_2 \equiv \frac{\cos\theta_i - \cos\theta_r - \frac{3}{2}}{\cos\theta_i \cos\theta_r} \quad (3.80)$$

$$c_2 \equiv \frac{\frac{3}{4} - \cos\theta_i}{\cos^2\theta_i} \quad (3.81)$$

Again we can solve for $Q'_{x,r}$ and eliminating the false root yields the second order expression for $Q'_{x,r}$

$$Q'_{x,r} = \frac{b_1 + b_2 Q'_{x,i}}{2a}\left(\sqrt{1 - \frac{4a(c_1 Q'_{x,i} + c_2 Q'^2_{x,i} - c_3)}{(b_1 + b_2 Q'_{x,i})^2}} - 1\right) + O\left(\frac{Q_x}{c_o h_o}\right)^3 \quad (3.82)$$

which can be used instead of (3.77).

It is important to notice that the expansion in $\frac{Q_x}{c_o h_o}$ requires that the second term under the square root is small since c_3 is also proportional to $\frac{Q_x}{c_o h_o}$. Also notice that $\frac{Q_{x,i}}{\cos\theta_i}$ is consistently set equal to zero when $\theta_i = \pm\frac{\pi}{2}$. Performing a binomial expansion on the square root in (3.82) yields

$$Q'_{x,r} = \frac{b_1 + b_2 Q'_{x,i}}{2a}\left(-\frac{2a(c_1 Q'_{x,i} + c_2 Q'^2_{x,i} - c_3)}{(b_1 + b_2 Q'_{x,i})^2}\right.$$

$$\left. - \frac{2a^2(c_1 Q'_{x,i} + c_2 Q'^2_{x,i} - c_3)^2}{(b_1 + b_2 Q'_{x,i})^4}\right) + O\left(\frac{Q_x}{c_o h_o}\right)^3 \quad (3.83)$$

Expanding only to the first term in the binomial expansion (and setting $b_2 = 0$ and $c_2 = 0$) retrieves (3.77), which approximates (3.82) to within a few percent

for $\frac{Q_x}{c_o h_o} \sim \frac{\bar{\zeta}}{h_o} < 0.05$. Similarly, the expansion to the second term (3.83) is nearly identical to (3.82) up to $\frac{Q_x}{c_o h_o} = 0.1$. This means that the boundary conditions can at least be applied to long waves with amplitudes of about 10% of the still water depth at the boundary. Furthermore, the expansions can clearly be extended to even higher order if needed or (3.70) can be solved directly by iteration.

Equations (3.77) and (3.82) have two unknowns, $Q'_{x,r}$ and θ_r, which can be determined by realizing that

$$\theta_r = \arctan\left(\frac{Q'_{y,r}}{Q'_{x,r}}\right) \tag{3.84}$$

This introduces the additional unknown $Q'_{y,r}$, which can be determined by using (3.62), which is rewritten as

$$Q'_{y,r} = \frac{\gamma\,(h_o + \bar{\zeta}) - Q_{y,i}}{c_o\, h_o} \tag{3.85}$$

in which $Q_{y,i}$ is specified and γ is determined by integration of the last of the characteristic equations (3.60).

In these expressions β^- is the Riemann-variable, which is updated to the next time level by (3.58) at the $x = 0$ boundary. (The value of β^- in the interior points, which is needed to calculate $\frac{\partial \beta^-}{\partial x}$ in (3.58), is constructed from Q_x and $\bar{\zeta}$ using (3.61)). From (3.77) or (3.82), and (3.84) and (3.85) we can find the unknowns $Q'_{x,r}$ and θ_r iteratively. With the incoming wave known through specification, the boundary value of total flux Q_x can then be determined at the next time step.

It should be emphasized that boundary conditions (3.77) and (3.82) are derived for the $x = 0$ boundary and that they can readily be generalized for any other boundary that is normal to a coordinate axis. The boundary conditions can also be generalized to boundaries that are not normal to a coordinate axis by

rotating the coordinate system in the solution presented here. For brevity, this derivation is omitted in this thesis.

3.2.4 Reflection Properties

The absorption properties of the boundary condition are tested for a unidirectional wave in a domain of constant depth for various angles of incidence and wave amplitudes. In the following examples waves are generated at the $x = 0$ and $y = 0$ boundaries only and absorbed at all four boundaries for both orders of the absorbing-generating boundary condition, see Fig. 3.7. The equivalent absorbing-generating boundary conditions are derived for and implemented at all four sides of the domain.

The physical parameters are still water depth h_o and wave length $\lambda = 100\, h_o$, which yields a period $T = 100\sqrt{h_o/g}$. To ensure sufficient accuracy we use the numerical parameters $\Delta x = \Delta y = \lambda/60$ and $\Delta t = T/100$, which yields a Courant number of 0.6. The numerical method used in all tests is a second-order Adams-Bashforth predictor scheme with a third-order Adams-Moulton corrector scheme for the time-integration and a second-order finite difference scheme in space. The predictor-corrector method, while derived for ODE's, has been applied to PDE's in many studies. One of the earlier references is Longuet-Higgins & Cokelet (1976).

In the following, we will first test the lowest-order expansion of the boundary condition (3.77) for a small wave amplitude-to-depth ratio using the linear equations. We will then conduct the same test using the nonlinear shallow water equations to show the influence of the nonlinear terms. Thirdly, we will repeat the second test for a larger amplitude-to-depth ratio to demonstrate its importance. Finally, we will implement the higher-order boundary condition (3.82) and test it

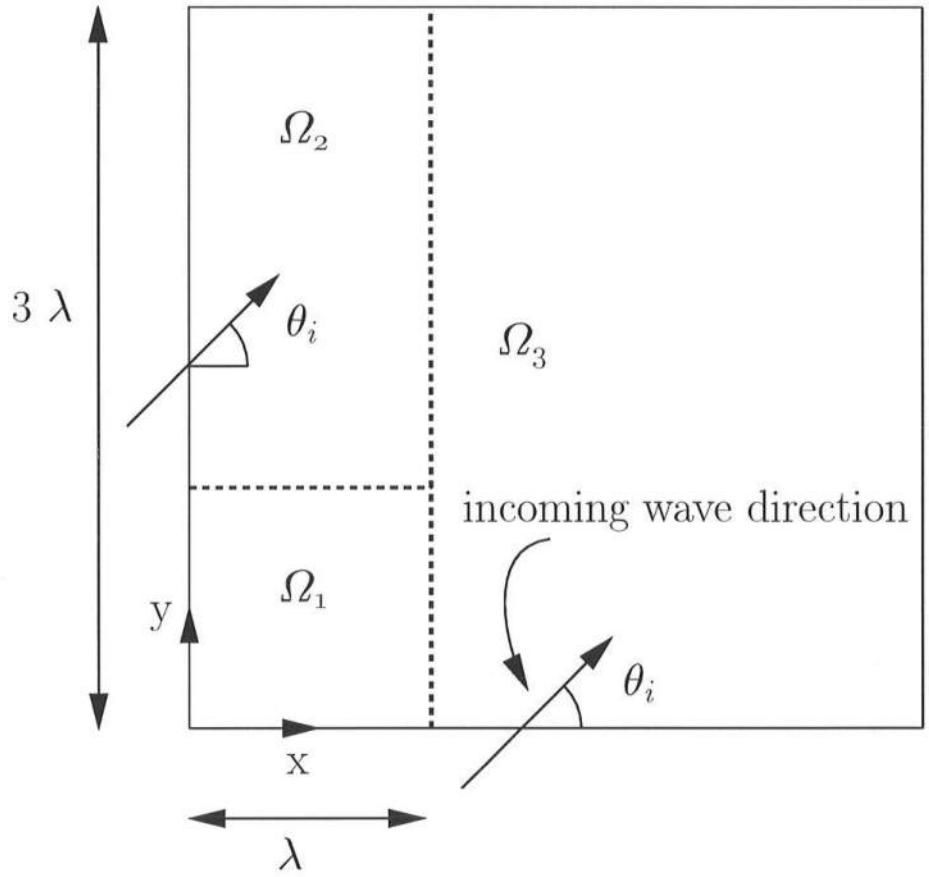

Figure 3.7: Definition sketch of the domains used in the reflection tests.

for the larger amplitude-to-depth ratio using the nonlinear equations to illustrate the performance improvement over the third test.

3.2.4.1 Linear waves

In the first test, sinusoidal waves with a small amplitude $A/h_o = 0.01$ are propagated using the linear equations and absorbed using the boundary condition that applies the lowest order expansion of $Q_{x,r}$, (3.77). Sinusoidal waves are specified as the initial condition. This case was previously shown in Van Dongeren *et al.* (1994).

The reflection properties are computed for a square domain

$$\Omega_1 = \{(x, y) : 0 \leq x \leq \lambda, 0 \leq y \leq \lambda\} \tag{3.86}$$

where we want to make sure that the reflections are caused by one absorbing boundary (at $x = \lambda$) only. This is accomplished as follows. Solutions are computed in two domains: a rectangular domain

$$\Omega_2 = \{(x, y) : 0 \leq x \leq \lambda, 0 \leq y \leq 3\lambda\} \tag{3.87}$$

and a larger, square domain,

$$\Omega_3 = \{(x, y) : 0 \leq x \leq 3\lambda, 0 \leq y \leq 3\lambda\} \tag{3.88}$$

See Fig. 3.7 for a definition sketch.

The non-generating boundaries in domain Ω_3 are placed so far away that they have no effect on the solution in the smaller domain Ω_1 during the duration of the simulation. Therefore inside the smaller domain we can consider the Ω_3-solution free of reflection errors. Similarly, in domain Ω_2 the non-generating boundary at $y = 3\,\lambda$ will not influence the solution in the smaller domain Ω_1. Hence the difference between the two solutions can only be caused by the absorbing boundary at $x = \lambda$. The two solutions are subtracted from each other at the instant in time $t^n = \min(T/\cos\theta_i, T/\sin\theta_i)$ when the initial condition has propagated out of Ω_1 and the difference is normalized by the amplitude A

$$\epsilon_1(x, y, t^n; \theta_i) = \frac{|\,\bar{\zeta}_{\Omega_3}(x, y, t^n; \theta_i) - \bar{\zeta}_{\Omega_2}(x, y, t^n; \theta_i)\,|}{A} \tag{3.89}$$

where $\bar{\zeta}_{\Omega_2}$ and $\bar{\zeta}_{\Omega_3}$ are the solutions for the test runs in the domains Ω_2 and Ω_3, respectively.

Eq. (3.89) yields a spatial picture of the reflection error in Ω_1 due to the absorbing boundary condition at $x = \lambda$. Figs. 3.8a, c and e show contours of the

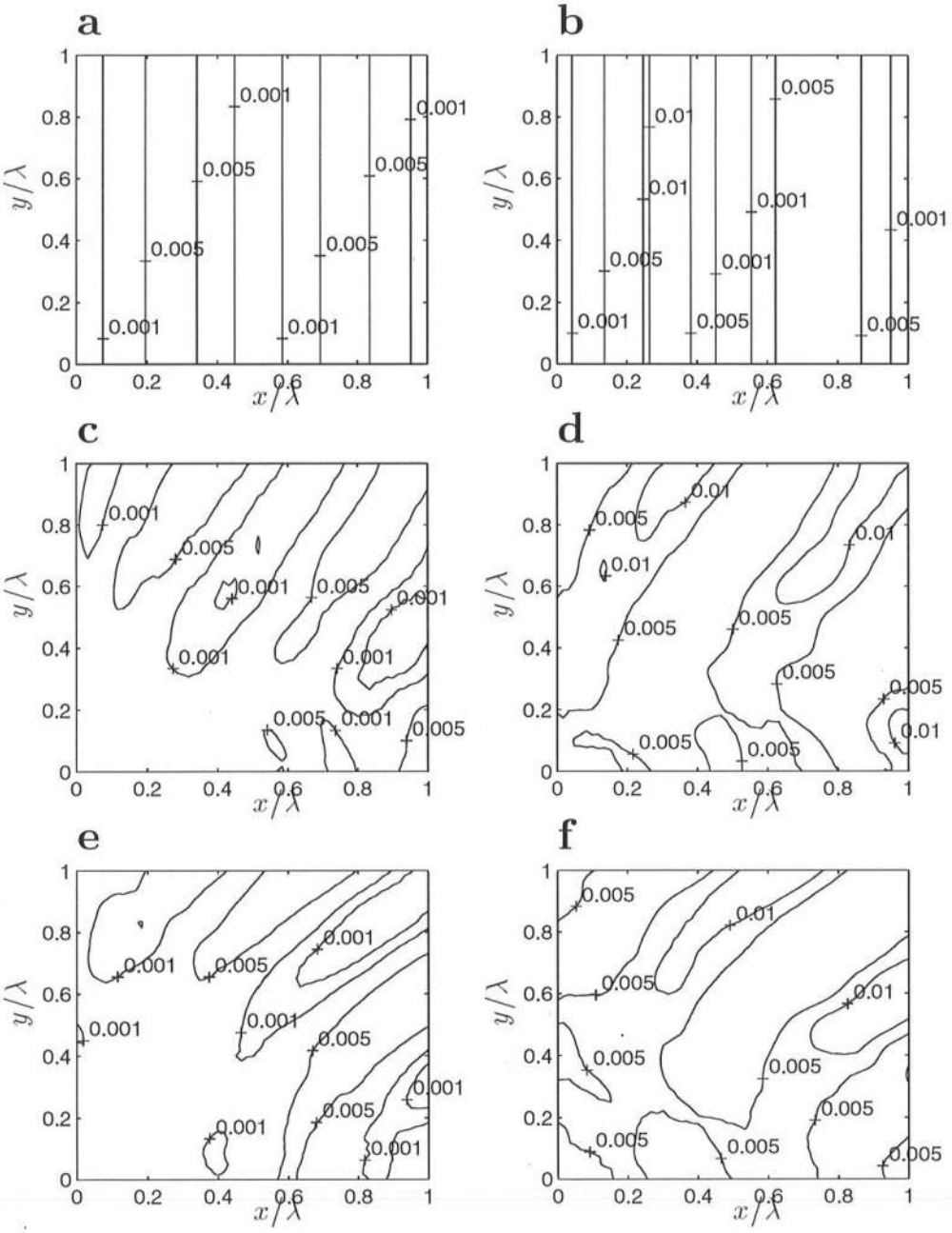

Figure 3.8: Reflection errors vs. $(x/\lambda, y/\lambda)$ for wave amplitude $\mathrm{A}/h_o = 0.01$ using (3.77) (a) linear scheme, $\theta_i = 0$, at $t^n = T$; (b) nonlinear scheme, $\theta_i = 0$, at $t^n = T$; (c) linear scheme, $\theta_i = \frac{\pi}{6}$, at $t^n = T/\cos\frac{\pi}{6}$; (d) nonlinear scheme, $\theta_i = \frac{\pi}{6}$, at $t^n = T/\cos\frac{\pi}{6}$; (e) linear scheme, $\theta_i = \frac{\pi}{4}$, at $t^n = T/\cos\frac{\pi}{4}$; (f) nonlinear scheme, $\theta_i = \frac{\pi}{4}$, at $t^n = T/\cos\frac{\pi}{4}$.

spatial errors for three angles of incidence: $\theta_i = 0, \frac{\pi}{6}$ and $\frac{\pi}{4}$ where θ_i is defined as the angle between the direction of propagation and the x-axis. The errors are of the order 0.005 or 0.5%.

Note that the boundary condition is derived based on the nonlinear equations in characteristic form while the waves themselves are run under the linear equations, which is in itself inconsistent but allowable for small amplitude waves.

3.2.4.2 Nonlinear waves

To show the effect of the nonlinear terms in the equations, a second test is run for the same parameters, the same angles of incidence and with the same order of the boundary condition but using the nonlinear equations. The waves generated at the boundary are again sinusoidal. The spatial errors are plotted in Figs. 3.8b, d and f. Comparison to the previous case shows that including the nonlinear terms in the governing equations increases the error by a factor 2: they are now of the order of 1%. This is due to the fact that in the first order approximation (3.77), Eqs. (3.68) and (3.69) reduce to the linear relationships of constant form

$$Q_{x,i} = c_o \bar{\zeta}_i \cos\theta_i \tag{3.90}$$

$$Q_{x,r} = -c_o \bar{\zeta}_r \cos\theta_r \tag{3.91}$$

where c_o is given by (3.66). This means that in this approximation of the boundary condition the waves are assumed to propagate through the boundary with constant form. This is true for linear waves, but not quite for nonlinear waves. Hence, the nonlinear properties of the wave contribute to the reflection error at the boundary.

As can be seen in Fig. 3.8, the errors are spatially dependent. In order to obtain a single measure of the error as a function of the angle of incidence, the

relative L^2-error is computed (Strikwerda, 1989). This L^2-error is defined as the squared difference of $\bar{\zeta}_{\Omega_2}$ and $\bar{\zeta}_{\Omega_3}$ evaluated in the domain Ω_1 and normalized by the RMS of the larger area solution at the time instant $t = t^n$ when the initial condition has propagated out (which is different for each θ_i)

$$\epsilon_2(t^n;\theta_i) = \frac{\sqrt{\sum_{\Omega_1}(\bar{\zeta}_{\Omega_2}(x,y,t^n;\theta_i) - \bar{\zeta}_{\Omega_3}(x,y,t^n;\theta_i))^2}}{\sqrt{\sum_{\Omega_1}(\bar{\zeta}_{\Omega_3}(x,y,t^n;\theta_i))^2}} \tag{3.92}$$

Figure 3.9 shows the L^2-error for the range of angles of incidence of $\theta_i = [0, \frac{\pi}{12}, \frac{\pi}{6}, \ \ldots\ , \frac{\pi}{2}]$ for both the linear and nonlinear low-amplitude cases described above.

Also plotted in Figure 3.9 is the error incurred when the Sommerfeld radiation condition (3.48) is applied for sinusoidal waves. That condition shows near-perfect absorption for waves of normal incidence but shows large errors for more obliquely incident waves. In fact, the error is 100% for glancing angles. In contrast, the errors due to the boundary condition derived in Subsection 3.2.3 are of the order of 0.5% to 1% for the whole range of angles of incidence, which is acceptable for most applications.

However, the error is a function of the nonlinearity parameter, $\delta = A/h_o$. The absolute error is $O(\delta^2)$, while the relative error, which is the absolute error normalized by the exact flux, is $O(\delta)$.

In a third test, the model is run for the same parameters as the previous test but with a wave with an amplitude ten times as large, $A/h_o = 0.1$. The spatial variation of the reflection errors, see Fig. 3.10a, c and e, are about one order of magnitude larger than in the previous test, as one should expect. Fig. 3.11 (dashed line) shows that the relative L^2-error versus θ_i for a single absorption boundary is about 10%, or $\delta * 100\%$, which is too large for practical purposes.

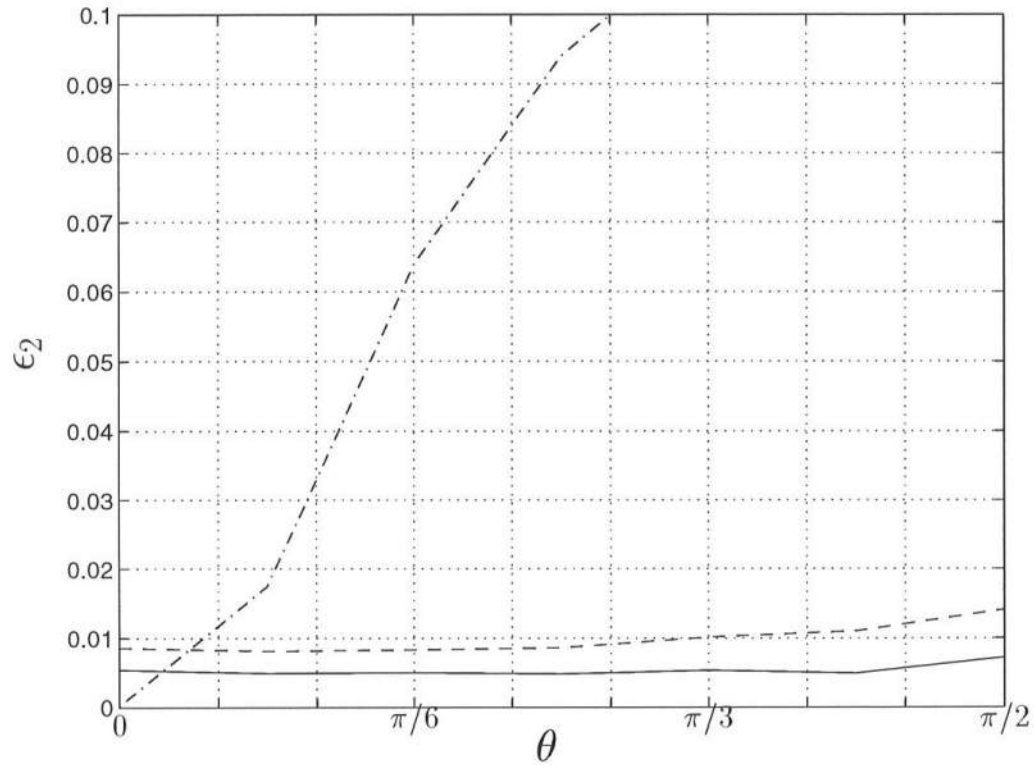

Figure 3.9: Reflection error vs. angle of incidence θ_i for $A/h_o = 0.01$. First order BC: linear scheme (——), nonlinear scheme (– –). Sommerfeld radiation condition: linear scheme. (– ·)

As mentioned in Subsection 3.2.3, a major error source for large amplitude waves is the first order expansion of (3.70). For larger amplitudes, it is therefore advantageous to use the second-order approximation (3.82) as the boundary condition. A fourth test was conducted with the same parameters as in the previous case but with the second-order approximation of the boundary condition (3.82) implemented at all four boundaries. The spatial errors for this test as calculated by (3.89) are shown in Fig. 3.10b, d and f. We see that the error is now reduced by a factor 5 compared to the left-hand side panels. For a single absorbing boundary, the relative L^2-error versus the angle of incidence θ_i as calculated by

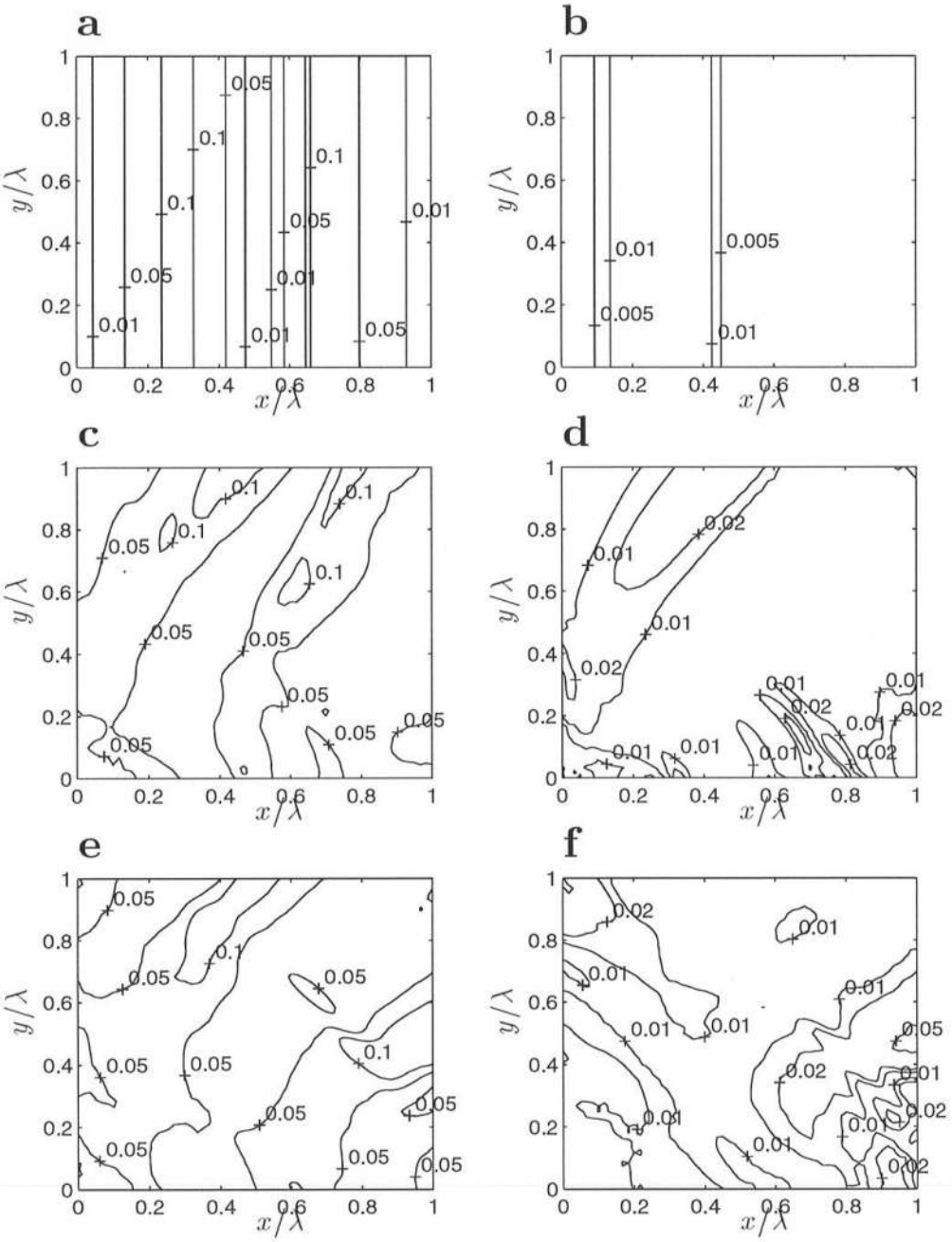

Figure 3.10: Reflection errors vs. $(x/\lambda, y/\lambda)$ for wave amplitude $A/h_o = 0.1$ and a nonlinear scheme (*a*) $\theta_i = 0$, at $t^n = T$, first order BC; (*b*) $\theta_i = 0$, at $t^n = T$, second order BC; (*c*) $\theta_i = \frac{\pi}{6}$, at $t^n = T/\cos\frac{\pi}{6}$, first order BC; (*d*) $\theta_i = \frac{\pi}{6}$, at $t^n = T/\cos\frac{\pi}{6}$, second order BC; (*e*) $\theta_i = \frac{\pi}{4}$, at $t^n = T/\cos\frac{\pi}{4}$, first order BC; (*f*) $\theta_i = \frac{\pi}{4}$, at $t^n = T/\cos\frac{\pi}{4}$, second order BC.

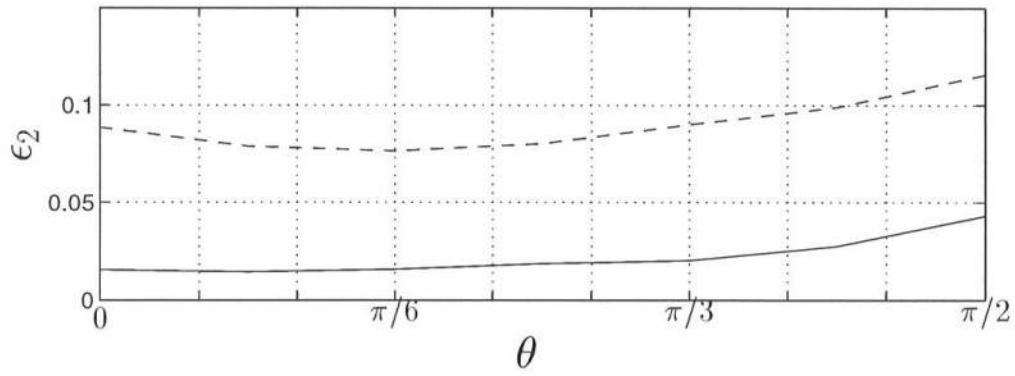

Figure 3.11: Reflection error vs. angle of incidence θ_i for $A/h_o = 0.1$. First order BC (– –), second order BC (——).

(3.92) is shown in Fig. 3.11 (solid line). It has a magnitude of about 3%, which is close to the theoretical normalized relative error $\epsilon_2 \sim \delta^2$ for the second order approximation. For our purposes, this magnitude of the error for medium height waves is acceptable.

Since the second order approximation (3.82) is explicit in $Q_{x,r}$, it does not require considerably more computational time than the linear expression (3.77) and it will therefore be used in the remainder of this section.

3.2.5 Example of Simultaneous Absorption and Generation

To illustrate the application of the boundary condition for the case of simultaneous absorption and generation of waves at one boundary, consider a domain with an absorbing-generating boundary at the $x = 0$ boundary and a wall at $x = L_b = 0.75\lambda$. From a cold start, incoming waves are generated at normal incidence from $t = 0\,T - 10\,T$, tapered with a hyperbolic tangent function during the first and last period of generation in order to suppress transients due to shocks.

This wave train will reflect off the wall at $x = 0.75\,\lambda$ and produce a standing wave until the incident waves are turned off at $T = 10\,T$. The physical parameters used are: water depth $h_o = 1\,m$, wave length $\lambda = 100 h_o$, $T = \lambda / \sqrt{g\,h_o}$, $A = 0.04\,h_o$, so $\delta = 0.04$. The numerical parameters are $\Delta x = \Delta y = \frac{\lambda}{120}$ and $C_r = 0.6$. Two tests are conducted: one for the above parameters using the linearized governing equations and one using the nonlinear equations.

For the first case, Fig. 3.12a shows the time series of the specified volume flux of the incident waves at $x = 0$, normalized by $c_o\,h_o$. The effect of the hyperbolic tangent function is clearly visible as the amplitude grows to its full value in little more than one wave period. Fig. 3.12b shows the flux of the outgoing wave train at the same point as calculated by (3.82). The front of the outgoing wave flux has a delay of $1.5\,T$ because it has to travel back and forth through the domain. The wave flux has a phase shift of π because it is traveling in the $-x$ direction. Some small trailing waves around $t = 12\,T$ can be seen. Still water is recovered almost immediately after the outgoing wave passes through the $x = 0$ boundary, which indicates that the reflections are small. We can quantify the error ϵ_3 as the normalized difference of the amplitude of the incoming and outgoing wave trains, or

$$\epsilon_3 = \frac{|A_i - A_r|}{A_i} = 1.47 \cdot 10^{-4} \tag{3.93}$$

in this case, where A_i is the amplitude of incoming wave train and A_r is the amplitude of the computed outgoing wave train at the $x = 0$ boundary.

The time series of the total flux in Fig. 3.12c, which is the sum of the two time series above, shows first a progressive wave in the $+x$ direction, then the anti-node of the flux of a standing wave, then a progressive wave in the $-x$ direction and finally still water.

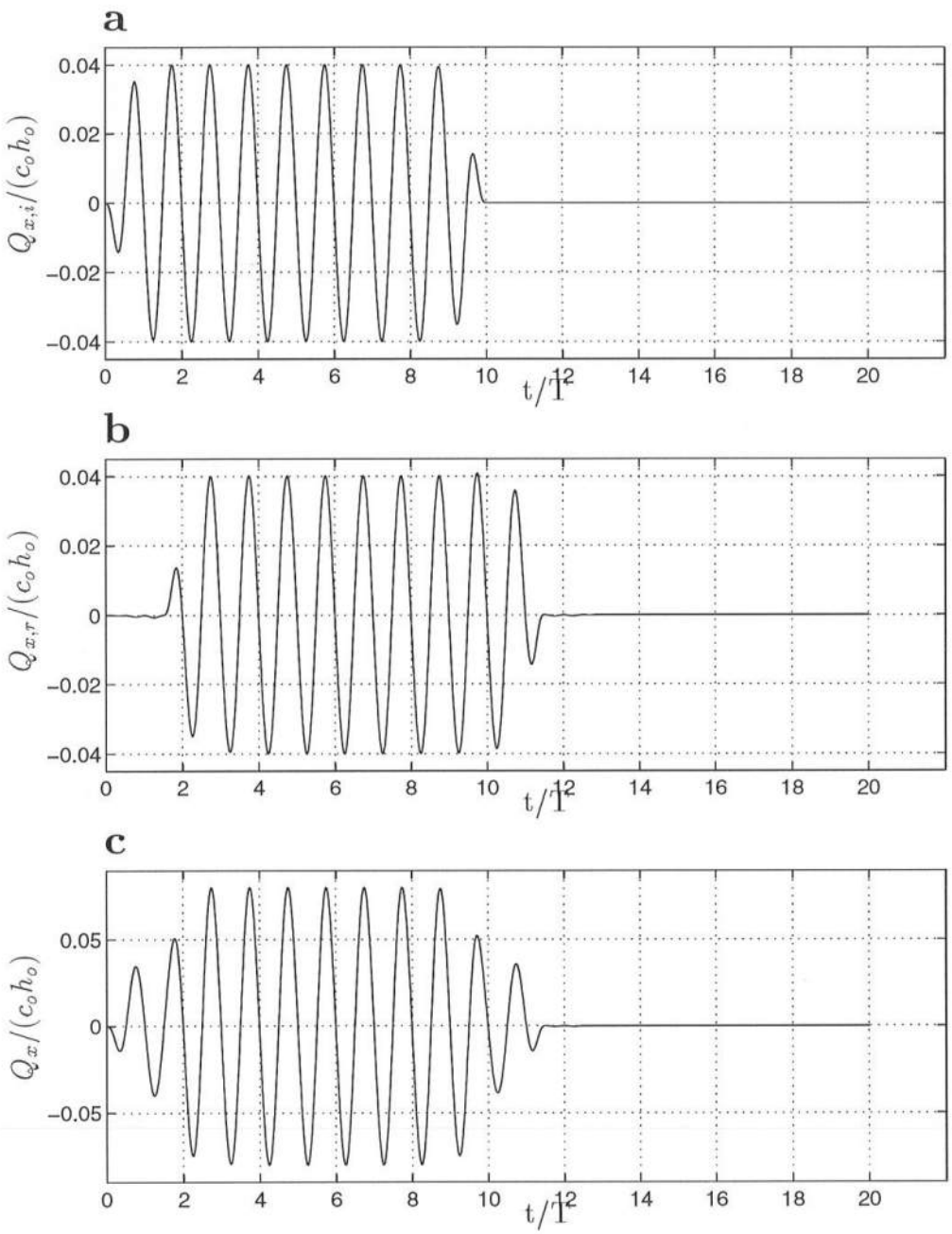

Figure 3.12: Time series at $x = 0$ for the linear equations: (a) incident wave flux. (b) outgoing wave flux. (c) total flux.

In the second test, the second-order boundary condition (3.82) is tested for the same parameters as above but using the nonlinear equations. In the nonlinear case, wave crests propagate faster than wave troughs, which means that the wave fronts steepen up and "break" if a wave is allowed to propagate over a sufficient distance. This distance becomes shorter as the wave amplitude is increased. A wave crest propagates with a celerity

$$(\bar{u} + c)_{crest} = c_o \left(1 + \frac{3}{2}\delta + O(\delta^2)\right) \tag{3.94}$$

where we have used $\bar{u} = c\,\bar{\zeta}_{crest}/h$ from (3.67) and $\bar{\zeta}_{crest} = A$. Similarly, for the speed at the trough we have

$$(\bar{u} + c)_{trough} = c_o \left(1 - \frac{3}{2}\delta + O(\delta^2)\right) \tag{3.95}$$

This means that at the point of generation the difference in time between a trough and the following crest, $\Delta\tau$, by definition is equal to $T/2$ and decreases with distance traveled as

$$\Delta\tau\,(x) = \frac{T}{2} + x\left(\frac{1}{(\bar{u} + c)_{crest}} - \frac{1}{(\bar{u} + c)_{trough}}\right) = T\left(\frac{1}{2} - 3\delta\,\frac{x}{\lambda}\right) \tag{3.96}$$

In order to avoid numerical dissipation at the wave front, we will require that a wave will not have steepened up too much after it has traveled back and forth through the domain over a distance $x = 2\,L_b$ so that

$$\Delta\tau\,(2\,Lb) = T\left(\frac{1}{2} - 6\delta\,\frac{L_b}{\lambda}\right) \leq \frac{3}{10}\,T \tag{3.97}$$

which shows that there is an inverse relationship between the basin length L_b we can use in this test and the nonlinearity δ. Our choice of $L_b = 0.75\,\lambda$ and $\delta = 0.04$ satifies this condition. To facilitate comparison we have used the same parameters in the linear case above, even though (3.97) is not a restriction there.

It should be emphasized that these steepening effects are inherent in the NSW-equations, in which the dispersive terms have been neglected, and that they

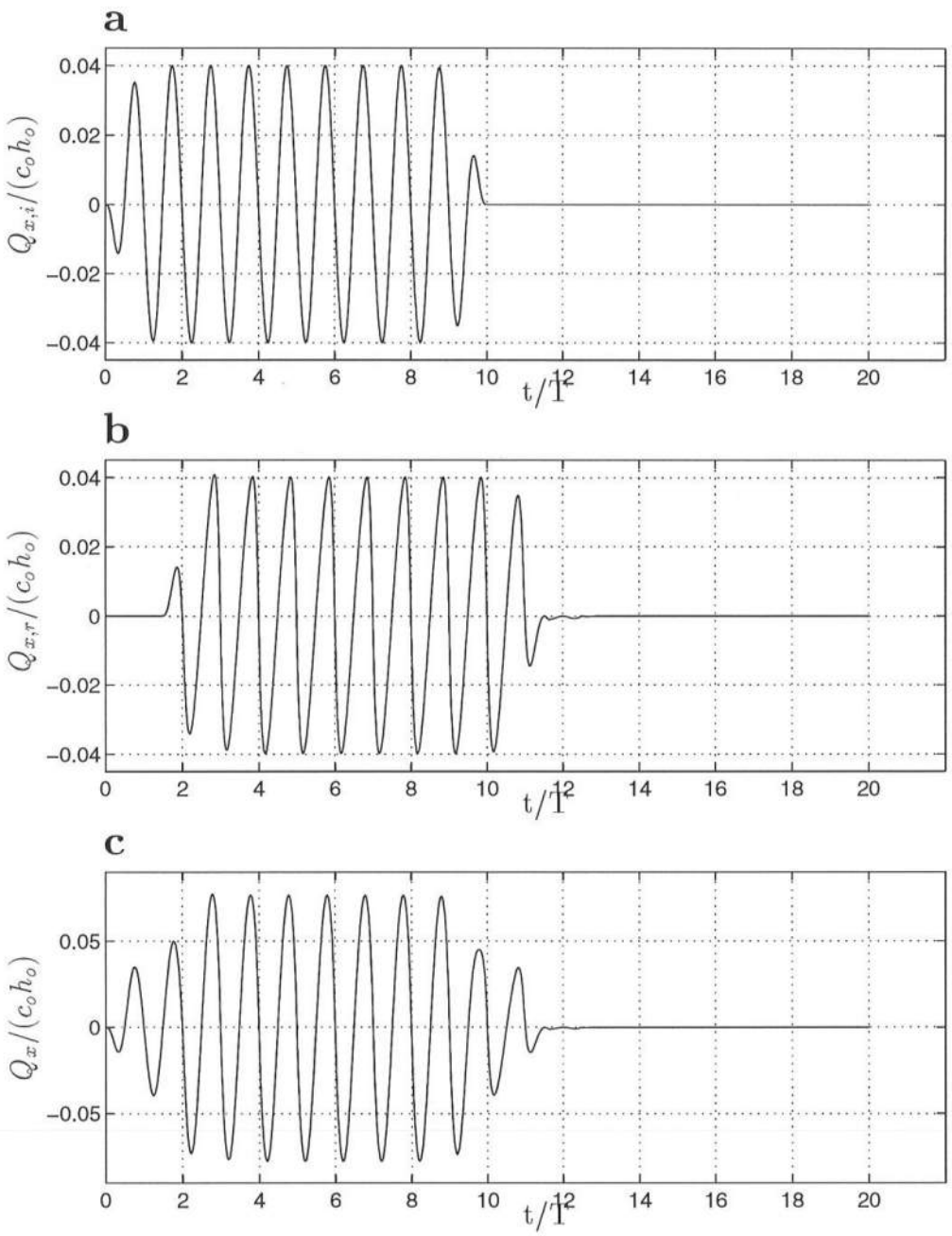

Figure 3.13: Time series at $x = 0$ for the nonlinear equations: (a) incident wave flux. (b) outgoing wave flux. (c) total flux.

are not due to the boundary condition. However, we need to avoid these effects in order to fairly test the boundary condition.

For the nonlinear case, Fig. 3.13a and Fig. 3.13b show the time series of the flux of the incoming and outgoing wave trains, respectively. Notice that the outgoing waves are asymmetric because the wave crests propagate faster than the troughs under the nonlinear equations. As before, we can quantify the error of the boundary condition in this case as

$$\epsilon_3 = \frac{|A_i - A_r|}{A_i} = 8.17 \cdot 10^{-4} \tag{3.98}$$

which, as expected, is larger than the error found in (3.93), and of the order $\epsilon_2 \sim \delta^2 = O(10^{-3})$, as found in the previous subsection, even though the error calculation methods are different. Fig. 3.13c shows the total flux in $x = 0$, similar to Fig. 3.12c.

These examples show that the derived boundary condition performs equally well in the case of simultaneous absorption and generation as in the case of absorption only.

3.2.6 Discussion

The numerical tests described above show that the reflection errors due to the present boundary condition are only a few percent for cases of absorption-generation as well as absorption only. This is a remarkable improvement over the absorption properties of the widely-used radiation conditions based on the wave equation, which only absorb waves at one specific angle of incidence perfectly and produce large errors for other angles of incidence.

It is mentioned that for simplicity the present form of the boundary condition does not account for time-varying or steady currents. However, the mathematical modification of either (3.77) or (3.82) to include currents is straightforward. Accounting for a nonzero current flux $\overline{\overline{Q}}$ and IG-wave averaged surface elevation $\overline{\overline{\zeta}}$, we can generalize (3.63) and (3.64) to

$$Q_x = Q_{x,i} + Q_{x,r} + \overline{\overline{Q}} \tag{3.99}$$

$$\bar{\zeta} = \overline{\overline{\zeta}} + \bar{\zeta}_i + \bar{\zeta}_r \tag{3.100}$$

Following the same procedure as in section 3.2.3, the Riemann-variable (3.61) can now be expanded as

$$\frac{\beta^-}{c_o} = \frac{\overline{\overline{Q}} + Q_{x,i} + Q_{x,r}}{c_o h_o} \left(1 + \frac{\overline{\overline{\zeta}} + \bar{\zeta}_i + \bar{\zeta}_r}{h_o}\right)^{-1} - 2\sqrt{1 + \frac{\overline{\overline{\zeta}} + \bar{\zeta}_i + \bar{\zeta}_r}{h_o}} \tag{3.101}$$

Substituting for the x-components of the incoming and outgoing waves from (3.67)

$$Q_{x,i} = (U + c)\,\bar{\zeta}_i \cos\theta_i \tag{3.102}$$

$$Q_{x,r} = (U - c)\,\bar{\zeta}_r \cos\theta_r \tag{3.103}$$

and expanding to lowest order yields (after some rearranging)

$$Q'_{x,r} = \frac{1}{b'_1}\left(c_3 - c'_1\, Q'_{x,i} - \frac{\overline{\overline{Q}}}{c_o\, h_o} + \frac{\overline{\overline{\zeta}}}{h_o}\right) + O\left(\frac{Q_x}{c_o h_o}\right)^2 \tag{3.104}$$

where c_3 is given by (3.76) and

$$b'_1 \equiv \frac{((1 - \frac{U}{c_o})\cos\theta_r + 1)}{(1 - \frac{U}{c_o})\cos\theta_r} \tag{3.105}$$

$$c'_1 \equiv \frac{((1 + \frac{U}{c_o})\cos\theta_i - 1)}{(1 + \frac{U}{c_o})\cos\theta_i} \tag{3.106}$$

The real problem, as stated in Subsection 3.2.2, lies in the philosophical distinction between currents and long waves and in the fact that currents will have to be known à priori and specified along all boundaries of the domain. This means that the terms involving the long-term averaged value of the water surface elevation $\overline{\overline{\zeta}}$, the current velocity U, and the net volume flux $\overline{\overline{Q}}$ in (3.104) need to be known and specified in order to close the problem. A similar expansion to second order is straightforward.

In its present form the boundary condition has one drawback. It cannot absorb multiple waves with wave number vector directions that deviate more than $\frac{\pi}{2}$. This is due to the fact that by using (3.68) and (3.69) the set of multiple waves at the boundary is essentially approximated by one representative progressive wave, which is not a valid assumption when two or more wave trains intersect at oblique angles.

3.2.7 Conclusions

In this section an absorbing-generating boundary condition for the non-linear shallow water equations is derived based on the Method of Characteristics. Numerical tests show that by using this boundary condition, reflection errors are limited to a few percent of the incident wave amplitude for the full range of angles of incidence, which is an improvement over the classical radiation conditions. Unlike those radiation conditions, the present boundary condition allows simultaneous specification of an incident wave train and absorption of an outgoing wave train at the same boundary, which makes it particularly suitable for application on artificial oceanside boundaries in shallow water models.

3.3 Shoreline Boundary Condition

In the present model it is necessary to impose a boundary condition at the shoreline in order to simulate the inundation/drainage process. This boundary condition needs to be stable and accurate so that the results in the nearshore region are not adversely affected. It also needs to be numerically efficient so that the necessary computational time does not increase dramatically.

The advantage of using a fixed spatial grid is that the governing equations can be coded easily and efficiently. The main disadvantage is that a fluctuating surface elevation will cause nodes in the swash zone to change from being inundated to being dry and vice versa as opposed to so-called "moving grid" models in which the spatial grid is adapted to the changing surface elevation.

In the literature only a few shoreline boundary procedures on a fixed spatial grid have been described in detail. Reid & Bodine (1968) were the first to describe a procedure in which dry land is inundated if the water level exceeds the bathymetric level of the land. Hibberd & Peregrine (1979) described the run-up and run-down of a uniform bore on a sloping beach. They linearly extrapolated the surface elevation in the most shoreward "wet" node to determine whether the next point will become "wet" or stay "dry" in the next time step. If the depth in this most shoreward "wet" node fell below a small threshold value δ this node would become "dry" itself and the procedure would be repeated for the next "wet" node at the next time step. They report good agreement with analytical solutions for non-breaking waves (Carrier & Greenspan, 1958; Spielvogel, 1976). Kobayashi *et al.* (1987) and Kobayashi & Johnson (1995) used the same technique and improved on the tendency of this boundary condition to become unstable. However, the procedure becomes very complicated. Brocchini & Peregrine (1996) provided a theoretical outline for a shoreline boundary condition but

did not give an application of the theory.

In this thesis we apply an alternative procedure based on the physical principle of storing a volume of water between the most landward inundated node and the actual shoreline. First we will discuss the longshore uniform (or 1- D) case and then make an extension to the two-dimensional horizontal situation. The boundary condition will be tested against a nonlinear analytical solution by Carrier & Greenspan (1958) for the longshore uniform case and against two numerical solutions (Zelt, 1986; Özkan-Haller & Kirby, 1997) for the two-dimensional case.

3.3.1 One-dimensional Procedure

The one-dimensional procedure is essentially as illustrated in Fig. 3.14. At a given time $t = t^n$, the water surface and the beach have a point of contact, which lies between the fixed grid points x_o and $x_o + \Delta x$. Nodes at $x \leq x_o$ are then inundated (or *wet*) while points $x > x_o$ are dry. This implicitly assumes a monotonically varying water depth in the swash zone. The variable s^n denotes the distance between the last wet node x_o and the actual shoreline position.

The volume (or rather, area in the one-dimensional case) of water stored landward of node x_o at $t = t^n$ can be calculated as

$$\Omega_1 = \int_{x_o}^{x_o+s^n} \int_{-h_o}^{\zeta^n} dz\, dx = \int_{x_o}^{x_o+s^n} (h_o + \zeta^n)\, dx \tag{3.107}$$

Expanding the depth and surface elevation in Taylor-series about the last wet node at $x = x_o$ and integrating yields

$$\Omega_1 = \int_{x_o}^{x_o+s^n} \left(h_o|_{x_o} + \left.\frac{\partial h_o}{\partial x}\right|_{x_o} (x - x_o) + \right.$$

$$\left. \zeta^n|_{x_o} + \left.\frac{\partial \zeta^n}{\partial x}\right|_{x_o} (x - x_o) + O(\Delta x^2) \right) dx =$$

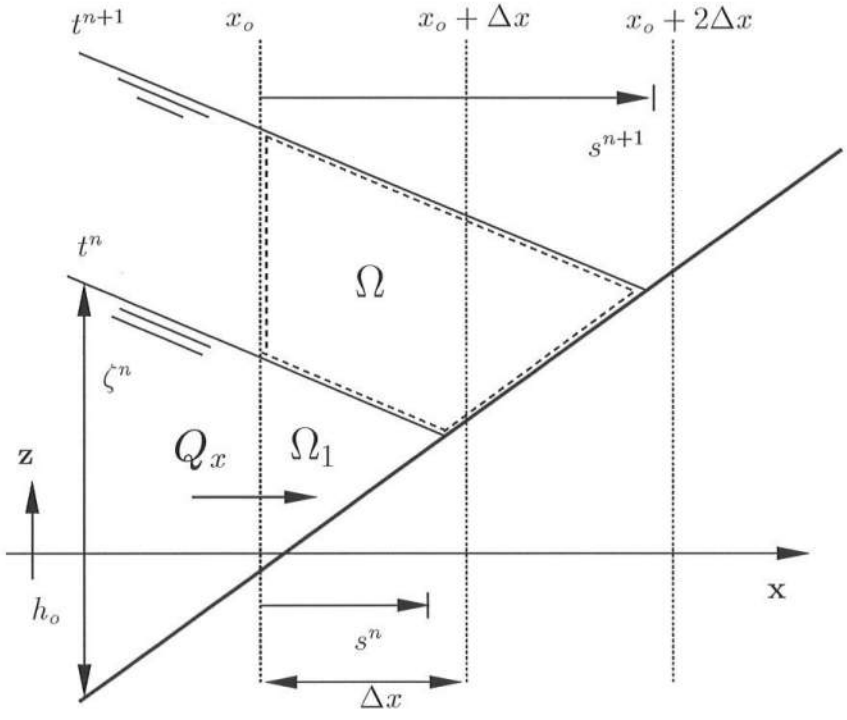

Figure 3.14: Schematic representation of a cross-section near the shoreline.

$$(h_o + \zeta^n)|_{x_o} s^n + \frac{1}{2}\left(\frac{\partial h_o}{\partial x} + \frac{\partial \zeta^n}{\partial x}\right)\Big|_{x_o} (s^n)^2 + O(\Delta x^3) \quad (3.108)$$

The horizontal distance s^n can be found from the intersection of the free surface and the bathymetry, again expanded about the last wet node x_o, where from now on we will drop the x_o-index.

$$-h_o - \frac{\partial h_o}{\partial x} s^n = \zeta^n + \frac{\partial \zeta^n}{\partial x} s^n \Leftrightarrow$$

$$s^n = -\frac{h_o + \zeta^n}{\frac{\partial h_o}{\partial x} + \frac{\partial \zeta^n}{\partial x}} \quad (3.109)$$

Substituting (3.109) into (3.108) yields

$$\Omega_1 = -\frac{1}{2}\frac{(h_o+\zeta^n)^2}{\frac{\partial h_o}{\partial x}+\frac{\partial \zeta^n}{\partial x}} \tag{3.110}$$

which, as stated before, is the volume stored shorewards of $x = x_o$ at $t = t^n$. In the small time step Δt from $t = t^n$ to $t = t^{n+1}$ the time-integrated flux $\bar{Q}_x$ through the cross-section at the most shoreward wet point x_o will add or subtract water to this volume. This integrated flux yields a volume Ω

$$\Omega = \int_{t^n}^{t^{n+1}} \bar{Q}_x\Big|_{x_o}\, dt \tag{3.111}$$

where we can use a predictor-corrector scheme for the numerical time-stepping, as was done for the governing equations themselves. The variable $\bar{Q}$ at $x = x_o$ in (3.111) is itself updated from the x-momentum equation, which includes friction terms.

In the case of uprush, Ω is stored in the dashed box beyond the last wet point x_o in addition to the volume Ω_1, already present. To the first approximation the water surface gradient does not change in this small time step, we can calculate the surface elevation in node x_o at the next time level $t = t^{n+1}$. At that time we then have

$$\Omega_1 + \Omega = -\frac{1}{2}\frac{(h_o+\zeta^{n+1})^2}{\frac{\partial h_o}{\partial x}+\frac{\partial \zeta^n}{\partial x}} \quad \Leftrightarrow$$

$$\zeta^{n+1} = \sqrt{-2\,(\Omega_1+\Omega)\left(\frac{\partial h_o}{\partial x}+\frac{\partial \zeta^n}{\partial x}\right)} - h_o \tag{3.112}$$

which means that the surface elevation in $x = x_o$ at the next time step $t = t^{n+1}$ is known. Similarly we can calculate the new point of contact between the bed and the water surface at the next time $t = t^{n+1}$ as

$$s^{n+1} = \sqrt{-2\,\frac{\Omega_1+\Omega}{\frac{\partial h_o}{\partial x}+\frac{\partial \zeta^n}{\partial x}}} \tag{3.113}$$

If the new point of contact lies shoreward of the dry point $x_o + \Delta x$, as is the case in Fig. 3.14, this grid point then becomes "wet", i.e., the new shorewardmost node.

The point of contact at $x = x_o + s^{n+1}$ does not necessarily coincide with a grid point. However, using the fact that the cross-shore flux at $x_o + s^{n+1}$ is zero by definition, we can find the cross-shore flux in the shorewardmost node by linear interpolation between the flux in the point of contact (which is zero) and the flux in the next-to-last "wet" node.

In the case of a receding water level in the downrush phase the integrated flux through the last wet point is subtracted from the volume stored landwards of that point. The procedure is essentially the same as described for the uprush with one exception. If the integrated flux exceeds the stored volume, the point x_o becomes dry and the point $x_o - \Delta x$ becomes the new most landward dry point.

In the next time step the procedure is repeated for the new shorewardmost point. At that time level the local surface gradient in the last "wet" node is evaluated from the updated values of the surface elevation in the three shorewardmost grid points, which allows the gradient to be different from the gradient at $t = t^n$.

3.3.2 Two-dimensional Procedure

The procedure in two dimensions is an extension of the previous subsection. We now must take into account the longshore variation of the surface elevation, the flux and the bathymetry. Consider a spatial grid and an arbitrary shoreline at $t = t^n$ as illustrated in the plan view of Fig. 3.15. The solid nodes are the inundated nodes in the ocean, and the open nodes are the dry nodes at time step $t = t^n$.

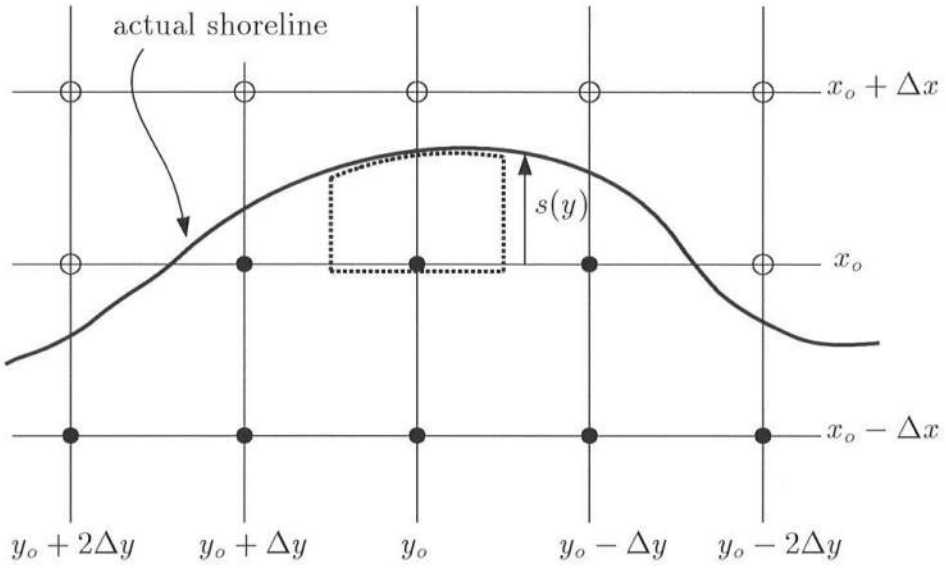

Figure 3.15: Plan view of an arbitrary shoreline on a fixed grid with inundated nodes (•) and "dry" nodes (○).

In order to update the variables at a grid point (x_o, y_o), which is the closest "wet" node to the shoreline in the x-direction for a given $y = y_o$, we first consider the volume of water stored in the control volume indicated by the dashed lines at $t = t^n$

$$\Omega_1 = \int_{y_o-\frac{\Delta y}{2}}^{y_o+\frac{\Delta y}{2}} \int_{x_o}^{x_o+s^n(y)} \int_{-h_o}^{\zeta^n} dz\, dx\, dy =$$

$$\int_{y_o-\frac{\Delta y}{2}}^{y_o+\frac{\Delta y}{2}} \int_{x_o}^{x_o+s^n(y)} (h_o + \zeta^n)\, dx\, dy \tag{3.114}$$

Using (3.108) for the inner integrals we have

$$\Omega_1 = \int_{y_o-\frac{\Delta y}{2}}^{y_o+\frac{\Delta y}{2}} \left((h_o + \zeta^n)|_{(x_o,y)}\, s^n(y) + \frac{1}{2} \left(\frac{\partial h_o}{\partial x} + \frac{\partial \zeta^n}{\partial x} \right)\Bigg|_{(x_o,y)} (s^n(y))^2 \right.$$

$$\left. + O(\Delta x^3) \right) dy \tag{3.115}$$

Expanding about $y = y_o$, dropping the indices and truncating to $O(\Delta y)^2$ yields

$$\Omega_1 = \int_{y_o-\frac{\Delta y}{2}}^{y_o+\frac{\Delta y}{2}} \Bigg((h_o + \frac{\partial h_o}{\partial y}(y-y_o) + \zeta^n + \frac{\partial \zeta}{\partial y}(y-y_o) + O(\Delta y)^2)$$

$$+ (s^n + \frac{\partial s^n}{\partial y}(y-y_o) + O(\Delta y)^2) \; + \frac{1}{2}\left(\frac{\partial h_o}{\partial x} + \frac{\partial \zeta^n}{\partial x}\right)(s^n(y))^2$$

$$+ O(\Delta x^3, \Delta y^2)\Big)\, dy \tag{3.116}$$

Integrating with respect to y yields

$$\Omega_1 = (h_o + \zeta^n)\, s^n\, \Delta y + \frac{1}{2}\left(\frac{\partial h_o}{\partial x} + \frac{\partial \zeta^n}{\partial x}\right)(s^n)^2\, \Delta y$$

$$+ O(\Delta x^3, \Delta y^3) \tag{3.117}$$

where all variables are evaluated at (x_o, y_o). As before we can substitute (3.109) and we then get

$$\Omega_1 = -\frac{1}{2}\frac{(h_o+\zeta^n)^2}{\frac{\partial h_o}{\partial x} + \frac{\partial \zeta^n}{\partial x}}\Delta y + O(\Delta x^3, \Delta y^3) \tag{3.118}$$

where all variables are evaluated at (x_o, y_o). Notice that for this order of the approximation (3.118) is equal to (3.110) multiplied by the longshore grid space Δy.

Similar to the previous case we can calculate the net in- or outflow through the boundaries of the control volume in the time step Δt from $t = t^n$ to $t = t^{n+1}$. The net inflow through the three boundaries is

$$\Omega = \int_{t^n}^{t^{n+1}} \int_{y_o-\frac{\Delta y}{2}}^{y_o+\frac{\Delta y}{2}} Q_x|_{(x_o,y)}\, dy + \int_{x_o}^{x_o+s(y_o-\frac{\Delta y}{2})} Q_y|_{(x,y_o-\frac{\Delta y}{2})}\, dx -$$

$$\int_{x_o}^{x_o+s(y_o+\frac{\Delta y}{2})} Q_y|_{(x,y_o+\frac{\Delta y}{2})}\, dx\, dt \tag{3.119}$$

We expand the first integral in Taylor-series about (x_o, y_o), the second integral about $(x_o, y_o - \frac{\Delta y}{2})$ and the third integral about $(x_o, y_o + \frac{\Delta y}{2})$

$$\Omega = \int_{t^n}^{t^{n+1}} \left(\int_{y_o - \frac{\Delta y}{2}}^{y_o + \frac{\Delta y}{2}} Q_x|_{(x_o,y_o)} + \left.\frac{\partial Q_x}{\partial y}\right|_{(x_o,y_o)} (y - y_o) + O(\Delta y^2)\, dy \right)$$

$$+ \left(\int_{x_o}^{x_o + s(y_o - \frac{\Delta y}{2})} Q_y|_{(x_o, y_o - \frac{\Delta y}{2})} + \left.\frac{\partial Q_x}{\partial x}\right|_{(x_o, y_o - \frac{\Delta y}{2})} (x - x_o) + O(\Delta x^2)\, dx \right)$$

$$- \left(\int_{x_o}^{x_o + s(y_o + \frac{\Delta y}{2})} Q_y|_{(x_o, y_o + \frac{\Delta y}{2})} + \left.\frac{\partial Q_x}{\partial x}\right|_{(x_o, y_o + \frac{\Delta y}{2})} (x - x_o) + O(\Delta x^2)\, dx \right)$$

$$dt \tag{3.120}$$

and evaluate the spatial integrals to find

$$\Omega = \int_{t^n}^{t^{n+1}} \Big(Q_x|_{(x_o,y_o)}\, \Delta y$$

$$+ Q_y|_{(x_o, y_o - \frac{\Delta y}{2})} s|_{(y_o - \frac{\Delta y}{2})} + \left.\frac{\partial Q_x}{\partial x}\right|_{(x_o, y_o - \frac{\Delta y}{2})} s^2|_{(y_o - \frac{\Delta y}{2})}$$

$$- Q_y|_{(x_o, y_o + \frac{\Delta y}{2})} s|_{(y_o + \frac{\Delta y}{2})} - \left.\frac{\partial Q_x}{\partial x}\right|_{(x_o, y_o + \frac{\Delta y}{2})} s^2|_{(y_o + \frac{\Delta y}{2})} \Big)\, dt$$

$$+ O(\Delta x^3, \Delta y^3) \tag{3.121}$$

We then expand this expression about (x_o, y_o), keep terms up to $O(\Delta x^3, \Delta y^3, s^3)$ where $s = O(\Delta x)$ and omit the indices to get

$$\Omega = \int_{t^n}^{t^{n+1}} \Big(Q_x\, \Delta y + Q_y\, s - Q_y \frac{\Delta y}{2} \frac{\partial s}{\partial y} - \frac{\Delta y}{2} \frac{\partial Q_y}{\partial y} s + \frac{\partial Q_y}{\partial x} s^2$$

$$- Q_y\, s - Q_y \frac{\Delta y}{2} \frac{\partial s}{\partial y} s - \frac{\Delta y}{2} \frac{\partial Q_y}{\partial y} s - \frac{\partial Q_y}{\partial x} s^2$$

$$+ O(\Delta x^3, \Delta y^3) \Big)\, dt \tag{3.122}$$

After some rearranging we then get

$$\Omega = \Delta y \int_{t^n}^{t^{n+1}} \left(Q_x - \frac{\partial Q_y s}{\partial y} \right) dt + O(\Delta x^3, \Delta y^3) \qquad (3.123)$$

Again, similarly to the one-dimensional procedure, we add Ω, from (3.123), and Ω_1, from (3.118) to find the surface elevation at (x_o, y_o, t^{n+1}) and we can calculate the distance s^{n+1} from x_o to the actual shoreline. If this distance exceeds Δx, the previously dry node $x_o + \Delta x$ becomes wet during this time step in the case of local run-up. In the case of local run-down the last wet node becomes dry if the flux out of the control volume exceeds the stored volume.

This procedure is repeated for all nodes in y, where x_o is the most shoreward "wet" node for every cross-section in y.

3.3.3 Numerical Tests

The shoreline boundary condition was tested against an analytical solution by Carrier & Greenspan (1958) for the longshore uniform case and against two numerical solutions by Zelt (1986) and Özkan-Haller & Kirby (1997) for the two-dimensional case of a concave beach.

3.3.3.1 One-dimensional case: Carrier & Greenspan (1958)

Carrier & Greenspan (1958) derived a nonlinear analytical solution for the problem of the run-up of a non-breaking shallow water wave on a plane beach. They were able to find an explicit solution by a transformation of the independent variables (x, t). They studied the run-up of a single surge after the release of a mound of water offshore and also the run-up as a result of a periodic forcing offshore. We choose to compare the model results to the analytical solution for the last case.

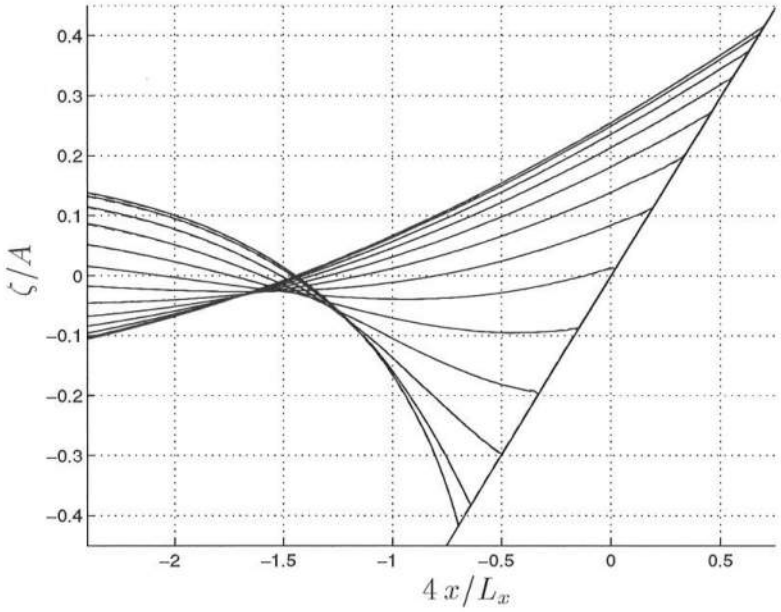

Figure 3.16: Comparison of present model (——) to Carrier & Greenspan (– –) for $A = 0.7$ for time-instances at intervals of 0.13 T

The parameters governing the solution are the horizontal length scale L_x, the bottom slope h_x and the amplitude of the wave motion A. For this comparison, we choose $L_x = 50\,m$ and $h_x = 1/30$. These parameters define the period of the motion as $T = \sqrt{L_x/(g\,h_x)} = 12.36s$.

The model equations used in this test are the NSW equations with friction or forcing. The numerical parameters are $\Delta x = \frac{1}{8}m$ and a Courant number $\nu = 0.7$. The model is first tested for an amplitude of $A = 0.7$. Figure 3.16 shows the comparison between the present model and the analytical solution at time intervals of 0.13 T. The surface elevation is normalized by the amplitude A. The model results agree so well with the analytical solution that it is difficult to see the difference between the solid and the dashed line.

Figure 3.17 shows the comparison between the present model and time

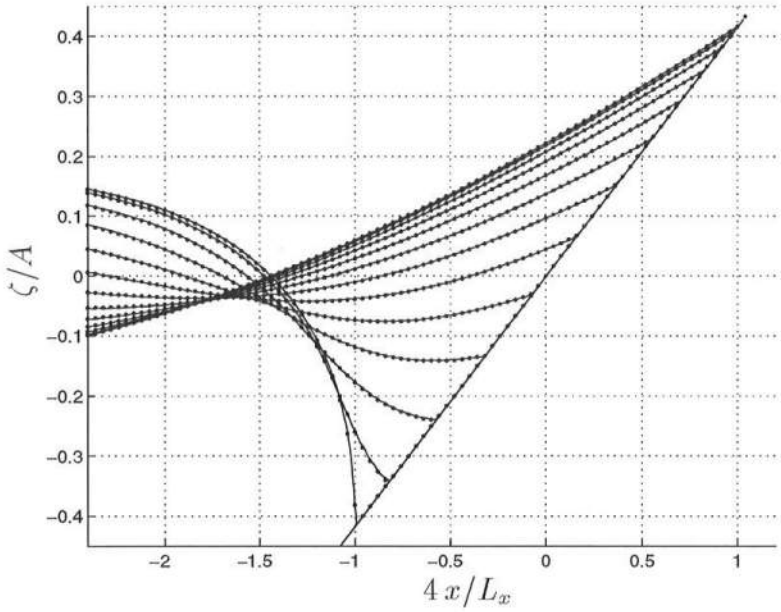

Figure 3.17: Comparison of present model (——) to Carrier & Greenspan (• • •) for $A = 1.0$ for time-instances at intervals of 0.13 T

instances of the analytical solution at intervals of 0.13 T for $A = 1.0$, which is the maximum non-breaking wave amplitude. We see that the model and theory agree very well in this case also. Of course, the agreement will become less if a larger space step is used. This test shows that the numerical model converges to the analytical solution.

3.3.3.2 Two-dimensional case: Zelt (1986) and Özkan-Haller & Kirby (1997)

The two-dimensional shoreline boundary condition is tested against two numerical solutions for the run-up of a solitary wave on a concave beach with a sloping bottom. One solution is by Zelt (1986), who used this case to test a fully Lagrangian finite element model of the shallow water equations, which included

some dissipative and dispersive terms. Özkan-Haller & Kirby (1997) used the same case to test their Fourier-Chebyshev Collocation model of the nonlinear shallow water equations.

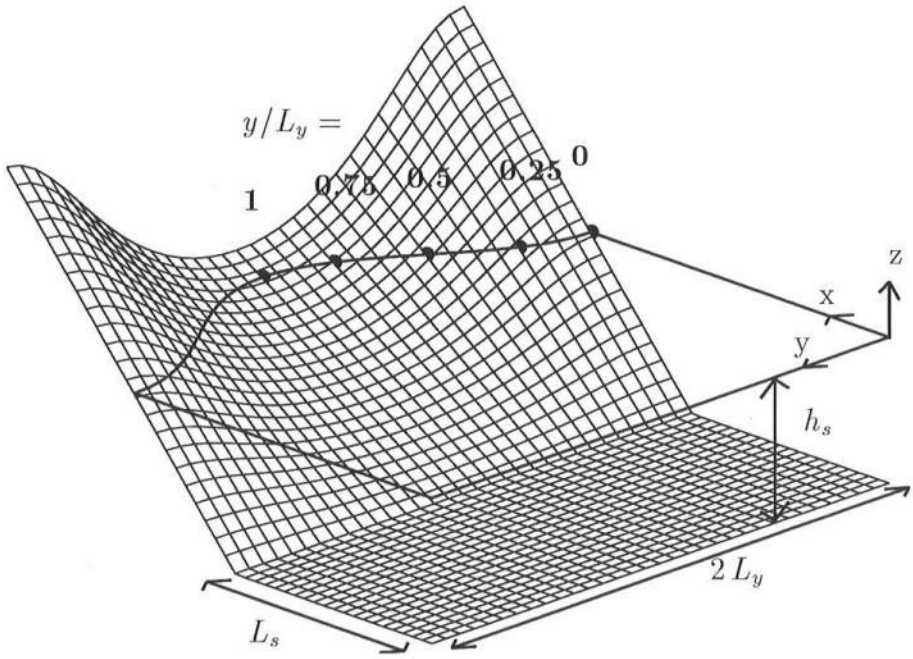

Figure 3.18: Definition sketch of the concave beach bathymetry (courtesy Dr. H.T. Özkan-Haller)

Figure 3.18 shows the definition sketch of the concave beach bathymetry in the present coordinate system, converted from the original system by Zelt (1986). The bathymetry consists of a flat bottom part and a beach part with a sinusoidally varying slope. For Zelt (1986)'s fixed parameter choice of $\sqrt{\beta} = \frac{h_s}{L_y} = \frac{4}{10\pi}$, the bathymetry is given by

$$h = \begin{cases} h_s & , \quad x \leq L_s \\ \\ h_s - \frac{0.4\,(x - L_s)}{3 - \cos\left(\frac{\pi y}{L_y}\right)} & , \quad x > L_s \end{cases} \tag{3.124}$$

where h_s is the shelf depth, L_s is the length of the shelf in the modeled domain and L_y is the length scale of the longshore variation of the beach. This results in a beach slope of $h_x = \frac{1}{10}$ in the center of the bay and of $h_x = \frac{1}{5}$ normal to the "headlands". In the following we chose $L_y = 8\,m$, which determines $h_s = 1.0182\,m$. We set $L_s = L_y$. Different values for L_s only cause phase shifts in the results, but no qualitative difference, so this parameter is not important in this problem. Also indicated in the Figure are the five stations where the vertical run-up (the surface elevation at the shoreline) will be measured.

At the offshore ($x = 0$) boundary we specify an incoming solitary wave, which in dimensional form reads

$$\bar{\zeta}_i(t) = \alpha\, h_s\, \mathrm{sech}^2\left(\sqrt{\frac{3\,g}{4\,h_s}\,\alpha\,(1+\alpha)}\;\;(t - t_o)\right) \tag{3.125}$$

which is similar to Zelt (1986)'s Eq. (5.3.7). The phase shift t_o is chosen such that the surface elevation of the solitary wave at $t = 0$ is 1% of the maximum amplitude. The only parameter yet to be chosen is α. We will compare our model to Zelt's case of $\alpha = \frac{H}{h_s} = 0.02$, where H is the offshore wave height. Zelt found that the wave broke for a value of $\alpha = 0.03$, so the present test should involve no breaking, but has a large enough nonlinearity to exhibit a pronounced two-dimensional run-up.

Any outgoing waves will be absorbed at the offshore boundary by the absorbing-generating boundary condition described in Section 3.2. At the lateral boundaries $y = 0$ and $y = 2\,L_y$ we specify a no-flux (wall) boundary condition following Zelt. The model equations used in this test are the nonlinear shallow water equations without forcing or friction. The numerical parameters are $\Delta x = \Delta y = \frac{1}{8}\,m$ with a Courant number $\nu = 0.7$.

Fig. 3.19a shows the normalized vertical run-up at the five cross-sections

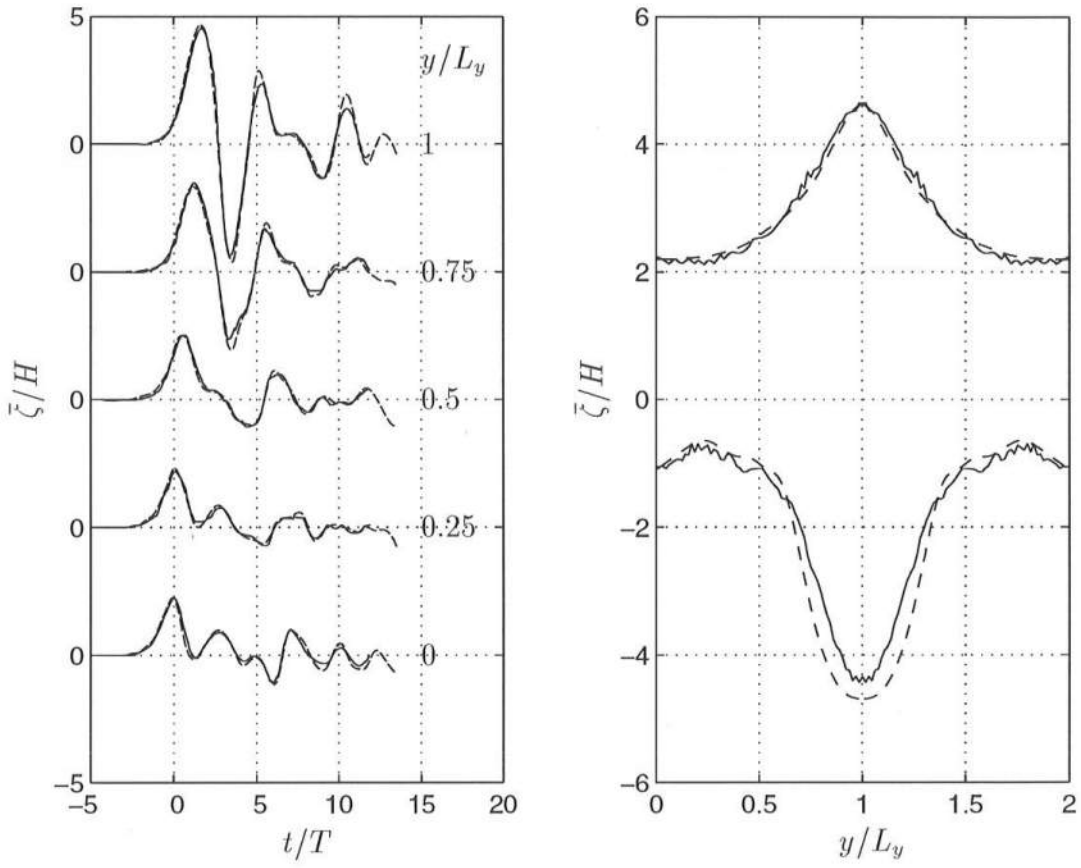

Figure 3.19: Comparison of present model (——) to Zelt (1986) (– –) for $\alpha = 0.02$: (a) Timeseries of run-up in 5 stations, (b) Maximum run-up and run-down.

indicated in Fig. 3.18 as a function of time, which is normalized by $\sqrt{g\,h_s}/L_y$. The solid lines represent the present model results while the dashed lines denotes Zelt's numerical results. Here $y/L_y = 0$ is the position at the headland, while $y/L_y = 1$ represents the midpoint of the bay. We see that the agreement is generally good, except that the present model does not capture the second peak in the time series at $y/L_y = 0$ very well. This secondary peak or "ringing" is due to the wave energy that is trapped along the coast and propagates towards the midpoint of the bay (Zelt, 1986). It is suspected that this focusing mechanism is not properly

captured because the present method approximates the shoreline as a staircase pattern, which in effect lengthens the shoreline. Also, the spatial derivatives are not evaluated parallel and perpendicular to the actual shoreline but in the fixed x and y directions. The first trough in the time-series at $y/L_y = 0.75$ is also not captured well, but this will be shown to improve in the comparison below. The agreement at the locations $y/L_y = 0.25$ and $y/L_y = 0.5$ is generally good despite the large gradient of the local shoreline relative to our grid.

Fig. 3.19b shows the maximum vertical run-up and run-down, normalized by H, versus the alongshore coordinate y. It is seen that the maximum run-up agrees well with Zelt but that the maximum run-down is not represented well in the center of the domain. The "wiggles" in the solid line are evidence of the staircasing of the shoreline: since the shoreline is not treated as a continuous but rather as a discrete function, so is the run-up in the individual nodes.

As stated above, Zelt modeled the NSW equations including some dispersive and dissipative terms, which the present model does not have. For that reason, we also compared our model to the results of Özkan-Haller & Kirby (1997) who modeled the NSW equations using a Fourier-Chebyshev Collocation method, which does not have any numerical dissipation or dispersion errors. They use a moving, adapting grid with a fixed Δy (which is equal to the present model's Δy in this comparison) but with a spatially and temporally varying Δx so that the grid spacing in x near the shoreline is very small. In the present model Δx is set equal to Δy, which means that we can expect to have less resolution at the shoreline than Özkan-Haller & Kirby (1997).

Fig. 3.20a shows the normalized vertical run-up at the five cross-sections versus normalized time. We see that the present model (solid lines) agrees better with Özkan-Haller & Kirby (1997)'s results (dashed lines) than with Zelt (1986)'s,

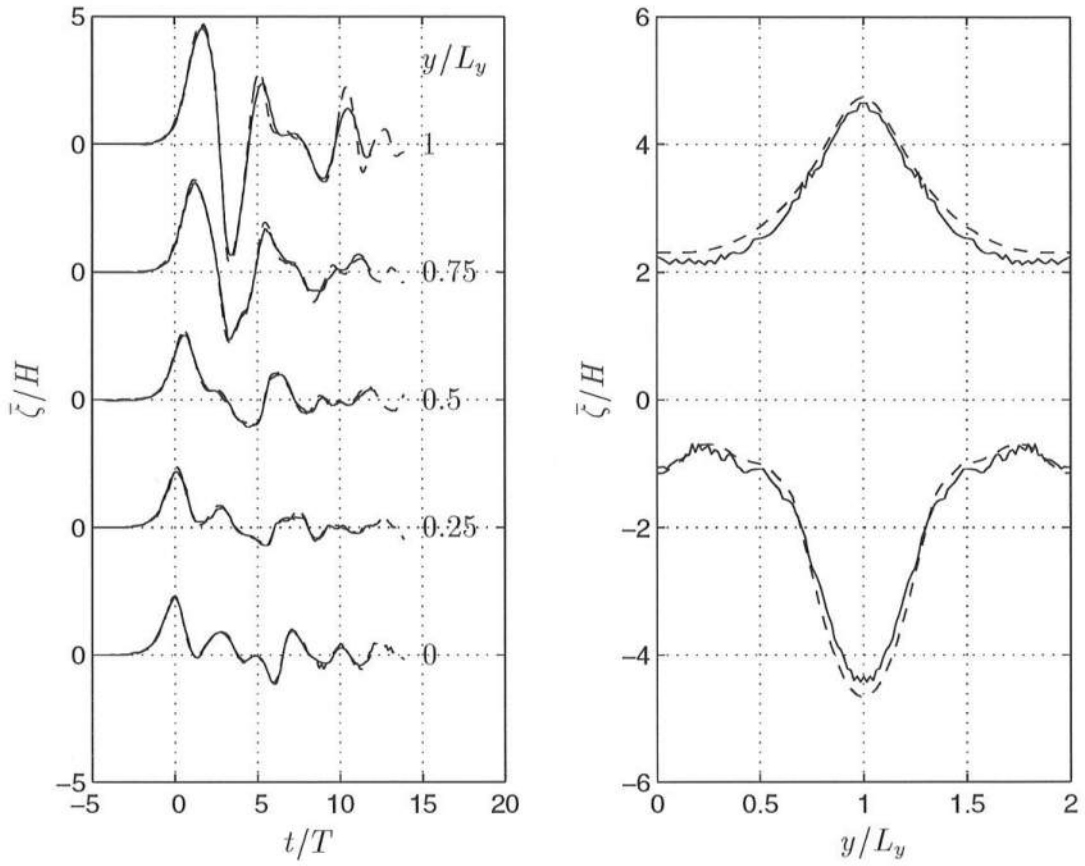

Figure 3.20: Comparison of present model (——) to Özkan-Haller & Kirby (1997) (– –) for $\alpha = 0.02$: (a) Timeseries of run-up in five stations, (b) Maximum run-up and run-down.

especially around the local maxima and minima. Both models agree with the prediction of the first trough in the time-series at $y/L_y = 0.75$, which means that the dispersive and dissipative terms that Zelt included in his equations might have become important at that point.

Fig. 3.20b shows the normalized maximum vertical run-up and run-down versus y. We see that the present model has a better overall agreement with Özkan-Haller & Kirby (1997)'s than with Zelt (1986)'s computations.

In conclusion, the shoreline boundary condition agrees well with the analytical solutions for the longshore uniform case but shows some discrepancies for the case of a concave beach, which can be attributed to the "staircase" discretization of the shoreline.

Chapter 4

GENERATION OF SHORE-NORMAL INFRAGRAVITY WAVES

In this chapter the depth-integrated, shortwave-averaged nearshore circulation model SHORECIRC is applied to study the generation of infragravity waves due to normally-incident wave groups on a plane beach.

In Section 4.1 an overview of the existing literature on the generation of infragravity waves is given, including references on relevant field data. In Section 4.2 the model is linearized to study the simplest possible case of surfbeat (one-dimensional infragravity wave) generation, which will prove to contain many of the relevant mechanisms. The relevant parameters are identified and variation of these parameters shows that different shoaling curves of the long-wave amplitudes can be found. As a consequence, the energy of the outgoing long wave can be larger or smaller than that of the incoming long wave.

The effect of the choice of the parameters on the generation of infragravity waves can be assessed using the "reflection coefficient" R, which is defined as the ratio of the amplitude of the outgoing wave and the amplitude of the incoming wave. Following Schäffer (1993), the value of R on the shelf can be interpreted as an integral parameter to characterize the net energy gain or loss in the infragravity waves as a result of shoaling and breaking of the short-wave groups and their

interaction with the long waves. Moreover, we will study the transfer of energy from the groups to the incoming and outgoing long waves separately as a function of depth. In this way, we can examine the process of infragravity wave generation on the slope.

In Section 4.3, the nonlinear terms corresponding to the nonlinear shallow water equations are included. It is shown that the mean set-up makes the most important contribution to the generation of long waves, in particular very close to the shoreline. Finally, in Section 4.4 the model is validated against laboratory data by Kostense (1984).

This chapter is essentially an expansion of Van Dongeren *et al.* (1996).

4.1 Introduction

It is well-known that a forced long wave propagates with short-wave groups at the group speed (Longuet-Higgins & Stewart, 1962). When these groups propagate onto a beach, the short waves shoal and break. In the shoaling process the incoming, bound long wave, which traveled with the group, gains energy and is released from the groups. The incoming long wave propagates shoreward, interacts with the breaking process, eventually reflects off the beach and propagates seaward as a free wave.

The total motion of the incoming and outgoing long waves produces a standing wave-like pattern that was called "surf beat" by Munk (1949) and Tucker (1950), who were the first to report field measurements of this phenomenon. Later, these low-frequency motions (whose periods are of the order of several minutes in the field) became known as "infragravity waves" and were confirmed in a number of field campaigns (Wright *et al.*, 1979, 1982; Huntley *et al.*, 1981; Holman, 1981;

Guza & Thornton, 1982, 1985; Oltman-Shay & Guza, 1987; Howd *et al.* 1991) to contain a significant portion of the total energy in the wave field. Gallagher (1971), Guza & Bowen (1975) and Bowen & Guza (1978) showed theoretically that energy may be transferred from obliquely-incident wave groups to edge waves. This was confirmed in experiments by Guza & Chapman (1979). However, these interactions have to satisfy the edge wave dispersion relation exactly, which is too limited a condition to explain the omnipresence of these phenomena in field data.

The generation of infragravity waves was explained more convincingly by Symonds *et al.* (1982), who assumed that the groupiness which existed outside the breaker zone is destroyed by the breaking and that the short waves inside the surf zone will decay with a saturated wave height. This implies that the position of the break point varies over the period of the wave group because higher waves in the group will break further offshore than smaller waves. The break point then acts as a wave maker and generates long waves at the frequency of the break point oscillations, which is equal to the frequency of the short-wave groups. Because the groupiness is destroyed in the breaking region, no long-wave generation takes place inside the surf zone.

Schäffer & Svendsen (1988) examined the other extreme where all short waves regardless of their height are assumed to break at a fixed break point. This means that the groupiness outside the surf zone is transmitted into the surf zone where long-wave generation can take place.

It is likely that neither mechanism is exclusively responsible for long-wave generation but that it is due to a combination of both effects. Therefore Schäffer (1993) merged the two extreme mechanisms into one hybrid analytical solution for the total long-wave envelope in which a parameter κ is used to interpolate between the two extremes. He analyzed some of the effects of parameter variations.

Some field studies suggest that there is more energy in the free (outgoing or trapped) waves than in the incoming bound waves (Munk, 1949; Tucker, 1950; Elgar *et al*, 1992; Herbers *et al*, 1995 to name a few). This indicates that in the nearshore region energy has been transferred from the short waves to the long waves. However, other observations (Guza & Thornton, 1985; Kostense, 1984) show that the energies of the incoming and outgoing long waves are about equal, which means that no net long-wave energy was gained in the nearshore region.

This inconclusive field evidence suggests that gain or loss of infragravity wave energy may be a function of the relevant parameters. In the next section the linearized model is analyzed and its response to the variation in the governing parameters is studied.

4.2 Linear Analysis

In this section the model is linearized to study the simplest possible case of surfbeat (one-dimensional infragravity wave) generation, which will prove to contain many of the relevant mechanisms. First, we will state the governing linear equations and give expressions for the short-wave forcing and the boundary conditions. Then, we will non-dimensionalize the model and identify the governing parameters. For a number of sets of these parameters, we will compare the model results to the analytical solution by Schäffer (1993). The incoming and outgoing long waves are separated linearly and the envelopes of each long wave are shown. The growth rate of the amplitudes of the incoming and outgoing long waves is analyzed and explained using the work term in the energy equation of the long waves, and the phase differences between the waves and the forcing. It is shown that different growth rates of the long waves can be found for different parameter choices and that the "reflection coefficient" R on the shelf can be used

to characterize the net energy transfer to the infragravity waves.

4.2.1 Model Formulation

To study the mechanisms of infragravity wave generation, the depth-integrated, time-averaged mass and momentum equations (2.8) and (2.71) are reduced for the case of depth-uniform long waves propagating in the shore-normal x-direction to

$$\frac{\partial \bar{\zeta}}{\partial t} + \frac{\partial \bar{Q}}{\partial x} = 0 \tag{4.1}$$

$$\frac{\partial \bar{Q}}{\partial t} + \frac{\partial}{\partial x}\left(\frac{\bar{Q}^2}{h}\right) + g\,(h_o + \bar{\zeta})\frac{\partial \bar{\zeta}}{\partial x} + \frac{1}{\rho}\frac{\partial S_{xx}}{\partial x} + \frac{\tau_x^B}{\rho} = 0 \tag{4.2}$$

These equations represent a set of nonlinear shallow water equations with forcing and friction, where the radiation stress gradient provides the forcing on the long waves. In this section we will linearize the model to

$$\frac{\partial \bar{\zeta}}{\partial t} + \frac{\partial \bar{Q}}{\partial x} = 0 \tag{4.3}$$

$$\frac{\partial \bar{Q}}{\partial t} + g\,h_o\frac{\partial \bar{\zeta}}{\partial x} + \frac{1}{\rho}\frac{\partial S_{xx}}{\partial x} = 0 \tag{4.4}$$

in order to analyze the simplest possible case of linear waves propagating on a flat shelf connected to a plane beach, where the forcing is generated by a frequency-modulated bichromatic short-wave group. As will be shown, even this simple case will provide insight into the long-wave generation mechanisms.

Following Schäffer (1993), we can generate a radiation stress forcing by superimposing two monochromatic short-wave trains of slightly different frequencies

$$\omega_1 = \omega\,(1 + \epsilon) \tag{4.5}$$

$$\omega_2 = \omega\,(1 - \epsilon) \tag{4.6}$$

where ω is the mean short-wave frequency and ϵ is the frequency modulation. As Schäffer (1993) notes, this perturbation is an alternative to the wave number perturbation by Mei & Benmoussa (1984), Schäffer & Svendsen (1988) and Liu (1989).

Using the results of Schäffer's derivation we can write the radiation stress forcing in our notation as

$$S_{xx} = \frac{1}{2}\rho g \left(2n - \frac{1}{2}\right) \begin{cases} a_1^2 \left(1 + 2\delta \cos(\int \frac{\Delta\omega}{c_g} dx - \Delta\omega\, t)\right), & h \geq h_b \\ \\ \frac{1}{4}\gamma^2 h_o^2 \left(1 + 2\delta(1-\kappa) \cos(\int \frac{\Delta\omega}{c_g} dx - \Delta\omega\, t)\right), & h \leq h_b \end{cases} \tag{4.7}$$

where κ is the parameter controlling the breaking mechanism: $\kappa = 0$ corresponds to the case of a fixed break point, while $\kappa = 1$ represents the time-varying break point case. $n = c_g/c$ where c_g is the group speed. a_1 is the wave amplitude of the primary short wave in the group while the groupiness $\delta = a_2/a_1$ is the ratio of the amplitudes of the secondary wave and the primary waves. h_b is the depth at breaking.

The difference frequency between the two short waves

$$\Delta\omega = \omega_1 - \omega_2 = 2\,\epsilon\,\omega \tag{4.8}$$

is also the long-wave forcing frequency. Inside the surf zone, we use a saturated short-wave amplitude over water depth criterion

$$a_1 = \frac{1}{2}\gamma\, h \tag{4.9}$$

where γ is a constant, so that the short-wave amplitude is a function of the local water depth only.

It is important to notice that the forcing consists of a steady part (the first term in (4.7)), which causes a steady set-up, and a time-varying part (the second

term in (4.7)), which forces a long wave. In our analysis we are interested only in the latter and in the rest of this section we show only the time-varying part of the solution. The forcing of the time-varying solution can be written

$$S_{xx}^{(1)} = \rho\, g\, \left(2\,n - \frac{1}{2}\right) \begin{cases} a_1^2\, \delta \cos(\int \frac{\Delta\omega}{c_g}\, dx - \Delta\omega\, t), & h \geq h_b \\ \\ \frac{1}{4}\gamma^2 h_o^2\, \delta(1-\kappa) \cos(\int \frac{\Delta\omega}{c_g}\, dx - \Delta\omega\, t), & h \leq h_b \end{cases} \tag{4.10}$$

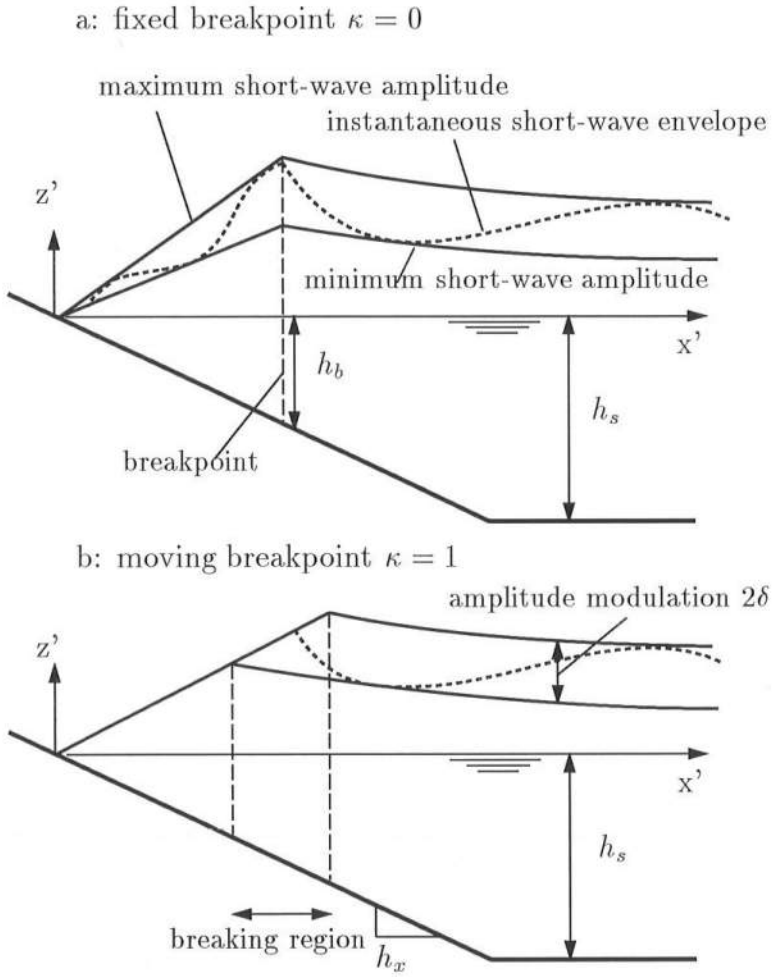

Figure 4.1: Definition sketch of the generation mechanisms: a) Schäffer & Svendsen (1988)'s fixed breakpoint generation mechanism. b) Symonds *et al.* (1982)'s moving breakpoint generation mechanism. (Reproduced from Schäffer, 1993)

Fig. 4.1a shows a definition sketch of Schäffer & Svendsen (1988)'s fixed breakpoint generation mechanism. Indicated in the figure are the instantaneous short-wave envelope and the maximum and minimum short-wave amplitudes as a function of the horizontal coordinate x'. The difference between the minimum and maximum values of the amplitude is twice the amplitude modulation δ. Notice that this amplitude modulation is transferred into the surf zone. Fig. 4.1b shows the principle of Symonds *et al.* (1982)'s generation mechanism. Short waves of different amplitude break at different locations in the *breaking region* and no modulation is transmitted into the surf zone.

It is also assumed that the shelf is wide enough so that at the toe of the beach the incoming long wave corresponds to the equilibrium bound long wave for the flat shelf

$$\bar{\zeta}_i = -\frac{1}{\rho}\frac{S_{xx}^{(1)}}{(g\,h_s - c_{gs}^2)} \tag{4.11}$$

where the subscript $_s$ denotes conditions on the shelf. This equation corresponds to the "geometrical optics" solution (i.e., the first term in a WKB-expansion (Bender & Orzag, 1978)), which assumes a *local equilibrium* between the forcing and the long wave amplitude at any depth on the slope. This solution was first found by Longuet-Higgins & Stewart (1962), who derived (4.11) for constant depth from (4.3) and (4.4) by assuming that in the equilibrium state the long wave is bound to the wave groups, which travel with c_g so that

$$\frac{\partial}{\partial t} = -c_g\frac{\partial}{\partial x} \tag{4.12}$$

which means (4.3) and (4.4) can be combined to

$$(g\,h_o - c_g^2)\,\frac{\partial\bar{\zeta}}{\partial x} = -\frac{1}{\rho}\,\frac{S_{xx}}{\partial x} \tag{4.13}$$

Integrated by parts, this yields

$$\bar{\zeta} - \bar{\zeta}(0) = -\frac{1}{\rho}\frac{S_{xx}}{g\,h_o - c_g^2}\,|_{x=x'} + \frac{1}{\rho}\frac{S_{xx}}{g\,h_o - c_g^2}\,|_{x=0}$$

$$+ \int_0^{x'} S_{xx} \frac{\partial}{\partial x}\left(\frac{1}{g\,h_o - c_g^2}\right) dx \tag{4.14}$$

This equation reduces to (4.11) for constant depth where the integration constants on the right and left-hand sides cancel. It turns out that in the following cases the last term in (4.14) is small. It is important to emphasize that the solution (4.11) only exists on a flat shelf. Notice also that (4.11) becomes singular if the water depth is allowed to go to zero slowly, i.e., if the infragravity wave propagates slowly relative to the depth variation. It is one of the purposes of the present study to investigate what the growth rate of the infragravity wave is if the bottom varies "fast" relative to the propagation speed of the infragravity wave.

The outgoing wave is absorbed using the absorbing-generating boundary condition derived in Chapter 3.2. In the linearized form of the model we impose a no-flux condition at the still water shoreline.

4.2.2 Non-dimensionalization and Relevant Parameters

In order to identify the relevant parameters in this problem, we first combine the governing equations (4.3) and (4.4) for the time-varying motion into the wave equation

$$\frac{\partial^2 \bar{\zeta}}{\partial t^2} - g\frac{\partial}{\partial x}\left(h_o \frac{\partial \bar{\zeta}}{\partial x}\right) = \frac{1}{\rho}\frac{\partial^2 S_{xx}^{(1)}}{\partial x^2} \tag{4.15}$$

We will apply the following non-dimensionalization

$$\begin{aligned} t &= \frac{t'}{\Delta\omega} \qquad & x &= \frac{h_s - h_o}{h_x} = \frac{h_s}{h_x}(1 - h') \qquad & \bar{\zeta} &= \bar{\zeta}_s\,\bar{\zeta}' \\ Q &= \sqrt{g\,h_s}\,\bar{\zeta}_s\,Q' \qquad & a_1 &= a_s\,a' \qquad & S_{xx}^{(1)} &= \rho\,g\,\delta\,a_s^2\,S_{xx}'^{(1)} \end{aligned} \tag{4.16}$$

where the subscript $_s$ denotes conditions on the shelf and the ' denotes the nondimensional quantities. We choose to non-dimensionalize the surface elevation in such a way that the equilibrium bound long wave in (4.11) becomes an $O(1)$ quantity. Using (4.16) we get

$$\bar{\zeta}_s \, \bar{\zeta}_i' = -\frac{\rho \, g \, \delta \, a_s^2}{\rho \, g \, h_s} \, \frac{a'^2 \left(2n - \frac{1}{2}\right)}{(1 - \frac{c_{gs}^2}{g \, h_s})} \cos\left(\frac{\Delta\omega}{h_x}\sqrt{\frac{h_s}{g}} \int \frac{\sqrt{g \, h_s}}{c_g} \, dh' + t'\right) \tag{4.17}$$

From this we can see that the proper scale for the surface elevation in this problem is

$$\bar{\zeta}_s = \frac{\delta \, a_s^2}{h_s} \tag{4.18}$$

so that the non-dimensional $\bar{\zeta}'$ from (4.16) becomes

$$\bar{\zeta} = \frac{\delta \, a_s^2}{h_s} \bar{\zeta}' \tag{4.19}$$

The non-dimensional wave equation then becomes after some rearranging

$$\frac{\partial^2 \bar{\zeta}'}{\partial t'^2} - \frac{g \, h_x^2}{h_s \, \Delta\omega^2} \frac{\partial}{\partial h'}\left(h' \frac{\partial \bar{\zeta}'}{\partial h'}\right) = \frac{g \, h_x^2}{h_s \, \Delta\omega^2} \frac{\partial^2 S_{xx}'^{(1)}}{\partial h'^2} \tag{4.20}$$

This analysis shows that the relative slope steepness parameter

$$S_\Delta = \frac{g \, h_x^2}{h_s \, \Delta\omega^2} \tag{4.21}$$

is relevant. Notice that the parameter ${S_\Delta}^{-\frac{1}{2}}$ also appears in the cosine in (4.17). Notice that S_Δ resembles the Irribarren number (Irribarren & Nogales, 1949) and the surf similarity parameter (Battjes, 1974) if the wave height H is used as a scaling parameter instead of the shelf depth h_s.

Using the fact that the wave length of the incoming bound wave L_s on the shelf can be expressed as

$$L_s = c_{g,s} \frac{2\,\pi}{\Delta\omega} \tag{4.22}$$

where $c_{g,s}$ is the group speed on the shelf, we can write (4.21) as

$$S_\Delta = \frac{1}{4\,\pi^2}\left(h_x \frac{L_s}{h_s}\right)^2 \frac{g\,h_s}{c_{g,s}^2} \tag{4.23}$$

where we recognize the second factor as the square of the slope parameter S, as identified by Schäffer & Svendsen (1988). The third factor is the ratio between the (squared) free and forced long-wave celerities. The parameter S_Δ is thus a modified version of S, which describes the gentleness of the bottom slope and hence is the appropriate slope parameter for gently-sloping beaches. For further discussion see Svendsen & Putrevu (1996).

The local amplitude of the mean short wave and the position of the break-point is determined from the conservation of energy flux in the shoaling region

$$c_{g,b}\,a_b^2 = c_{g,s}\,a_s^2 \tag{4.24}$$

where the subscript $_b$ denotes the (mean) break point. We assume that the short waves will break if they exceed the wave height to water depth ratio γ (4.9), so that (4.24) can be written

$$\frac{h_b}{h_s} = \frac{2}{\gamma}\sqrt{\frac{c_{g,s}}{c_{g,b}}}\,\frac{a_s}{h_s} \tag{4.25}$$

This implicit parameter essentially states that the non-dimensionalized break point is determined by a parameter governing the breaking (γ), and by parameters that control the shoaling process (a_s/h_s and the ratio of the group celerities at the break point and the shelf.) Furthermore, the parameter κ, which governs the type of breaking mechanism, will be relevant.

To summarize, we have identified three parameters that govern the generation of infragravity waves: S_Δ, $\frac{h_b}{h_s}$ and κ. This choice is an alternative to the five parameters that Schäffer (1993) identified, which are (in the present notation)

$$\frac{h_x\,\omega}{\Delta\omega}\,, \qquad \kappa\,, \qquad \hat{h}_s\,, \qquad \hat{a}_{1,s}\,, \qquad \gamma \tag{4.26}$$

where the $\hat{}$ denotes his non-dimensionalization using the fictitious deep-water wave number $k_\infty = \frac{\omega^2}{g}$. The difference between the two methods is that we non-dimensionalize by the shelf depth, which is a physical parameter, instead of by k_∞. In this way we essentially combine Schäffer's first and third parameters into S_Δ. We also combine his parameters $\hat{a}_{1,s}$ and γ, which govern the short-wave transformation, into the break point parameter (4.25). Please note that the present parameters can trivially be rewritten in terms of Schäffer's and are therefore essentially equivalent but in our opinion more convenient.

In the remainder of this section we will investigate the importance of each of these parameters by varying their values. The breaking index γ will be assumed known from measurements and therefore kept constant. In the process of this analysis, we will address the separation of incoming and outgoing long waves and the nature of free and forced long waves. Also investigated are the energy transfer from the wave groups to the long waves and the relative phase differences between the forcing and the long waves. It will be shown that varying the governing parameters has a profound effect on the value of the "reflection coefficient" R and that the transfer of energy from the short-wave groups to the infragravity waves can be characterized by the integral value of R on the shelf.

4.2.3 Case 1: Fixed Breakpoint

The first case considered is that of a fixed breakpoint ($\kappa = 0$) corresponding to the mechanism proposed by Schäffer & Svendsen (1988). An example that illustrates the different effects is obtained if we use the following parameter values: primary wave amplitude $a_{1,s} = 0.4415\,m$ on the shelf, groupiness $\delta = 0.1$, saturated breaking with $\gamma = 0.7$, beach slope $h_x = 1/30$ and shelf depth $h_s = 6\,m$. We choose $\omega = 1.8\,s^{-1}$ and $\epsilon = 0.1173$, so that the forcing

frequency $\Delta\omega = 0.422\,s^{-1}$ by (4.8). For these parameters, $S_\Delta = 1.02 \cdot 10^{-2}$ according to (4.21). This corresponds to a value of Schäffer & Svendsen (1988)'s slope parameter of $S = 0.25$, which is relatively mild. The breaking depth is $h_b/h_s = 0.21$ according to (4.25).

Fig. 4.2a (solid lines) shows the envelope of the time-varying long wave versus the horizontal coordinate with the origin at the shoreline, normalized by h_x/h_s, so that $x' = 1$ corresponds to the toe of the slope. This long wave is the sum of the incoming long wave, which is modified by the short-wave forcing, and a seaward propagating (outgoing) long wave, which has reflected off the shoreline. The surface elevations are normalized by $a_{1,s}^2\,\delta/h_s$, according to (4.19). Also plotted is the analytical solution by Schäffer & Svendsen (1988) (dashed line) which is computed on the slope only ($x' \leq 1$). This confirms that the model results agree very well with the analytical solution. The break point is located at $x' = 0.21$ and is indicated in this and further figures.

The total long-wave motion can be separated into an incoming and an outgoing long wave using linear superposition of the surface elevation and of the flux

$$\bar{\zeta} = \bar{\bar{\zeta}} + \bar{\zeta}_i + \bar{\zeta}_r \qquad \text{and} \qquad \bar{Q} = \bar{Q}_i + \bar{Q}_r \tag{4.27}$$

where $\bar{\bar{\zeta}}$ is the steady set-up, subscript $_i$ denotes the incoming wave and subscript $_r$ denotes the outgoing wave. Also, we know that for waves propagating without change in shape we have

$$\bar{Q} = c\,\bar{\zeta} \tag{4.28}$$

which was proven in Appendix B and used in Chapter 3.2. The computations will show that

$$\bar{Q}_i = c_g\,\bar{\zeta}_i \qquad \text{and} \qquad \bar{Q}_r = -\sqrt{g\,h_o}\,\bar{\zeta}_r \tag{4.29}$$

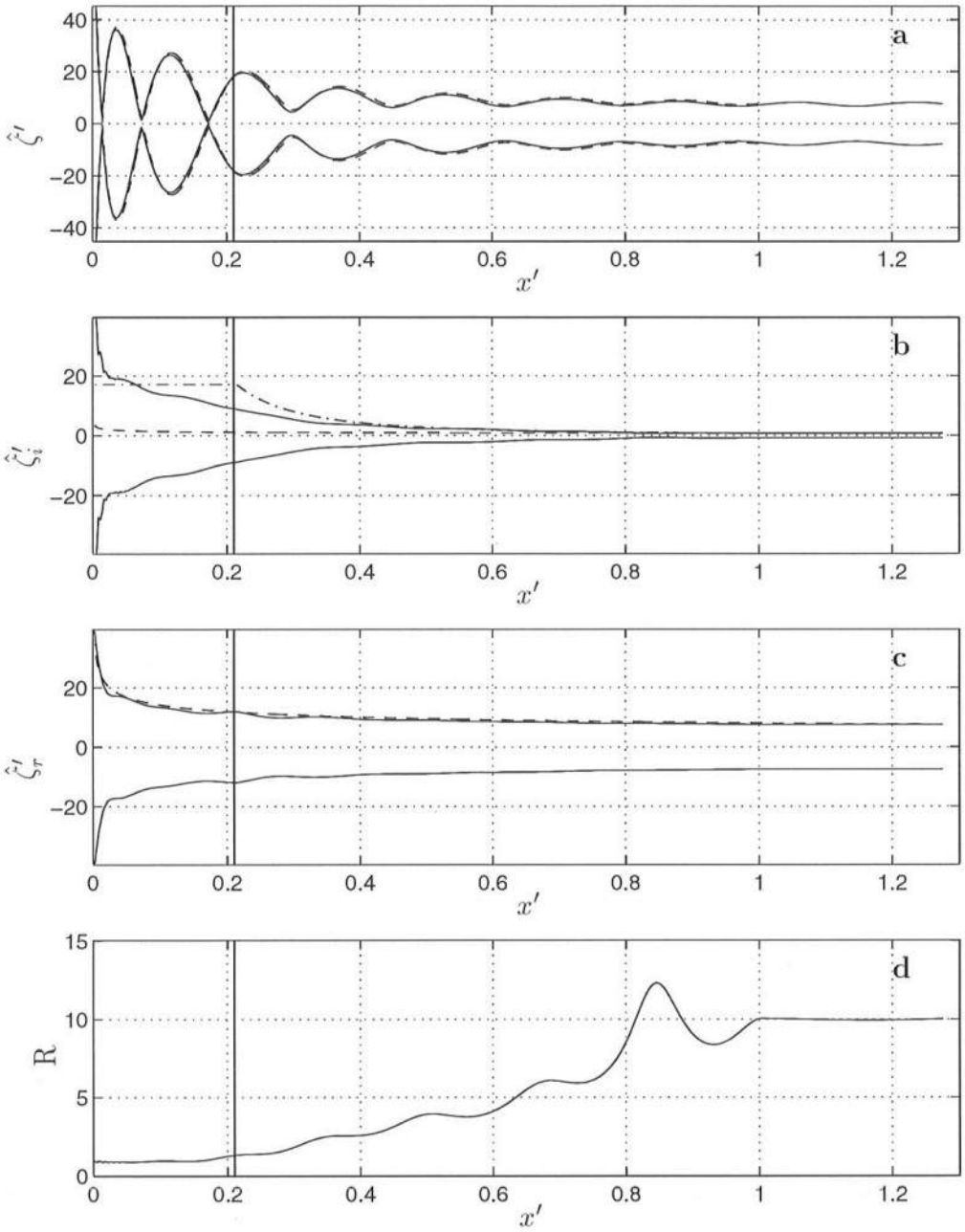

Figure 4.2: Case 1: (a) Envelope of the total long-wave motion vs. the nondimensional horizontal coordinate: present model (——) and analytical solution (– –); (b) Envelope of the incoming long wave: present model (——), Green's Law (– –) and Longuet-Higgins & Stewart (1962)'s steady state solution (– ·); (c) Envelope of the outgoing long wave: present model (——) and Green's Law (– –); (d) Reflection coefficient.

which implies that the incoming wave essentially propagates with group speed c_g and the free outgoing wave propagates with the shallow water wave speed. Solving for $\bar{\zeta}_i$ and $\bar{\zeta}_r$ from the four equations (4.27) and (4.29) yields

$$\bar{\zeta}_i = \frac{\sqrt{g\,h_o}\,(\bar{\zeta} - \overline{\overline{\zeta}}) + \bar{Q}}{c_g + \sqrt{g\,h_o}} \qquad \text{and} \qquad \bar{\zeta}_r = \frac{c_g\,(\bar{\zeta} - \overline{\overline{\zeta}}) - \bar{Q}}{c_g + \sqrt{g\,h_o}} \tag{4.30}$$

These equations are essentially modified versions of those given by Guza *et al.* (1984), who used the shallow water celerity for both the incoming and the outgoing waves. The separation of the incoming and outgoing wave implies assumptions about the speed of the waves used in the *interpretation* of the model output. These assumptions are not used in the model itself.

The solid lines in Fig. 4.2b show the envelope $\hat{\zeta}_i$ of the *incoming* long wave. This envelope is obtained by separation of the model output $\bar{\zeta}$ and $\bar{Q}$ of the total wave motion into an incoming and outgoing part using (4.30) and determining the maximum and minimum surface elevation of the incoming wave over an infragravity wave period at every location.

Note that the long wave shoals faster than as predicted by Green's Law ($\hat{\zeta} \propto h^{-1/4}$, the dashed line), which means that energy must have been transferred to the long wave. Also shown is the shoaling curve according to Longuet-Higgins & Stewart (1962)'s steady state theory, (4.11) (the dash-dotted line), which is plotted as a function of the local depth, even though it is theoretically only valid on the flat shelf. This means (4.11) corresponds to the "geometrical optics" solution, which assumes a local equilibrium between the forcing and the long-wave amplitude at any depth on the slope. Outside the surf zone, this curve grows much faster than the actual wave, which indicates that on a sloping beach the bound long wave does not have "time" to attain local equilibrium but that it depends on its history. Inside the surf zone (4.11) is nearly constant, as was found by Schäffer (1993).

The nature of the shoaling of the incoming long wave amplitude is discussed in more detail below.

In Fig. 4.2c the envelope of the outgoing long wave (solid lines) closely follows Green's Law (dashed line) which suggests that this wave is a free long wave. However, there are some oscillations noticable around the dashed line because energy is traded back and forth with the incoming short-wave group, as will be explained below.

Figure 4.2d shows the ratio of the amplitude of the outgoing wave and the incoming wave (the "reflection coefficient" R) versus the local depth. This ratio is by definition equal to unity at the shore. For the chosen parameter values, the ratio is larger than unity everywhere else. This means that there is more energy in the outgoing wave than in the incoming wave at every position, which indicates that net energy has been transferred from the short waves to the long waves.

In fact, the energy in the outgoing wave is 100 times the energy of the incoming wave on the shelf for the present choice of parameters. As stated above, the value of R on the shelf is an integral parameter that can be used to characterize the net energy transfer to the infragravity waves as a result of shoaling and breaking of the short-wave groups and their interaction with the long waves. It will be seen in the next subsections that varying the governing parameters will have an effect on the local value of R as well as on the integral value of R on the shelf.

4.2.3.1 Nature of Free and Forced Incoming Long Waves

It is useful to analyze the relationship between the different theoretical results and the model results a little further. In Fig. 4.3 the computed amplitude

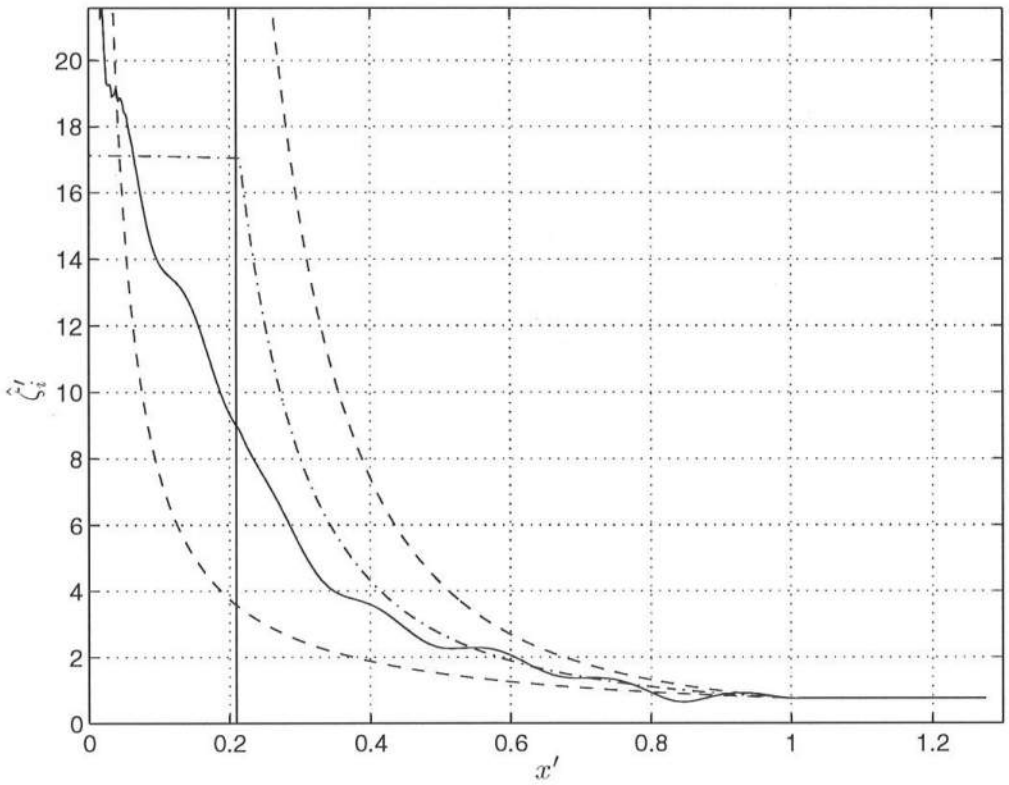

Figure 4.3: Case 1: Envelope of the incoming long wave: present model (——), Longuet-Higgins & Stewart (1962)'s steady state solution (–·), deep water asymptote (lower – –) and shallow water asymptote (top – –).

(solid line) and the "geometrical optics" solution (4.11) (dashed line) of Fig. 4.2b are plotted again. In Longuet-Higgins & Stewart (1962), (4.11) is expanded in terms of $\mu = k\,h$ where k is the mean wave number of the *short* waves. An expanded version of their derivation can be found in Appendix C for reference. Longuet-Higgins & Stewart (1962) found

$$\hat{\zeta}_i \propto h_o^{-\frac{5}{2}} \tag{4.31}$$

which is valid for *short* waves propagating in shallow or shallow-to-intermediate depth water (because $\mu < 1$). For the present example, however, this is not the case. In fact, the value of μ on the shelf is about 2, which means that the short waves propagate in intermediate depth. The relationship (4.31) is therefore only

an asymptotic value of the equilibrium equation (4.11), but it has been used in field data analysis nevertheless (e.g., Elgar *et al.*, 1992).

The other extreme, the asymptote for deep water short waves, can be derived from (4.11) as

$$\begin{aligned} \hat{\zeta}_i &= -\frac{1}{\rho}\frac{\hat{S}_{xx}}{(g\,h_o - c_g^2)} \\ &= -\frac{1}{\rho}\frac{E\,c_g\left(\frac{2}{c} - \frac{1}{2\,c_g}\right)}{g\,h_o - n^2\,c^2} \end{aligned} \tag{4.32}$$

and since for deep water $n = \frac{1}{2}$ and $c = \frac{g}{\omega}$ we get

$$\hat{\zeta}_i = -\frac{1}{\rho}\frac{\frac{1}{2}E}{g\,h_o - \frac{1}{4}\frac{g^2}{\omega^2}} \propto h_o^{-1} \tag{4.33}$$

following a similar expansion as outlined in Appendix C. This shows that for large depths the amplitude of the incoming long wave varies as h_o^{-1}.

Elgar *et al.* (1992) used (4.31) to estimate the growth rate of the energy and found that in a bound wave $E_{bound} \sim \hat{\zeta}_{bound}^2 \propto h_o^{-5}$. On the other hand, the energy growth rate in a free wave is assumed to follow Green's Law, so $E_{free} \propto h_o^{-\frac{1}{2}}$. Since their data analysis shows that the energy between two arrays at $8\,m$ and $13\,m$ grows approximately as $E_{data} \propto h_o^{-1.1}$, they conclude that the free IG-wave energy is more important than the energy in the bound waves. However, the "swell and sea" (short-wave) frequencies in their data set ranged from $f = 0.08\,Hz$ to $f = 0.24\,Hz$ in a local depth of $8\,m$. Using linear theory, this implies that at that location μ ranges from about 0.5 to 2. In other words, the use of the asymptote (4.31) might not be warranted. The energy in the bound waves might grow with a rate between h_o^{-5} and h_o^{-1}, which are the squares of the asymptotic growth rates of the amplitudes. The latter of these values is much closer to the observed rate of growth.

The growth curves corresponding to both (4.31) and (4.33) are plotted in Fig. 4.3 as well. It is seen that the "geometrical optics" curve lies between the two asymptotes.

The computed growth (solid line) of the amplitude of the incoming long wave does not increase as a simple power of h_o, as might be expected, but exhibits an oscillatory behavior as well. This phenomenon was also shown by Molin (1982) and Mei & Benmoussa (1984), who attribute these oscillations to "interference" between the bound wave in equilibrium with the local forcing and the generated free waves.

Qualitatively the oscillatory behavior can be explained as follows: as the long wave propagates over the shelf it is in equilibrium with the forcing, which implies that no net energy is exchanged with the short waves. According to (4.11), the incoming long wave and the forcing are exactly in anti-phase and that the long wave consists of a bound wave only, which propagates with the group velocity c_g. As the short-wave groups propagate onto the sloping beach, the amplitude of the short waves in the group changes due to shoaling and consequently the amplitude of the radiation stress forcing changes as well. This means that the amplitude of the incoming long wave is no longer in local equilibrium (4.11) with the forcing. In order to reach that local equilibrium, energy must be transferred from the groups to the incoming long wave, which is only possible if the phase difference of the incoming wave changes to a value other than π.

This is possible if free waves are generated on the slope. Such a wave will propagate with the shallow water speed. The incoming long wave is therefore composed of a bound as well as a free component. When the total incoming long wave is no longer in anti-phase with the forcing, energy is transferred to the long wave and its amplitude will grow faster than Green's Law predicts. However, the

short-wave forcing is continuously changing, which means that the local equilibrium is also changing. If the rate of change of the forcing (which is a function of the beach slope and the forcing frequency) is too "fast," the incoming long wave does not have enough "time" (as Longuet-Higgins & Stewart (1962) describe it) to adjust to the new equilibrium and will therefore always be lagging behind. In the present case, the approximate amplitude growth is $\bar{\zeta}_i \propto h_o^{-2}$ which means that it is slower than can be expected from the equilibrium or "geometrical optics" theory.

4.2.3.2 Energy Transfer in Infragravity waves

As a tool to study this energy transfer in more detail we can use the long-wave energy equation (2.97), repeated for the one-dimensional case

$$\frac{\partial}{\partial t}\left(\frac{1}{2}\rho\left(g\,\bar{\zeta}^2+\frac{\bar{Q}^2}{h}\right)\right)+\frac{\partial}{\partial x}\left(\frac{1}{2}\rho\,\bar{Q}\left(\frac{\bar{Q}}{h}\right)^2+\rho g\bar{\zeta}\bar{Q}\right)+$$

$$\frac{\bar{Q}}{h}\frac{\partial S_{xx}}{\partial x_\alpha}+\tilde{U}\,\tau_b=0 \tag{4.34}$$

which in linearized form becomes

$$\frac{\partial E}{\partial t}+\frac{\partial E_f}{\partial x}+\frac{\bar{Q}}{h_o}\frac{\partial S_{xx}}{\partial x}=0 \tag{4.35}$$

where E is the long-wave energy, $E_f = \rho g\,\bar{\zeta}\,\bar{Q}$ is the energy flux and the third term represents the work the short waves do on the long wave through the radiation stress. Averaging over the IG-wave period (denoted by the double overbar) eliminates the temporal variation and yields a balance between the energy flux and the work

$$\frac{\partial\overline{\overline{E_f}}}{\partial x}+\overline{\overline{\frac{Q}{h_o}\frac{\partial S_{xx}}{\partial x}}}=0 \tag{4.36}$$

The two terms can be each split into an incoming and outgoing part

$$\frac{\partial \overline{\overline{E_{f,i}}}}{\partial x} + \frac{\partial \overline{\overline{E_{f,r}}}}{\partial x} + \overline{\overline{\frac{Q_i}{h_o}\frac{\partial S_{xx}}{\partial x}}} + \overline{\overline{\frac{Q_r}{h_o}\frac{\partial S_{xx}}{\partial x}}} = 0 \tag{4.37}$$

Figure 4.4a shows the balance between the energy flux gradient (dashed line) and the work term (solid line) in (4.36) across the domain for the same parameter values as in Fig. 4.2. Both terms are non-dimensionalized using (4.16) and (4.19) so that

$$\frac{\partial \overline{\overline{E_f}}}{\partial x} = \rho g \sqrt{g h_s}\, \frac{h_x \delta^2 a_s^4}{h_s^3} \frac{\partial \overline{\overline{E'_f}}}{\partial h'} \tag{4.38}$$

$$\frac{\bar{Q}}{h_o}\frac{\partial S_{xx}}{\partial x} = \rho g \sqrt{g h_s}\, \frac{h_x \delta^2 a_s^4}{h_s^3} \frac{\bar{Q}'}{h'} \frac{\partial S'_{xx}}{\partial h'} \tag{4.39}$$

Notice that in the present model the short-wave forcing and therefore the short-wave amplitudes are specified. This means that energy can be transferred from the short waves to the long waves without reducing the energy in the former. Conversely, a transfer of energy from the long waves to the short waves results in a decrease of energy in the long waves only without a corresponding increase in the short-wave energy. This is a general restriction of linearized models.

Figure 4.4b shows the work done on the incoming wave, which is the third term in (4.37). It is negative across the whole domain (except in a small region just shorewards of the toe but invisible on this scale of the plot), which means that energy flux is gained. The work term also exhibits oscillations which are not visible on this scale. The gain in energy flux is consistent with the finding of Fig. 4.2 that the incoming long wave increases faster in amplitude than a free long wave. Conversely, Fig. 4.4c reveals that the work done by the short waves on the outgoing long wave oscillates around zero, which means that energy is traded back and forth but that over the whole domain the long wave loses or gains very little

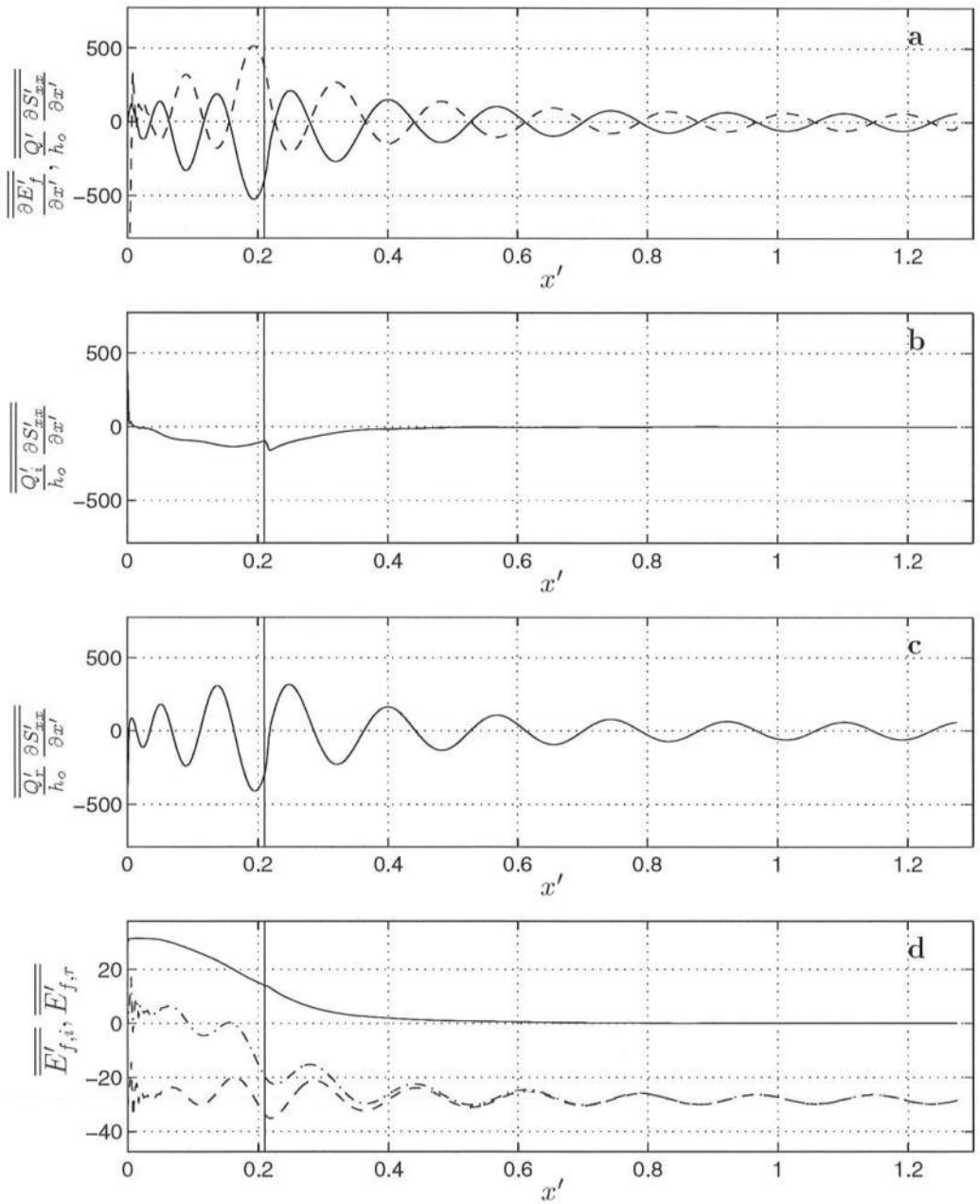

Figure 4.4: Case 1: (a) Work done on total long wave (——) and energy flux (– –); (b) Work on incoming long wave; (c) Work on outgoing long wave; (d) Energy flux of incoming wave (——), energy flux of outgoing wave (– –), and energy flux of total long wave (– ·).

energy. It essentially decreases in amplitude as a free long wave, as was already seen in Fig. 4.2c.

In Fig. 4.4d the energy fluxes of the incoming, the outgoing and the total long-wave motion are shown, normalized by

$$E_f = \rho g \sqrt{g h_s} \frac{\delta^2 a_{1,s}^4}{h_s^2} E_f' \tag{4.40}$$

Notice that the incoming wave already gains about 50 percent of energy flux seaward of the break point. The incoming long wave reaches its maximum energy flux at the shoreline where it is fully reflected. The outgoing wave shows an oscillating energy flux. The total energy flux becomes increasingly negative seawards, which means that energy is propagating in that direction, as a consequence of the net transfer of energy from the short waves to the long waves.

4.2.3.3 Phase Differences between Long Waves and Forcing

Another way to visualize the process of the generation of infragravity waves is to compute the phase difference between the incoming and outgoing long waves and the forcing. Fig. 4.5a shows the phase difference $\Delta\phi_S$ between the incoming long wave and the radiation stress (dashed line). This phase difference is defined as the time lag between the maximum values of the incoming long wave and the forcing normalized by the infragravity wave frequency.

In the equilibrium situation on the shelf, the incoming long wave and the forcing are in anti-phase (i.e., the phase difference is π) as can be seen from (4.11). As is shown in Fig. 4.5a, the phase difference starts to change when the wave groups and the long wave propagate onto the shelf. It is first slightly larger than π, then smaller than π, and finally larger than π again.

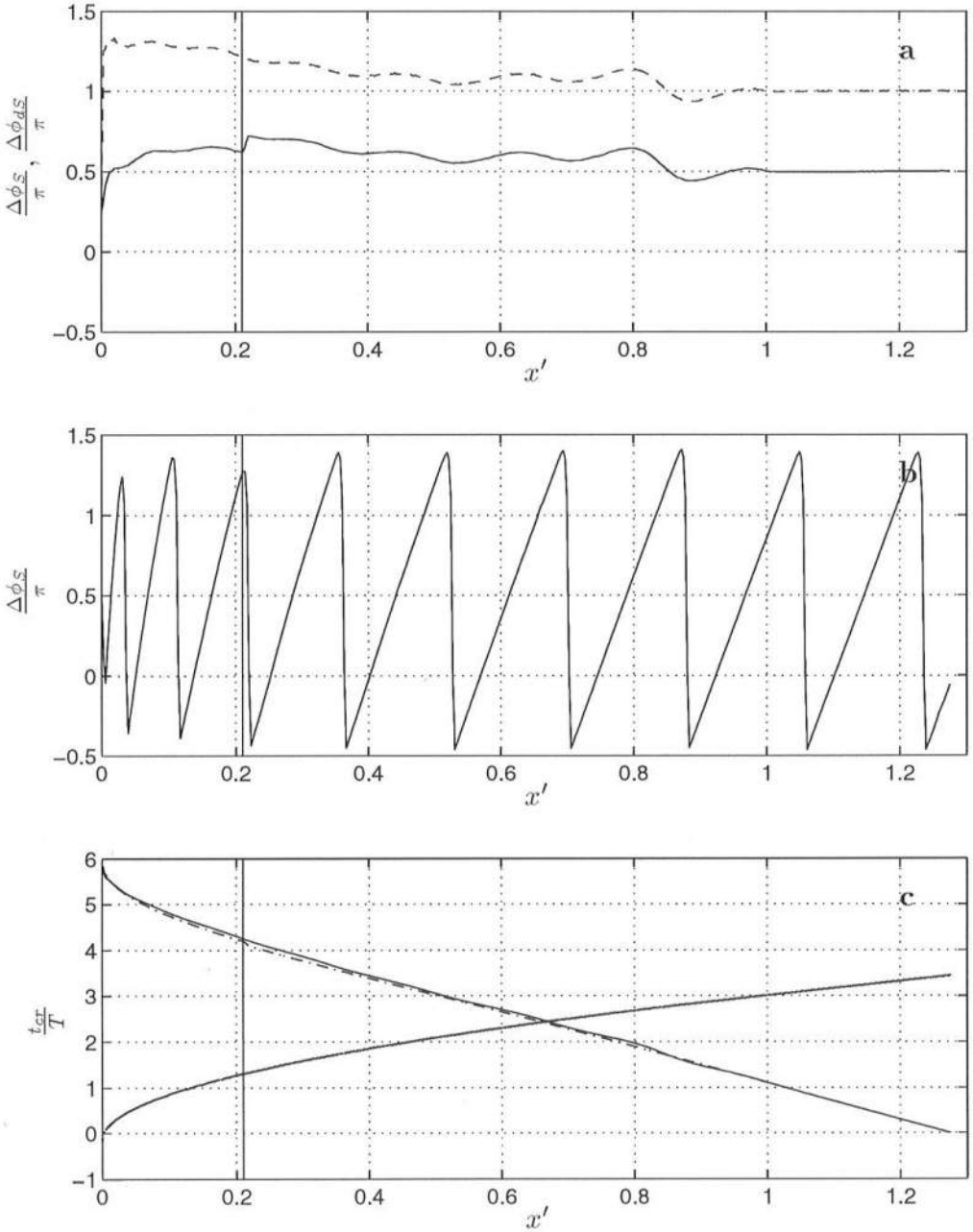

Figure 4.5: Case 1: (a) Phase difference $\Delta\phi_S$ between the incoming long wave and the radiation stress gradient (——) and phase difference $\Delta\phi_{dS}$ between the incoming long wave and the radiation stress (– –); (b) Phase difference between the outgoing long wave and the radiation stress gradient; (c) Track of the crest of the radiation stress gradient (– ·), the calculated incoming long wave (——), and the calculated outgoing long wave (– –) and the theoretical free long wave (· · ·).

The phase difference of the long wave relative to the radiation stress *gradient* $\Delta\phi_{dS}$ (Fig. 4.5a, solid line) is equal to $\frac{\pi}{2}$ on the shelf, becomes slightly larger than $\frac{\pi}{2}$ just after the toe, then smaller than $\frac{\pi}{2}$ and finally larger than $\frac{\pi}{2}$ again.

The value of $\Delta\phi_{dS}$ provides information about the sign of the work term. From (4.29) the work term on the incoming long waves can be written as

$$\overline{\overline{\frac{Q_i}{h_o}\frac{\partial S_{xx}}{\partial x}}} = \overline{\overline{\frac{c_g\,\bar{\zeta}_i}{h_o}\frac{\partial S_{xx}}{\partial x}}} \tag{4.41}$$

We can write the incoming long wave and the forcing gradient in terms of an amplitude and a phase function

$$\begin{aligned} \bar{\zeta}_i &= \hat{\zeta}_i \cos(\phi - \Delta\phi_{dS}) \\ \frac{\partial S_{xx}}{\partial x} &= \frac{\partial \hat{S}_{xx}}{\partial x}\cos\phi \end{aligned} \tag{4.42}$$

where ϕ is the phase function, and $\hat{\zeta}_i$ and $\frac{\partial \hat{S}_{xx}}{\partial x}$ are the amplitudes of the incoming long wave and the forcing gradient. Substituting these expressions in (4.41) we get

$$\begin{aligned} \overline{\overline{\frac{c_g\,\bar{\zeta}_i}{h_o}\frac{\partial S_{xx}}{\partial x}}} &= \frac{c_g\,\hat{\zeta}_i}{h_o}\frac{\partial \hat{S}_{xx}}{\partial x}\overline{\overline{\cos(\phi - \Delta\phi_{dS})\cos\phi}} \\ &= \frac{1}{2}\frac{c_g\,\hat{\zeta}_i}{h_o}\frac{\partial \hat{S}_{xx}}{\partial x}\cos\Delta\phi_{dS} \end{aligned} \tag{4.43}$$

Eq. (4.43) shows that the work term should be negative for $\Delta\phi_{dS} > \frac{\pi}{2}$. In Fig. 4.5a we see that we have this condition on most of the sloping beach region and this result corresponds to the negative sign of the work term in Fig. 4.4b. Notice that in Fig. 4.5a the phase difference $\Delta\phi_{dS} < \frac{\pi}{2}$ in the small region $0.85 < x' < 0.95$. This indicates that the work term is positive in that region. This corresponds to positive values of the work term in Fig. 4.4b, which are not visible due to the scale, however.

Fig. 4.5b shows the phase difference between the outgoing wave and the radiation stress gradient. Since the forcing and this long wave propagate in opposite directions, the phase difference continually varies over the whole range $-\frac{\pi}{2}$ and $\frac{3\pi}{2}$. This means that the work done on the outgoing wave is alternately positive and negative, which results in the oscillatory behavior of the amplitude of the outgoing wave, as was already seen in Fig. 4.2c.

In Fig. 4.5c the crests of the forcing (dash-dotted line), the incoming wave (solid line) and the outgoing wave (dashed line) are tracked in time, normalized by the period $T = \frac{2\pi}{\Delta\omega}$ of the infragravity wave. It turns out that the forcing propagates with the group speed c_g, while the incoming long wave has a speed which is slightly off the group speed. In fact, the incoming wave slows down a little bit right after the toe, which is what generates the phase difference required for the energy transfer. The outgoing free long wave propagates with the shallow water speed $\sqrt{g\,h_o}$, the theoretical value of which is plotted in the figure as the dotted line. The calculated and theoretical speeds are indistinguishable.

4.2.4 Case 2: Fixed Breakpoint with Halved Frequency Modulation

To illustrate the effect of the variation of the parameters, the frequency modulation ϵ is halved to $\epsilon = 0.0587$. This decrease means that the forcing frequency $\Delta\omega$ is also half of the value of case 1, while all other parameters remain the same. For these values we have $S_\Delta = 4.08 \cdot 10^{-2}$, which is four times the value of S_Δ in case 1. Schäffer & Svendsen (1988)'s equivalent slope steepness parameter is then $S = 0.5$, which incidates that the relative slope is steeper in this case. The breaking depth remains at $h_b/h_s = 0.21$ according to (4.25) and is indicated in the figures.

Fig. 4.6a again shows that the computed long-wave envelope (solid lines)

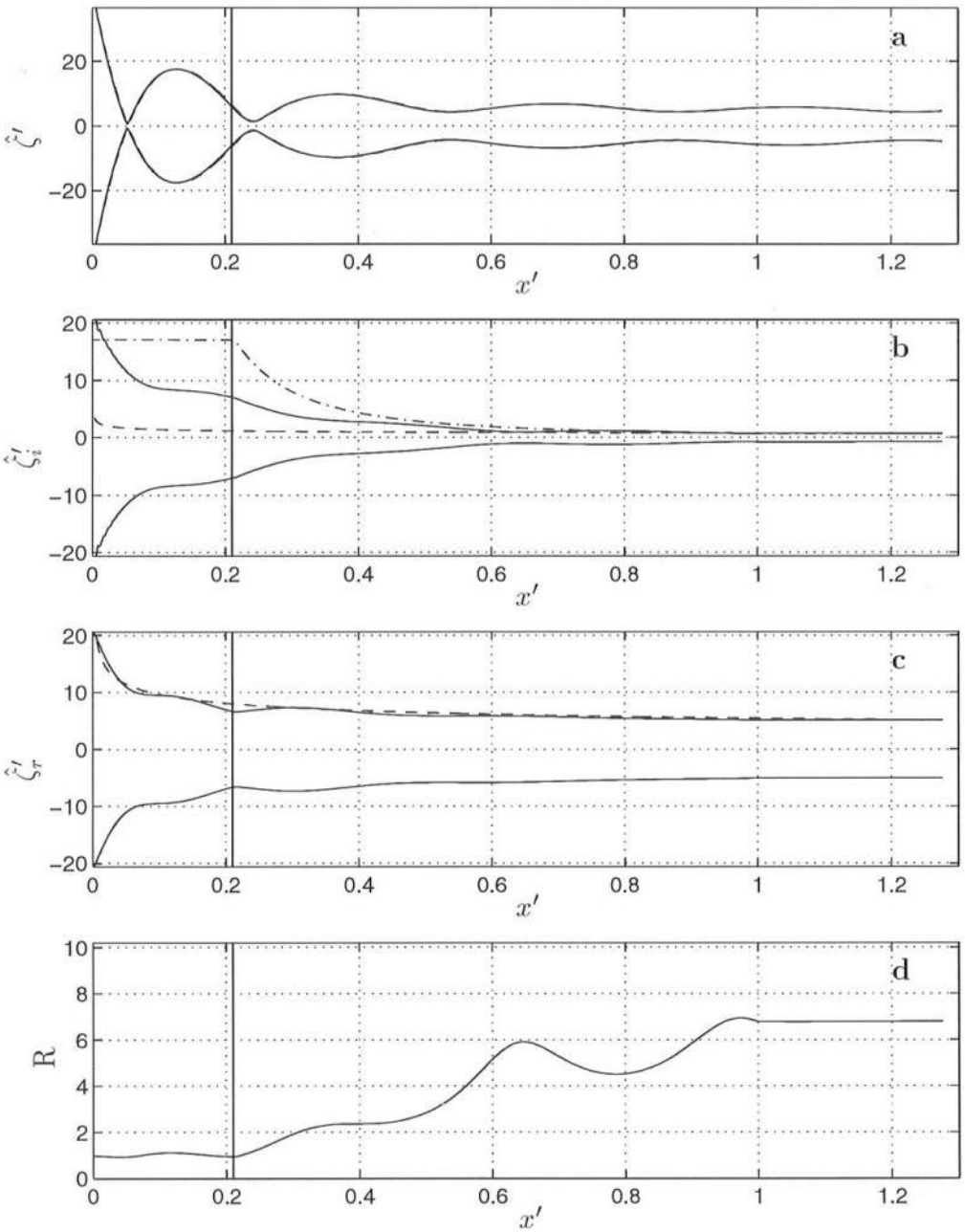

Figure 4.6: Case 2: Labels as Fig. 4.2

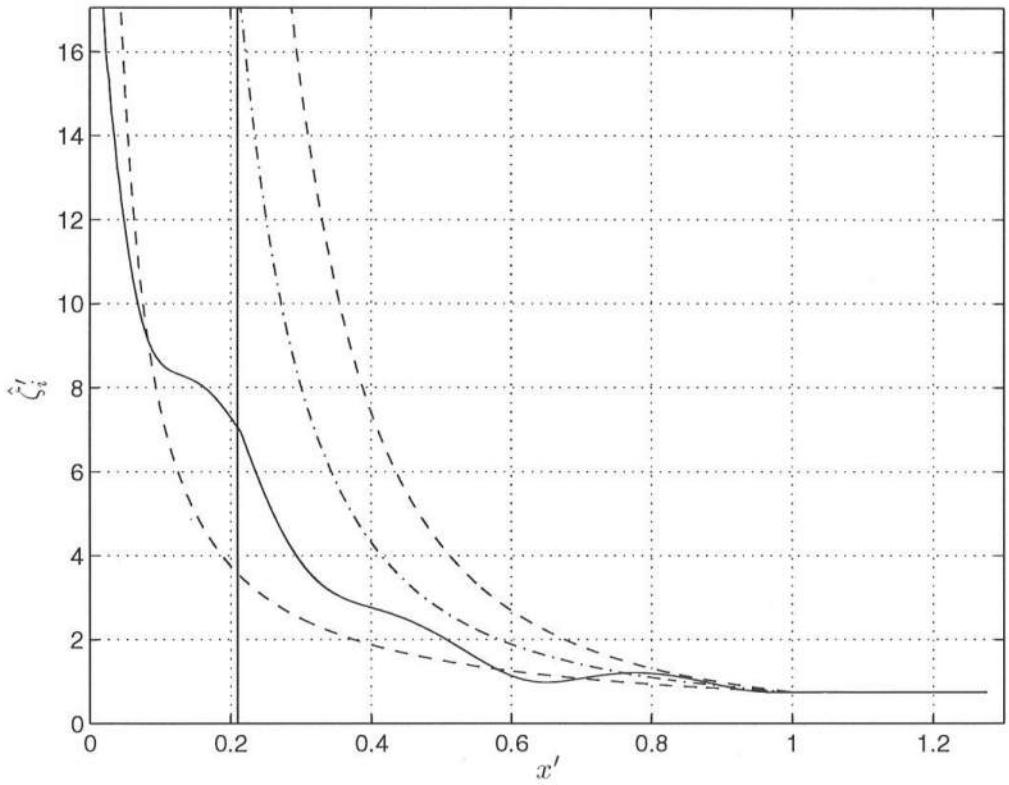

Figure 4.7: Case 2: Labels as in Fig. 4.3

agrees very well with Schäffer (1993)'s analytical solution (dashed line). As in Fig. 4.2b, the growth of the amplitude of the incoming long wave in Fig. 4.6b is larger than Green's Law predicts but is smaller than the "geometrical optics" theory suggests. Fig. 4.6c shows that the outgoing long wave essentially decreases in amplitude again as a free long wave. The "reflection coefficient" (the ratio of the amplitude of the outgoing wave and the incoming wave) is larger than unity in the whole domain in this case (as in the previous case), which means that the outgoing wave is more energetic than the incoming wave. The value of R is smaller than in case 1, however, which indicates that less energy has been transferred than before.

The amplitude of the incoming bound long wave (solid line) in Fig. 4.7

again shows oscillations as it grows with decreasing depth. The wave length of the oscillation is larger than in Fig. 4.3, however, which is due to the fact that the period of the long wave in this case is twice the value of the period in case 1. Also, it is seen that the trend in the growth is slower than was observed in Case 1. Thus an increase in the long-wave period (through a decrease in the frequency modulation in this case) causes the wave to adjust more slowly to the changing forcing.

Fig. 4.8a shows the energy flux of the total long-wave motion (dashed line) and the work that the forcing does on the total wave motion (solid line). Notice that the oscillations are twice as long as in the previous case (see Fig. 4.4a). Also, the magnitude of the terms has decreased relative to Case 1, because a decrease in the forcing frequency reduces the size of the radiation stress gradients, as can be seen from taking the x derivative of (4.10).

Fig. 4.8b shows that the work done by the forcing on the incoming long wave is negative as before. The work done on the outgoing long wave (see Fig. 4.8c) again exhibits an oscillation. Fig. 4.8d shows that the energy flux of the incoming wave (solid line) increases steadily with decreasing depth. Note that the energy flux of the incoming wave at the break point is already 50 percent of the value it has at the shoreline. The energy flux of the outgoing wave (dashed line) shows oscillations as in Case 1.

Fig 4.9a shows the phase lag between the incoming long wave and the radiation stress (dashed line) and between the incoming long wave and the radiation stress gradient (solid line). As in the previous case, the phase lag indicates that the work done by the forcing on the incoming long wave is negative. Fig 4.9b shows the phase lag between the outgoing wave and the forcing, which changes continually as before. Note that the distance over which the phase lag varies is

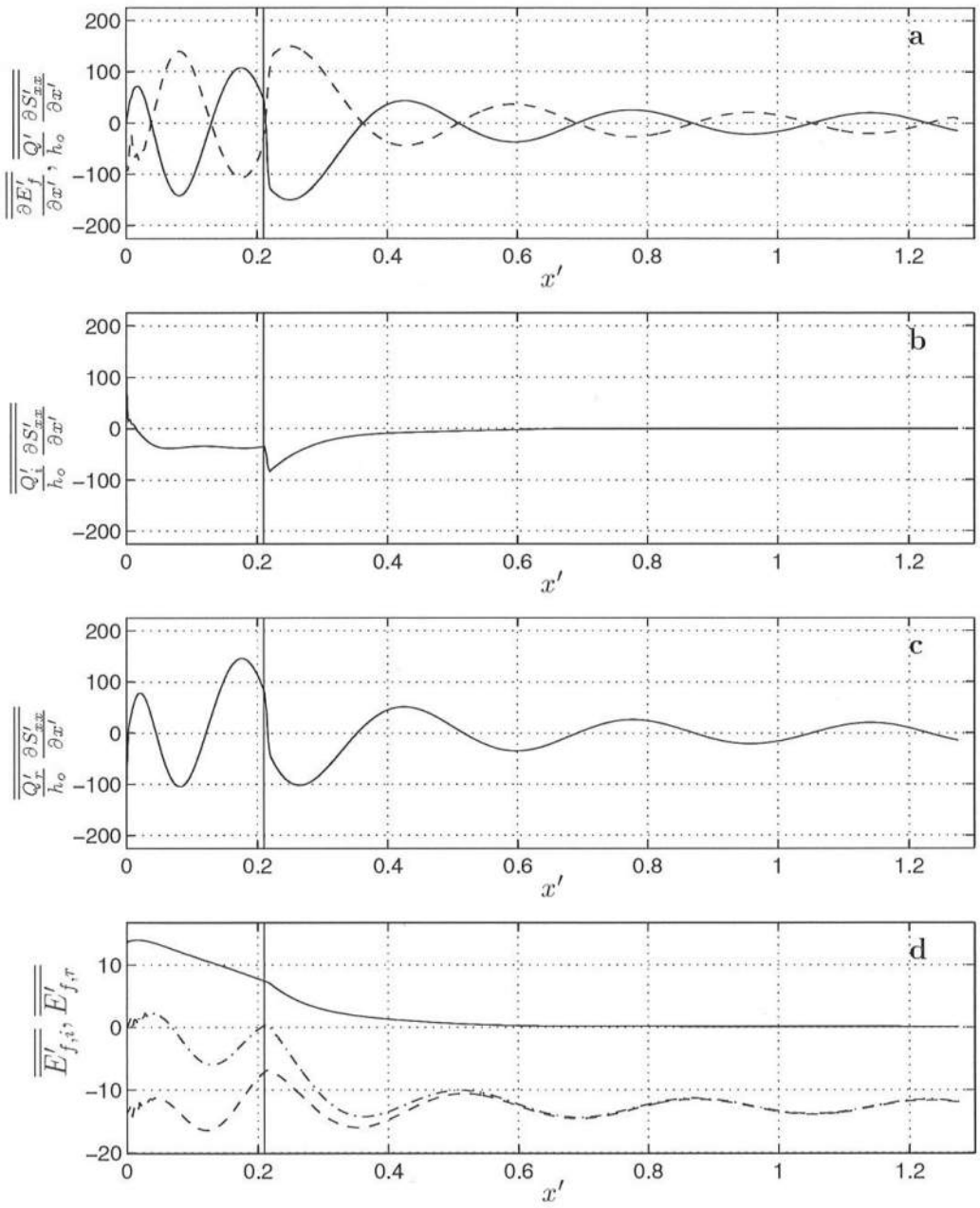

Figure 4.8: Case 2: Labels as in Fig. 4.4

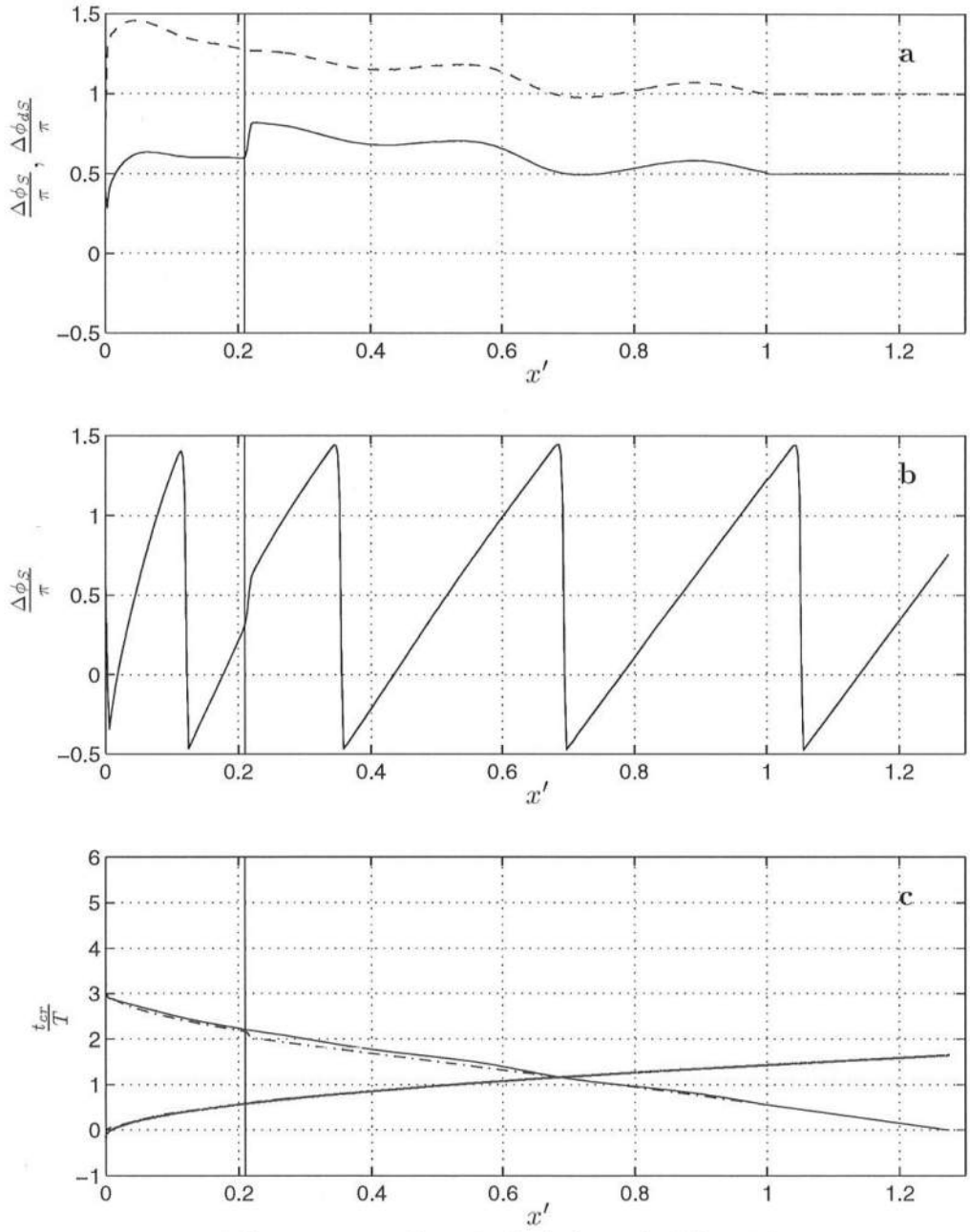

Figure 4.9: Case 2: Labels as in Fig. 4.5

twice the distance of the previous case.

The track of the crests of the incoming wave (solid line), the radiation stress gradient (dash-dotted line) and the outgoing wave (dashed line) are plotted in Fig. 4.9c. It shows that the incoming long wave propagates with a speed slightly (but necessarily) off the group speed c_g. The theoretical value of the speed of a free outgoing long wave is plotted as the dotted line again and is indistinguishable from the calculated speed of the outgoing wave.

Essentially, the characteristic behavior of the long waves in this case is similar to the behavior of the previous case. The main difference between the two cases is that an increase in the long wave period (through a decrease in the frequency modulation) reduces the net energy gained in the process of short-wave shoaling and breaking.

4.2.5 Case 3: Fixed Breakpoint with Double Slope

The third case is designed so that in combination with Cases 1 and 2 it demonstrates the significance of the parameter S_Δ. Here the frequency modulation ϵ is reset to the value $\epsilon = 0.1173$ of Case 1. The only parameter that is changed relative to Case 1 is the beach slope which is chosen as $h_x = \frac{1}{15}$. According to (4.21) it can be expected that this change in the slope will have the same effect as the halved frequency modulation of Case 2, since in this case $S_\Delta = 4.08 \cdot 10^{-2}$ also. The breaking depth is again $h_b/h_s = 0.21$.

Indeed, Fig. 4.10 shows the same results as Fig. 4.6. The growth of the amplitude of the incoming wave Fig. 4.11 exhibits the same behavior as Fig. 4.7. The figures showing the work terms and the phase lags are not repeated, since they are identical to Figs. 4.8 and 4.9.

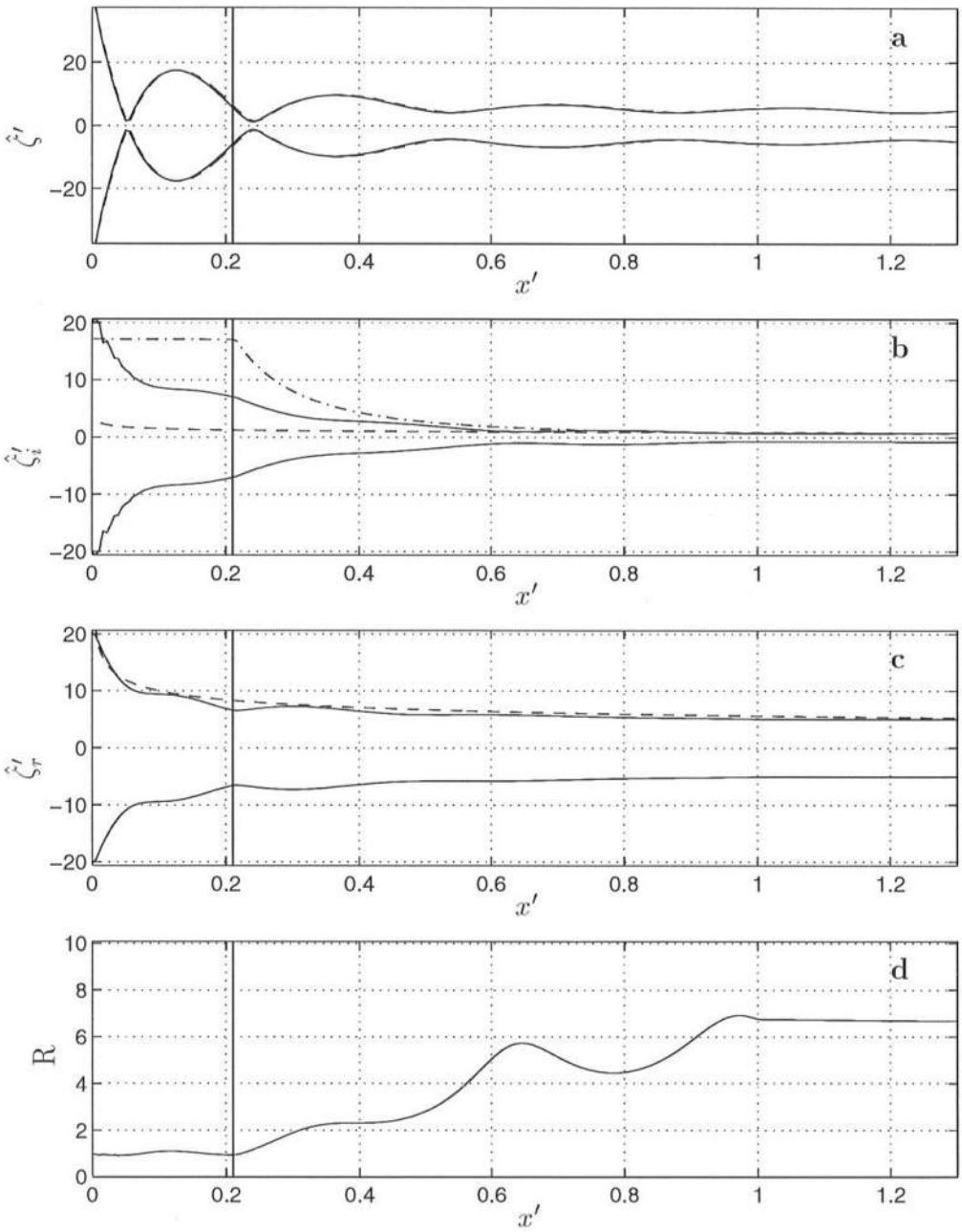

Figure 4.10: Case 3: Labels as Fig. 4.2

These computations confirm the importance of the parameter (4.21).

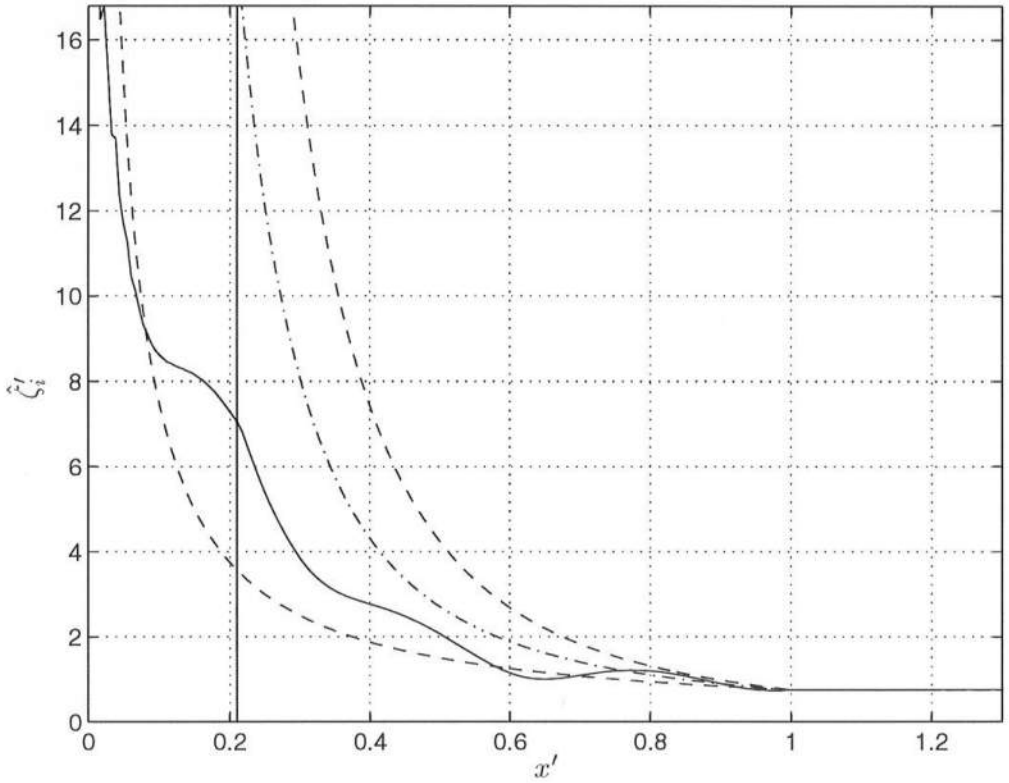

Figure 4.11: Case 3: Labels as in Fig. 4.3

4.2.6 Case 4: Fixed Breakpoint with Different Shelf Depth

In Case 4, we will vary the shelf depth h_s. If the values of the forcing frequency $\Delta\omega$, the bottom slope h_x and all other parameters are kept the same as in Case 1, but we reduce the shelf depth by a factor 4, we could expect the same results as in Cases 2 and 3, since we again have $S_\Delta = 4.08 \cdot 10^{-2}$ according to (4.21).

However, changing the shelf depth will change the value of h_b/h_s in (4.25). To obtain model results which are identical to Cases 2 and 3, we have to keep this parameter constant (at $h_b/h_s = 0.21$) as well. This can be achieved when γ, and

the ratios $c_{g,s}/c_{g,b}$ as well as a_s/h_s remain unchanged. Keeping the ratio $c_{g,s}/c_{g,b}$ constant essentially implies that $n_s = c_{g,s}/c_s$ or $k_s\,h_s$ remain unchanged. Since we reduced the shelf depth by a factor 4, it would then be required that the wave number of the short waves on the shelf k_s is increased by a factor 4, which by the linear dispersion relation

$$\omega^2 = g\,k_s\,\tanh\,k_s\,h_s \tag{4.44}$$

implies that the mean short-wave frequency be doubled from its value of Case 1. In order to keep the value of $\Delta\omega$ constant, this implies that the frequency modulation ϵ is halved relative to its value in Case 1, because of the relation (4.8). Finally, maintaining the ratio a_s/h_s will require that the amplitude of the short waves is reduced by a factor 4 as well.

Thus in order to achieve results similar to Cases 2 and 3 for a shelf depth of $h_s = 1.5\,m$, the other parameter values become: $a_{1,s} = 0.1104\,m$, $\delta = 0.1$, $\gamma = 0.7$, $h_x = 1/30$, $\omega = 3.6\,s^{-1}$ and $\epsilon = 0.05865$. It turns out that again the results are identical with the results shown in Figs. 4.6-4.9 and are not repeated here.

4.2.7 Case 5: Moving Breakpoint

In this section we will consider the case of a moving breakpoint ($\kappa = 1$) corresponding to the mechanism proposed by Symonds *et al.* (1982). The same parameter values as in Case 1 are used.

Figure 4.12a shows the comparison of the long-wave envelope as predicted by the model and the analytical solution by Schäffer (1993). The difference between the two solutions is due to the fact that in the analytical solution the breaking region (ranging from $0.2 \leq x' \leq 0.24$ in this case) is contracted into a

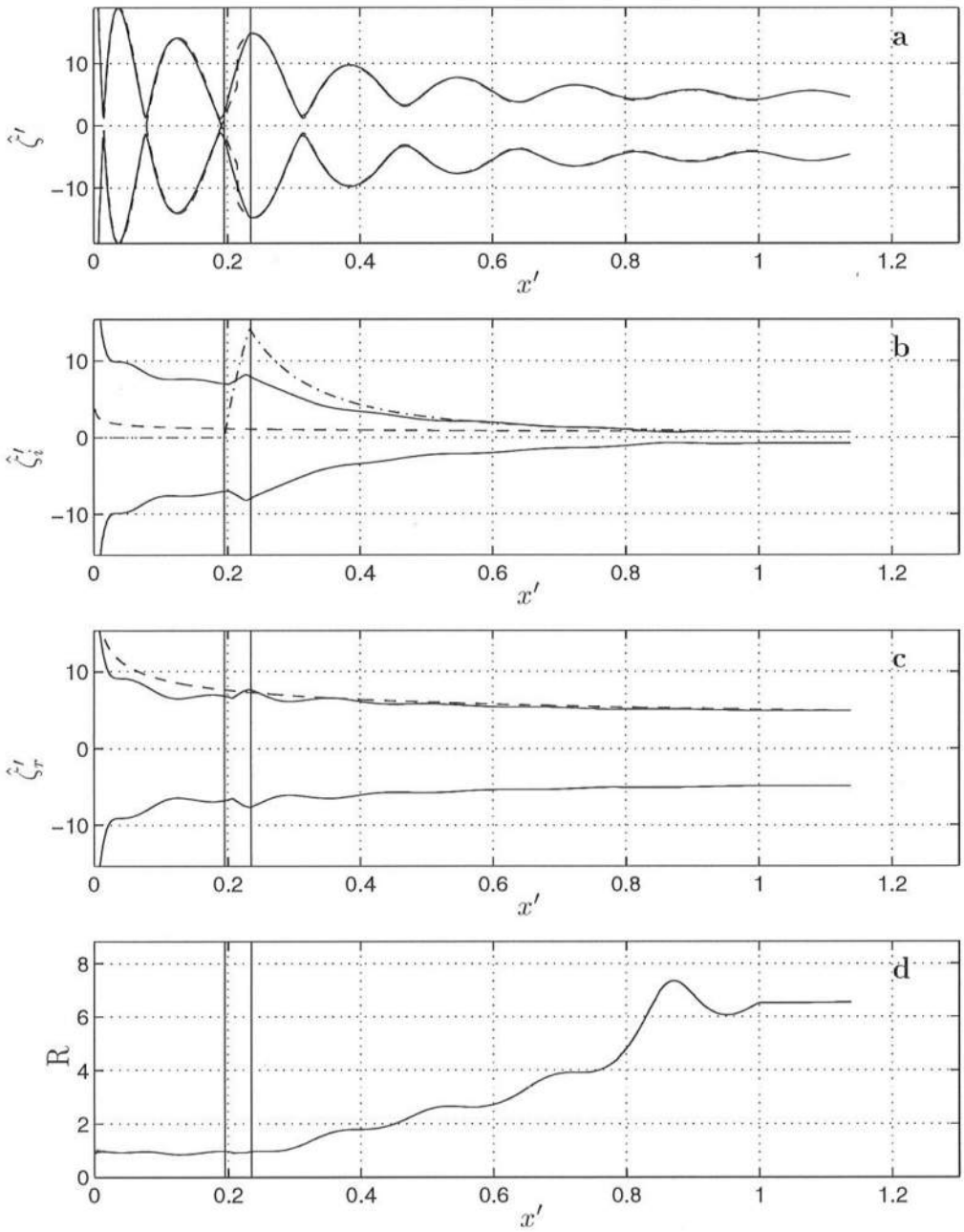

Figure 4.12: Case 5: Labels as Fig. 4.2

point at $x' = 0.22$ whereas in the numerical model no such simplification is made. The breaking region is indicated in this and further figures by two vertical lines.

Up to the point where breaking starts, the incoming long wave in Fig. 4.12b gains amplitude (or energy flux) as before. Over the breaking region, however, it can be seen that the amplitude actually decreases, a feature which is investigated in more detail below. Inside the surf zone ($h/h_s \leq 0.2$) a standing long wave occurs due to the absence of forcing in that region, see Figs. 4.12b and c. Figure 4.12c shows that outside the surf zone the outgoing long wave again decreases in amplitude according to Green's Law.

Finally, the ratio of the amplitudes of the outgoing wave and the incoming wave is shown in Fig. 4.12d. The "reflection coefficient" is about unity in the surf zone and in the breaking region and becomes larger than 1 in the shoaling region, which indicates that there is more energy in the outgoing wave than in the incoming wave.

The IG-wave generation process is further illustrated by the direct analysis of the energy transfer in Fig. 4.13. Fig. 4.13a shows the balance between the energy flux gradient (dashed line) and the total work (solid line). Fig. 4.13b shows that the work that the short waves do on the incoming long wave is negative in the shoaling region, as was seen in previous cases. The work done in the breaking region is *positive*, which indicates that energy flux is lost. This is consistent with the loss of amplitude shown in Fig. 4.12b. Inside the surf zone no forcing occurs, so the work is zero.

Fig. 4.13c shows that through the breaking region the work done on the outgoing wave is negative so that energy flux is *gained* (in magnitude) when the wave propagates out. Seaward of breaking the work is oscillating around zero as

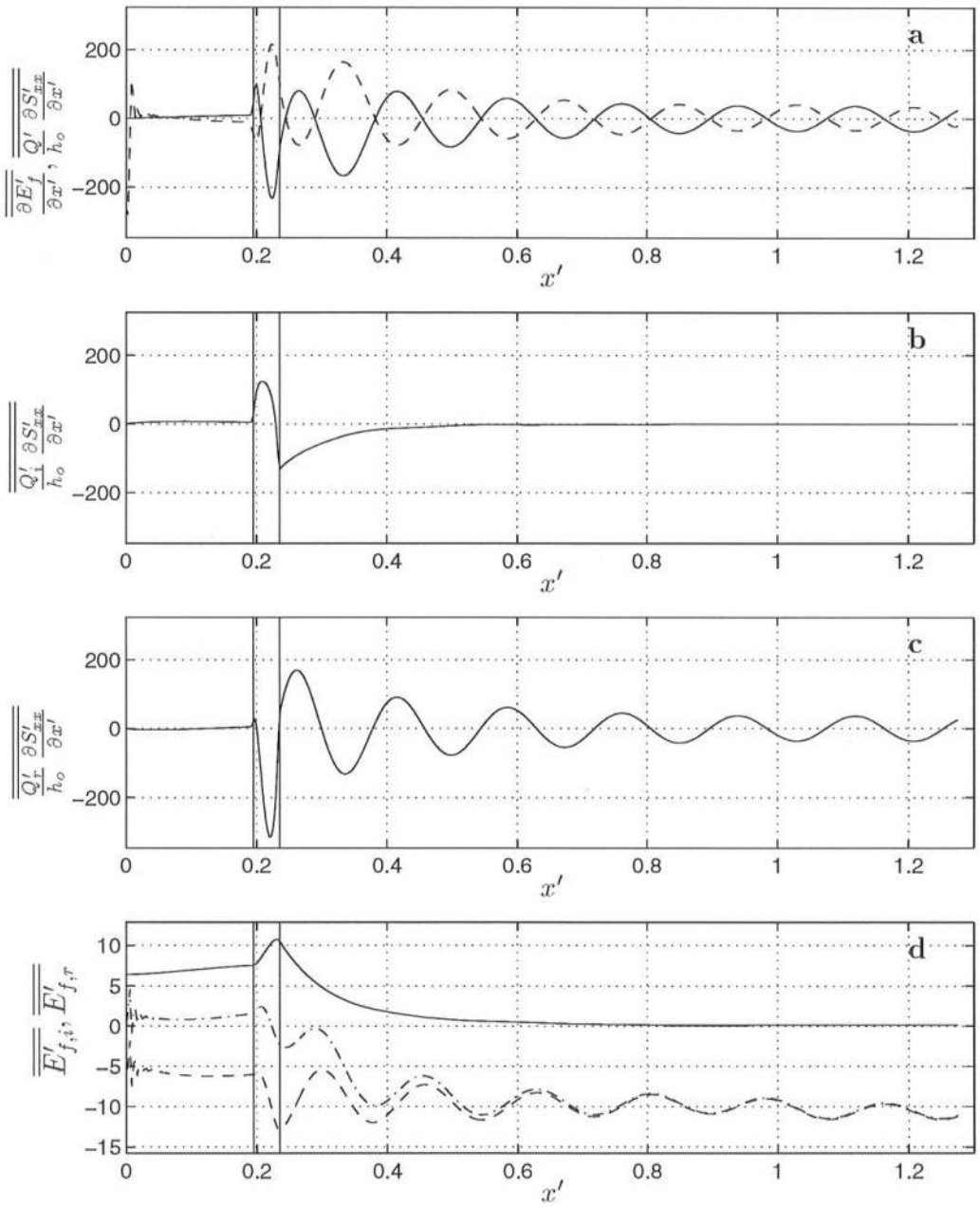

Figure 4.13: Case 5: Labels as in Fig. 4.4

in Case 1. The energy fluxes of the incoming, outgoing and total wave are plotted in Fig. 4.13d.

To summarize, the moving break point mechanism introduces a breaking region, in which the short-wave forcing does positive work on the incoming long wave and negative work on the outgoing long wave. The work that is done on the long waves in the breaking region influences the amplitudes and by extension the "reflection coefficient".

4.2.8 Case 6: Moving Breakpoint with Halved Frequency Modulation

Next we will change the frequency modulation to its value in Case 2, so that $\epsilon = 0.05865$, which is half the value of Case 5. The other parameters used are the same as in Case 2 but $\kappa = 1$. (As was shown in Cases 3 and 4, we could have changed the beach slope h_x or the shelf depth h_s to obtain equivalent results.) It turns out, however, that for $\kappa = 1$ a profound change occurs relative to the case of a fixed break point.

We first verify that the deviation between the model and the slightly simpler analytical solution is negligible, as is shown in Fig. 4.14a. Fig. 4.14b shows that the amplitude of the incoming wave increases outside of the breaking region and decreases in the breaking region itself, similar to the previous case. Inside the surf zone forcing is absent and a standing wave occurs, see Figs. 4.14b and c. In this case, however, the outgoing long wave *loses* amplitude when propagating out through the breaking region, see Fig. 4.14c. This results in a reflection coefficient R less than unity inside the breaking region. R becomes larger further offshore, see Fig. 4.14d, but due to the loss of energy in the breaker region the offshore value of the "reflection coefficient" has been reduced by about 100 percent relative to the previous case.

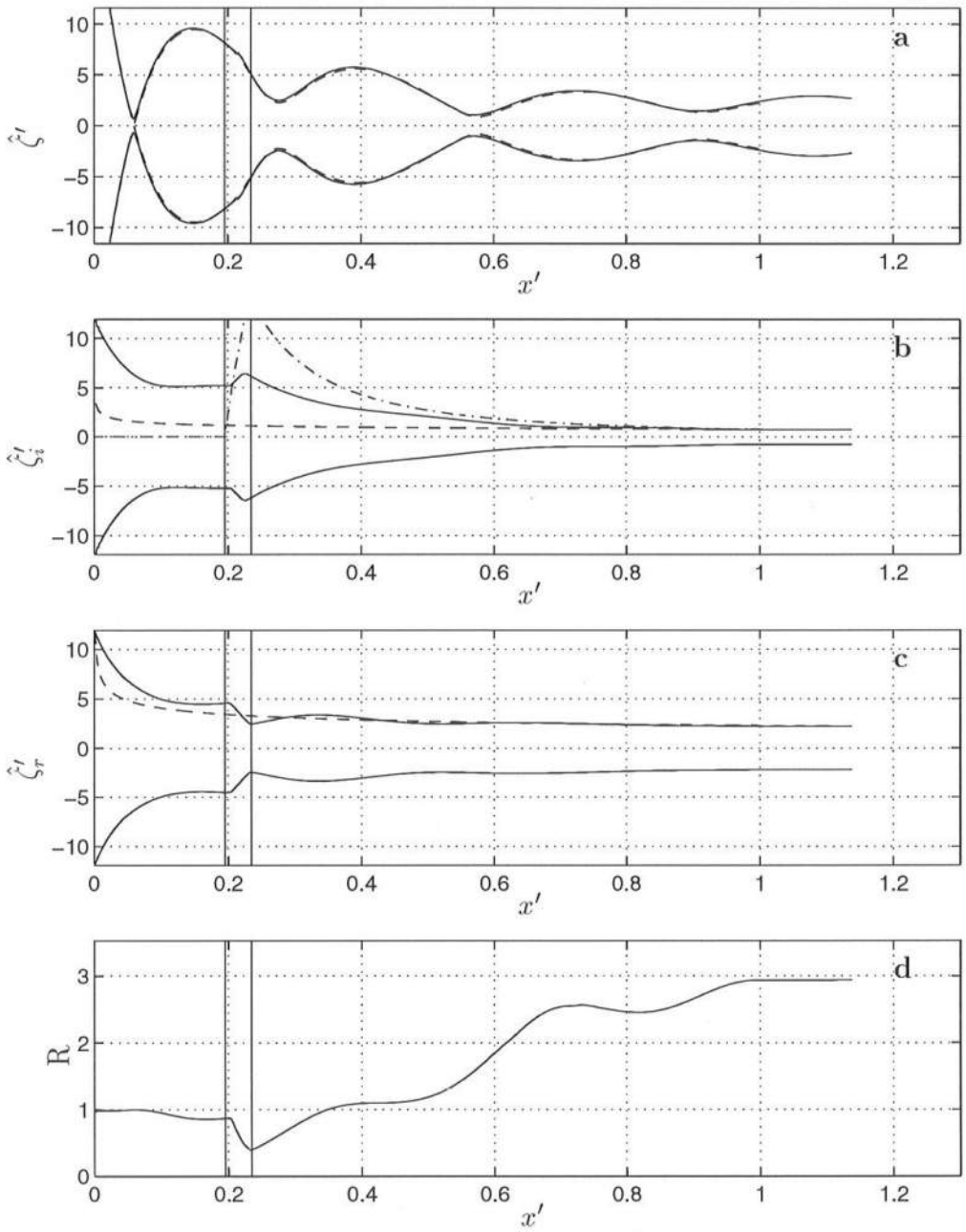

Figure 4.14: Case 6: Labels as Fig. 4.2

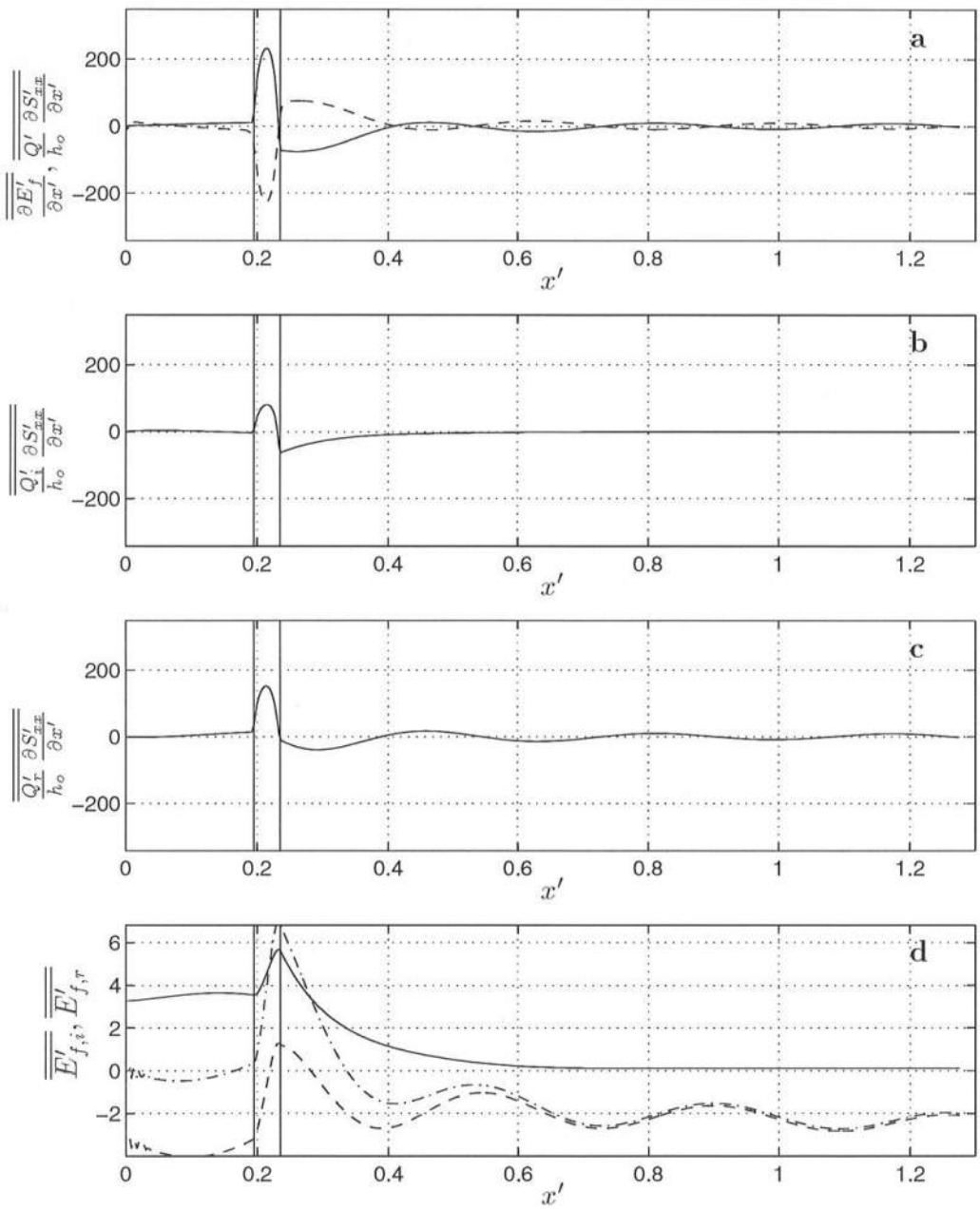

Figure 4.15: Case 6: Labels as in Fig. 4.4

Analysis of the energy transfer confirms this result. Figure 4.15a once again shows the balance between the terms in (4.36). The work on the incoming wave in Fig. 4.13b is similar to Fig. 4.13b, but Fig. 4.15c shows that contrary to the previous case, the work the short waves do on the outgoing long wave is now positive, which means that the energy flux decreases in magnitude as the long wave propagates out through the breaking region.

The reason for this different behavior is the phase difference between the short-wave groups and the incoming and outgoing long waves in the breaking region. As the short waves propagate onto the beach, the phase shift between the associated incoming long wave and the groups grows from 0.5π to about 0.6π, as we have seen in the previous cases. This phase shift causes the work to be negative so energy is transferred to the long waves. In the breaking region the forcing is varying in time (when the short waves in the group are smaller and break closer to shore) or constant (when the waves are larger and break further offshore). This causes the longwave-averaged work done on the incoming long wave to be positive in the breaking region. This behavior is independent of the period of the incoming wave groups, because the breaking region is small relative to the length of the groups.

With the destruction of the wave groups by the varying break point, the long wave is released in the breaking region and propagates shoreward as a free wave, where it is reflected and propagates seaward through the breaking region. The sign of the work that the short waves do on the outgoing wave is then dependent on the relative phase between them, which is a function of the time it takes the long wave to propagate through the surf zone and back. For a plane beach this time lag can be calculated as twice the propagation time from the shore to

the mean break point h_b:

$$\Delta T = 2 \int_0^{h_b} \frac{dh}{h_x \sqrt{g\,h}} = \frac{4}{h_x} \sqrt{\frac{h_b}{g}} \tag{4.45}$$

where $\Delta T = 44\,s$ in Cases 5 and 6 considered here.

In Case 5 the ratio of the time lag ΔT to the group period $T_g = 2\,\pi/\Delta\omega$ is

$$\frac{\Delta T}{T_g} = \frac{2}{h_x} \sqrt{\frac{2\,a_b}{\gamma\,g}} \frac{\Delta\omega}{\pi} \approx 3 \tag{4.46}$$

This integer value means that the outgoing long wave is "in phase" with the incoming long wave in the breaking region (which is short relative to the long-wave length). Because these waves propagate in opposite directions, the signs of the work terms are opposite as well, as was shown in Fig. 4.13. In Case 6 the ratio $\Delta T/T_g$ is about 1.5 (because the forcing frequency was halved), which means the incoming and outgoing waves are in "anti-phase", which causes the work on the incoming and outgoing waves to have the same sign.

The ratio $\Delta T/T_g$ essentially specifies the number of wave groups in the surf zone. As can be seen from (4.46) it depends on the forcing frequency, the beach slope and on the short-wave amplitude at breaking. Instead of changing the forcing frequency, an equivalent variation of the beach slope would yield the same result.

This ratio is equivalent to the parameter $\mathcal{X}$ which was already found by Symonds et al. (1982) and the slope parameter $S_b = h_x\,L_b/h_b$ used by Schäffer & Svendsen (1988) where L_b is the length of the surf zone and h_b is the depth at breaking. Rewriting those parameters yields

$$\mathcal{X} \equiv \frac{\Delta\omega^2\,h_b}{g\,h_x^2} = \frac{\pi^2}{4} \left(\frac{\Delta T}{T_g}\right)^2 = 4\,\pi^2\,S_b^{-2} \tag{4.47}$$

This case shows that the choice of the number of wave groups in the surf zone influences the sign of the work done on the outgoing wave. In this particular case, the work done in the breaking region reduces the energy flux in the outgoing wave and therefore reduces the "reflection coefficient".

4.2.9 Case 7: Moving Breakpoint with Halved Shelf Depth

In this section, it will be shown that for a suitable choice of parameters, we can achieve a "reflection coefficient" that is less than unity outside the surf zone, which would mean that the incoming long wave is more energetic than the outgoing wave and that the infragravity waves would have experienced a net loss of energy.

The parameters chosen in this case are the same as in Case 6, but now the shelf depth $h_s = 3\,m$. We choose $a_s = 0.4221\,m$ so that the energy flux on the shelf is equal to the energy flux in the previous case to ensure that the short waves will break at the same dimensional depth.

Fig. 4.16a shows the comparison of the model (solid line) to the analytical solution, which is nearly identical except in the breaking region. Notice that because offshore distance is normalized by h_s/h_x where in this case the shelf depth has been halved relative to the previous case, the breaking region now extends from $0.39 \leq x' \leq 0.47$. As in the previous case, we see that the amplitude of the incoming wave in Fig. 4.16b decreases in the breaking region. The amplitude of the outgoing wave again decreases when it propagates seaward through the breaking region in Fig. 4.16c. The most important change relative to the previous case is that the "reflection coefficient" in Fig. 4.16d, which is about unity in the surf zone ($x' \leq 0.39$), decreases sharply in the breaking region and has a value of $R = 0.6$ on the shelf ($x' \geq 0.39$). This indicates that the outgoing wave is

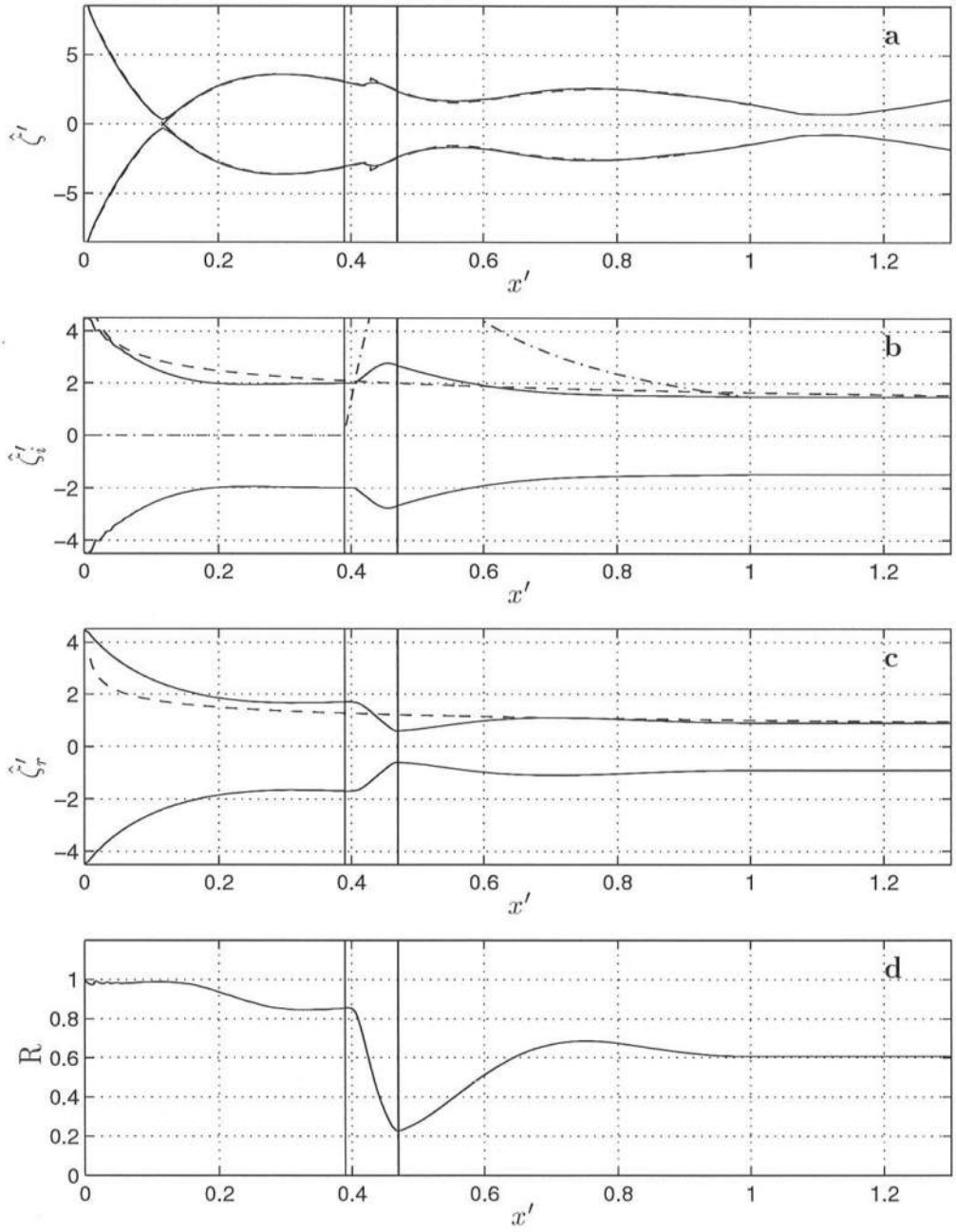

Figure 4.16: Case 7: Labels as Fig. 4.2

less energetic than the incoming long wave, meaning that the infragravity wave actually lost energy in the wave group shoaling and breaking process.

This result can be attributed to the fact that the reduction of the shelf depth reduces the length of the shoaling region in which energy is transferred from the short waves to the long waves as was shown in all previous cases. This is the only region in which the infragravity wave gains net energy, as can be seen in Fig. 4.17b. The infragravity wave loses energy when it propagates shoreward (Fig. 4.17b) and seaward (Fig. 4.17c) through the breaking region, which for this particular choice of parameters amounts to a net loss of energy in the entire process.

Fig. 4.17c shows the energy fluxes of the incoming long wave (solid line), the outgoing long wave (dashed line) and the total (dash-dotted line). It is seen that energy flux is gained when the wave propagates into shore in the shoaling region. Energy flux is lost when the wave propagates back and forth through the breaking region.

4.2.10 Case 8: Moving Breakpoint with Reversal of Groupiness

As a final case, we will show the effect of a choice of the breaking mechanism parameter $\kappa = 2$. As can be seen from (4.7), this choice of κ implies that the groupiness is not only transmitted into the surf zone (as was the case for a fixed breakpoint) but that it is also reversed. In this case, infragravity waves are generated both in the breaking region (Symonds *et al.* (1982)'s mechanism) and in the surf zone (Schäffer & Svendsen (1988)'s mechanism). Physically, this situation corresponds to a situation in which the higher short waves in the group break closer to shore than the lower ones. The other parameters are the same as in Case 1.

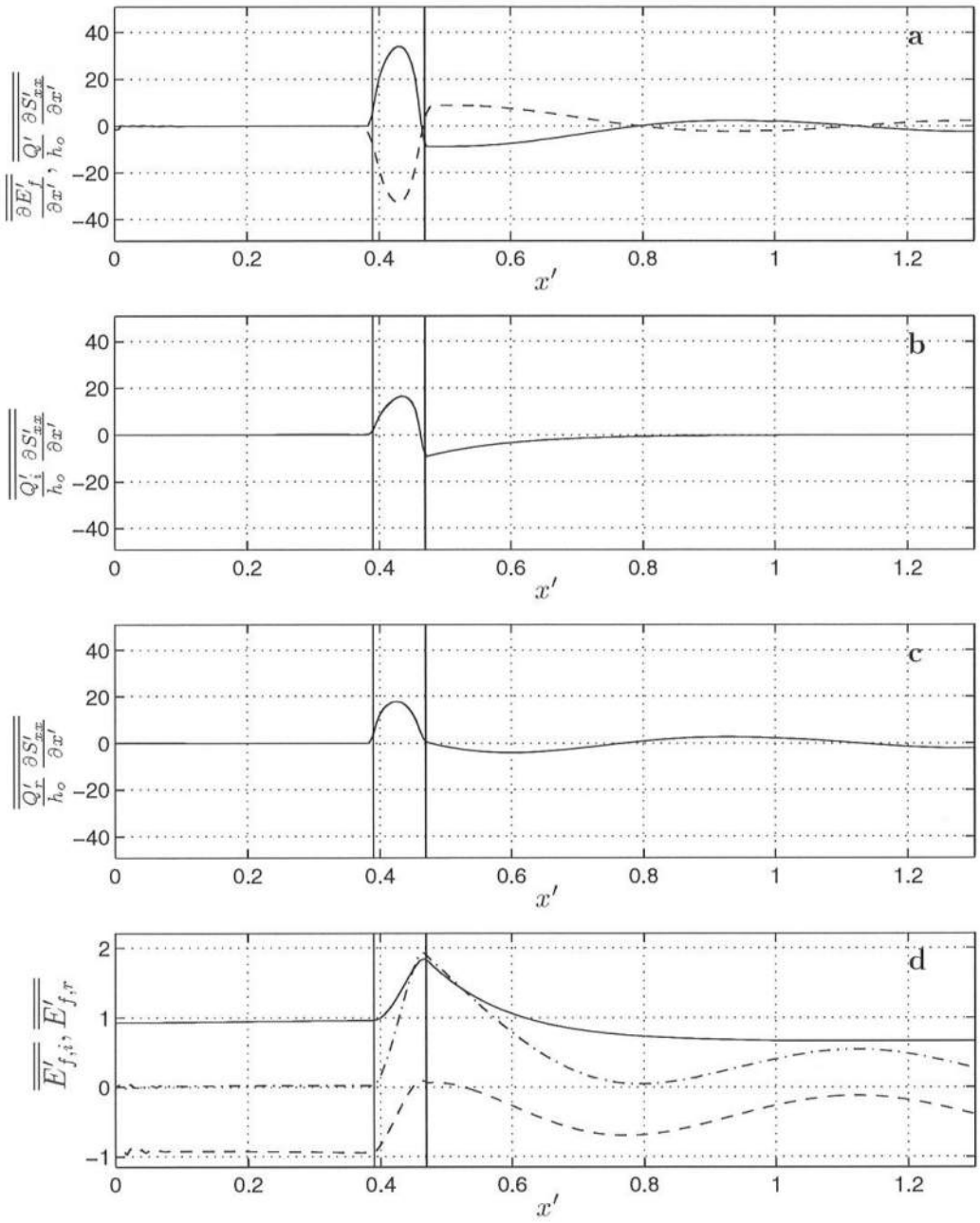

Figure 4.17: Case 7: Labels as in Fig. 4.4

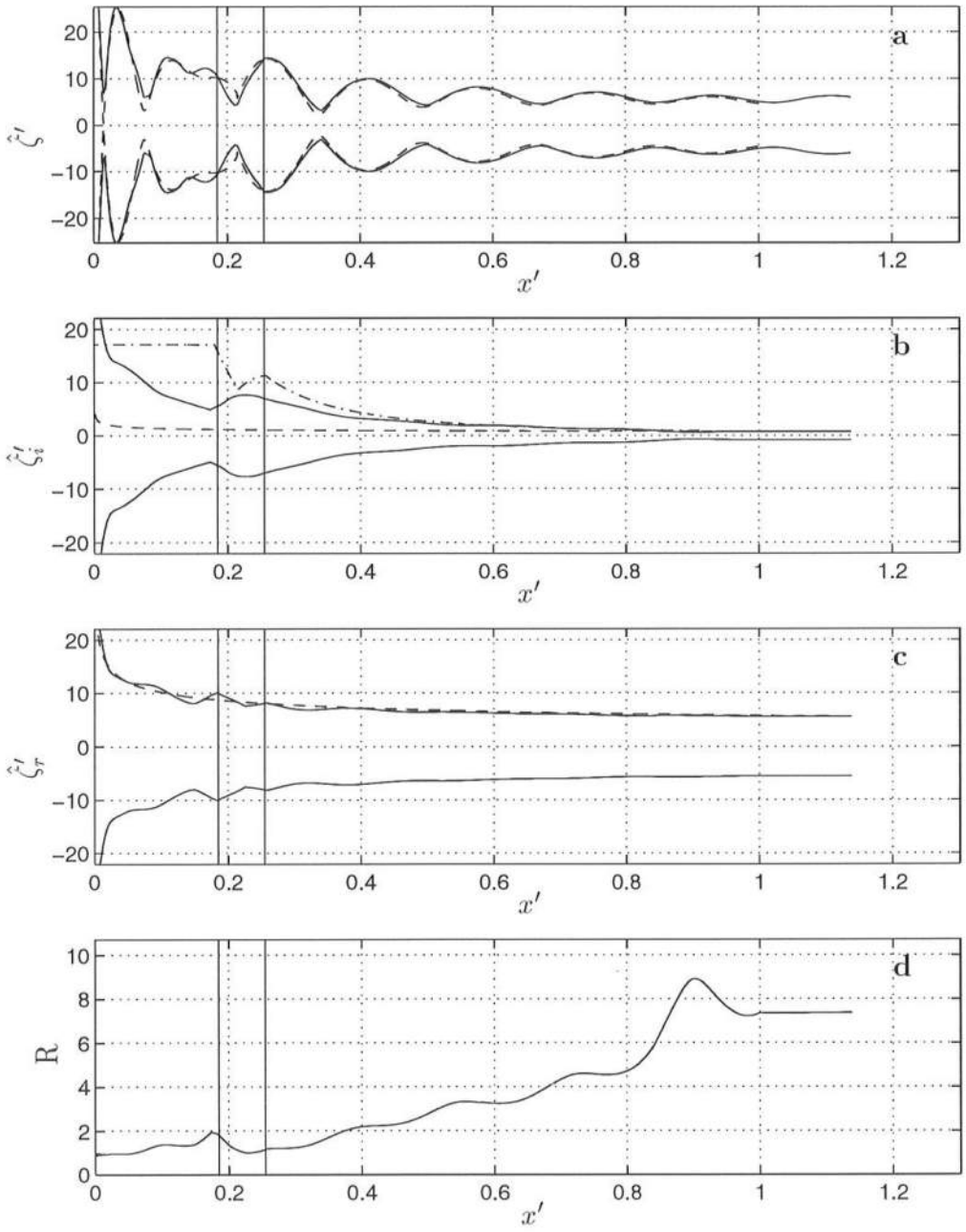

Figure 4.18: Case 8: Labels as Fig. 4.2

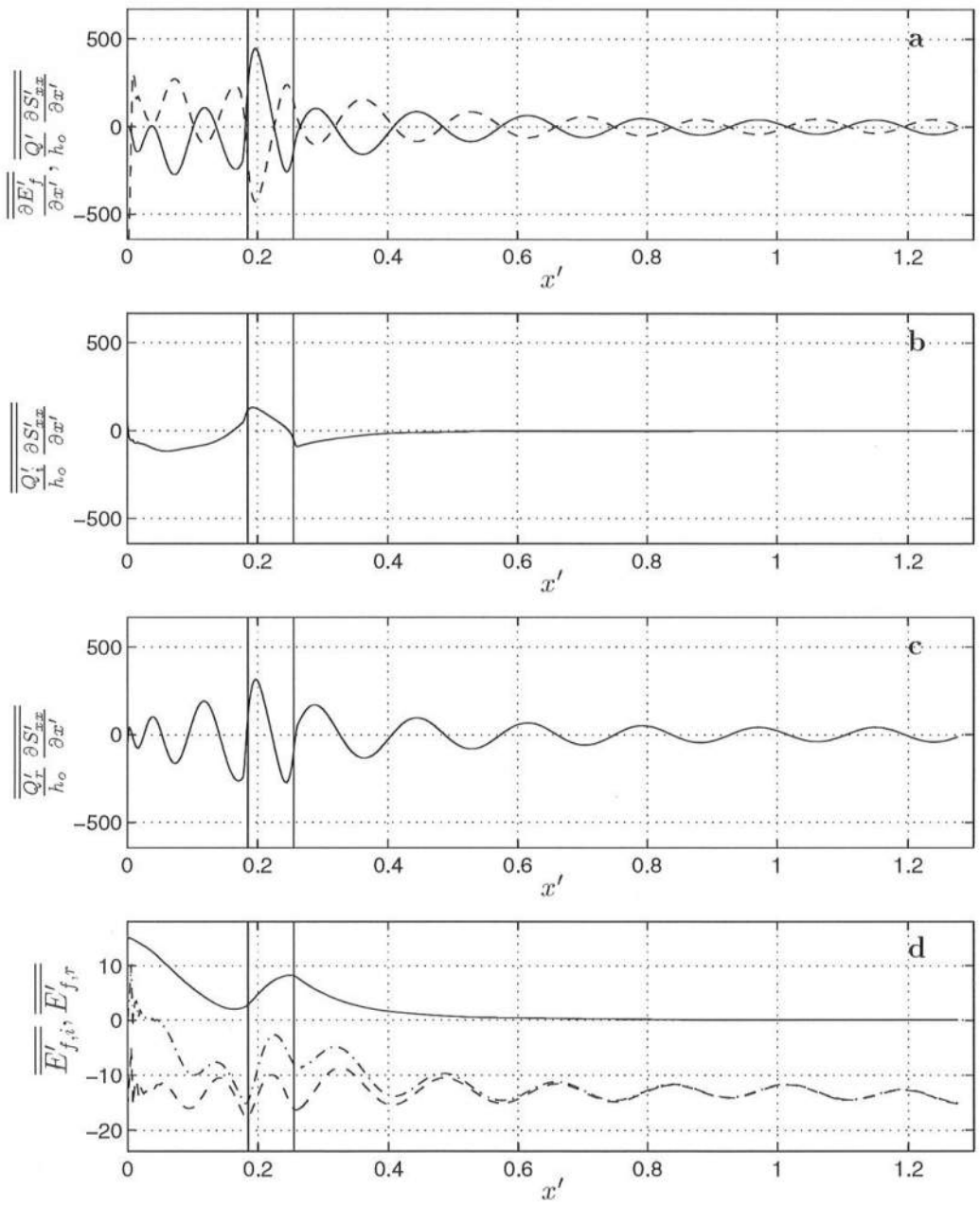

Figure 4.19: Case 8: Labels as in Fig. 4.4

Fig. 4.18a shows again the comparison between the present model (solid line) and the analytical solution (dashed line) which exhibits small differences in the breaking region. The incoming wave in Fig. 4.18b grows in the shoaling region and shows first an increase and then a decrease in the breaking region. Inside the surf zone, the amplitude becomes larger relative to the value in the breaking region. The outgoing wave more or less decreases according to Green's Law, see Fig. 4.18c. The "reflection coefficient" is about unity throughout the surf zone, decreases in the breaking region and increases in the shoaling region, see 4.18d.

The analysis of the work terms in the energy equation confirms this result. Fig. 4.19a shows the balance between the energy flux gradient and the work. In Fig. 4.19b it is shown that the work done on the incoming long wave is first negative in the breaking region, then positive and finally negative in the inner surf zone, which corresponds to the growth of the amplitude in Fig. Fig. 4.18b. The outgoing wave exhibits much of the same behavior as was seen in Fig. 4.4c. The energy flux of the incoming waves (solid line in Fig. 4.4d) increases outside the surf zone, decreases in the breaking region and grows again in the surf zone. The energy flux in the outgoing wave (dashed line) shows the oscillatory behavior, which was shown before.

4.2.11 Summary of Cases

To summarize the results, the three governing parameters as well as the reflection coefficients R, which is measured on the shelf, are listed in Table 4.1 for all eight cases. It can be seen that R on the shelf is reduced if the parameter S_Δ is increased. As stated above, this is due to the fact that less work is done on long waves that have a longer period (as in Case 2) or that propagate on a steeper

slope (as in Case 3), so that less energy is transferred. It has been shown that for $\kappa = 1$ energy flux is lost in the breaking region depending on the phase between the forcing and the long waves. Furthermore, in Case 7 we saw that if the shelf depth is reduced, the shoaling region in which net energy is transferred to the long waves is reduced also, so that it is possible that the outgoing long wave has less energy than the incoming long wave.

Table 4.1: Summary of eight cases: governing parameters S_Δ, $\frac{h_b}{h_s}$ and κ and reflection coefficient R_s on the shelf.

Case	S_Δ	$\frac{h_b}{h_s}$	κ	R_s
1	$1.02 \cdot 10^{-2}$	0.21	0	10.0
2-4	$4.08 \cdot 10^{-2}$	0.21	0	6.79
5	$1.02 \cdot 10^{-2}$	0.21	1	6.54
6	$4.08 \cdot 10^{-2}$	0.21	1	2.94
7	$8.14 \cdot 10^{-2}$	0.42	1	0.61
8	$1.02 \cdot 10^{-2}$	0.21	2	7.38

4.3 Importance of Nonlinear Terms

To investigate the importance of nonlinearities on the results, the model is run with the parameters of Case 7, but with a frequency modulation $\epsilon = 0.1173$. The particular choice of the parameters is not really important in this example since the general effect of the nonlinearities that we will show in this section is independent of the values of the parameters.

The model is run using the nonlinear equations (4.1) and (4.2). In this case it is impossible to linearly separate the incoming and outgoing long waves. Therefore, we will study the envelope of the total long-wave motion. Fig. 4.20a shows

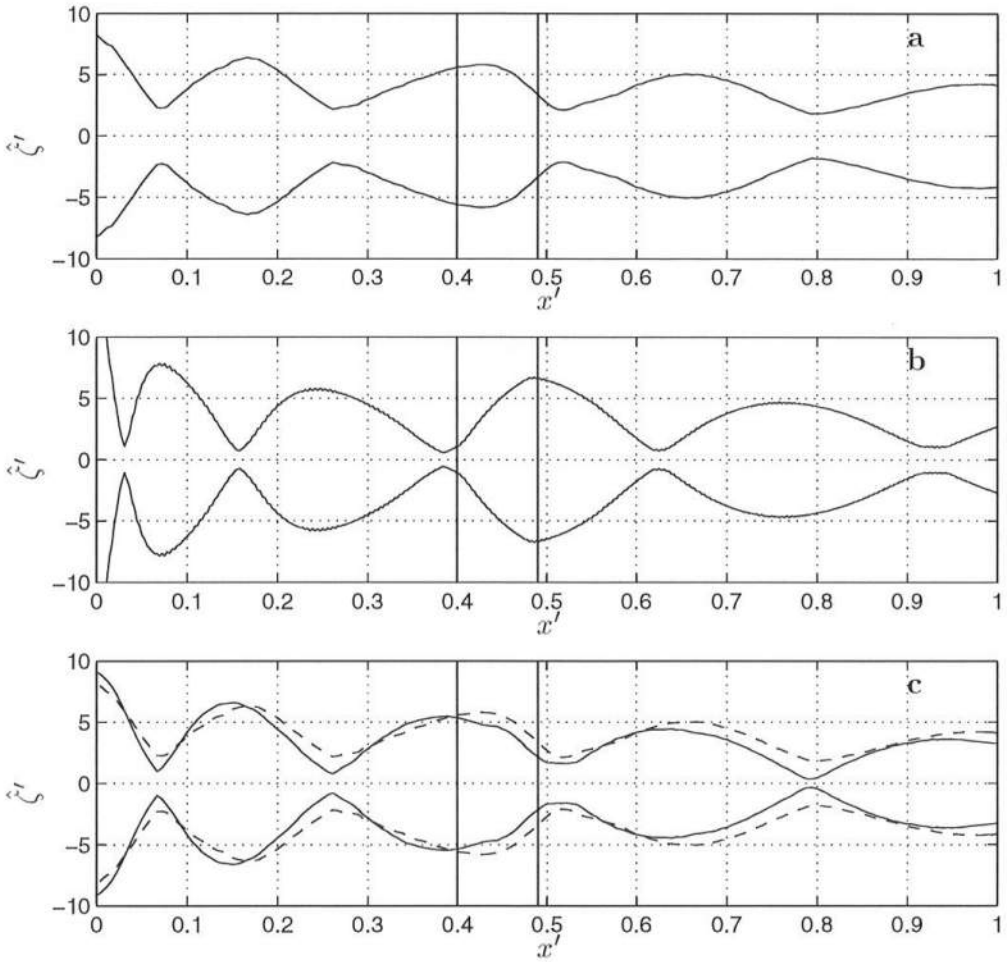

Figure 4.20: Envelopes of the total long-wave motion: (a) Nonlinear version; (b) Linear version; (c) Linear version with mean set-up included in the depth (——) and nonlinear version (repeated from (a)) (– –).

the envelope when the nonlinear equations are used. The envelope computed using the linearized model in Fig. 4.20b shows a distinctly different behavior. The nodes and anti-nodes are shifted in space relative to the nonlinear model results. This is due to the fact that in the nonlinear version of the model the travel time ΔT is dependent on the still water depth h_o as well as the set-up $\bar{\zeta}$. In short, the set-up effectively changes the beach slope in the surf zone experienced by the long waves. If we artificially include the mean set-up $\overline{\bar{\zeta}}$ in the linear model, the nodes shift, see Fig. 4.20c (solid line). Comparing to the nonlinear result from

Fig. 4.20a, which is repeated in Fig. 4.20c (dashed line), we see that the two solutions agree well. This indicates that the mean set-up is the most important nonlinear term.

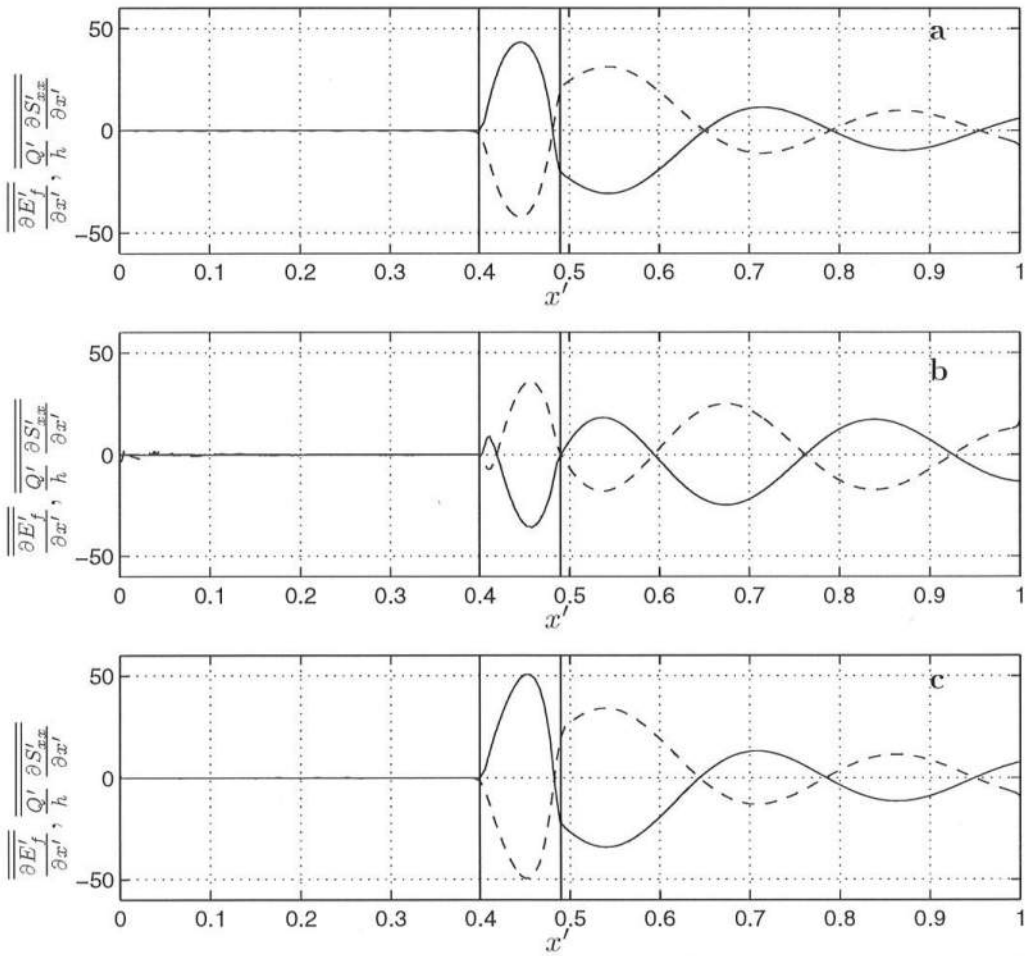

Figure 4.21: Work done on total long wave (——) and energy flux (– –): (a) Nonlinear version; (b) Linear version; (c) Linear version with mean set-up included in the depth.

Another way to visualize this is to examine the terms in the nonlinear long-wave equation (2.97), averaged over the IG-wave period

$$\frac{\partial}{\partial x}\overline{\overline{\left(\frac{1}{2}\,\rho\,\frac{Q^3}{h^2}+\rho\,g\,\zeta\,Q\right)}}+\overline{\overline{\frac{Q}{h}\,\frac{\partial S_{xx}}{\partial x}}}+\overline{\overline{U\,\tau_{b,x}}}=0 \tag{4.48}$$

which is the nonlinear extension of (4.36). The work that the bottom friction does on the current is small and is neglected in the following. The energy flux and the work balance each other, as can be seen in Fig. 4.21a. For the same set of parameter values the results obtained with the linearized equations (Fig. 4.21b) show a change of sign of the terms. When we artificially add the mean set-up in the linearized equations, we see that the sign of the work and energy flux gradient terms is reversed such that Figs. 4.21a and c qualitatively agree, although there are differences in the absolute values.

In conclusion, the results in this section show that including the mean set-up changes the linearized model in such a way that its results agree well with the nonlinear model results.

4.4 Comparison to Laboratory Data of Kostense (1984)

As a validation of the nonlinear version of the model, SHORECIRC was tested against Kostense's (1984) laboratory data as well as a nonlinear time domain model (Roelvink, 1993) and the linear, analytical solution by Schäffer (1993).

Kostense (1984) performed careful measurements of the amplitudes of the incoming and outgoing long waves in a wave flume at Delft Hydraulics with a constant depth section and a section with a constant slope of $h_x = 1/20$. The wave paddle motion included second-order wave generation and was able to absorb the outgoing free long wave, which means that free standing waves could be avoided. Experiments were conducted for four series of tests labeled A through D, see Table 4.2. In series A and B the difference frequency $\Delta\omega$ was varied, while for series C and D the wave height a_1 of the primary wave was varied. For all cases the bottom slope is $h_x = 1/20$, the depth of the toe of the beach $h_s = 0.5\,m$ and the amplitude modulation $\delta = 0.2$.

Table 4.2: Input and Output for Kostense (1984) data sets. Notice that the pairs D1 and A3, and B2 and C2 are the same.

Series	ω_1 (s^{-1})	ω_2 (s^{-1})	ω (s^{-1})	ϵ	a_1 (m)	$\Delta\omega$ (s^{-1})	$\hat{\zeta}_i$ (mm)	$\hat{\zeta}_r$ (mm)
$A1$	3.062	2.145	2.6035	0.1761	0.055	0.9169	5.168	0.986
$A2$	3.062	2.296	2.6790	0.1430	0.055	0.7662	4.885	1.672
$A3$	3.065	2.456	2.7605	0.1103	0.055	0.6088	4.588	2.069
$A4$	3.077	2.618	2.8475	0.0806	0.055	0.4590	4.312	1.144
$A5$	3.063	2.755	2.9090	0.0529	0.055	0.3078	4.121	0.573
$B1$	4.295	3.372	3.8335	0.1204	0.055	0.9231	2.351	1.300
$B2$	4.065	3.293	3.6790	0.1049	0.055	0.7719	2.569	0.578
$B3$	4.070	3.455	3.7625	0.0817	0.055	0.6148	2.448	1.626
$B4$	4.071	3.609	3.8400	0.0602	0.055	0.4623	2.346	0.820
$B5$	4.070	3.762	3.9160	0.0393	0.055	0.3077	2.250	0.786
$C1$	4.294	3.522	3.9080	0.0988	0.08	0.7722	4.700	1.017
$C2$	4.065	3.293	3.6790	0.1049	0.055	0.7719	2.569	0.578
$C3$	4.295	3.523	3.9090	0.0987	0.035	0.7716	0.923	0.886
$D1$	3.065	2.456	2.7605	0.1103	0.055	0.6088	4.588	2.069
$D2$	3.065	2.456	2.7605	0.1103	0.035	0.6089	1.875	1.539
$D3$	3.065	2.456	2.7605	0.1103	0.03	0.6089	1.380	1.346

The model uses a_1 and $\Delta\omega$ (columns 6 and 7 in Table 4.2) as input as well as $\delta = 0.2$ and the bathymetry of the experimental set-up. At the wave-maker side we apply the absorbing-generating boundary condition, while at the shoreline we implement the one-dimensional shoreline boundary condition derived in Chapter 3.3.1. The short-wave forcing was calculated from the energy equation of the short waves (2.96)

$$\frac{\partial}{\partial t}\left(E - \frac{1}{2}\rho\frac{Q_w^2}{h}\right) + \frac{\partial}{\partial x}\left(E_f + \tilde{U}\,E - \frac{1}{2}\bar{Q}\left(\frac{Q_w}{h}\right)^2\right) +$$

$$S'_{xx}\frac{\partial \tilde{U}}{\partial x_\alpha} - \frac{Q_w}{h}\frac{\partial S'_{xx}}{\partial x_\alpha} + \tilde{U}\,\tau_b = \mathcal{D} \tag{4.49}$$

where $\mathcal{D}$ is the dissipation term analogous to a bore (Svendsen, 1984a).

$$\mathcal{D} = -\rho g h \frac{2 a_1^3}{d_t d_c T} \tag{4.50}$$

In this equation d_c and d_t are the total water depths at crest and trough and $T = \frac{2\pi}{\Delta\omega}$ is the period of the long wave. By calculating the short-wave energy E from (4.49), we allow for a feedback mechanism of energy from the long waves back to the short waves through the terms involving the $\bar{Q}$ and $\tilde{U}$. This mechanism was not present when we specified the radiation stress forcing using (4.7) or (4.10) in the linearized model. In the linear case, the short waves transfer energy to the long waves without gaining any energy back from the long waves. However, a limitation of the use of (4.49) is that we still need a theory to calculate the short-wave forcing from the short-wave energy E. In the present model, we use linear long-wave theory, which we know is inaccurate, particularly inside the surf zone (Svendsen & Putrevu, 1993).

An expression for the weak-current bottom shear stress, as found by Liu & Dalrymple (1978), is chosen

$$\tau_b = \frac{2}{\pi} \rho f_{cw} u_o \tilde{U}_b \tag{4.51}$$

where the coefficient $f_{cw} = 0.02$, u_o is the wave velocity amplitude and $\tilde{U}_b$ is the long-wave velocity at the bottom. The breaking parameter $\gamma_b = 2\,a_b/h_b = 0.75$ is used. The amplitudes of the incoming and outgoing long waves as calculated by the model at the wave-maker side boundary are given in the last two colums of Table 4.2.

As can be seen in Fig. 4.22, for the incoming long wave the present model's prediction of the amplitudes (left-hand side panels) is in close agreement with the data and the other models. The prediction of the amplitudes of the outgoing wave (right-hand side panels) shows more variation, especially for cases C2 (which is

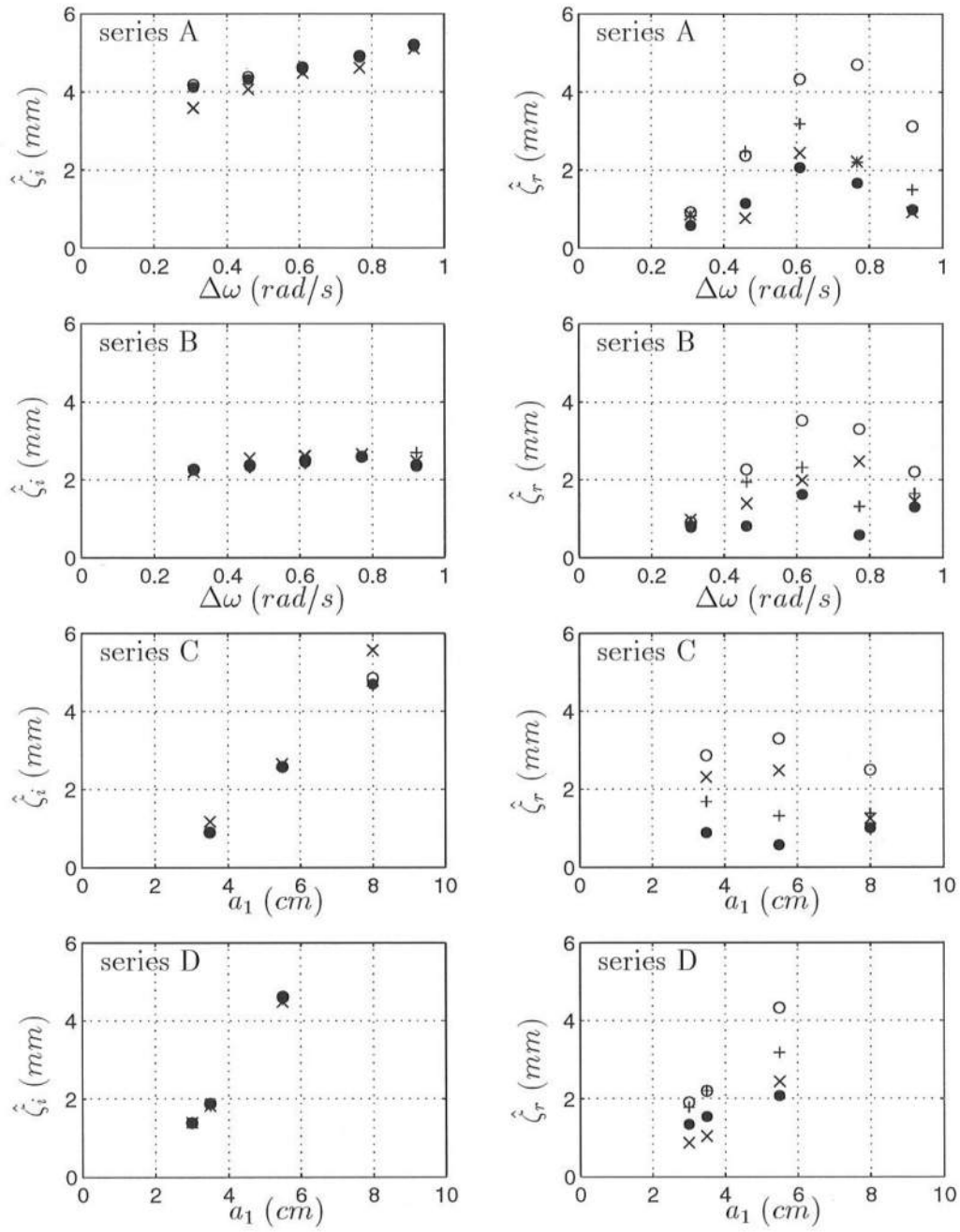

Figure 4.22: Amplitudes of the incoming long wave, $\hat{\zeta}_i$, (left-hand panels) and outgoing long wave, $\hat{\zeta}_r$, (right-hand panels) for four series of Kostense's (1984) laboratory data (×), present model (•), Roelvink's (1993) model (+) and Schäffer's (1993) model (○).

the same as B2) and C3. It is interesting that the other models' results also show a large deviation from the measured values for those cases. The present model's predictions all fall in the range of predictions by the data and by other models. In fact, except for two values of series C, SHORECIRC actually performs better, which gives us confidence in its physical accuracy.

4.5 Conclusions

In this Chapter, the SHORECIRC model has been used to study infragravity wave generation. First, three external parameters governing this process are identified. These parameters S_Δ, $\frac{h_b}{h_s}$ and κ are related to the geometry of the problem. They are an alternative to the five parameters identified by Schäffer (1993).

The linearized version of the model showed excellent agreement with the analytical solution by Schäffer (1993). In order to be able to analyze the generation of infragravity waves further, the incoming and outgoing long waves are separated. As expected, the incoming long wave already gains energy flux outside the surf zone due to the changing forcing. Increasing the parameter S_Δ, by increasing the slope or the forcing period, reduces the work done on the incoming wave and as a consequence also energy flux gain. In any case, this increase is not nearly as fast as Longuet-Higgins & Stewart (1962)'s steady state theory for bound waves suggests, which is an important finding in the analysis of field data. We find that the growth rate of the bound long waves is not a simple function of the depth variation, but is also dependent on the short-wave characteristics such as the relative water depth $k\,h_o$.

In the cases with a fixed break point the energy flux gain continues inside the surf zone, whereas in the cases with a moving break point, it is found that the

incoming wave loses energy flux in the breaking region.

In the cases with a fixed break point the outgoing long wave is seen to exchange energy flux with the short waves with very little net gain over the domain, so that it essentially decreases in amplitude according to Green's Law. When the breakpoint is allowed to move, however, the outgoing wave either gains or loses flux depending on the phase between the short-wave forcing and the outgoing wave in the breaking region. This phase difference is a function of the length of the surf zone relative to the length of the wave groups, which in other words means that the number of wave groups in the surf zone is an important parameter.

The terms in the linear energy equation are shown to be an important tool in the analysis of the energy transfer process. From the sign of these terms it can be deduced whether the infragravity waves gain or lose energy. The generation of infragravity waves can also be visualized by showing the phase difference between the long waves and the short-wave forcing. The variation of the phase differences correspond to the variation of the energy in the long waves.

It is shown that a variation of the parameters results in a variation in the ratio of outgoing to ingoing wave energy, which may explain the seemingly inconclusive field evidence. The value of the "reflection coefficient" R can be interpreted as a characteristic measure of the net transfer of energy to the infragravity waves as a result of shoaling and breaking of the short-wave groups and their interaction with the long waves.

Extending the model to include the nonlinear terms shows the importance of the steady set-up over the other nonlinear terms.

Finally, the nonlinear model has been tested against the Kostense (1984) data set. It is shown that the model predictions and the laboratory results agree

very well. In most cases, the present model's predictions are better than previous models except for a few data points where other models also showed a large deviation relative to the laboratory data.

Chapter 5

EFFECTS OF QUASI 3-D DISPERSIVE MIXING

In this chapter we will investigate the importance and the effect of the quasi 3-D (also called dispersive mixing) terms, which were derived in Chapter 2, in two particular cases: the start-up of a longshore current and infragravity waves forced by obliquely-incident wave groups.

In Section 5.1 the start-up of a longshore current on a plane beach is studied. This case was also shown in Van Dongeren *et al.* (1994). It turns out that, because of the longshore uniformity in both the bathymetry and the hydrodynamical conditions, only one of the dispersion terms in the y momentum equation is significant and most other terms vanish. This remaining dispersion term, however, has been shown to have a profound effect on the shape of the horizontal longshore current profile (Svendsen & Putrevu, 1994a). Furthermore, it is shown that the time scale to attain steady state is much larger for the longshore current than for the cross-shore current. The three-dimensional development of the current spirals is shown. For the steady state, the magnitude of the quasi 3-D coefficients as a function of the cross-shore coordinate is analyzed and compared to an approximate value.

In Section 5.2 the effect of the quasi 3-D terms on infragravity waves, forced by obliquely-incident wave groups, is examined. This case will be more interesting

to analyze than the longshore current case, because the hydrodynamical conditions are longshore periodic instead of longshore uniform, and more terms in the momentum equations are retained.

First, the results of the linearized model are compared to the analytical solution by Schäffer (1994). Then, the effect of the nonlinear terms, corresponding to the 2D-H equations, and the effect of the quasi 3-D dispersive mixing terms are shown. Also shown is the variation of the longshore and cross-shore infragravity wave profiles over an IG-wave period for a number of locations both inside and outside the surf zone. We will investigate the magnitude of the quasi 3-D coefficients as a function of the cross-shore distance. Finally, the relative importance of the quasi 3-D terms in the momentum equations is shown, after which we can make recommendations about which terms can be neglected in the equations for this application.

5.1 Start-up of the Longshore Current

In the first application of the quasi 3-D equations (2.8) and (2.71), we will study the start-up of a longshore current on a plane beach induced by imposing short-wave forcing due to shoaling and breaking monochromatic waves in a domain at rest at $t = 0$. For reference, we repeat the governing quasi 3-D equations here

$$\frac{\partial \overline{\zeta}}{\partial t} + \frac{\partial \bar{Q}_\alpha}{\partial x_\alpha} = 0 \tag{5.1}$$

$$\frac{\partial \bar{Q}_\beta}{\partial t} + \frac{\partial}{\partial x_\alpha}\left(\tilde{V}_\alpha \tilde{V}_\beta\, h + M_{\alpha\beta}\right)$$

$$-\frac{\partial}{\partial x_\alpha}\left[h\left(D_{\beta\gamma}\frac{\partial \tilde{V}_\alpha}{\partial x_\gamma} + D_{\alpha\gamma}\frac{\partial \tilde{V}_\beta}{\partial x_\gamma} + B_{\alpha\beta}\frac{\partial \tilde{V}_\gamma}{\partial x_\gamma}\right)\right] + \frac{\partial}{\partial x_\alpha}\left[A_{\alpha\beta\gamma}\tilde{V}_\gamma\right]$$

$$= -g\,h\,\frac{\partial \bar{\zeta}}{\partial x_\beta} - \frac{1}{\rho}\frac{\partial}{\partial x_\alpha}\left(S_{\alpha\beta} - \overline{\int_{-h_o}^{\zeta} \tau_{\alpha\beta}\,dz}\right) + \frac{\tau_\beta^S - \tau_\beta^B}{\rho} \tag{5.2}$$

In the case of monochromatic waves we can express the radiation stress as

$$S_{\alpha\beta} = \rho\,g\,P_{\alpha\beta}\begin{cases} H^2\,, & h \geq h_b \\ \gamma^2\,h_o^2\,, & h \leq h_b \end{cases} \tag{5.3}$$

where H is the wave height, which is calculated from conservation of energy flux outside the surf zone. We assume that the short waves break when the breaking index $\gamma = H/h_o = 0.75$ is exceeded. Assuming sine wave theory for the short waves, the shape factor $P_{\alpha\beta}$ in (5.3) is defined as

$$P_{\alpha\beta} = \frac{1}{16}\left[(1 + \frac{2\,k\,h_o}{\sinh\,2\,k\,h_o})\frac{k_\alpha\,k_\beta}{k^2} + \frac{2\,k\,h_o}{\sinh\,2\,k\,h_o}\,\delta_{\alpha\beta}\right] \tag{5.4}$$

where k_α and k_β are the wave numbers of the mean short wave in the horizonal $_\alpha$ and $_\beta$ directions and $\delta_{\alpha\beta}$ is the Kronecker delta.

The eddy viscosity is assumed to be constant over depth, but is varying in the cross-shore direction as

$$\nu_t = \begin{cases} 0.01\,h_o\,\sqrt{g\,h_o}\,, & h_o \leq h_b \\ \\ \left(0.8\left(\frac{h_o}{h_b}\right)^{-4} + 0.2\right)\,\nu_{tb}, & h_o \geq h_b \end{cases} \tag{5.5}$$

where $\nu_{tb} = 0.01\,h_b\,\sqrt{g\,h_b}$ and h_b is the breaking depth. The variation of the eddy viscosity inside the surf zone was found by Svendsen *et al.* (1987) and Okayasu *et al.* (1988). The variation outside the surf zone was first used by Svendsen & Putrevu (1994a) and was based on the only available measurements of the turbulent kinetic energy by Nadaoka & Kondoh (1982). The shortwave-induced volume flux is assumed as (Svendsen, 1984b)

$$Q_{w\alpha} = \frac{1}{8}\sqrt{g\,h_o}\,h_o\,\left(\frac{H}{h_o}\right)^2\begin{Bmatrix} \cos\,\theta \\ \sin\,\theta \end{Bmatrix} \tag{5.6}$$

The bottom friction is modeled using a weak-current assumption (Liu & Dalrymple, 1978) where the cross-shore current is assumed to be nearly parallel and the longshore current is nearly perpendicular to the direction of the short-wave groups so that

$$\tau_x^b = \frac{2}{\pi}\rho\, f_{cw}\, u_o\, \tilde{U}_b$$
$$\tau_y^b = \frac{1}{\pi}\rho\, f_{cw}\, u_o\, \tilde{V}_b \tag{5.7}$$

In these expresssions the friction coefficient is chosen as $f_{cw} = 0.02$, u_o is the short-wave velocity amplitude and $\tilde{V}_{b\beta}$ is the long-wave velocity at the bottom.

At the offshore boundary (at $x = 0$) we will impose the absorbing-generating boundary condition developed in Chapter 3.2. At the landward side we impose the shoreline boundary condition developed in Chapter 3.3, while at the lateral boundaries we will use a periodicity condition.

The quasi 3-D "D," "M," "A" and "B" coefficients in the momentum equations (2.71)/(5.2) are calculated from the expressions (2.81), (2.82), (2.83) and (2.84). These expressions were derived using the steady-state solution of the local, shortwave-averaged momentum equation (the "profile equation") (2.47), repeated here,

$$\frac{\partial V_{1\beta}^{(0)}}{\partial t} - \frac{\partial}{\partial z}\left(\nu_t \frac{\partial V_{1\beta}^{(0)}}{\partial z}\right) = -\beta_\beta + \frac{1}{\rho\, h}\frac{\partial}{\partial x_\alpha}\left(S_{\alpha\beta} - \overline{\int_{-h_o}^{\zeta} \tau_{\alpha\beta}\, dz}\right) - \frac{\tau_\beta^S - \tau_\beta^B}{\rho\, h} \tag{5.8}$$

which, using the boundary conditions (2.49) and (2.50) yielded (2.54). Defining the vertical coordinate from the bottom up, we can rewrite (2.54) as (2.75), which is repeated here,

$$V_{1\beta}^{(0)} = \frac{f_\beta}{2\,\nu_t}\xi^2 + \frac{\tau_\beta^B}{\rho\,\nu_t}\xi - \left(\frac{f_\beta}{6\,\nu_t}h^2 + \frac{\tau_\beta^B}{\rho\,\nu_t}\frac{h}{2} + \frac{Q_{w\beta}}{h}\right) \tag{5.9}$$

The parameters used in this example are offshore depth $h_s = 3\,m$, beach slope $h_x = 1/20$, angle of incidence of the monochromatic wave $\theta_s = 22.4^o$ and wave height $H_s = 0.61\,m$ at the offshore shelf. With these parameters the fixed breakpoint is located at $h = 0.9\,m$. The numerical parameters are $\Delta x = 1\,m$ and $C_r = 0.7$.

We can define the surf zone width L_b as the relevant length scale. For the present parameters we have $L_b = \frac{h_b}{h_x} = 18\,m$. The time interval T in which a long wave propagates from the breakpoint to the shore and back can be considered the relevant time scale. For the present parameters we have

$$T = \frac{L_b}{\sqrt{g\,h_b}} = 6.05\,s \tag{5.10}$$

Fig. 5.1 shows the surface elevation versus normalized time for a number of locations both inside and outside the surf zone. We see that the impulsive application of the short-wave forcing at $t = 0$ initiates a surge in the mean surface elevation. After reflection from the beach, it propagates seawards and is absorbed by the ocean-side boundary condition. The steady state in the set-up is reached in about $15\,T$.

On the other hand, it is found that the longshore current velocity (normalized by the long-wave celerity at the breakpoint $\sqrt{g\,h_b}$) in Fig. 5.2 (solid lines) does not attain steady state until about $50\,T$, which indicates a difference in time scales of cross-shore and longshore motion. In fact, the steady state is only approached asymptotically as the net forcing of bottom friction, the radiation stress and the dispersive mixing decreases to zero. This difference in time scales is due to the fact that the wave groups refract to near-normal incidence, which means that the forcing in the cross-shore direction is much larger than the forcing in the longshore direction.

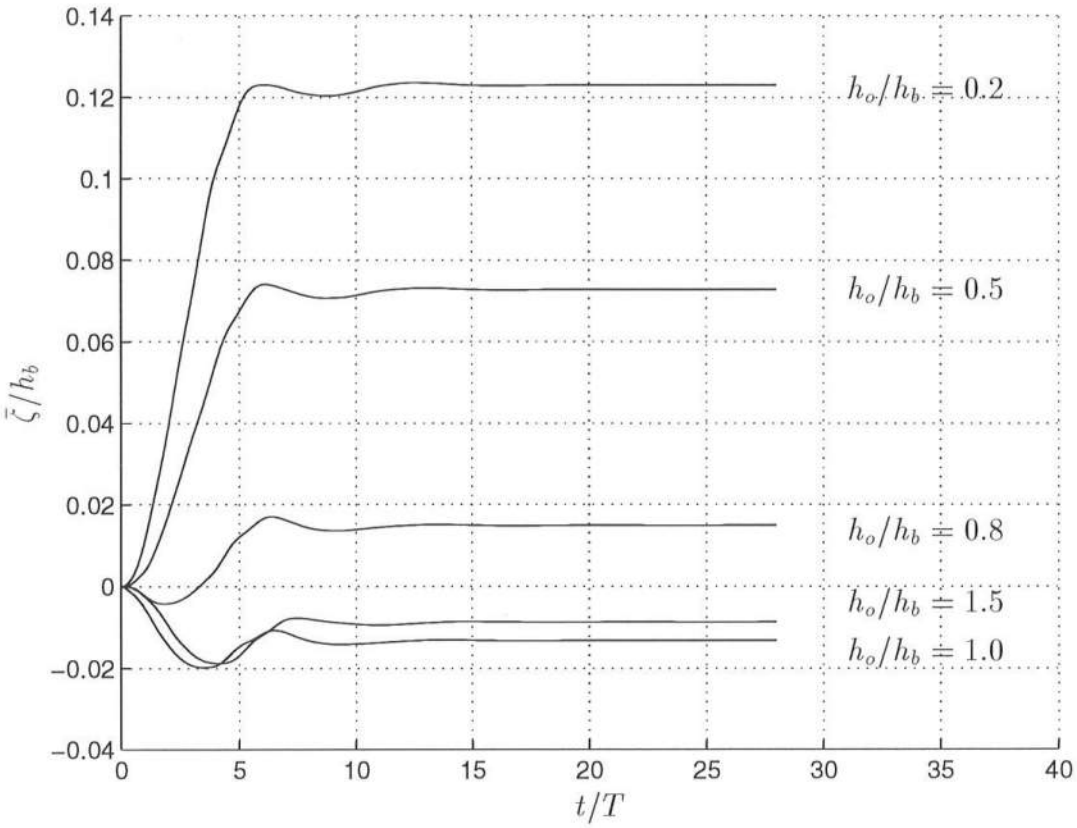

Figure 5.1: Normalized surface elevation versus normalized time for cross-shore positions indicated in the Figure.

The figure shows that the cross-shore profile of the longshore current is initially triangular (as would be predicted by Longuet-Higgins (1970) for the case of no lateral mixing mechanism). The turbulent and dispersive mixing cause a spreading of momentum (i.e., longshore current velocity) away from the break-point, which quickly modifies the triangular shape into a more curved longshore current profile. However, the momentum spreads relatively slowly, particularly outside the surf zone. Notice that the shoreline boundary condition allows for a run-up above the still water line.

Also indicated in Fig. 5.2 (dashed lines), are the horizontal longshore

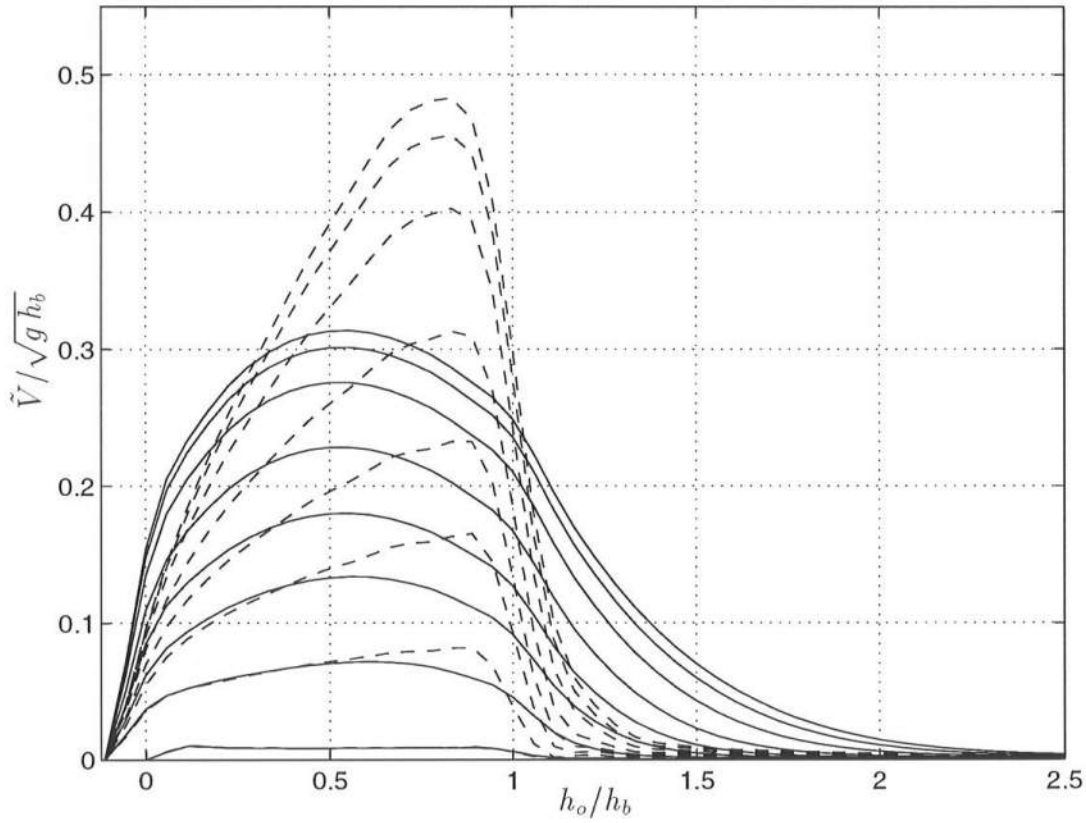

Figure 5.2: Normalized longshore current velocities versus normalized depth *with* quasi 3-D terms (——) and *without* quasi 3-D terms (– –) at $t = 0, 2, 6, 10, 14, 20, 30, 40$ and $48\,T$.

current profiles at the same time-instances for the case where the quasi 3-D mixing is artificially neglected in (5.2). We see that the profile is essentially triangular and is only slightly modified by the turbulent mixing effect, which diffuses a relatively small amount of momentum seawards of the breakpoint. In the absence of a large mixing effect, the radiation shear stress gradient is balanced by the bottom friction only, which results in a much stronger longshore current than in the case which included the quasi 3-D mixing.

Returning to the case with quasi 3-D mixing, we see that, as the cross-shore

balance is approached, the total cross-shore velocity $\frac{\bar{Q}_x}{h} = \tilde{U} \rightarrow 0$. Because of this, and because of the longshore uniformity (which implies $\frac{\partial}{\partial y} = 0$), the y momentum equation (2.71) reduces to

$$\frac{\partial \bar{Q}_y}{\partial t} + \frac{\partial}{\partial x}\left(\frac{\bar{Q}_x \bar{Q}_y}{h} + M_{xy}\right) - \frac{\partial}{\partial x}\left(h\left(D_{xx} + \nu_t\right)\frac{\partial \tilde{V}}{\partial x}\right)$$

$$+ \frac{\partial}{\partial x}\left(A_{xyy}\,\tilde{V}\right) + \frac{1}{\rho}\frac{\partial S_{xy}}{\partial x} + \frac{\tau_y^B}{\rho} = 0 \tag{5.11}$$

Of the quasi 3-D terms in this equation, the dispersive mixing term

$$D_{xx}\frac{\partial \tilde{V}}{\partial x}$$

is the most important, as will be shown in the next section. Recall that according to (2.81)

$$D_{xx} \equiv \frac{1}{h}\int_{-h_o}^{\bar{\zeta}} U_1^{(0)} \int_z^{\bar{\zeta}} \frac{1}{\nu_t} \int_{-h_o}^{z} U_1^{(0)}\,(dz)^3 \tag{5.12}$$

This term is essentially the same as the D_c term defined by Svendsen & Putrevu (1994a). (For a reduction of the governing equations to the case of a longshore uniform steady state, see Chapter 2.3.2.) Hence in this case we can essentially determine the dispersive mixing from the cross-shore circulation only.

For completeness it is mentioned that the computations were performed with a very short coast to ensure that no instabilities in the form of shear waves developed.

5.1.1 Three-dimensional Current Profiles

As was described in Chapter 2 (and in the previous section), the calculation of the nonlinear integrals in the depth-integrated momentum equations (2.71) requires that the current profiles are determined. The slow development in the

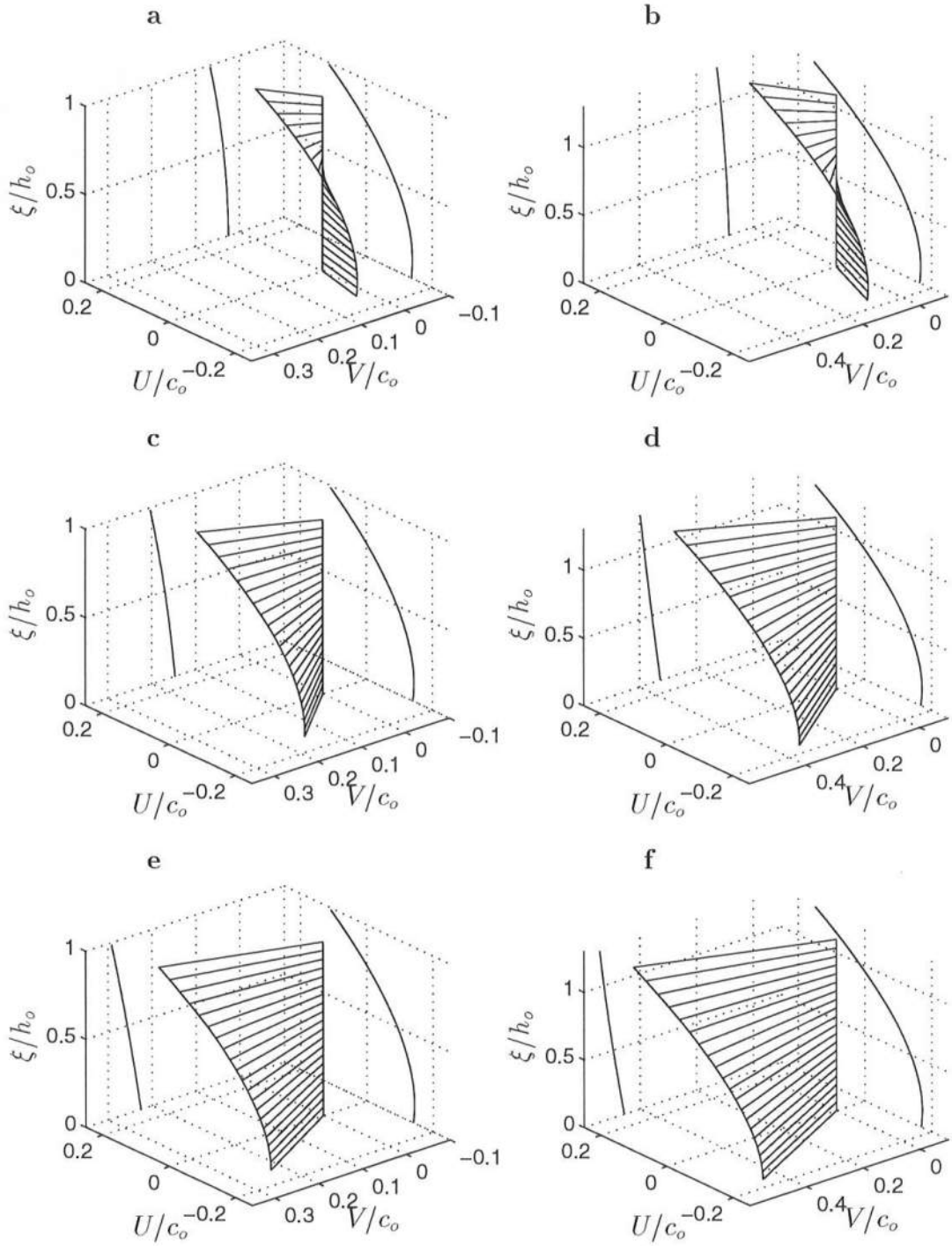

Figure 5.3: Three-dimensional current profile evolution at the breakpoint ($\frac{h_o}{h_b} = 1$): (a) at $t = 6\,T$. (c) at $t = 20\,T$. (e) at $t = 48\,T$. Three-dimensional current profile well inside the surf zone ($\frac{h_o}{h_b} = 0.35$): (b) at $t = 6\,T$. (d) at $t = 20\,T$. (f) at $t = 48\,T$.

flow implies that the vertical velocity profiles can be considered a quasi-steady response to the instantaneous forcing. Thus, we can solve the vertical profile equations (2.47) for the quasi-steady state, which yields the equations for the vertical profiles of the current (2.75), which were repeated as (5.9). This also give us an opportunity to trace the development in the three-dimensional current profiles in the process of starting up a longshore current.

Figs. 5.3 (a), (c), and (e) (the left-hand column) show three snapshots of the 3-D current spiral at the breakpoint ($h_o/h_b = 1$) at three time instances $t = 6, 20, 48\,T$. Figs. 5.3 (b), (d), and (f) (the right-hand column) show the current spirals at the same times for a position in the surf zone ($h_o/h_b = 0.35$). The cross-shore and longshore current profiles are also shown as projections in the figures. The current velocities, U and V, are normalized by the local wave celerity at still water $c_o = \sqrt{g\,h_o}$. The vertical position above the bed, ξ, is normalized by the still water level h_o.

The figures show that just as the overall cross-shore momentum balance is established relatively quickly, the cross-shore current profile (the "undertow") is also quickly established and thereafter remains fairly constant. The longshore current, on the other hand, grows slowly in time, as was shown in Fig. 5.2. The combined development of the two components results in a gentle turning of the current spiral.

The consequence is that the different time scales for the cross-shore and longshore motion cause the velocity spirals to change quite significantly during the start-up of the longshore current. With time-varying forcing from random waves, the variation will probably be less dramatic. However, the results for the 2DH case with weak wave groups analyzed by Svendsen and Putrevu (1994b) suggest that the vertical currents profiles can vary significantly.

It is important to emphasize that the depth-variation of the currents is critical to the existence of dispersive mixing. If the longshore current were assumed to be depth-uniform, the dispersive mixing coefficient D_{xx} would be zero identically. This can be seen directly from the derivations in Chapter 2.3. If we consider the y momentum equation (so that the subscript $_\beta = {}_y$) and assume that the longshore current V is depth-uniform, which means that in (2.28) we have

$$V \equiv \tilde{V} \quad \text{and} \quad V_1 \equiv 0 \tag{5.13}$$

The depth-dependent integrals in (2.59) in this case reduce to

$$\begin{aligned} I &= \int_{-h_o}^{\bar{\zeta}} V_{1\alpha}\, V_1\, dz + \overline{\int_{\zeta_t}^{\zeta} u_{w\alpha} V_1 + v_w V_{1\alpha}\, dz} \\ &= \overline{\int_{\zeta_t}^{\zeta} v_w V_{1\alpha}\, dz} \approx V_{1\alpha}(\bar{\zeta}) \overline{\int_{\zeta_t}^{\zeta} v_w\, dz} = V_{1\alpha}(\bar{\zeta})\, Q_{w,y} \end{aligned} \tag{5.14}$$

The nonlinear integrals now only contribute to the $M_{\alpha y}$ term in the y momentum equation, as can be seen following the derivation in Chapter 2.3. The more important D_{xx} term is lost completely.

5.1.2 Relative Magnitude of Quasi 3-D Coefficients

It is important to realize that the quasi 3-D $D_{\alpha\beta}$, $M_{\alpha\beta}$, $A_{\alpha\beta\gamma}$ and $B_{\alpha\beta}$ coefficients do not necessarily become zero themselves in the steady state, but that the *terms* in which they appear become zero because the velocity $\tilde{V}_\alpha$ or its horizontal gradients become zero. It is useful to show the cross-shore variation of the size of these coefficients, even though their net contribution may be small, because this will enable us to contrast the magnitudes found in this analysis to the magnitudes that will be calculated in the next section for time-varying motion. We will also compare the magnitudes in this analysis to an approximate value that can be obtained under a simplifying assumption, as will described below.

The quasi 3-D coefficients were defined in (2.63), (2.69) and (2.70) and are repeated here for convenience.

$$A_{\alpha\beta\gamma} \equiv -\int_{-h_o}^{\bar{\zeta}} V_{1\alpha}^{(0)} \int_z^{\bar{\zeta}} \frac{1}{\nu_t} \left(\frac{\partial}{\partial x_\gamma} \int_{-h_o}^{z} V_{1\beta}^{(0)}\, dz - V_{1\beta}^{(0)} \frac{\partial h_o}{\partial x_\gamma} \right) (dz)^2$$

$$-\int_{-h_o}^{\bar{\zeta}} V_{1\beta}^{(0)} \int_z^{\bar{\zeta}} \frac{1}{\nu_t} \left(\frac{\partial}{\partial x_\gamma} \int_{-h_o}^{z} V_{1\alpha}^{(0)}\, dz - V_{1\alpha}^{(0)} \frac{\partial h_o}{\partial x_\gamma} \right) (dz)^2 \quad (5.15)$$

$$B_{\alpha\beta} \equiv \frac{1}{h} \int_{-h_o}^{\bar{\zeta}} V_{1\alpha}^{(0)} \int_z^{\bar{\zeta}} \frac{1}{\nu_t} \int_{-h_o}^{z} V_{1\beta}^{(0)}\, (dz)^3 - \frac{1}{h} \int_{-h_o}^{\bar{\zeta}} V_{1\alpha}^{(0)} \int_z^{\bar{\zeta}} \frac{1}{\nu_t} V_{1\beta}^{(0)}\, (h_o + z)\, (dz)^2$$

$$-\frac{1}{h} \int_{-h_o}^{\bar{\zeta}} V_{1\beta}^{(0)} \int_z^{\bar{\zeta}} \frac{1}{\nu_t} V_{1\alpha}^{(0)}\, (h_o + z)\, (dz)^2 \quad (5.16)$$

and

$$D_{\alpha\gamma} \equiv \frac{1}{h} \int_{-h_o}^{\bar{\zeta}} V_{1\alpha}^{(0)} \int_z^{\bar{\zeta}} \frac{1}{\nu_t} \int_{-h_o}^{z} V_{1\gamma}^{(0)}\, (dz)^3 \quad (5.17)$$

We will split the $M_{\alpha\beta}$ term in (2.66) into an integral term

$$C_{\alpha\beta} = \int_{-h_o}^{\bar{\zeta}} V_{1\alpha}^{(0)}\, V_{1\beta}^{(0)}\, dz \quad (5.18)$$

and a term for the surface contribution

$$E_{\alpha\beta} = V_{1\alpha}^{(0)}(\bar{\zeta})\, Q_{w\beta} + V_{1\beta}^{(0)}(\bar{\zeta})\, Q_{w\alpha} \quad (5.19)$$

so that

$$M_{\alpha\beta} = C_{\alpha\beta} + E_{\alpha\beta} \quad (5.20)$$

The value of these coefficients can be calculated from the expressions (2.81), (2.82), (2.83) and (2.84). These expressions were derived using the quasi-steady state solution of the local, shortwave-averaged momentum equation (2.47) (the "profile equation"). This yields the equations for the vertical profiles of the current (2.75), which were repeated as (5.9).

The cross-shore variation of the quasi 3-D coefficients will be shown in Figs. 5.4, 5.5 and 5.6 (solid lines). Also shown in these figures as the dashed lines are the magnitudes of these coefficients if we assume that the velocity profiles are depth-invariant below trough, as was done in Putrevu & Svendsen (1997) in their discussion, so that

$$V_{1\beta}^{(0)} = -\frac{Q_{w\beta}}{h} \tag{5.21}$$

This corresponds to a uniformly distributed return flow to compensate for the volume flux $Q_{w\beta}$, which is positive for the chosen angle of incidence of the short waves. Using this expression, we can approximate the quasi 3-D coefficients (5.15) - (5.19) as

$$A'_{\alpha\beta\gamma} = -\frac{h^3}{3\,\nu_t}\frac{\partial}{\partial x_\gamma}\left(\frac{Q_{w\alpha}\,Q_{w\beta}}{h^2}\right) \tag{5.22}$$

$$B'_{\alpha\beta\gamma} = 0 \tag{5.23}$$

$$D'_{\alpha\beta} = \frac{Q_{w\alpha}\,Q_{w\beta}}{3\,\nu_t} \tag{5.24}$$

$$C'_{\alpha\beta} = \frac{Q_{w\alpha}\,Q_{w\beta}}{h} \tag{5.25}$$

and

$$E'_{\alpha\beta} = -2\,\frac{Q_{w\alpha}\,Q_{w\beta}}{h} \tag{5.26}$$

In this approximation the quasi 3-D coefficients can be calculated from (2.81), (2.82), (2.83) and (2.84) if we set the coefficients

$$a_1 = b_1 = a_2 = b_2 = 0$$

The breakpoint is indicated by the vertical lines in the next figures.

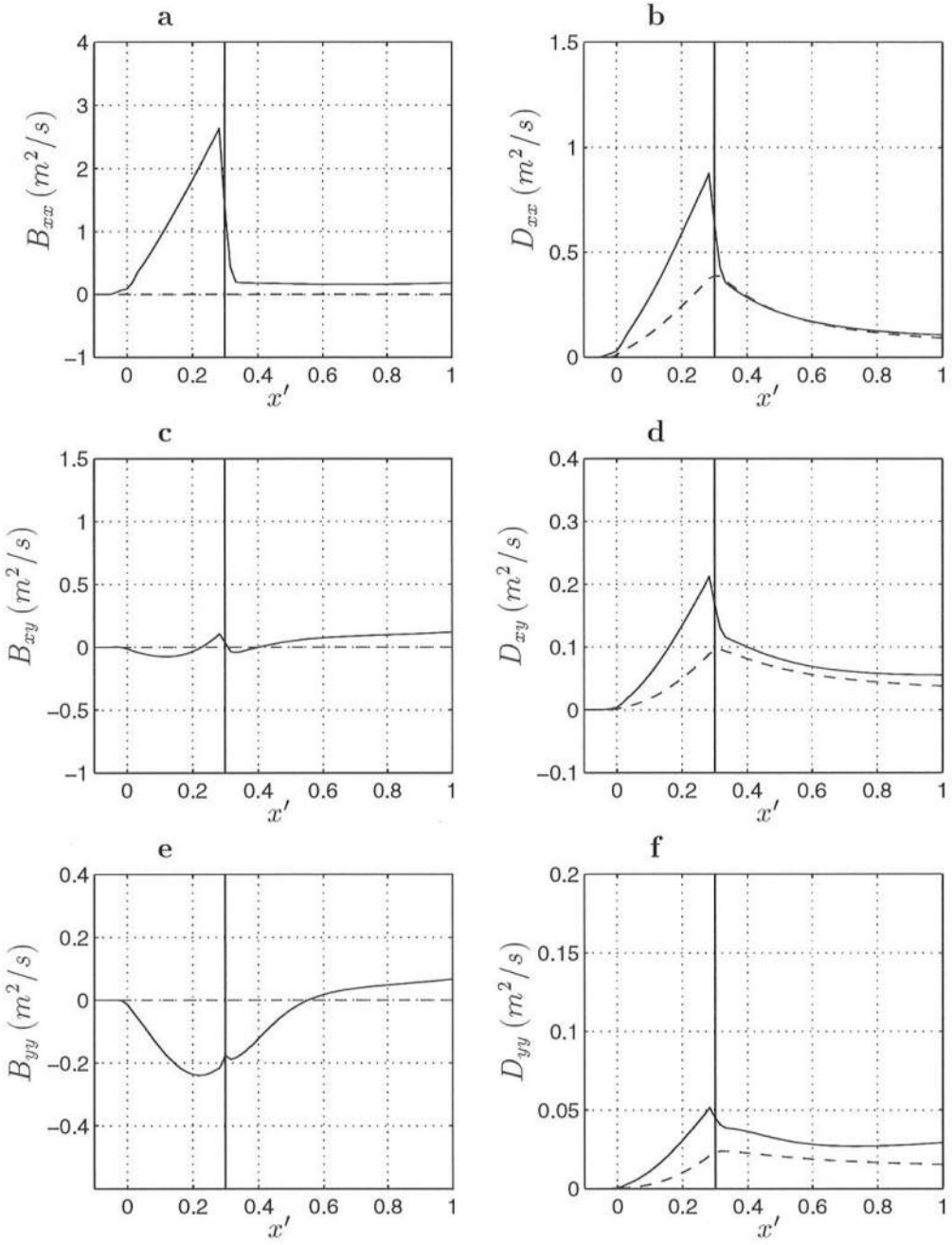

Figure 5.4: Magnitude of B and D coefficients vs. cross-shore distance x' at steady state: (a) B_{xx} (——) and B'_{xx} (– –). (b) D_{xx} (——) and D'_{xx} (– –). (c) B_{xy} (——) and B'_{xy} (– –). (d) D_{xy} (——) and D'_{xy} (– –). (e) B_{yy} (——) and B'_{yy} (– –). (f) D_{yy} (——) and D'_{yy} (– –).

Fig. 5.4 (a) shows the variation of B_{xx} calculated by (2.84) versus the cross-shore coordinate. Its value is fairly constant outside the surf zone and becomes much larger just shoreward of the breakpoint, which is due to the fact that the "undertow" profiles are much more curved in the surf zone. Because of the simple short-wave modeling, this transition in curvature occurs very rapidly, which will increase the cross-shore gradients in the quasi 3-D coefficients. Notice that the value of the quasi 3-D coefficients in these figures is not made dimensionless so that they can only be compared to each other. If we compare the magnitude of B_{xx} to D_{xx} in Fig. 5.4 (b) (solid line), we see that the former is much larger across the domain. This is a surprising result since B'_{xx}, the depth-invariant approximation of B_{xx}, is zero, see Fig. 5.4 (a) (dashed line). However, the contribution of B_{xx} to the momentum equation is relatively small since it is multiplied by $\frac{\partial \tilde{U}}{\partial x}$ and $\frac{\partial \tilde{V}}{\partial y}$, which *in this case* both become zero when the steady state in the cross-shore direction is reached.

The D_{xx} term in Fig. 5.4 (b) has a much larger contribution to the momentum equations since it is multiplied by $\frac{\partial \tilde{V}}{\partial x}$, which remains nonzero, as can be seen from (5.11). The depth-invariant approximation (dashed line) is virtually equal to the steady-state solution (2.81) outside the surf zone. This is due to the fact that the undertow profiles are nearly vertical because the local forcing is very small. Inside the surf zone, the value of D_{xx} in the depth-invariant approximation is about a factor two smaller than the solid line, because there the undertow profiles are in reality very much curved and the assumption of depth-invariant profiles is obviously violated. This is an important finding, which indicates that using the depth-invariant current profiles significantly underpredicts the magnitude of the dispersion coefficients.

Figs. 5.4 (c) and (e) show the variation of B_{xy} and B_{yy}, respectively, as

calculated by (2.84). Each of these coefficients is at least of the same order as the corresponding D_{xy} and D_{yy} term in Figs. 5.4(d) and (f), but will make a smaller contribution to the momentum equations because they are multiplied by smaller gradients in the velocities. Figs. 5.4(d) and (f) (dashed lines) also show the approximate values when the depth-invariant velocity profiles are used. We see that this would underpredict the actual value across the domain because in this approximation the tilt that the longshore currents exhibit (as was shown in the previous section) is neglected.

Figs. 5.5(a), (c) and (e) show the magnitude of the $C_{\alpha\beta}$ coefficients, as defined in (5.18), versus the cross-shore coordinate. It can be seen that the magnitude of these coefficients is significantly underpredicted if the curvature of the current profiles is neglected, especially in the surf zone. The approximation is much better outside the surf zone where the cross-shore velocity profile is almost depth-invariant.

Figs. 5.5(b), (d) and (f) show the $E_{\alpha\beta}$ coefficients, which were defined in (5.19) and represent the surface velocity contributions to the $M_{\alpha\beta}$ term. Again, the magnitude of the coefficients is underpredicted if the depth-variation of the currents is not taken into account. Inside the surf zone, even the sign of the coefficients is predicted incorrectly. This is due to the fact that (5.21) will predict negative velocities at the surface under the assumption of depth-invariant currents, because they are assumed to balance the positive wave-induced volume flux. However, the velocities at the surface are really positive, as was seen in Fig. 5.3, so that the $E_{\alpha\beta}$ coefficients are also positive in the surf zone.

Finally, the magnitude of the $A_{\alpha\beta\gamma}$ is shown in Fig. 5.6. As was seen in the previous figures, the assumption of depth-invariant currents below trough (dashed lines) causes an underprediction of the magnitude of the $A_{\alpha\beta x}$ coefficients

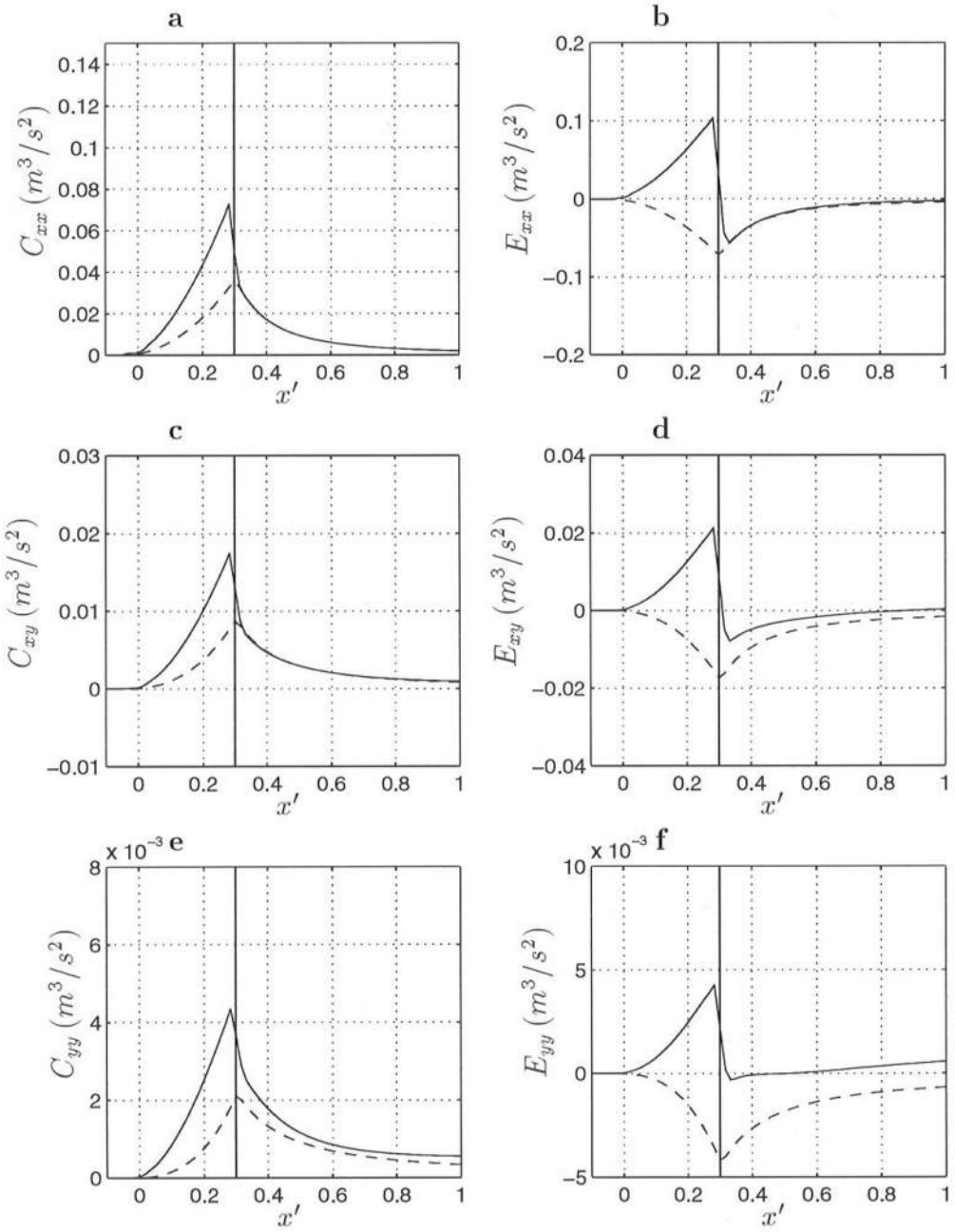

Figure 5.5: Magnitude of C and E coefficients vs. cross-shore distance x' at steady state: (a) C_{xx} (——) and C'_{xx} (– –). (b) E_{xx} (——) and E'_{xx} (– –). (c) C_{xy} (——) and C'_{xy} (– –). (d) E_{xy} (——) and E'_{xy} (– –). (e) C_{yy} (——) and C'_{yy} (– –). (f) E_{yy} (——) and E'_{yy} (– –).

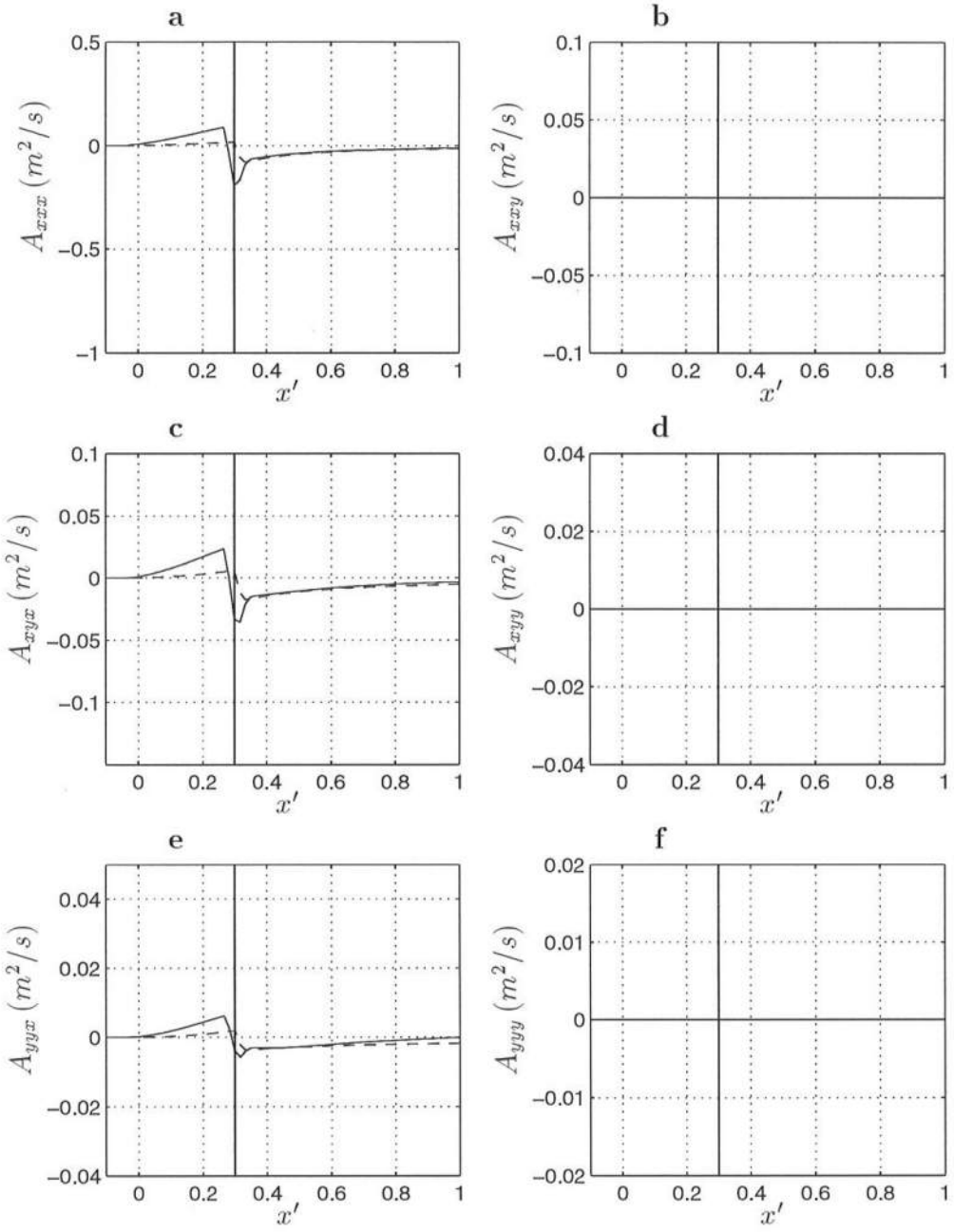

Figure 5.6: Magnitude of A coefficients vs. cross-shore distance x' at steady state: (a) A_{xxx} (——) and A'_{xxx} (– –). (b) A_{xxy} (——) and A'_{xxy} (– –). (c) A_{xyx} (——) and A'_{xyx} (– –). (d) A_{xyy} (——) and A'_{xyy} (– –). (e) A_{yyx} (——) and A'_{yyx} (– –). (f) A_{yyy} (——) and A'_{yyy} (– –).

that would be calculated by (2.83) (solid lines), see Figs. 5.6(a), (c) and (e). Figs. 5.6(b), (d) and (f) show that the $A_{\alpha\beta y}$ coefficients are identically zero because the third index in A represents derivatives in the longshore uniform y direction, as can be seen in (5.15).

Summarizing, we have found that the quasi 3-D coefficients are in general nonzero and exhibit a significant cross-shore variation. The contribution of these coefficients to the momentum equations may be small or zero due to the fact that they are multiplied by (gradients of) the depth-averaged velocities. We will refer back to Figs. 5.4-5.6 in the next section, where we will study infragravity waves forced by obliquely-incident wave groups.

5.2 Infragravity Waves Forced by Obliquely-incident Wave Groups

In this section the effect of the quasi 3-D terms on infragravity waves due to obliquely-incident wave groups is studied. These wave groups consist of two sinusoidal short waves that have a slightly different frequency but have the same direction of propagation. As these wave groups propagate towards shore at the group speed c_g, they refract towards the shore-normal direction. The incoming bound infragravity wave that propagates with the groups in the same direction will also refract in. As the wave groups shoal onto the beach and are destroyed, this incoming IG wave is modified by the wave group transformation and is released. It will then reflect off the shore and propagate and refract seawards as a free long wave, see Fig. 5.7 for a definition sketch. This process of infragravity wave generation is essentially the same as was described for normally-incident infragravity waves in Chapter 4, except for the effect of the nonzero angle of incidence.

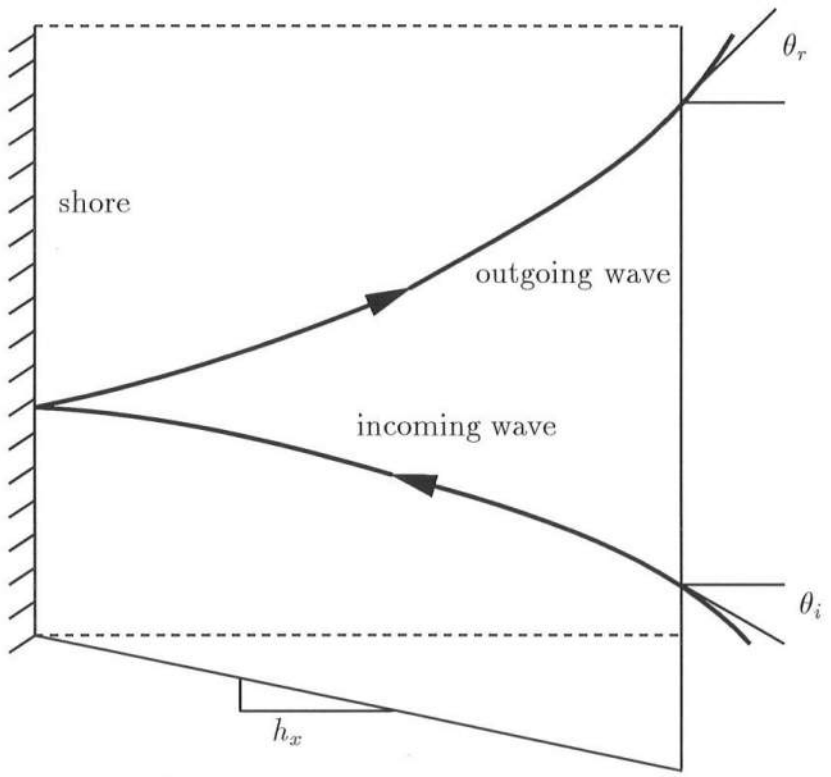

Figure 5.7: Definition sketch of obliquely-incident and obliquely-reflected infragravity waves.

This case will be more interesting to analyze than the previous one, because the hydrodynamical conditions are longshore periodic instead of longshore uniform, and therefore more terms in the momentum equations are expected to be non-zero.

First, we will compare the linearized model results to the linear, analytical solution of Schäffer (1994). Then, we will show the effect that the nonlinear terms corresponding to the 2-DH shallow water equations have on the solution. Next, we will include the quasi 3-D terms (sometimes called "dispersive mixing" terms), which arise from the non-uniformity over depth of the infragravity waves and were derived in Chapter 2. The infragravity wave profiles in the x and y direction are

shown. The relative importance of these terms is shown in the x and y momentum equations. This also means that recommendations can be made about which terms can be neglected for this case.

5.2.1 Comparison to the Linear Analytical Solution

As was done in Chapter 4, we will first linearize the governing equations in order to compare to the analytical solution of Schäffer (1994) for the time-varying motion on a plane beach. For reference, these equations of continuity and momentum read

$$\frac{\partial \bar{\zeta}}{\partial t} + \frac{\partial \bar{Q}_\alpha}{\partial x_\alpha} = 0 \tag{5.27}$$

$$\frac{\partial \bar{Q}_\beta}{\partial t} + g\, h_o \frac{\partial \bar{\zeta}}{\partial x_\beta} + \frac{1}{\rho}\frac{\partial S_{\alpha\beta}}{\partial x_\alpha} = 0 \tag{5.28}$$

The short-wave forcing is caused by a wave group consisting of two sinusoidal short waves that have a slightly different frequency but have the same direction of propagation. This is essentially the two-dimensional extension of the case described in Chapter 4. Given this short-wave forcing, the radiation stress $S_{\alpha\beta}$ can be written as (Schäffer, 1994)

$$S_{\alpha\beta} = \rho\, g\, P_{\alpha\beta} \begin{cases} H_1^2\,(1 + 2\delta\,\cos(2\,\vartheta))\,, & h \geq h_b \\ \\ \gamma^2\, h_o^2\,(1 + 2\delta\,(1-\kappa)\,\cos(2\,\vartheta))\,, & h \leq h_b \end{cases} \tag{5.29}$$

where the wave height modulation $\delta = H_2/H_1$ is the ratio of the wave heights of the secondary wave to the primary wave in the group. κ is the breaking parameter, as defined by Schäffer (1994) and in Chapter 4. The breaking criterion is $H_1 =$

$\gamma\, h_o$. The shapefactor $P_{\alpha\beta}$ was defined in (5.4). The phase function is defined following Schäffer (1994), his Eqs. (5) and (6), as

$$2\,\vartheta \;=\; \int_0^x K_x\, dx \;+\; K_y\, y \;-\; \Delta\omega\, t \tag{5.30}$$

The forcing frequency $\Delta\omega$ is the difference frequency between the frequencies ω_1 and ω_2 of the two short waves in the group

$$\Delta\omega \;\equiv\; \omega_1 \;-\; \omega_2 \;=\; 2\,\epsilon\,\omega \tag{5.31}$$

where ϵ is the frequency modulation between the two waves in the wave group and ω is the mean frequency of ω_1 and ω_2. These expressions are similar to the ones found for the case of normally-incident waves in Chapter 4. In (5.30) K_x and K_y are the x and y components of the wave number of the wave group, or in other words, they are the x and y components of the difference between the wave number components of the two short waves, $k_x^{(1)}$ and $k_x^{(2)}$. After some manipulation, this can be rewritten as

$$K_x \;\equiv\; k_x^{(1)} \;-\; k_x^{(2)} \;=\; 2\,\epsilon\,\frac{k}{\cos\theta_i}\left(\frac{1}{n} \;-\; \frac{\sin^2\theta_i}{n_s}\right) \tag{5.32}$$

where $n = c_g/c$ and θ_i is the angle of incidence of the short waves with respect to the normal and the subscript $_s$ denotes conditions on the shelf. This equation is similar to Schäffer (1994)'s Eq. (7). We also have

$$K_y \;\equiv\; k_y^{(1)} \;-\; k_y^{(2)} \;=\; 2\,\epsilon\,\frac{k\,\sin\theta_i}{n_s} \tag{5.33}$$

which is consistent with Schäffer (1994)'s Eq. (8). In the case of normally-incident short-wave groups, (5.29) reduces to (4.7).

On the shelf we will assume an incoming equilibrium bound long wave (Longuet-Higgins & Stewart, 1962) which propagates in the direction of the wave groups. The outgoing free wave will be absorbed using the absorbing-generating

boundary condition developed in Chapter 3.2. In the linearized version of the model, we impose a no-flux condition at the still water shoreline. At the lateral boundaries we impose periodicity. The alongshore domain length is put equal to the alongshore projection of the infragravity wave length.

It is important to note here that the incoming short-wave group and therefore the incoming bound long wave propagate in the same direction with the group speed c_g. The outgoing long wave, however, does not propagate with the group speed but with the shallow water speed $\sqrt{g\,h_o}$. These different celerities turn out to have a profound effect on the refraction of these waves. According to Snell's Law, the alongshore wave number K_y in (5.33) is conserved as the short-wave groups refract towards shore. The alongshore wave number $K_{y,r}$ of the outgoing long wave

$$K_{y,r} = \frac{\Delta\omega}{\sqrt{g\,h_o}} \sin\theta_r \tag{5.34}$$

is also conserved as it refracts out to sea. In fact, since the long waves are fully reflected at the shoreline, the alongshore wave number of the incoming wave must equal the alongshore wave number of the outgoing wave, so that from (5.33) and (5.34) we have

$$2\,\epsilon\,\frac{k\,\sin\theta_i}{n_s} = \frac{\Delta\omega}{\sqrt{g\,h_o}} \sin\theta_r \tag{5.35}$$

where θ_i and θ_r are the angles of the incoming and outgoing waves, respectively. Using (5.31) we can rewrite this equation as

$$\frac{\sin\theta_i}{\sin\theta_r} = \frac{\omega\,n_s}{k\,\sqrt{g\,h_o}} = \frac{c_g}{\sqrt{g\,h_o}}\,\frac{n_s}{n} \tag{5.36}$$

or

$$\theta_r = \sin^{-1}\left(\sin\theta_i\,\frac{\sqrt{g\,h_o}}{c_g}\,\frac{n}{n_s}\right) \tag{5.37}$$

where c_g denotes the group speed. From this we can deduce that for a given shelf depth and short-wave group parameters, it is possible that the angle of the outgoing wave may become 90^o well before it reaches the shelf again. The depth at which this occurs is called the "caustic." At this caustic depth we have

$$\sin\theta_{i,c}\,\frac{\sqrt{g\,h_{o,c}}}{c_{g,c}}\,\frac{n_c}{n_s} \;=\; 1 \tag{5.38}$$

where the caustic depth is denoted by the subscript $_c$. The maximum angle of incidence on the shelf for which the caustic will *not* occur on the slope (i.e., where the caustic depth equals the shelf depth) is then given by

$$\theta_{i,s}^{max} \;=\; \sin^{-1}\left(\frac{c_{g,s}}{\sqrt{g\,h_s}}\right) \tag{5.39}$$

If the caustic does occur on the slope, the outgoing wave will be "trapped" along the shore. In the following examples, however, we will limit the discussion to cases for which the input parameters are chosen such that there is no caustic on the slope, which means that the outgoing waves propagate out to the shelf. These waves are called "leaky."

The input parameters for the following case are: shelf depth $h_s = 3\,m$ and mean short-wave frequency $\omega = 1.8s^{-1}$, so that $k_s\,h_s = 1.192$. The wave height of the primary short wave on the shelf $H_{1,s} = 0.6\,m$ and the wave height modulation $\delta = 0.1$. The frequency modulation is chosen as $\epsilon = 0.1$. The breaking index is $\gamma = 0.75$ with a fixed breakpoint $\kappa = 0$. The beach slope is chosen as $h_x = 1/20$. Finally, the angle of incidence on the shelf is chosen as $\theta_{i,s} = 22.37^o$, which is less than the limiting angle of incidence $\theta_{i,s}^{max} = 37.07^o$, according to (5.39), so that the infragravity wave is "leaky."

These parameters imply that the forcing frequency $\Delta\omega = 2\,\epsilon\,\omega = 0.36\,s^{-1}$ and that the short waves will break at $h_b = 0.9\,m$ or $\frac{h_b}{h_s} = 0.3$. The angle of

the outgoing wave on the shelf is $\theta_{r,s} = 38.4^o$. The numerical parameters are $\Delta x = \Delta y = 1\,m$ and the Courant number $\nu = 0.7$.

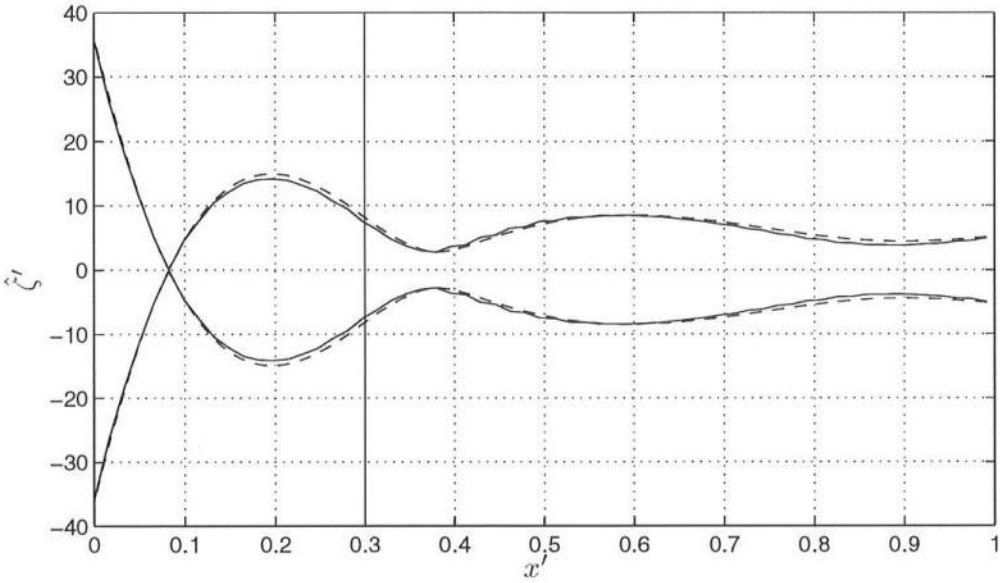

Figure 5.8: Envelope of the total long-wave motion vs. depth : present model (——) and analytical solution (– –).

Fig. 5.8 shows the comparison of the envelope of the total long-wave motion where the solid line indicates the present model and the dashed line indicates the analytical solution by Schäffer (1994). The agreement is very good, which gives us confidence in the accuracy of our model. The envelope represents the maximum surface elevation, which itself is periodic both in time and in the alongshore coordinate y. As in Chapter 4, the surface elevation is normalized by $\delta a_1^2/h_s$ and the shore normal coordinate is made dimensionless by h_x/h_s, so that $x' = 0$ corresponds to the still water shoreline and $x' = 1$ to the toe of the slope. The breakpoint is located at $x' = 0.3$ in this case.

5.2.2 Importance of Nonlinear 2D-H Terms

As a next step we will include in the model the nonlinear terms so that the governing equations correspond to the nonlinear shallow water equations with forcing, which for reference read

$$\frac{\partial \bar{\zeta}}{\partial t} + \frac{\partial \bar{Q}_\alpha}{\partial x_\alpha} = 0 \tag{5.40}$$

$$\frac{\partial \bar{Q}_\beta}{\partial t} + \frac{\partial}{\partial x_\alpha}\left(\frac{\bar{Q}_\alpha \bar{Q}_\beta}{h}\right) + g\,(h_o + \bar{\zeta})\frac{\partial \bar{\zeta}}{\partial x_\beta}$$

$$+\frac{1}{\rho}\frac{\partial}{\partial x_\alpha}\left(S_{\alpha\beta} - \overline{\int_{-h_o}^{\zeta} \tau_{\alpha\beta}\, dz}\right) + \frac{\tau_\beta^B}{\rho} = 0 \tag{5.41}$$

where we have now also included the turbulent stresses which are modeled with an eddy-viscosity closure as

$$\frac{1}{\rho}\overline{\int_{-h_o}^{\zeta} \tau_{\alpha\beta}\, dz} = \nu_t\, h\left(\frac{\partial \tilde{V}_\alpha}{\partial x_\beta} + \frac{\partial \tilde{V}_\beta}{\partial x_\alpha}\right) \tag{5.42}$$

We have included friction terms in (5.41) so that the longshore current forced by the steady radiation shear stress remains bounded. At the landward side of the domain we now impose the shoreline boundary condition of Chapter 3.3 in order to allow for run-up and run-down.

Fig. 5.9 shows the envelope of the surface elevation (i.e., steady set-up and the long-wave motion) for the nonlinear shallow water equations (5.40) and (5.41) (solid line). Comparing to the linear solution (which is a linear superposition of the steady set-up and the long-wave envelope in Fig. 5.8), we see that including the nonlinear terms shifts the nodes and anti-nodes of the envelopes and changes the amplitudes of the anti-nodes. As was seen in Chapter 4.3, it turns out that the most important contribution of the nonlinear terms is the change in the local water depth: in the nonlinear shallow water model, the long waves propagate in

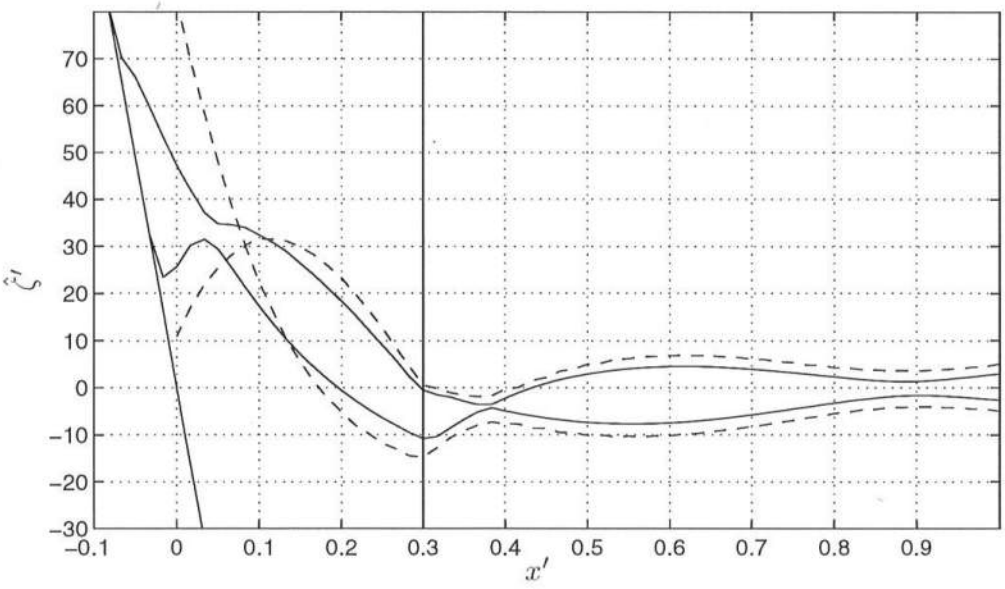

Figure 5.9: Envelope of the surface elevation vs. depth: present nonlinear model (——) and linear solution (– –).

the total water depth ($h = h_o + \bar{\zeta}$), whereas in the linear model they propagate in the still water depth only.

5.2.3 Importance of Quasi 3-D Terms

As was seen in Chapter 2, the depth-nonuniformity of the infragravity waves (or currents) result in additional terms in the governing equations. For reference, we will repeat the quasi 3-D momentum equations (2.71)

$$\frac{\partial \bar{Q}_\beta}{\partial t} + \frac{\partial}{\partial x_\alpha}\left(\tilde{V}_\alpha \tilde{V}_\beta\, h + M_{\alpha\beta}\right)$$

$$-\frac{\partial}{\partial x_\alpha}\left[h\left(D_{\beta\gamma}\frac{\partial \tilde{V}_\alpha}{\partial x_\gamma} + D_{\alpha\gamma}\frac{\partial \tilde{V}_\beta}{\partial x_\gamma} + B_{\alpha\beta}\frac{\partial \tilde{V}_\gamma}{\partial x_\gamma}\right)\right] + \frac{\partial}{\partial x_\alpha}\left[A_{\alpha\beta\gamma}\tilde{V}_\gamma\right]$$

$$= -g\,h\,\frac{\partial\bar{\zeta}}{\partial x_\beta} - \frac{1}{\rho}\frac{\partial}{\partial x_\alpha}\left(S_{\alpha\beta} - \overline{\int_{-h_o}^{\zeta} \tau_{\alpha\beta}\,dz}\right) + \frac{\tau_\beta^S - \tau_\beta^B}{\rho} \tag{5.43}$$

For emphasis it is mentioned again that the quasi 3-D $A_{\alpha\beta\gamma}$, $B_{\alpha\beta}$, $D_{\alpha\beta}$ and $M_{\alpha\beta}$ coefficients are calculated using the expressions (2.81), (2.82), (2.83) and (2.84). These expressions were derived using the quasi-steady state solution of the local, shortwave-averaged momentum equation (2.47) (the "profile equation"). This yields the equations for the vertical profiles of the current (2.75), which were repeated in the chapter as (5.9).

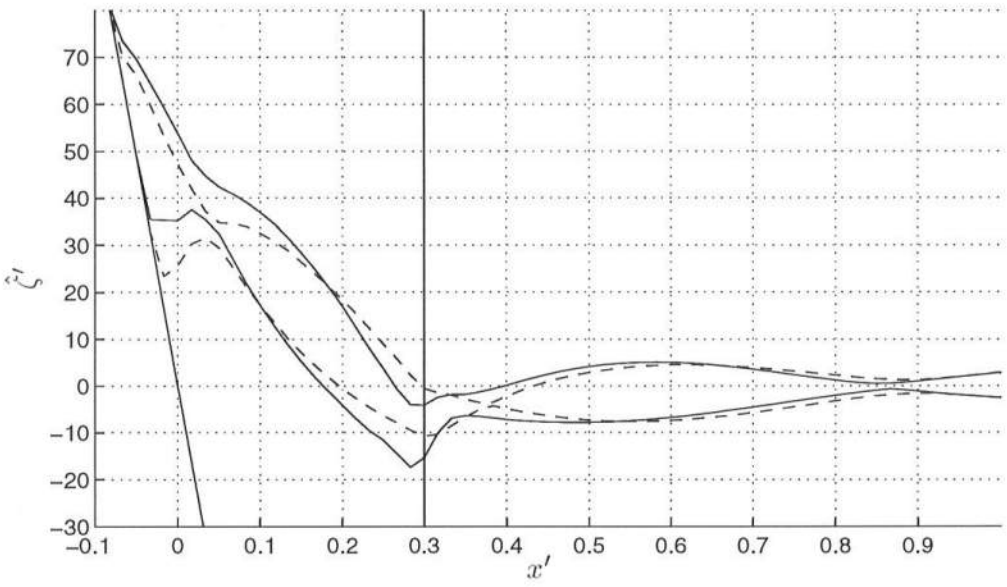

Figure 5.10: Envelope of the surface elevation vs. depth: quasi 3-D model (——); nonlinear shallow water model (– –).

The cross-shore envelope of the surface elevation using the quasi 3-D equations (2.8) and (2.71) is shown in Fig. 5.10 (solid line). Also shown is the envelope computed using the nonlinear shallow water equation (the solid line in Fig. 5.9, repeated here as the dashed line). We see that the quasi 3-D terms have a large effect on the envelope in the surf zone and in the area around the breakpoint, a

point which will be discussed in more detail below. The nodes of the envelope, however, do not seem to have shifted significantly relative to the 2-DH solution.

Fig. 5.11 shows a snapshot of the surface elevation at a particular time. For effect, we have shown three wave lengths in the longshore y direction.

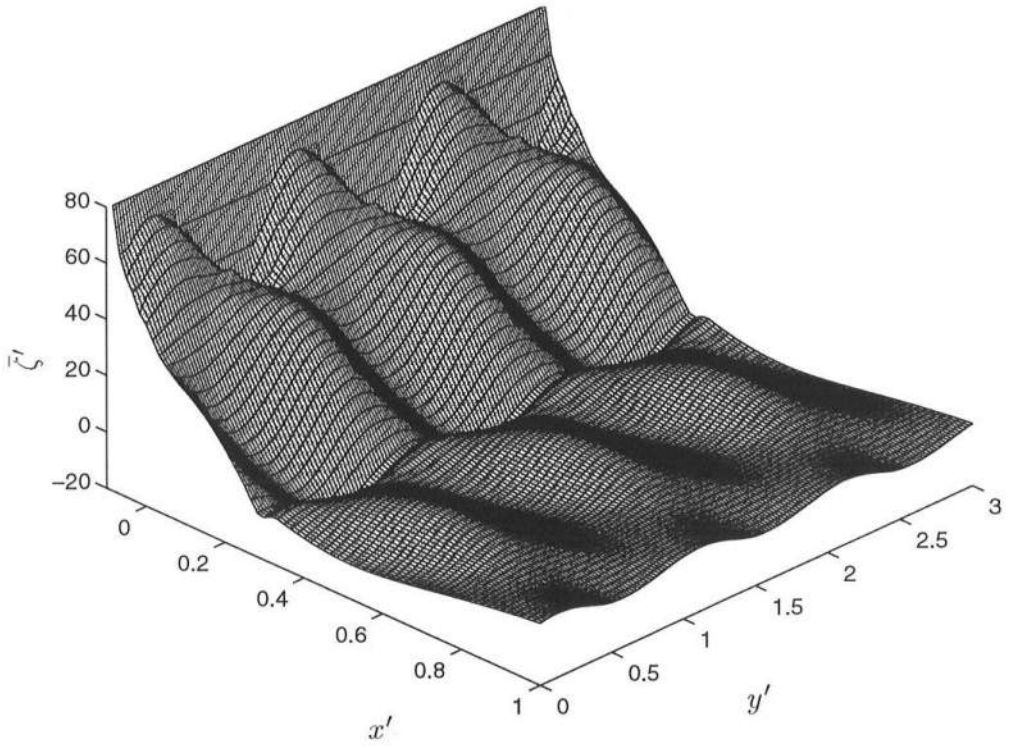

Figure 5.11: Snapshot of the surface elevation.

5.2.4 Three-dimensional Infragravity Wave Particle Velocity Profiles

In order to calculate the quasi 3-D terms in the momentum equations, we have to determine the vertical variation of the infragravity wave particle velocities by (2.75) (repeated in this chapter as (5.9)). This equation was derived under the assumption of quasi-steady state (see the discussion of this assumption in Chapter

2), which is obviously valid in the case of the slowly-developing longshore current in the previous section. In the case of time-varying infragravity waves, however, the quasi-steady state approximation might not be valid everywhere, especially in the region seaward of the break point. However, it is conjectured in Putrevu & Svendsen (1997) that the steady-state solution (2.75) is the first approximation to the complete solution of (2.47), so that the IG wave profiles computed by the present model are correct to leading order.

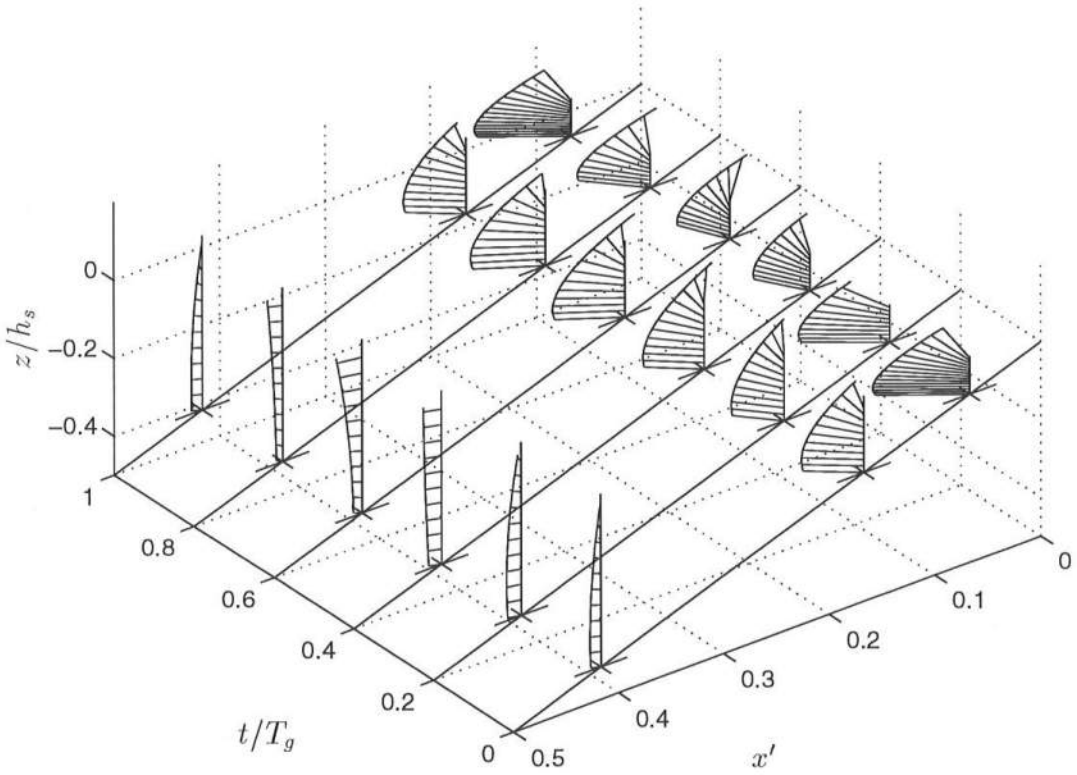

Figure 5.12: Infragravity wave profiles for three locations ($x' = 0.42$, 0.17 and 0.07) and for five time instances of the infragravity wave period. The breakpoint is located at $x' = 0.3$.

Fig. 5.12 shows the IG particle velocity profiles for three different locations ($x' = 0.42$, 0.17 and 0.07) and at five time intervals of the infragravity wave period.

The motion is a result of the forcing by the obliquely-incident wave groups, and of the incoming IG wave and the obliquely-reflected IG wave. Notice that the steady part of the short-wave forcing (5.29) drives a steady longshore current, and that the time-varying part of the forcing cause a variation of the velocity profiles over an IG period.

Since the breakpoint is located at $x' = 0.3$, the location $x' = 0.42$ is outside the surf zone. The IG wave velocity profiles at that location show a little bit of curvature in the cross-shore direction and essentially vary linearly with depth in the longshore direction. The two locations inside the surf zone show much more variation. The cross-shore velocity profiles vary significantly over one infragravity wave period, especially at $x' = 0.07$.

The details of the variation of the velocity profiles can better be seen in Fig. 5.13, which shows the projections of the profiles in the longshore and cross-shore direction. Fig. 5.13 (a) shows the cross-shore velocity (commonly called the "undertow") normalized by the local long-wave celerity c_o versus normalized depth at $x' = 0.42$, which is located well outside the surf zone, for ten intervals per infragravity wave period. It can be seen that the profiles are slightly curved due to the (time-varying) forcing f_x in (2.75). This term (defined in (2.48)) is a function of the radiation stress gradients and the gradients in the short-wave velocities. These gradients are larger in the time-varying case than in the time-steady case as can also be seen by taking the spatial derivatives of (5.29).

Qualitatively, the results are similar to calculations made by Smith & Svendsen (1995, 1996) for cross-shore time-varying infragravity wave profiles using an eigenfunction expansion. Similar to their results, the greatest velocity gradients occur near the surface and that the velocities near the surface and the bottom are in anti-phase. Unlike Smith & Svendsen (1995, 1996) we find that in

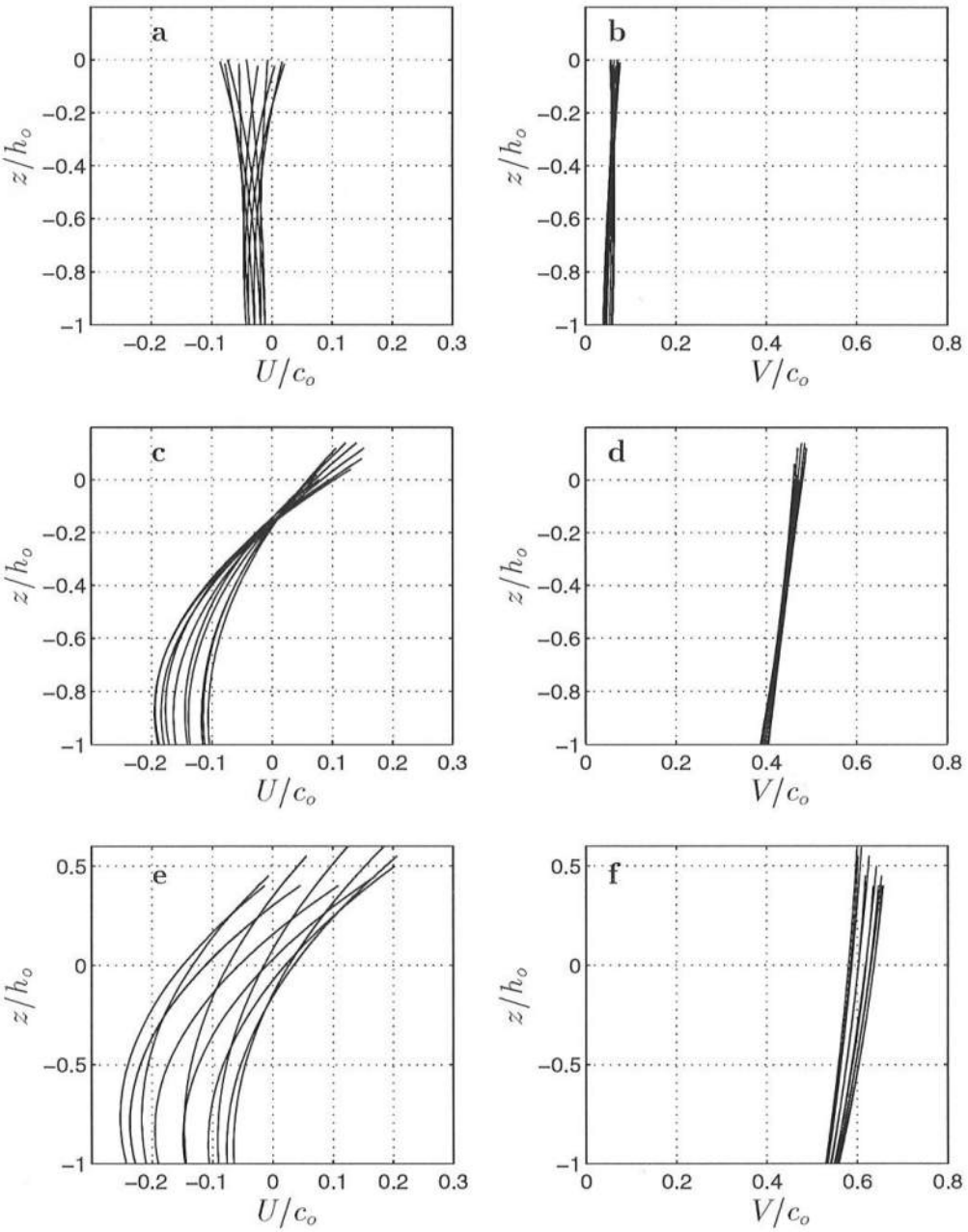

Figure 5.13: IG wave particle velocities in the cross-shore and longshore direction normalized by the longwave celerity c_o vs. normalized depth for ten intervals per IG wave period: (a) Cross-shore velocity U at $x' = 0.42$. (b) Longshore velocity V at $x' = 0.42$. (c) U at $x' = 0.17$. (d) V at $x' = 0.17$. (e) U at $x' = 0.07$. (f) V at $x' = 0.07$.

the present model the depth-mean of each of the profiles below the mean surface elevation is negative. This is to be expected since (2.50) was used as a boundary condition, which states that the wave-induced volume flux has to be balanced by a non-zero depth-mean current.

As was stated above, the assumption of quasi steady state is the least likely to be valid at larger depths (i.e., more seaward of the break point), since the eddy viscosity becomes smaller away from the breaking region, which is the primary source of turbulence. It is possible, therefore, that the omission of the acceleration term in (2.47) increases the curvature of the infragravity wave profiles.

Fig. 5.13 (b) shows the longshore velocity V at the same location. Due to the relatively small angle of incidence of the short-wave groups, the forcing induced by the short waves in the y direction is also small. This means that these profiles are fairly linear with only a slight curvature. The profiles exhibit a non-zero mean over depth due to the momentum that has advected out of the surf zone due to the dispersive mixing, as was also seen in the case of a steady longshore current in the previous section.

The cross-shore profiles in Figs. 5.13 (c) and (e) exhibit the typical characteristic undertow profile in the surf zone that were previously shown for the steady case by a number of authors (Svendsen, 1984b; Dally and Dean, 1984, 1986; De Vriend & Stive, 1987; Svendsen *et al.*, 1987; Svendsen & Hansen, 1988; Okayasu *et al.*, 1988; Roelvink & Stive, 1989 to mention but a few) and also in the previous section, and for the time-varying case by Putrevu & Svendsen (1995). The longshore profiles in Figs. 5.13 (d) and (f) are slightly more tilted than the longshore current profile in Fig. 5.13 (b) because inside the surf zone a strong mean forcing is present due to the difference between the radiation stress gradient and the pressure gradient. The time variation of the longshore profiles is not very

large due to the fact that the short-wave groups have refracted to near normal incidence inside the surf zone.

5.2.5 Relative Magnitude of Quasi 3-D Coefficients

In this section we will discuss the relative magnitude of the quasi 3-D coefficients for the case of leaky infragravity waves. The magnitude of the quasi 3-D coefficients is calculated directly from the model results under the assumption of quasi-steady state, as discussed in the previous section. The computed magnitude is compared to the approximation by Putrevu & Svendsen (1997) who assumed that the velocity profiles are depth-invariant below trough. The analysis in this section is similar to the one performed in Subsection 5.1.2 and we will refer back to the expressions and results found there.

For completeness, we will expand the momentum equations (2.71) in both horizontal coordinates. For this purpose we divide the $M_{\alpha\beta}$ term into a $C_{\alpha\beta}$ and an $E_{\alpha\beta}$ term as was done in (5.20). The x-momentum equation then becomes

$$\frac{\partial \bar{Q}_x}{\partial t} + \frac{\partial}{\partial x}\left(\frac{\bar{Q}_x^2}{h} + C_{xx} + E_{xx}\right) + \frac{\partial}{\partial y}\left(\frac{\bar{Q}_x \bar{Q}_y}{h} + C_{xy} + E_{xy}\right)$$

$$-\frac{\partial}{\partial x}\left[h\left((2\,D_{xx} + 2\,\nu_t + B_{xx})\frac{\partial \tilde{U}}{\partial x} + 2\,D_{xy}\frac{\partial \tilde{U}}{\partial y} + B_{xx}\frac{\partial \tilde{V}}{\partial y}\right)\right]$$

$$-\frac{\partial}{\partial y}\left[h\left((D_{xy} + B_{xy})\frac{\partial \tilde{U}}{\partial x} + (D_{yy} + \nu_t)\frac{\partial \tilde{U}}{\partial y}\right.\right.$$

$$\left.\left. + (D_{xx} + \nu_t)\frac{\partial \tilde{V}}{\partial x} + (D_{xy} + B_{xy})\frac{\partial \tilde{V}}{\partial y}\right)\right]$$

$$+\frac{\partial}{\partial x}\left[A_{xxx}\,\tilde{U} + A_{xxy}\,\tilde{V}\right] + \frac{\partial}{\partial y}\left[A_{xyx}\,\tilde{U} + A_{xyy}\,\tilde{V}\right]$$

$$= -g\,h\,\frac{\partial \bar{\zeta}}{\partial x} - \frac{1}{\rho}\left(\frac{\partial S_{xx}}{\partial x} + \frac{\partial S_{xy}}{\partial y}\right) - \frac{\tau_x^B}{\rho} \tag{5.44}$$

Similarly, for the y-momentum equation we get

$$\frac{\partial \bar{Q}_y}{\partial t} + \frac{\partial}{\partial x}\left(\frac{\bar{Q}_x\,\bar{Q}_y}{h} + C_{xy} + E_{xy}\right) + \frac{\partial}{\partial y}\left(\frac{\bar{Q}_y^2}{h} + C_{yy} + E_{yy}\right)$$

$$-\frac{\partial}{\partial x}\left[h\left((D_{xy} + B_{xy})\frac{\partial \tilde{U}}{\partial x} + (D_{yy} + \nu_t)\frac{\partial \tilde{U}}{\partial y}\right.\right.$$

$$\left.\left. + (D_{xx} + \nu_t)\frac{\partial \tilde{V}}{\partial x} + (D_{xy} + B_{xy})\frac{\partial \tilde{V}}{\partial y}\right)\right]$$

$$-\frac{\partial}{\partial y}\left[h\left(B_{yy}\frac{\partial \tilde{U}}{\partial x} + 2\,D_{xy}\frac{\partial \tilde{V}}{\partial x} + (2\,D_{yy} + 2\,\nu_t + B_{yy})\frac{\partial \tilde{V}}{\partial y}\right)\right]$$

$$+\frac{\partial}{\partial x}\left[A_{xyx}\,\tilde{U} + A_{xyy}\,\tilde{V}\right] + \frac{\partial}{\partial y}\left[A_{yyx}\,\tilde{U} + A_{yyy}\,\tilde{V}\right]$$

$$= -g\,h\,\frac{\partial \bar{\zeta}}{\partial y} - \frac{1}{\rho}\left(\frac{\partial S_{xy}}{\partial x} + \frac{\partial S_{yy}}{\partial y}\right) - \frac{\tau_y^B}{\rho} \tag{5.45}$$

where in these equations we have used the eddy-viscosity closure (5.42). The definitions of the $A_{\alpha\beta\gamma}$, $B_{\alpha\beta}$ and $D_{\alpha\beta}$ coefficients were given in (2.63), (2.69) and (2.70), and repeated in this chapter as (5.15), (5.16) and (5.17). Please note that these definitions are slightly different in appearance from, but completely equivalent to those given in Putrevu & Svendsen (1997). For consistency in our notation, we will use the above definitions.

As stated above, the quasi 3-D coefficients were calculated using the expressions (2.81), (2.82), (2.83) and (2.84) found in Chapter 2.4. These expressions are valid for the (quasi) steady state of the time averaged local momentum equations (2.47) and are expected to be the first approximations to the full solution.

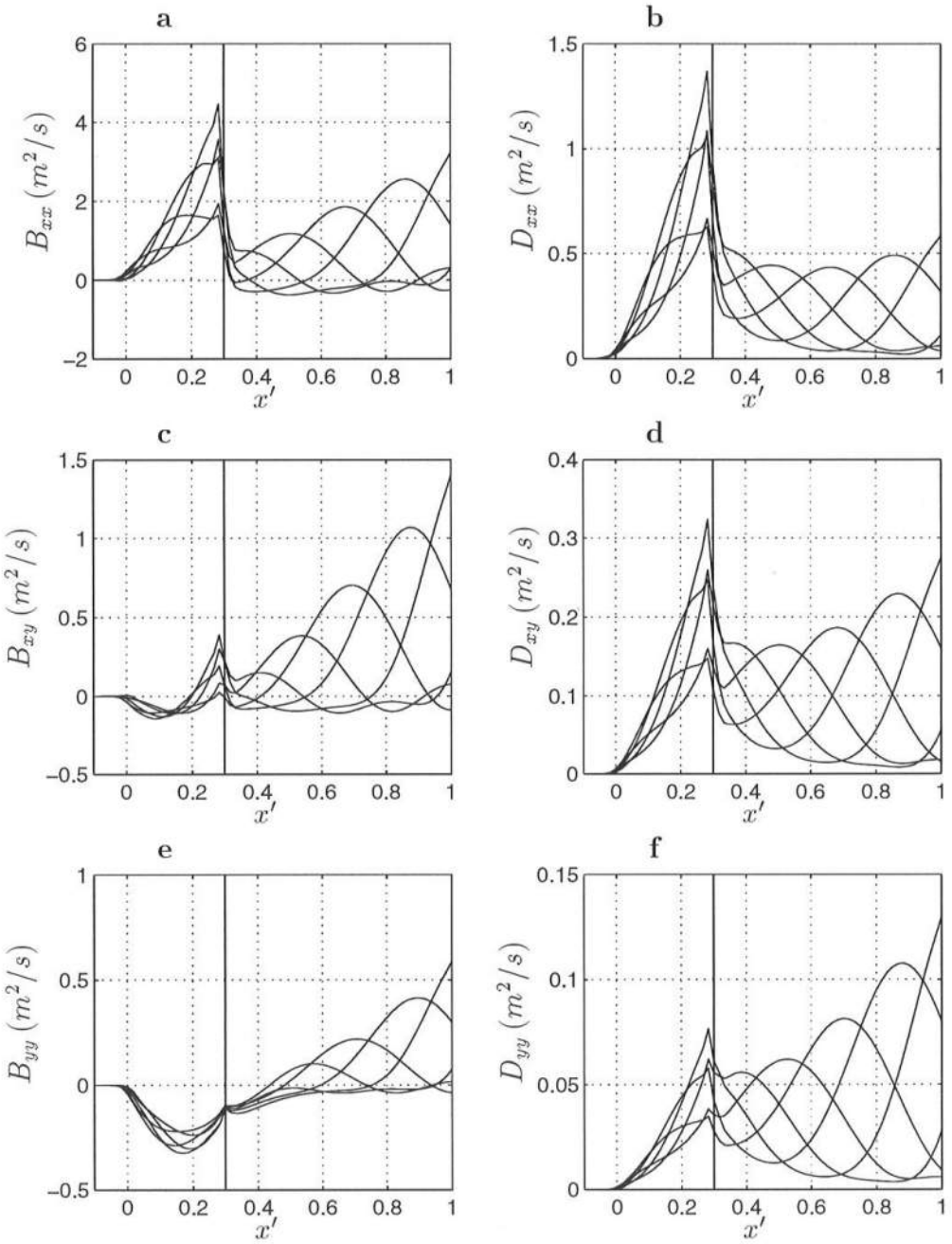

Figure 5.14: Magnitude of B and D coefficients vs. cross-shore distance x' for five intervals per IG wave period: (a) B_{xx}. (b) D_{xx}. (c) B_{xy}. (d) D_{xy}. (e) B_{yy}. (f) D_{yy}.

In Figs. 5.14, 5.16 and 5.19 the variation of the individual quasi 3-D coefficients in the cross-shore direction for five time intervals per infragravity wave period is shown. These figures give an indication of the relative magnitude of these coefficients to each other. However, they do not appear as isolated coefficients in the equations but rather appear in combination with the depth-invariant velocity or depth-invariant velocity gradients. Therefore, the individual terms in the equations will be studied in more detail below.

5.2.5.1 $B_{\alpha\beta}$ and $D_{\alpha\beta}$ Coefficients

Fig. 5.14 shows the variation of the $B_{\alpha\beta}$ and $D_{\alpha\beta}$ coefficients versus the cross-shore coordinate for five time intervals of the infragravity wave period. In the figures $x' = 0$ corresponds to the still water shoreline and $x' = 1$ to the toe of the beach. The coefficients themselves are not made dimensionless and can only be compared to each other.

The B and D coefficients exhibit quite a large variation over an IG wave period, which indicates that the local time-varying forcing is very important. It can be seen that the magnitude of all coefficients is increased significantly if we compare them to the magnitudes that were found in Fig. 5.4 for the steady case. As was already seen in Fig. 5.4, the values increase significantly across the breakpoint, since the "undertow" profiles become much more curved inside the surf zone due to the increased forcing. Because of the simple short-wave modeling, this transition in curvature occurs very rapidly, which will increase the cross-shore gradients in the quasi 3-D coefficients. The figure shows that the $B_{\alpha\beta}$ coefficients are in general larger than the corresponding $D_{\alpha\beta}$ coefficients, which was already seen in Fig. 5.4 also.

We also see that the D_{xx} and B_{xx} coefficients are larger than the D_{xy} and

B_{xy} coefficients, which are in turn larger than the D_{yy} and B_{yy} coefficients. This is because the short-wave groups refract to the normal, which means that the cross-shore velocities are more curved than the longshore velocities. This could already be seen in Fig. 5.13. The curvature of the velocity profiles directly influences the magnitude of the dispersive coefficients.

Fig. 5.15 shows the comparison of the D coefficients as calculated by the model (panels (a), (c) and (e), which are repeated from Fig. 5.14 (b), (d) and (f)) versus the approximate value that is obtained if we assume that velocity profiles are depth-invariant below the mean surface or

$$V_{1\beta}^{(0)} = -\frac{Q_{w\beta}}{h} \tag{5.46}$$

Under this assumption the expressions of the quasi 3-D coefficients become (5.22)-(5.26). These coefficients can be calculated from (2.81), (2.82), (2.83) and (2.84) if we set the coefficients

$$a_1 = b_1 = a_2 = b_2 = 0$$

The breakpoint is indicated by the vertical lines in the next figures.

Fig. 5.15 shows that in the approximation the magnitude of the dispersive coefficients is dramatically underpredicted when the (time-varying) curvature of the velocity profiles is neglected altogether. This underprediction is now not only significant inside the surf zone but also outside, even though the velocity profiles are only slightly curved, as could be seen in Fig. 5.13 (a) and (b).

5.2.5.2 $C_{\alpha\beta}$ and $E_{\alpha\beta}$ Coefficients

Fig. 5.16 show the dimensional values of $C_{\alpha\beta}$ and $E_{\alpha\beta}$ as defined in (5.18) and (5.19), respectively. The time variation is again very significant. As in the

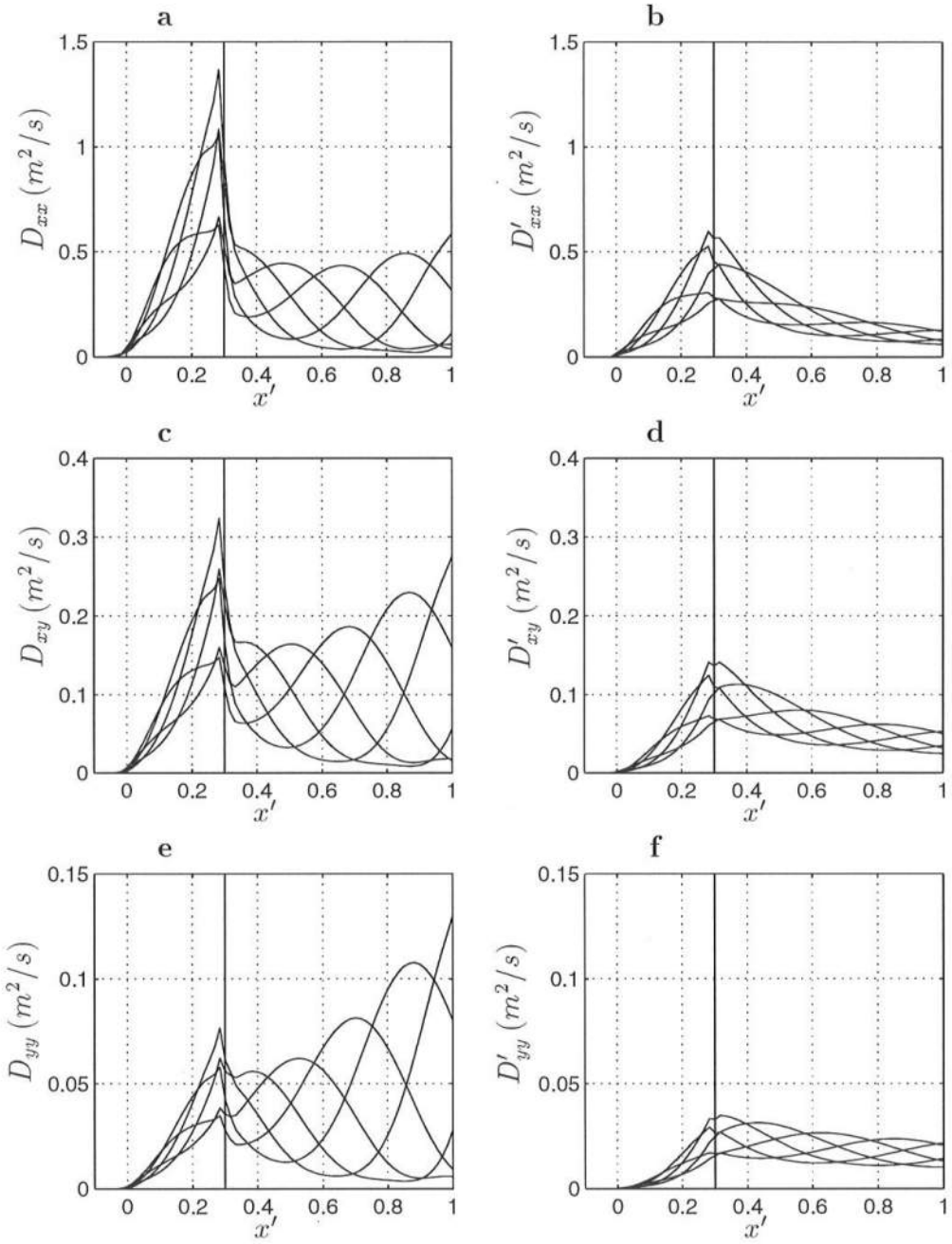

Figure 5.15: Comparison of D coefficients for five intervals per IG wave period: (a) D_{xx}. (b) $D'_{xx} = \frac{Q_{wx}^2}{3\,\nu_t}$. (c) D_{xy}. (d) $D'_{xy} = \frac{Q_{wx}\,Q_{wy}}{3\,\nu_t}$. (e) D_{yy}. (f) $D'_{yy} = \frac{Q_{wy}^2}{3\,\nu_t}$.

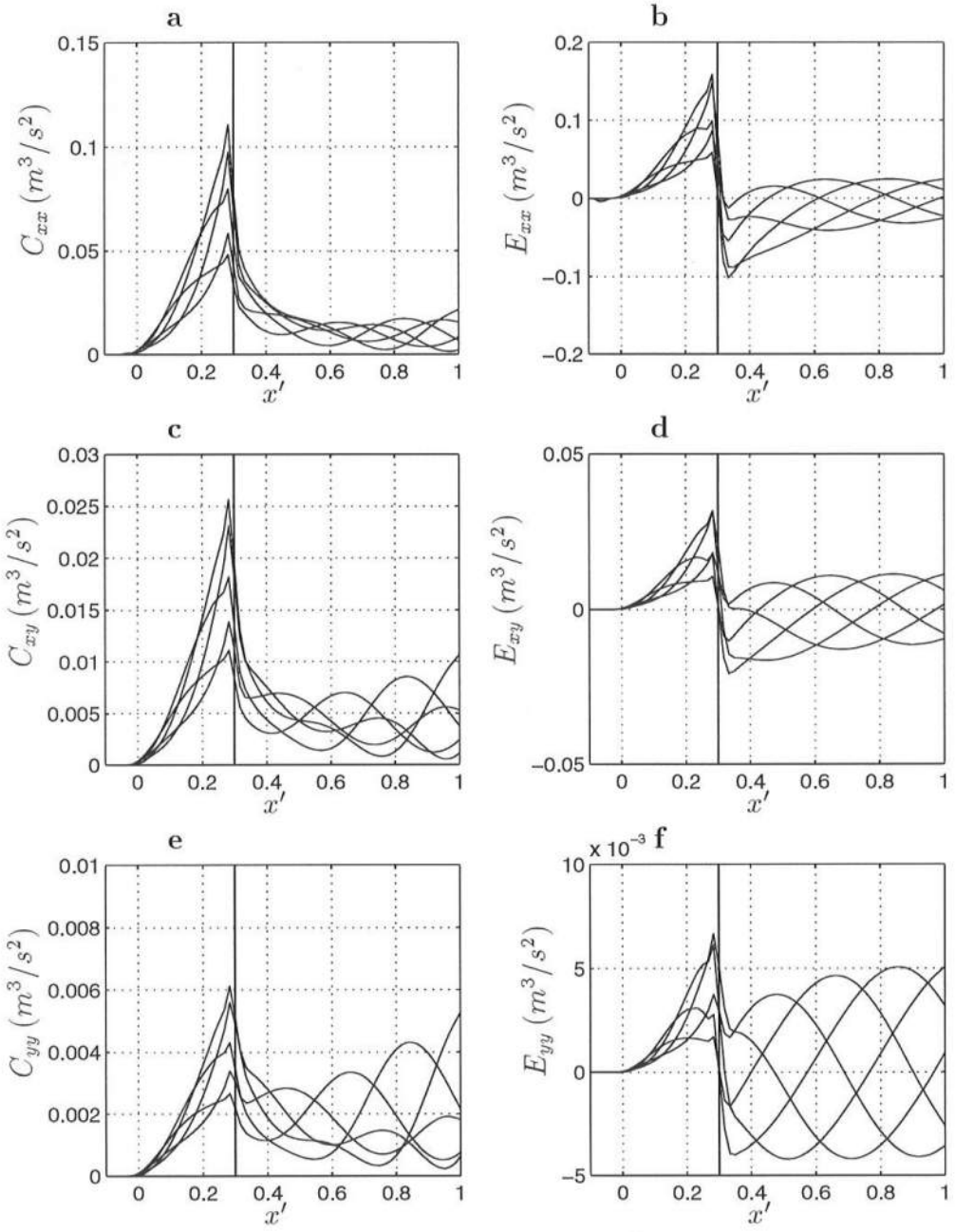

Figure 5.16: Magnitude of C and E coefficients vs. cross-shore distance x' for five intervals per IG wave period: (a) C_{xx}. (b) E_{xx}. (c) C_{xy}. (d) E_{xy}. (e) C_{yy}. (f) E_{yy}.

previous figure, the C_{xx} and E_{xx} coefficients are larger than the C_{xy} and C_{xy} coefficients, which are in turn larger than the C_{yy} and C_{yy} coefficients, due to the smallness of the angle of incidence of the wave-groups. The E coefficients are larger in magnitude than the corresponding C coefficients, especially just inside the breakpoint ($x' < 0.3$), where the surface velocities become large due to the large gradients in the forcing and the large local value of the shortwave-induced volume flux $Q_{w\beta}$. In fact, it will be shown below that these terms have a very significant effect around the breakpoint since their gradients contribute to the momentum equation.

The assumption of depth-invariant velocities (5.46) again underestimates the magnitude of these coefficients, especially around the breakpoint. Fig. 5.17 shows the comparison between the $C_{\alpha\beta}$ coefficients as calculated in the model and the approximate $C'_{\alpha\beta}$ value as calculated by (5.25). Fig. 5.18 shows the similar comparison between the $E_{\alpha\beta}$ coefficients as calculated in the model and the approximation $E'_{\alpha\beta}$ by (5.26). Similar to the steady case in Figs. 5.5 (b), (d) and (f), it can be seen that in the approximation the magnitude of the coefficients is underpredicted and that in the surf zone even the sign is predicted incorrectly. As was explained above, this is due to the fact that (5.21) will predict negative velocities at the surface under the assumption of depth-invariant currents whereas the velocities are really strongly positive, as can be seen in Fig. 5.13.

5.2.5.3 $A_{\alpha\beta\gamma}$ Coefficients

Finally, Fig. 5.19 shows the variation of the $A_{\alpha\beta\gamma}$ coefficients. Since this term is symmetrical in the first two indices (as was already seen in (2.83)), we can reduce the number of A coefficients from eight to six. The figure shows that the A_{xxx} term is much larger than all the other coefficients. It can be seen that the

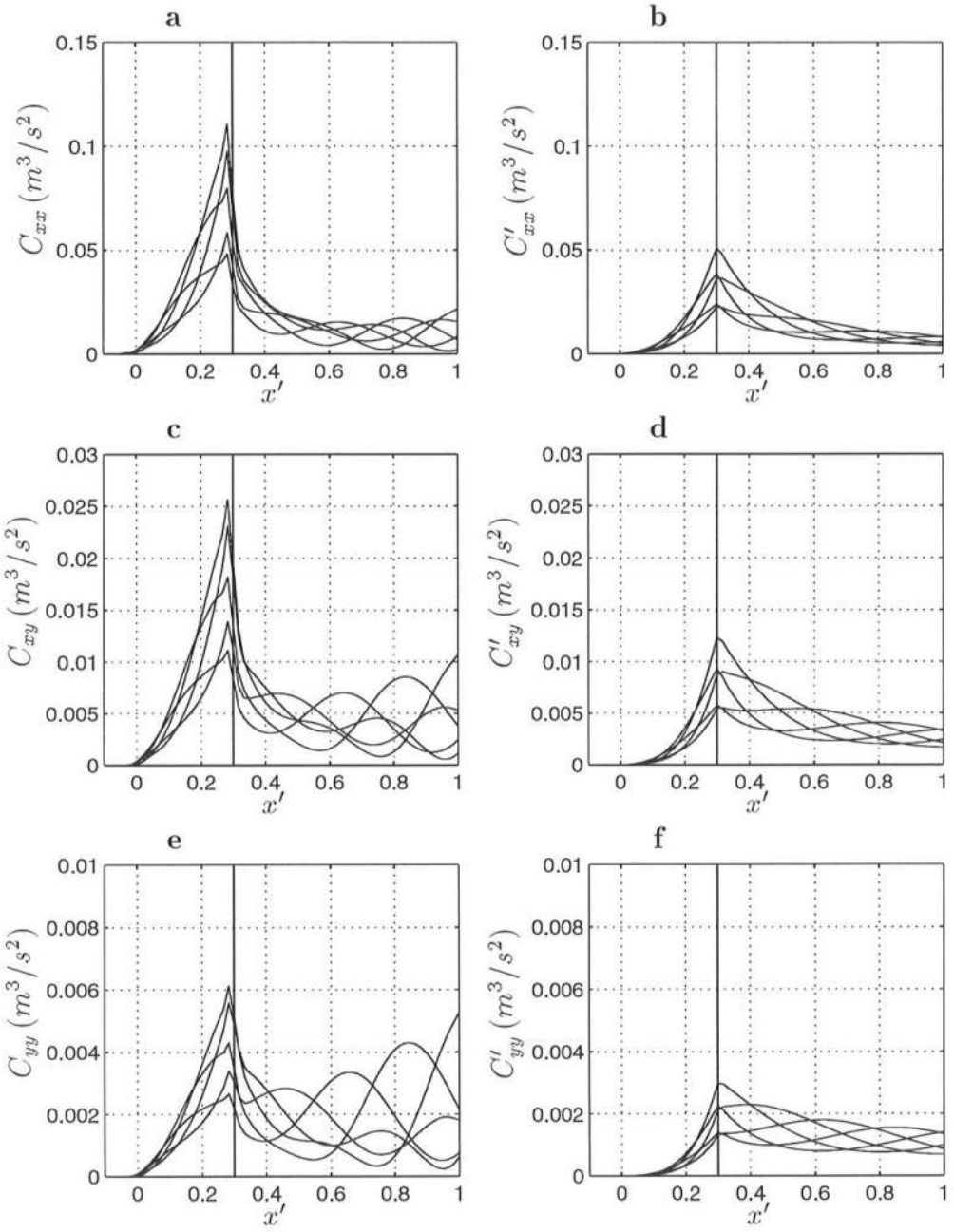

Figure 5.17: Comparison of C coefficients for five intervals per IG wave period: (a) C_{xx}. (b) $C'_{xx} = \frac{Q_{wx}^2}{h}$. (c) C_{xy}. (d) $C'_{xy} = \frac{Q_{wx}\,Q_{wy}}{h}$. (e) C_{yy}. (f) $C'_{yy} = \frac{Q_{wy}^2}{h}$.

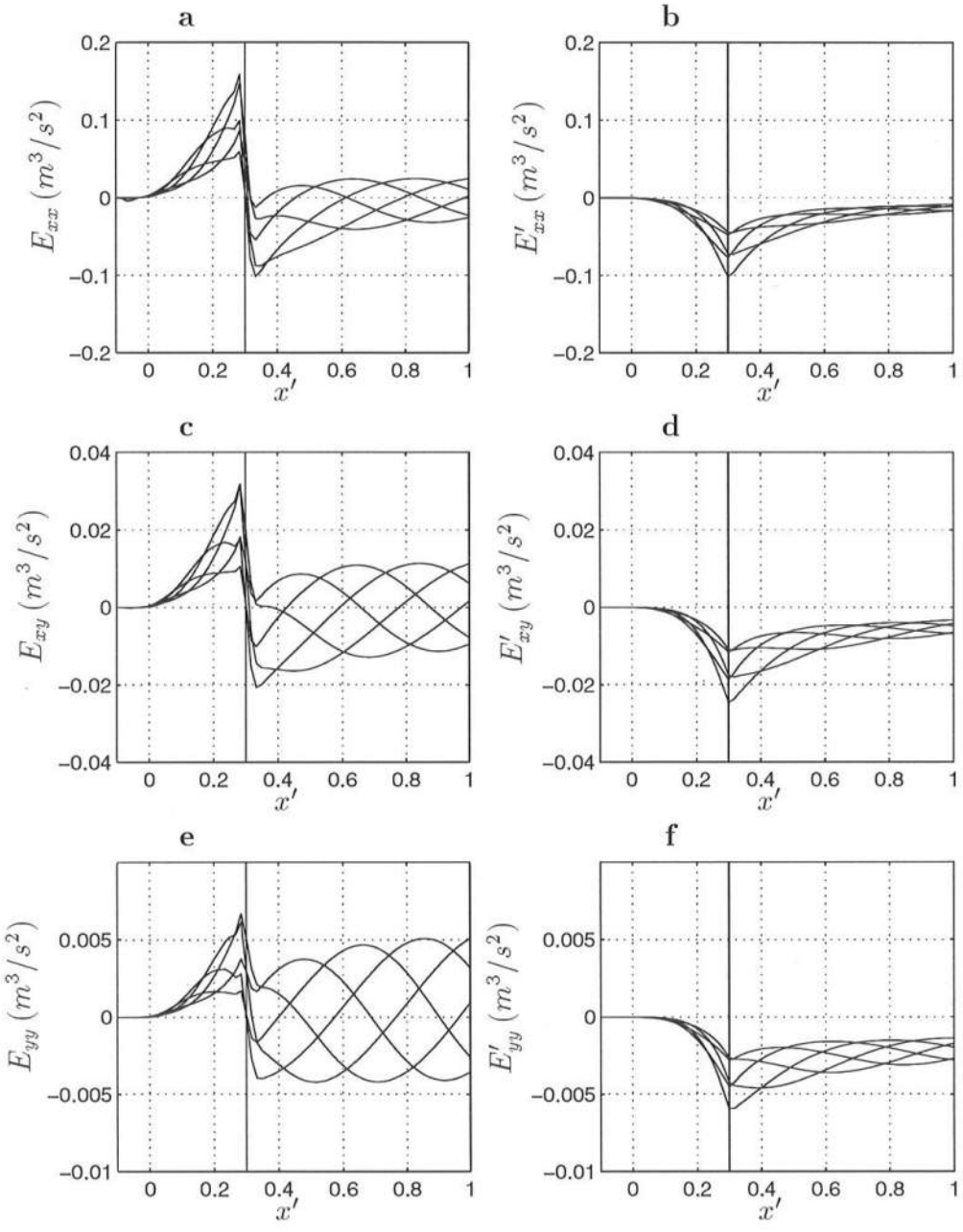

Figure 5.18: Comparison of E coefficients for five intervals per IG wave period: (a) E_{xx}. (b) $E'_{xx} = -2\,\frac{Q_{wx}^2}{h}$. (c) E_{xy}. (d) $E'_{xy} = -2\,\frac{Q_{wx}\,Q_{wy}}{h}$. (e) E_{yy}. (f) $E'_{yy} = -2\,\frac{Q_{wy}^2}{h}$.

value of all coefficients is larger seawards of the breakpoint than in the surf zone. However, in the momentum equations these coefficients are multiplied by $\tilde{U}$ and $\tilde{V}$, which both tend to zero offshore. The values of $A_{\alpha\beta\gamma}$ vary significantly across the breakpoint because the *horizontal gradients* of the rapidly-changing velocity profiles enter the expression (5.15). This means that, in the governing equations, we can expect some of these A terms to be large locally around the breakpoint. The contribution of these and all other quasi 3-D terms to the momentum equations will be shown in the next section.

5.2.6 Analysis of Quasi 3-D Contributions to the Momentum Equations

The analysis of the quasi 3-D mixing coefficients in the previous section only gives a partial picture of the mixing effect. In this section, therefore, a more direct assessment is obtained by looking at the magnitude of the terms in the momentum equations in which these quasi 3-D coefficients appear. The analysis is performed for an arbitrary time instance after the periodic state of the IG waves is reached and is strictly speaking only valid for this particular time. However, the magnitude of the terms in the equations at this time instance are characteristic for their magnitudes at any time in the periodic state. The conclusions that are drawn in this analysis are therefore representative for this case.

5.2.6.1 Cross-shore Momentum Equation

First, we analyze the terms in the x momentum equation. To reduce the large number of terms, we first define four "lump" terms

$$D_1 \equiv h\left((2\,D_{xx} + 2\,\nu_t + B_{xx})\frac{\partial \tilde{U}}{\partial x} + 2\,D_{xy}\frac{\partial \tilde{U}}{\partial y} + B_{xx}\frac{\partial \tilde{V}}{\partial y}\right) \tag{5.47}$$

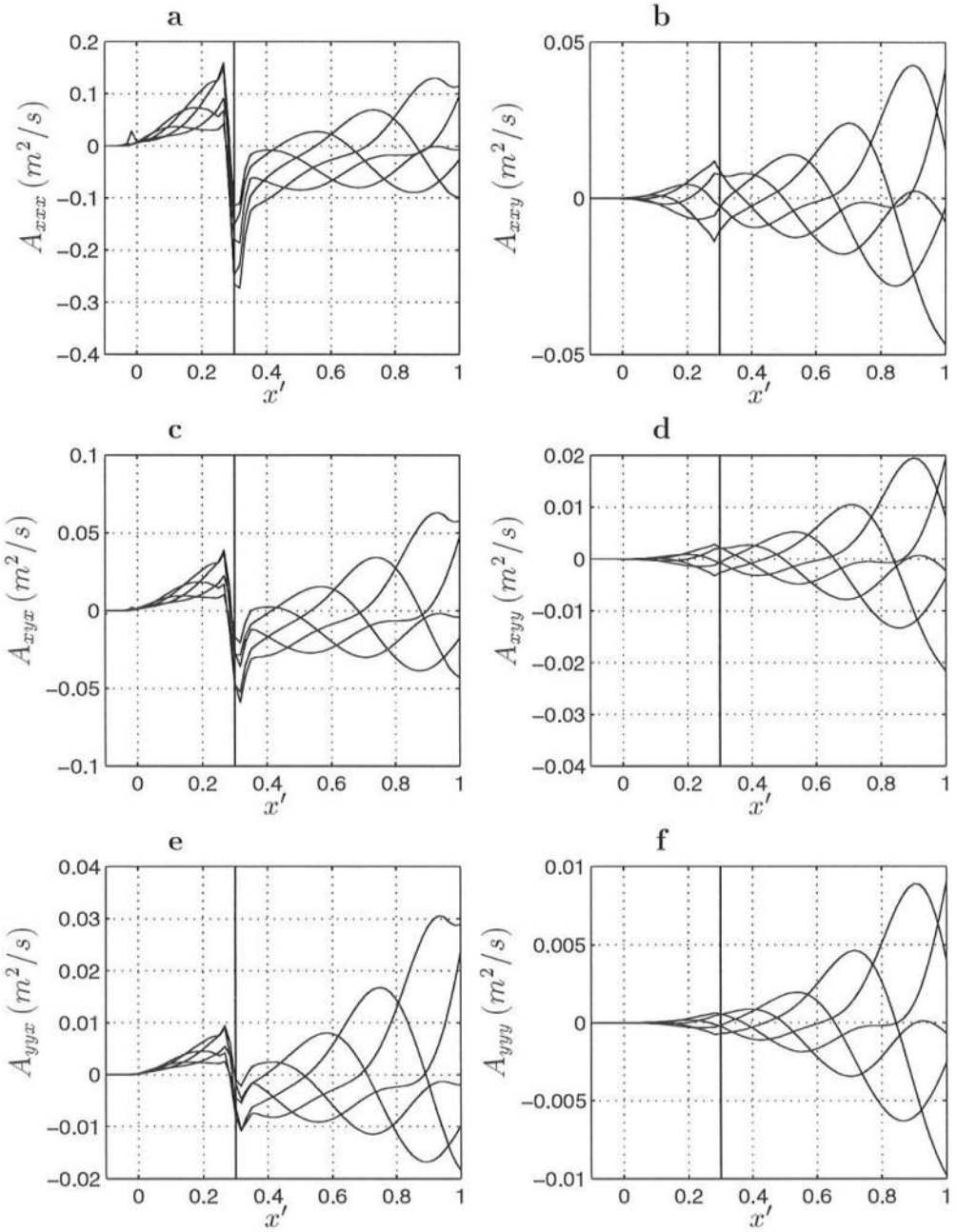

Figure 5.19: Magnitude of A coefficients vs. cross-shore distance x' for five intervals per IG wave period: (a) A_{xxx}. (b) A_{xxy}. (c) A_{xyx}. (d) A_{xyy}. (e) A_{yyx}. (f) A_{yyy}.

$$D_2 \equiv \quad h\left((D_{xy} + B_{xy})\frac{\partial \tilde{U}}{\partial x} + (D_{yy} + \nu_t)\frac{\partial \tilde{U}}{\partial y}\right.$$

$$\left. + (D_{xx} + \nu_t)\frac{\partial \tilde{V}}{\partial x} + (D_{xy} + B_{xy})\frac{\partial \tilde{V}}{\partial y}\right) \tag{5.48}$$

$$A_1 \equiv A_{xxx}\tilde{U} + A_{xxy}\tilde{V} \tag{5.49}$$

and

$$A_2 \equiv A_{xyx}\tilde{U} + A_{xyy}\tilde{V} \tag{5.50}$$

The x momentum equation (5.44) can then be written

$$\frac{\partial \bar{Q}_x}{\partial t} + \frac{\partial}{\partial x}\left(\frac{\bar{Q}_x^2}{h} + C_{xx} + E_{xx}\right) + \frac{\partial}{\partial y}\left(\frac{\bar{Q}_x \bar{Q}_y}{h} + C_{xy} + E_{xy}\right)$$

$$-\frac{\partial D_1}{\partial x} - \frac{\partial D_2}{\partial y} + \frac{\partial A_1}{\partial x} + \frac{\partial A_2}{\partial y}$$

$$+ g\,h\frac{\partial \bar{\zeta}}{\partial x} + \frac{1}{\rho}\left(\frac{\partial S_{xx}}{\partial x} + \frac{\partial S_{xy}}{\partial y}\right) + \frac{\tau_x^B}{\rho} = 0 \tag{5.51}$$

Fig. 5.20 (a) shows all terms in (5.51). It can be seen that the most important terms in the equation are the pressure gradient, the radiation stress gradient $\frac{\partial S_{xx}}{\partial x}$ and the local acceleration.

Of the quasi 3-D terms, only the $\frac{\partial E_{xx}}{\partial x}$ term is of the same order of magnitude locally at the breakpoint. This is due to the fact that the short waves are assumed to break at one location, which means that the cross-shore velocity profiles undergo a rapid change over a short distance. Since E_{xx}, which was defined in (5.19), is a function of the velocity at the surface, its gradient will therefore be large. The figure also shows that the $-\frac{\partial D_1}{\partial x}$ and the $\frac{\partial C_{xx}}{\partial x}$ terms are locally significant but smaller than the above terms at the breakpoint.

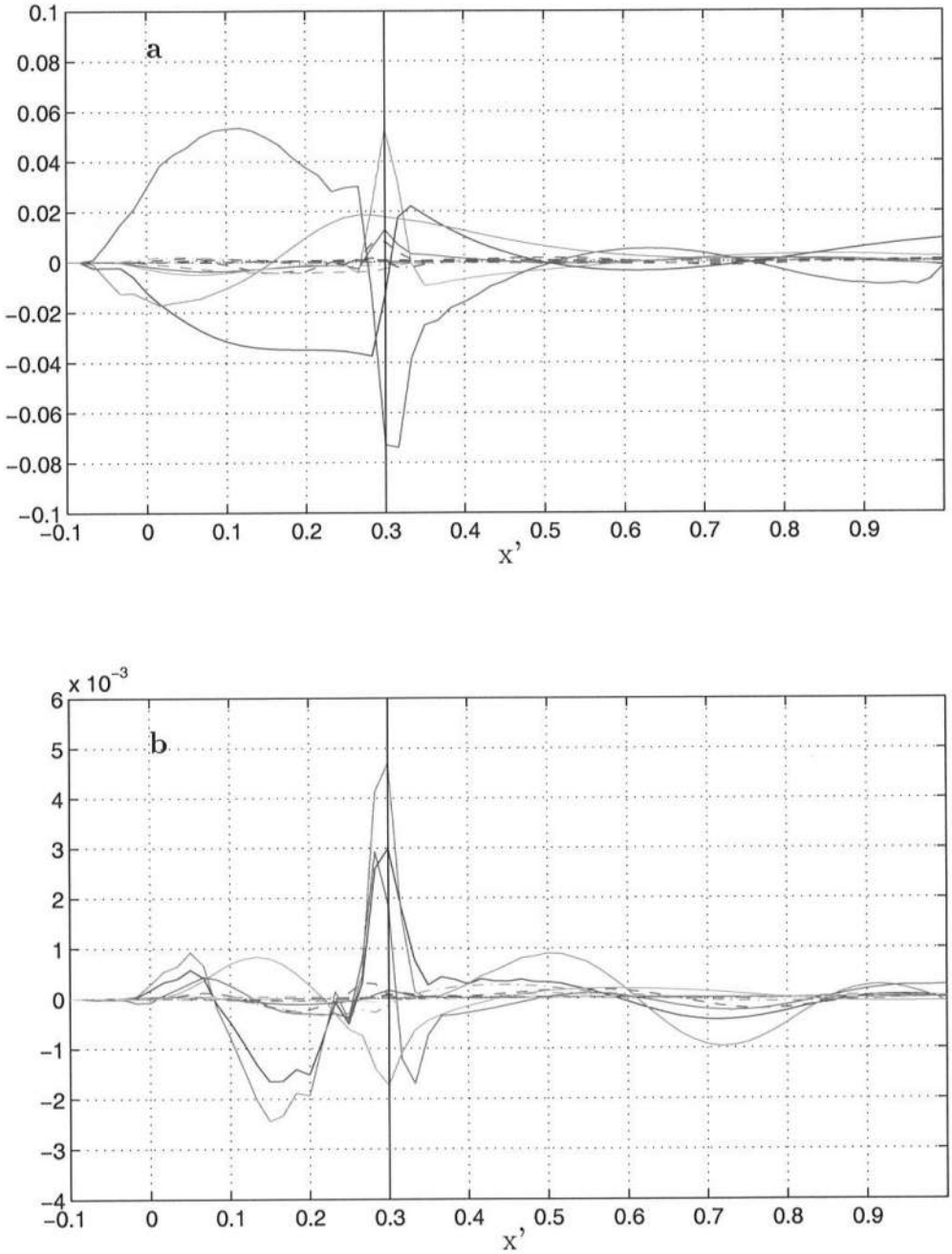

Figure 5.20: (a) Magnitude of dominant terms in the x momentum equation: pressure gradient (red ——); $\frac{\partial S_{xx}}{\partial x}$ (blue ——); local acceleration (green ——); $\frac{\partial E_{xx}}{\partial x}$ (cyan ——); $\frac{\partial C_{xx}}{\partial x}$ (purple ——); $-\frac{\partial D_1}{\partial x}$ (red – –); bottom friction (green – –). (b) Magnitude of dominant terms in "lump" terms: $-\frac{\partial}{\partial x}\left(hB_{xx}\frac{\partial \tilde{U}}{\partial x}\right)$ (green ——); $-\frac{\partial}{\partial x}\left(2hD_{xx}\frac{\partial \tilde{U}}{\partial x}\right)$ (blue ——); $\frac{\partial}{\partial x}\left(A_{xxx}\tilde{U}\right)$ (purple ——); $\frac{\partial}{\partial x}\left(A_{xxy}\tilde{V}\right)$ (cyan ——); $-\frac{\partial}{\partial x}\left(hB_{xx}\frac{\partial \tilde{V}}{\partial y}\right)$ (red – –) .

In Fig. 5.20 (b) the contributing terms to the quasi 3-D "lump" terms (5.47)-(5.50) are shown. It can be seen that of these terms

$$\frac{\partial}{\partial x}\left(h\,B_{xx}\frac{\partial \tilde{U}}{\partial x}\right) \qquad \frac{\partial}{\partial x}\left(2\,h\,D_{xx}\frac{\partial \tilde{U}}{\partial x}\right) \qquad \frac{\partial}{\partial x}\left(A_{xxx}\,\tilde{U}\right)$$

make the largest contributions. Notice that all these terms involve derivatives in x only, which means that we can assume that all terms involving y derivatives are small in this particular case.

5.2.6.2 Longshore Momentum Equation

In this section we will analyze the relative magnitude of the terms in the y momentum equation. If we define

$$D_3 \equiv h\left(B_{yy}\frac{\partial \tilde{U}}{\partial x} + 2\,D_{xy}\frac{\partial \tilde{V}}{\partial x} + (2\,D_{yy} + 2\,\nu_t + B_{yy})\frac{\partial \tilde{V}}{\partial y}\right) \tag{5.52}$$

and

$$A_3 \equiv A_{yyx}\,\tilde{U} + A_{yyy}\,\tilde{V} \tag{5.53}$$

we can rewrite the y momentum equation (5.45) as

$$\begin{aligned}
&\frac{\partial \bar{Q}_y}{\partial t} + \frac{\partial}{\partial x}\left(\frac{\bar{Q}_x\,\bar{Q}_y}{h} + C_{xy} + E_{xy}\right) + \frac{\partial}{\partial y}\left(\frac{\bar{Q}_y^2}{h} + C_{yy} + E_{yy}\right) \\
&- \frac{\partial D_2}{\partial x} - \frac{\partial D_3}{\partial y} + \frac{\partial A_2}{\partial x} + \frac{\partial A_3}{\partial y} \\
&+ g\,h\,\frac{\partial \bar{\zeta}}{\partial y} + \frac{1}{\rho}\left(\frac{\partial S_{xy}}{\partial x} + \frac{\partial S_{yy}}{\partial y}\right) + \frac{\tau_y^B}{\rho} = 0
\end{aligned} \tag{5.54}$$

Fig. 5.21 (a) shows that in the y direction there are a number of terms that are at least locally important. Of the depth-integrated (2-DH) terms, the local acceleration, the pressure gradient, the radiation shear stress $\frac{\partial S_{xy}}{\partial x}$, the bottom

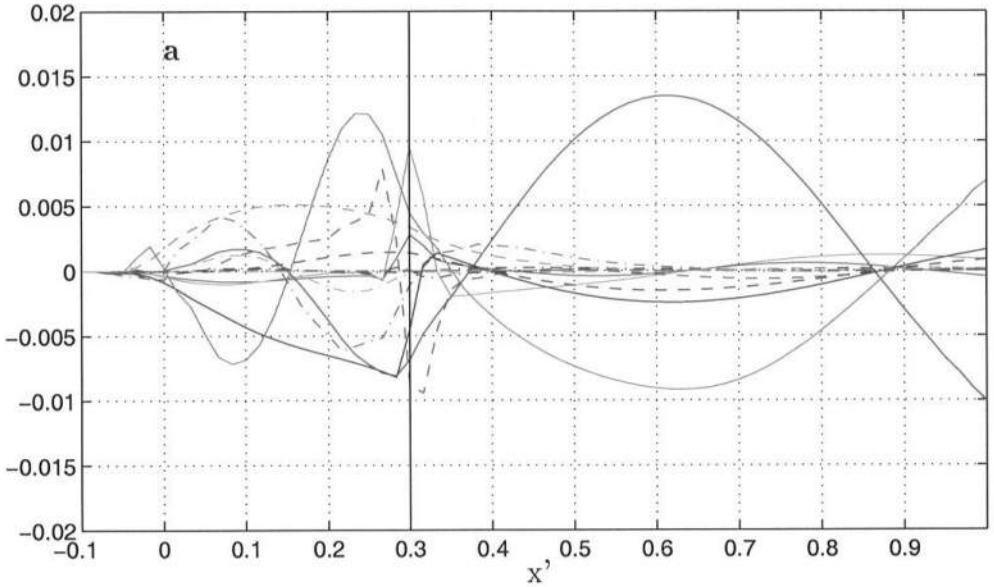

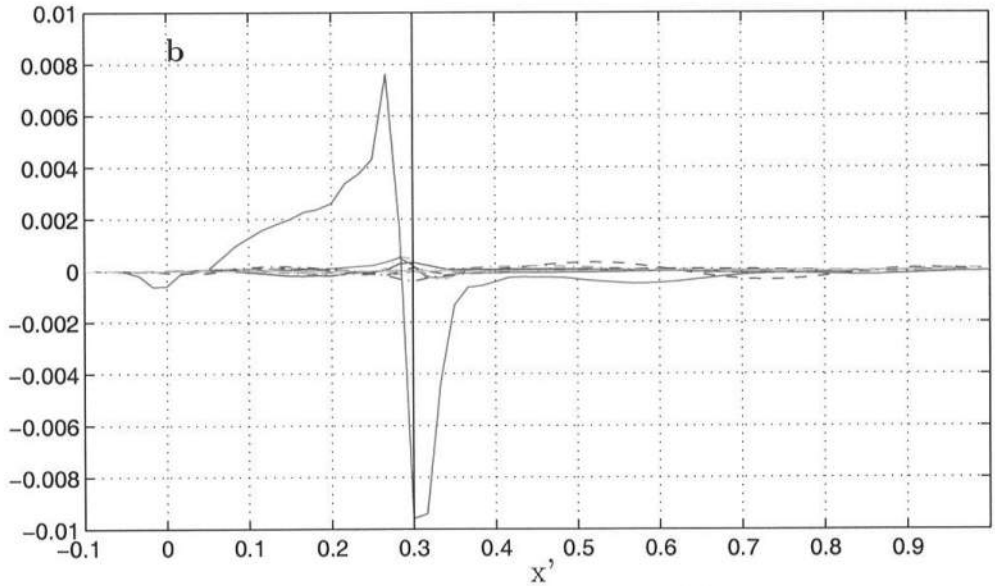

Figure 5.21: (a) Magnitude of dominant terms in the y momentum equation: pressure gradient (red ——); $\frac{\partial S_{xy}}{\partial x}$ (blue ——); local acceleration (green ——); $\frac{\partial E_{xy}}{\partial x}$ (cyan ——); $\frac{\partial C_{xy}}{\partial x}$ (purple ——); $-\frac{\partial D_2}{\partial x}$ (red – –); $\frac{\partial}{\partial x}\left(\frac{\bar{Q}_x \bar{Q}_y}{h}\right)$ (purple – ·); bottom friction (green – –). (b) Magnitude of dominant terms in "lump" terms: $-\frac{\partial}{\partial x}\left(hD_{xx}\frac{\partial \tilde{V}}{\partial x_\alpha}\right)$ (red ——); $-\frac{\partial}{\partial x}\left(hB_{xy}\frac{\partial \tilde{U}}{\partial x}\right)$ (blue – –) .

friction, and the advection term $\frac{\partial}{\partial x}\left(\frac{\bar{Q}_x \bar{Q}_y}{h}\right)$ are important. We also see that of the quasi 3-D terms

$$\frac{\partial E_{xy}}{\partial x} \qquad \frac{\partial D_2}{\partial x}$$

are important also. The first term is locally significant around the breakpoint for the same reason that the $\frac{\partial E_{xx}}{\partial x}$ was important in the x momentum equation. The second term is of the same order of magnitude as the 2-DH terms inside the surf zone.

In Fig. 5.21 (b) the contributing terms to the quasi 3-D "lump" terms are shown. It can be seen that of these terms, $\frac{\partial}{\partial x}\left(h\, D_{xx} \frac{\partial \tilde{V}}{\partial x}\right)$ makes by far the largest contribution. This is due to the fact that the steady short-wave forcing drives a longshore current that is relatively strong compared to the time-varying motion. This also means that the shear in the longshore current $\frac{\partial \tilde{V}}{\partial x}$ is much larger than the other gradients in the IG wave velocities.

For this particular case, we can simplify the equations by neglecting all the quasi 3-D terms that are small. Of course, the results described here only apply to this particular case. This analysis should be performed on a case-to-case basis which means that for every situation the complete quasi 3-D equations should be analyzed before the relative magnitude of the terms can be assessed. For some cases, for example situations with complicated bathymetries and time-varying hydrodynamical input, it is advisable to retain all the quasi 3-D terms in the equations because they might be significant locally in space and time.

5.3 Conclusions

In this chapter we applied the quasi 3-D SHORECIRC model to two cases: to the start-up of a longshore current and to infragravity waves forced by obliquely-incident wave groups.

In the first case, it was shown that a steady state in the cross-shore direction is achieved on a relatively short time scale. The time scale to reach a steady state in the longshore direction is much longer. This is due to the fact that the short-wave forcing in the shore normal direction is much stronger than in the longshore direction, because of the smallness of the angle of incidence of the wave groups. Also, in the cross-shore direction the forcing is balanced by a pressure gradient which is established relatively quickly, whereas in the longshore direction the forcing is balanced by the dispersive mixing and the bottom friction, whose equilibrium value is attained asymptotically.

The quasi 3-D dispersive mixing term is seen to have a large influence on the shape of the horizontal longshore current velocity profile. This mixing acts over and above the turbulent mixing and causes momentum to be spread seawards from the surf zone. It was also shown that, in the process of reaching a steady state, the current velocity profiles reveal a gently turning spiral shape. It is emphasized that the depth-variation of the currents is critical to the existence of dispersive mixing. In the hypothetical case of depth-uniform currents the dispersive mixing would be zero identically, which would dramatically change the horizontal longshore current velocity profile.

The magnitude of all quasi 3-D coefficients as a function of the cross-shore distance is shown. It turns out that these coefficients are not necessarily small or zero themselves but that their contribution to the momentum equations may

be negligible because they are multiplied by velocity gradients that may be small. The magnitude of these coefficients is also compared to an approximate value, which assumes that the velocity profiles are constant over depth below trough. It is shown that under this simplifying assumption the magnitude of the quasi 3-D coefficients is significantly underpredicted, especially in the surf zone, because the curvature of the profiles is neglected.

Thus, for the case of a longshore current on a cylindrical coast, we find that only one of the dispersive mixing terms, involving the D_{xx} term, is significant and can be determined from the (steady) cross-shore circulation.

In the second case for infragravity waves forced by obliquely-incident wave groups the hydrodynamical conditions are no longer longshore uniform but are longshore periodic, which means that more terms in the momentum equations are important.

It has been shown that the linearized model agrees well with the linear analytical solution for the long-wave envelope by Schäffer (1994). However, including nonlinear terms corresponding to the 2-DH shallow water equations reveals that the nodes and anti-nodes of the envelope shift shoreward.

The quasi 3-D terms are seen to have a significant influence on the long-wave envelope around the breakpoint and a lesser influence on the amplitude of the envelope elsewhere. It should be noted that the magnitude of the quasi 3-D terms around the breakpoint is influenced by the unrealistic short-wave modeling applied in this thesis. Although the details of the short-wave height variation around the breakpoint may be inaccurate, this does not change the fact that rapid variations of the wave height, the wave-averaged properties and the IG wave particle velocity profiles do occur around breaking, so that it can be expected that the results are

at least correct in a qualitative sense.

The calculation of the quasi 3-D coefficients requires that the infragravity wave particle velocity profiles be determined. These profiles show that the time-varying forcing has a large influence on the cross-shore motion ("the undertow"). Outside the breakpoint, it is seen that the cross-shore velocity profiles are slightly curved, while inside the surf zone they exhibit a strong curvature which is typical for undertow. These velocity profiles qualitatively agree with laboratory data (Smith & Svendsen 1995, 1996). Due to the refraction of the short-wave forcing to near-normal angles of incidence, the time-variation of the longshore motion is not as strong as the variation in the undertow. In this direction the steady forcing is dominant and causes the longshore velocity profiles to be pitched forward. This slight deviation from a depth-invariant velocity profile is critical to the existence of dispersive mixing, as was seen in the steady case.

As in the previous case, we have investigated the magnitudes of the quasi 3-D coefficients as a function of time and cross-shore distance. It is found that, especially outside the surf zone, the magnitudes are much larger in this case than in the previous (steady) case. This is due to the fact that the time-varying forcing causes the IG velocity profiles to be more curved, which directly influences the magnitude of the quasi 3-D coefficients. As before, the magnitude of these coefficients is also compared to the approximate values under the simplifying assumption of depth-invariant velocity profiles below trough. It is shown that in the approximation the quasi 3-D coefficients are significantly underpredicted.

Finally, the contribution of the quasi 3-D terms to the momentum equations is analyzed. In the cross-shore direction, it is shown that a number of quasi 3-D terms are locally significant around the breakpoint, where the infragravity wave velocity profiles undergo a large change in shape. In the longshore direction,

it turns out that the same dispersion term that was found in the steady case is dominant over all other quasi 3-D terms. This is due to the fact that in this particular case there is a relatively strong cross-shore shear in the longshore velocity, which is much larger than the other gradients in the IG wave velocities.

This dominance of one quasi 3-D term over the other is of course case-specific. This implies that an assessment of the relative magnitude of these terms should be performed on each individual case and that for particularly complicated cases it is advisable to retain all terms in the equations, since they may be significant locally in space and time.

Chapter 6

CONCLUSIONS AND RECOMMENDATIONS

6.1 Conclusions

In this thesis, a depth-integrated, shortwave-averaged quasi 3-D nearshore circulation model is developed. This model includes the depth-dependent long- and short-wave velocity interactions which induce nonlinear quasi 3-D mechanisms, and are important in the applications shown in this thesis.

In Chapter 2 the quasi 3-D equations were described. First, the depth-integrated, time-averaged governing equations were derived. The depth-dependent integral terms that occur in those equations were transformed into terms that are functions of the depth-integrated quantities and quasi 3-D coefficients. The latter require that the local, time-averaged momentum (or "velocity profile") equations are solved. In this thesis, the semi-analytical solution for the quasi steady state was given, which is the leading-order term in the time-dependent solution of the profile equations. The generalized quasi 3-D equations were shown to reduce to the special case of a long straight beach of Svendsen & Putrevu (1994a).

In Chapter 3 the numerical model SHORECIRC was described. First, the numerical integration method was described. An explicit second-order Adams-Bashforth predictor, third-order Adams-Moulton corrector time-stepping scheme

was chosen, which is easy to code and has a wide stability range. The leading-order truncation errors were shown to be of a dispersive nature.

The remainder of Chapter 3 was devoted to the development of accurate boundary conditions, which are essential to the performance of a numerical model. For the artificial ("seaward") boundaries we derived an absorbing-generating boundary condition based on the Method of Characteristics, which is capable of generating waves at a boundary while simultaneously absorbing any outgoing progressive wave with a mimimum of reflection. In a number of formal tests it was shown that this boundary condition induces reflection errors that are limited to only a few percent of the incident wave amplitude for the full range of angles of incidence and reflection, which is an improvement over the classical radiation (or "Sommerfeld") conditions. Unlike those radiation conditions, the present boundary condition allows simultaneous specification of an incident wave train and absorption of an outgoing wave train at the same boundary, which makes it particularly suitable for application on artificial oceanside boundaries in our model or any shallow water model.

At the shoreline we developed a boundary condition that is based on the principle of storage of volume. Cells at the shoreline boundary in the fixed numerical grid are either inundated or drained as a result of the integrated flux through the neighboring nodes. This simple boundary condition was shown to agree very well with the one-dimensional analytical solution by Carrier & Greenspan (1958). We found good agreement in the case of two-dimensional run-up of a solitary wave on a concave beach compared to other numerical solutions by Zelt (1986) and Özkan-Haller & Kirby (1997).

In the final two chapters of this thesis, the model was applied to a number of specific cases involving infragravity waves and longshore currents. It is emphasized

that the use of the SHORECIRC model is not limited to these cases, but has been developed so that it can be used to analyze nearshore circulation on any nearshore bathymetry and under any hydrodynamical condition.

In Chapter 4 the SHORECIRC model was applied to the case of generation of infragravity waves ("surf beat") due to normally-incident wave groups. It was shown that the process of generation of IG waves can be characterized by three external parameters: the relative slope steepness S_Δ, the mean short-wave breakpoint location $\frac{h_b}{h_s}$ and the breaking mechanism κ. These parameters are related to the geometry of the problem and are an alternative to the five parameters identified by Schäffer (1993).

The linearized version of the model showed excellent agreement with the analytical solution by Schäffer (1993), which indicates that our numerical model is sufficiently accurate. After separation of the incoming and outgoing IG waves, the respective envelopes were studied. The incoming long wave is shown to gain considerable energy flux outside the surf zone due to the changing forcing. However, this increase is not nearly as fast as Longuet-Higgins & Stewart (1962)'s steady state theory for bound waves suggests, which is an important finding in the analysis of field data.

The energy transfer between the short waves and the IG waves was analyzed using the terms in the linear energy equation. It is shown that a variation of the above-mentioned parameters results in a local variation in the ratio of outgoing to incoming wave energy, which may explain the seemingly inconclusive field evidence on this topic. The value of the "reflection coefficient" R can be interpreted as an integral measure of the net transfer of energy to the infragravity waves as a result of shoaling and breaking of the short-wave groups and their interaction with the long waves.

Extending the model to include the nonlinear terms showed the importance of the steady set-up over the other nonlinear terms. This nonlinear version of the model has been shown to agree well with the Kostense (1984)'s laboratory data set and Roelvink (1993)'s nonlinear model.

In Chapter 5, the SHORECIRC model was applied to the start-up of a longshore current and to infragravity waves forced by obliquely-incident wave groups. In the former case, it was shown that a steady state in the cross-shore direction is achieved on a relatively short time scale. The time scale to reach a steady state in the longshore direction is much longer. The quasi 3-D dispersive mixing term was seen to have a large influence on the shape of the horizontal longshore current velocity profile. This mixing acts over and above the turbulent mixing and causes momentum to be spread seawards from the surf zone. It was also shown that, in the process of reaching a steady state, the current velocity profiles develop a slowly-turning spiral shape. It is emphasized that the depth-variation of the currents is critical to the existence of dispersive mixing.

In the second case for infragravity waves forced by obliquely-incident wave groups the hydrodynamical conditions are no longer longshore uniform but are longshore periodic, which means that more terms in the momentum equations are significant. It was shown that the linearized model agrees well with the analytical solution for the long-wave envelope by Schäffer (1994). Including nonlinear terms corresponding to the 2-DH shallow water equations revealed that the nodes and anti-nodes of the envelope shift shoreward. The quasi 3-D terms were seen to have a significant influence on the long-wave envelope around the break point and a lesser influence on the amplitude of the envelope elsewhere.

The calculation of the quasi 3-D coefficients requires that the infragravity wave particle velocity profiles be determined. These profiles showed that the

time-varying forcing has a large influence on the cross-shore motion ("the undertow"). Outside the breakpoint, it was seen that the cross-shore velocity profiles are slightly curved, while inside the surf zone they exhibit a strong curvature which is typical for undertow. These velocity profiles qualitatively agreed with laboratory data (Smith & Svendsen 1995, 1996). The time-variation of the longshore motion is not as strong due to the refraction of the short-wave forcing to near-normal angles of incidence.

The magnitude of the quasi 3-D coefficients as a function of time and cross-shore distance were also examined. It was found that, especially outside the surf zone, the magnitudes are much larger than in the previous (steady) case. The magnitude of these coefficients was also compared to the approximate values under the simplifying assumption of depth-invariant velocity profiles below trough, which was shown to cause significant underpredictions.

Finally, the contribution of the quasi 3-D terms to the momentum equations was analyzed. In the cross-shore direction, it was shown that a number of quasi 3-D terms are locally significant around the breakpoint. In the longshore direction, it turned out that the same dispersion term that was found in the steady case, is dominant over all other quasi 3-D terms. This is because in this particular case there is a relatively strong shear in the longshore velocity which is much larger than any other gradients of the velocities.

The relative significance of the quasi 3-D terms is case-specific. This implies that an assessment of the relative magnitude of these terms should be performed on each individual case and that for particularly complicated cases it is advisable to retain all terms in the equations, since they may be significant locally in space and time.

6.2 Recommendations

In the future some of the shortcomings in the present SHORECIRC model should be addressed. First of all, semi-analytical solutions of the time-dependent local momentum equations should be developed in order to more accurately determine the IG wave profiles. This innovation might make a difference in the results. It should at least show how good an approximation the quasi steady-state solution is to the complete solution.

Secondly, a time-averaged model is no better than the short-wave driver it uses. In most of this thesis a linear analytical solution for the radiation stress variation is used. This has the obvious deficiency that it is based on a wave theory which is not valid for breaking waves. There is also no feedback mechanism to transfer energy from the long waves to the short waves, as was discussed in Chapter 4. In the comparison with Kostense (1984)'s data we used the energy equation for the short waves as a short-wave driver. Because this includes such a feedback mechanism, the use of this driver yields a more realistic prediction of the local short wave heights, but in the calculation of the radiation stresses we once again have to resort to linear theory for lack of a better alternative. A better short-wave driver (such as REF/DIF, which also uses sine waves) should be used or developed.

Another point to be addressed is the formulation of some of the parameters. In particular, the expression for the eddy viscosity parameter ν_t outside the surf zone is based on a single data set for turbulent kinetic energy by Nadoaka & Kondoh (1982). Some additional measurements should be performed to better model this critical parameter. A linearized expression for the bottom friction has been used in this thesis. This can easily be replaced by a nonlinear formulation but the real problem is the need for a general formulation of the friction coefficient

in the case of waves and currents under an angle.

In the present form, the absorbing-generating boundary condition is capable of absorbing progressive waves at the offshore boundaries. An extension for the case of waves and currents is outlined in Chapter 3.2 but not implemented in SHORECIRC as of yet. Another deficiency is that the boundary condition cannot treat non-planar waves, such as edge waves. In the analysis of "trapped" infragravity waves at the shore, the model should be modified to enable this without having to extend the domain too far offshore.

While the shoreline boundary condition showed good agreement with the analytical solution of Carrier & Greenspan (1958) and the numerical solutions by Zelt (1986) and Özkan-Haller & Kirby (1997), it is not very robust. Especially in the case of forced waves special care has to be taken that the calculation at the shoreline nodes does not "blow up." It is recommended that this boundary condition be modified, perhaps following Brocchini & Peregrine (1996)'s outline for the development of these types of boundary conditions.

Finally, we strongly encourage that this model be used in field data simulations. SHORECIRC has already been compared to Delilah 1990 and will be applied in the analysis of the forthcoming Sandy Duck 1997 data, but its use should not be limited to these data sets.

Appendix A

DETAIL OF THE DERIVATION OF QUASI 3-D INTEGRAL TERMS.

In this Appendix, we will give the detailed derivation of (2.67) from (2.62). For reference, (2.62) reads

$$I = \int_{-h_o}^{\bar{\zeta}} V_{1\alpha}^{(0)} V_{1\beta}^{(0)}\, dz - \int_{-h_o}^{\bar{\zeta}} V_{1\alpha}^{(0)} \int_z^{\bar{\zeta}} \frac{1}{\nu_t} \int_{-h_o}^{z} F_\beta\, dz\, dz\, dz$$

$$- \int_{-h_o}^{\bar{\zeta}} V_{1\beta}^{(0)} \int_z^{\bar{\zeta}} \frac{1}{\nu_t} \int_{-h_o}^{z} F_\alpha\, dz\, dz\, dz$$

$$+ V_{1\beta}^{(0)}(\bar{\zeta})\, Q_{w\alpha} + V_{1\alpha}^{(0)}(\bar{\zeta})\, Q_{w\beta} \tag{A.1}$$

The first triple integral in (A.1) reads

$$I_1 = \int_{-h_o}^{\bar{\zeta}} V_{1\alpha}^{(0)} \int_z^{\bar{\zeta}} \frac{1}{\nu_t} \int_{-h_o}^{z} F_\beta\, dz\, dz\, dz \tag{A.2}$$

If we substitute (2.56), repeated here,

$$F_\beta = V_{1\gamma}^{(0)} \frac{\partial \tilde{V}_\beta}{\partial x_\gamma} + \tilde{V}_\gamma \frac{\partial V_{1\beta}^{(0)}}{\partial x_\gamma} + W \frac{\partial V_{1\beta}^{(0)}}{\partial z} \tag{A.3}$$

into (A.2), we get

$$I_1 = \int_{-h_o}^{\bar{\zeta}} V_{1\alpha}^{(0)} \int_z^{\bar{\zeta}} \frac{1}{\nu_t} \int_{-h_o}^{z} \left(V_{1\gamma}^{(0)} \frac{\partial \tilde{V}_\beta}{\partial x_\gamma} + \tilde{V}_\gamma \frac{\partial V_{1\beta}^{(0)}}{\partial x_\gamma} + W \frac{\partial V_{1\beta}^{(0)}}{\partial z} \right) dz\, dz\, dz \tag{A.4}$$

The first term of (A.4) can be written as

$$I_a = \int_{-h_o}^{\bar{\zeta}} V_{1\alpha}^{(0)} \int_z^{\bar{\zeta}} \frac{1}{\nu_t} \int_{-h_o}^{z} V_{1\gamma}^{(0)} \frac{\partial \tilde{V}_\beta}{\partial x_\gamma} \, dz \, dz \, dz$$

$$= \int_{-h_o}^{\bar{\zeta}} V_{1\alpha}^{(0)} \int_z^{\bar{\zeta}} \frac{1}{\nu_t} \int_{-h_o}^{z} V_{1\gamma}^{(0)} \, dz \, dz \, dz \, \frac{\partial \tilde{V}_\beta}{\partial x_\gamma}$$

$$= h \, D_{\alpha\gamma} \frac{\partial \tilde{V}_\beta}{\partial x_\gamma} \tag{A.5}$$

where we have used the fact that the $\frac{\partial \tilde{V}_\beta}{\partial x_\gamma}$ is not a function of depth and where we have used (2.63) in the last step.

The second term in (A.4) can be rewritten using the Leibnitz rule on the inner integral as

$$I_b = \int_{-h_o}^{\bar{\zeta}} V_{1\alpha}^{(0)} \int_z^{\bar{\zeta}} \frac{1}{\nu_t} \int_{-h_o}^{z} \tilde{V}_\gamma \frac{\partial V_{1\beta}^{(0)}}{\partial x_\gamma} \, dz \, dz \, dz$$

$$= \tilde{V}_\gamma \int_{-h_o}^{\bar{\zeta}} V_{1\alpha}^{(0)} \int_z^{\bar{\zeta}} \frac{1}{\nu_t} \left[\frac{\partial}{\partial x_\gamma} \left(\int_{-h_o}^{z} V_{1\beta}^{(0)} \, dz \right) - V_{1\beta}^{(0)}(-h_o) \frac{\partial h_o}{\partial x_\gamma} \right] dz^2 \tag{A.6}$$

where $\tilde{V}_\gamma$ is not a function of depth.

In the third term in (A.4),

$$I_c = \int_{-h_o}^{\bar{\zeta}} V_{1\alpha}^{(0)} \int_z^{\bar{\zeta}} \frac{1}{\nu_t} \int_{-h_o}^{z} W \frac{\partial V_{1\beta}^{(0)}}{\partial z} \, dz \, dz \, dz \tag{A.7}$$

the inner integral is integrated by parts, so that

$$I_c = \int_{-h_o}^{\bar{\zeta}} V_{1\alpha}^{(0)} \int_z^{\bar{\zeta}} \frac{1}{\nu_t} \Big(W(z) \, V_{1\beta}^{(0)}(z) - W(-h_o) \, V_{1\beta}^{(0)}(-h_o) -$$

$$\int_{-h_o}^{z} V_{1\beta}^{(0)} \frac{\partial W}{\partial z} \, dz \Big) \, dz \, dz \tag{A.8}$$

We can substitute for the W terms from the continuity equation

$$\frac{\partial W}{\partial z} = -\frac{\partial V_\gamma}{\partial x_\gamma} \sim -\frac{\partial \tilde{V}_\gamma}{\partial x_\gamma} \tag{A.9}$$

where we have approximated the total velocity V_γ by its depth-averaged value $\tilde{V}_\gamma$. Integrating this equation once yields

$$W(z) = W(-h_o) - \frac{\partial \tilde{V}_\gamma}{\partial x_\gamma}(h_o + z) \tag{A.10}$$

At $z = -h_o$ we apply the bottom boundary condition

$$W(-h_o) = -\frac{\partial h_o}{\partial x_\gamma} V_\gamma(-h_o) \sim -\frac{\partial h_o}{\partial x_\gamma} \tilde{V}_\gamma \tag{A.11}$$

We substitute (A.9), (A.10) and (A.11) into (A.8), which then becomes

$$I_c = \int_{-h_o}^{\bar{\zeta}} V_{1\alpha}^{(0)} \int_z^{\bar{\zeta}} \frac{1}{\nu_t} \left(\frac{\partial h_o}{\partial x_\gamma} \tilde{V}_\gamma \left(V_{1\beta}^{(0)}(-h_o) - V_{1\beta}^{(0)} \right) - V_{1\beta}^{(0)}(h_o + z) \frac{\partial \tilde{V}_\gamma}{\partial x_\gamma} + \int_{-h_o}^{z} V_{1\beta}^{(0)}\, dz \frac{\partial \tilde{V}_\gamma}{\partial x_\gamma} \right) dz\, dz \tag{A.12}$$

Next, we will substitute (A.5), (A.6) and (A.12) into (A.2) so that

$$\begin{aligned} I_1 = I_a + I_b + I_c = h D_{\alpha\gamma} \frac{\partial \tilde{V}_\beta}{\partial x_\gamma} + \\ \tilde{V}_\gamma \int_{-h_o}^{\bar{\zeta}} V_{1\alpha}^{(0)} \int_z^{\bar{\zeta}} \frac{1}{\nu_t} \left[\frac{\partial}{\partial x_\gamma} \left(\int_{-h_o}^{z} V_{1\beta}^{(0)}\, dz \right) - V_{1\beta}^{(0)}(-h_o) \frac{\partial h_o}{\partial x_\gamma} \right] dz^2 + \\ \int_{-h_o}^{\bar{\zeta}} V_{1\alpha}^{(0)} \int_z^{\bar{\zeta}} \frac{1}{\nu_t} \left(\frac{\partial h_o}{\partial x_\gamma} \tilde{V}_\gamma \left(V_{1\beta}^{(0)}(-h_o) - V_{1\beta}^{(0)} \right) - \right. \\ \left. V_{1\beta}^{(0)}(h_o + z) \frac{\partial \tilde{V}_\gamma}{\partial x_\gamma} + \int_{-h_o}^{z} V_{1\beta}^{(0)}\, dz \frac{\partial \tilde{V}_\gamma}{\partial x_\gamma} \right) dz\, dz \end{aligned} \tag{A.13}$$

This can be rewritten as

$$\begin{aligned} I_1 = h D_{\alpha\gamma} \frac{\partial \tilde{V}_\beta}{\partial x_\gamma} + \\ \tilde{V}_\gamma \int_{-h_o}^{\bar{\zeta}} V_{1\alpha}^{(0)} \int_z^{\bar{\zeta}} \frac{1}{\nu_t} \left[\frac{\partial}{\partial x_\gamma} \left(\int_{-h_o}^{z} V_{1\beta}^{(0)}\, dz \right) - V_{1\beta}^{(0)} \frac{\partial h_o}{\partial x_\gamma} \right] dz^2 - \end{aligned}$$

$$\frac{\partial \tilde{V}_\gamma}{\partial x_\gamma} \int_{-h_o}^{\bar{\zeta}} V_{1\alpha}^{(0)} \int_z^{\bar{\zeta}} \frac{1}{\nu_t} V_{1\beta}^{(0)} (h_o + z)\, dz\, dz +$$

$$\frac{\partial \tilde{V}_\gamma}{\partial x_\gamma} \int_{-h_o}^{\bar{\zeta}} V_{1\alpha}^{(0)} \int_z^{\bar{\zeta}} \frac{1}{\nu_t} \int_{-h_o}^{z} V_{1\beta}^{(0)}\, dz\, dz\, dz \tag{A.14}$$

Then, using the definitions (2.63), (2.64) and (2.65), this equation becomes

$$I_1 \;=\; h\, D_{\alpha\gamma} \frac{\partial \tilde{V}_\beta}{\partial x_\gamma} + G_{1\alpha\beta\gamma}\, \tilde{V}_\gamma + G_{2\alpha\beta} \frac{\partial \tilde{V}_\gamma}{\partial x_\gamma} + h\, D_{\alpha\beta} \frac{\partial \tilde{V}_\gamma}{\partial x_\gamma} \tag{A.15}$$

Similarly, the second triple integral in (A.1) can be treated in the same way (with α and β switched) and becomes

$$I_2 \;=\; \int_{-h_o}^{\bar{\zeta}} V_{1\beta}^{(0)} \int_z^{\bar{\zeta}} \frac{1}{\nu_t} \int_{-h_o}^{z} F_\alpha\, dz\, dz\, dz \;=$$

$$h\, D_{\beta\gamma} \frac{\partial \tilde{V}_\alpha}{\partial x_\gamma} + G_{1\beta\alpha\gamma}\, \tilde{V}_\gamma + G_{2\beta\alpha} \frac{\partial \tilde{V}_\gamma}{\partial x_\gamma} + h\, D_{\beta\alpha} \frac{\partial \tilde{V}_\gamma}{\partial x_\gamma} \tag{A.16}$$

Using the results (A.15) and (A.16), and the definition (2.66) we can write (A.1) as

$$I \;=\; M_{\alpha\beta} - I_1 - I_2 =$$

$$M_{\alpha\beta} - h \left(D_{\alpha\gamma} \frac{\partial \tilde{V}_\beta}{\partial x_\gamma} + D_{\beta\gamma} \frac{\partial \tilde{V}_\alpha}{\partial x_\gamma} + 2\, D_{\alpha\beta} \frac{\partial \tilde{V}_\gamma}{\partial x_\gamma} \right) -$$

$$(G_{1\alpha\beta\gamma} + G_{1\beta\alpha\gamma})\, \tilde{V}_\gamma - (G_{2\alpha\beta} + G_{2\beta\alpha}) \frac{\partial \tilde{V}_\gamma}{\partial x_\gamma} \tag{A.17}$$

which is (2.67), Q.E.D.

Appendix B

DERIVATION OF $Q = C_A(\bar{\zeta} - \bar{\bar{\zeta}}) + \bar{\bar{Q}}$.

The relationship

$$Q = c_a(\bar{\zeta} - \bar{\bar{\zeta}}) + \bar{\bar{Q}} \tag{B.1}$$

is derived for a long wave in a slightly modified form adapted from Svendsen (1974). Here c_a is the celerity of the wave seen from a fixed coordinate system so that

$$c_a = c_r + U \tag{B.2}$$

where c_r is the wave celerity in a coordinate system moving with U, the uniform current velocity. In order to be consistent with the notation in this paper, the surface elevation of the long wave is denoted $\bar{\zeta}$ and we will use $\bar{\bar{\zeta}}$ to indicate the time-averaged value over a long wave period. This relationship is valid for any wave that propagates with permanent form in an ambient current and is not limited to long waves or small amplitude waves.

We consider the conservation of mass for a control volume framed by one fixed vertical boundary at x, see Fig. B.1, and one vertical section at $x_a = x_a(t)$, which is moving with celerity c_a. This means that the surface elevation $\bar{\zeta}_a$ at x_a is constant in time.

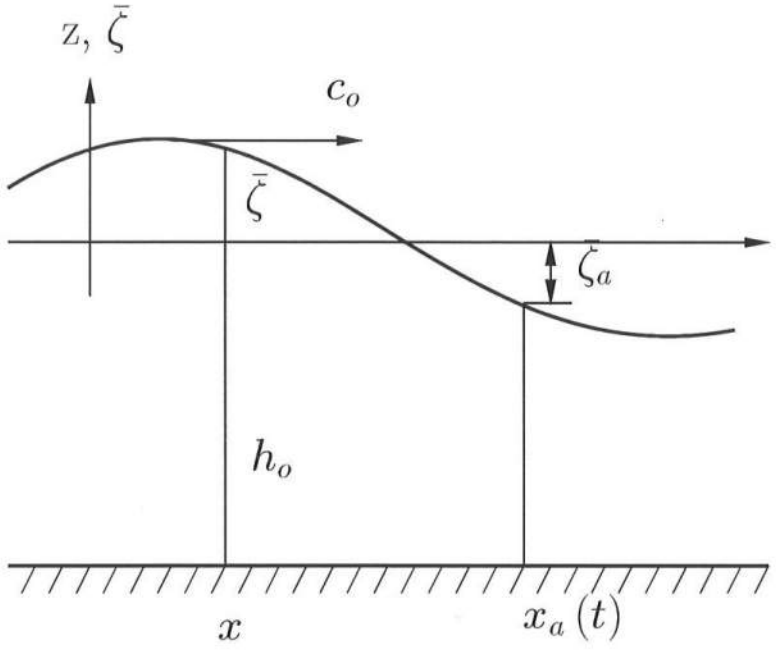

Figure B.1: Definition sketch of constant form wave on a horizontal bottom.

For this control volume the continuity equation reads

$$\int_{-h_o}^{\bar{\zeta}} (u_w + U)\, dz \; - \; \int_{-h_o}^{\bar{\zeta}_a} \left((u_w + U) \; - \; c_a \right) \, dz \; =$$

$$\int_{x}^{x_a} \frac{\partial \bar{\zeta}}{\partial t}\, dx \; + \; c_a \left(h_o + \bar{\zeta}_a \right) \tag{B.3}$$

where the u_w is the (long) wave component, and $\bar{u} = u_w + U$. We define

$$Q \equiv \int_{-h_o}^{\bar{\zeta}} (u_w + U)\, dz \tag{B.4}$$

and choose x_a such that

$$\int_{-h_o}^{\bar{\zeta}_a} u_w \, dz \; = \; 0 \tag{B.5}$$

We finally assume that the wave propagates with constant form, which means that

$$\frac{\partial \bar{\zeta}}{\partial t} \; = \; -c_a \frac{\partial \bar{\zeta}}{\partial x} \tag{B.6}$$

Substituting (B.4), (B.5) and (B.6) into (B.3) yields

$$Q = c_a\,(\bar{\zeta} - \bar{\zeta}_a) + U\,(h_o + \bar{\zeta}_a) \tag{B.7}$$

Taking the time-average over a long wave period of this equation yields

$$\overline{\overline{Q}} = c_a\,(\overline{\overline{\zeta}} - \bar{\zeta}_a) + U\,(h_o + \bar{\zeta}_a) \tag{B.8}$$

which can be used to eliminate the $\bar{\zeta}_a$-term in (B.7), which yields

$$Q = c_a\,(\bar{\zeta} - \overline{\overline{\zeta}}) + \overline{\overline{Q}} \tag{B.9}$$

Q.E.D.

It is emphasized that the only real assumption used in deriving this expression is that the wave is of permanent form. No assumptions about the height or shape of the wave have been used. For completeness it is also noted that the time-average of (B.4) yields

$$\overline{\overline{Q}} = \overline{\overline{\int_{-h_o}^{\bar{\zeta}} u_w\,dz}} + U\,(h_o + \overline{\overline{\zeta}}) = Q_w + U\,(h_o + \overline{\overline{\zeta}}) \tag{B.10}$$

where Q_w is the wave-induced mass flux. This means that strictly speaking $\overline{\overline{Q}}$ includes an ambient current and the wave-induced mass flux.

Appendix C

DERIVATION OF LONGUET-HIGGINS AND STEWART (1962) BOUND WAVE GROWTH.

In this Appendix, we will redo Longuet-Higgins and Stewart (1962)'s derivation of their Eq. (5.6) because of some typos in their paper (which did not influence the final result).

From (4.11)

$$\bar{\zeta}_i = -\frac{1}{\rho}\frac{S^{(1)}_{xx}}{(g\,h_s - c^2_{gs})} \tag{C.1}$$

we can write the amplitudes as

$$\hat{\zeta}_i = -\frac{1}{\rho}\frac{\hat{S}_{xx}}{(g\,h_o - c^2_g)} \tag{C.2}$$

In the denominator, we can write the radiation stress in terms of the energy flux $E\,cg$ and we can express the denominator in terms of μ to yield

$$\hat{\zeta}_i = -\frac{1}{\rho}\frac{E\,c_g\left(\frac{2}{c} - \frac{1}{2\,c_g}\right)}{g\,h_o - g\,h_o\,n^2\,\frac{\tanh\mu}{\mu}} \tag{C.3}$$

Expanding n, c_g and $\tanh\mu$ in terms of μ and keeping only the lowest order we have

$$\hat{\zeta}_i = -\frac{1}{\rho}\frac{E\,c_g\,\frac{\mu}{\omega\,h_o}\left(\frac{3}{2} - \frac{1}{6}\,\mu + O(\mu^4)\right)}{g\,h_o\,(\mu^2 + O(\mu^4))}$$

$$= -\frac{3}{2}\frac{E\,c_g}{\rho}\frac{1}{\omega\,g\,h_o^2\,\mu} + O(\mu)$$

$$= -\frac{3}{2}\frac{E\,c_g}{\rho}\frac{1}{\omega^2\,\sqrt{g}\,h_o^{2.5}} \tag{C.4}$$

where the energy in the short waves $E = \frac{1}{8}\rho\,g\,H^2$ and where in the last step we have made the lowest order substitution from the linear dispersion relation

$$\omega^2\,h_o = g\,\mu\,\tanh\,\mu = g\,\mu^2 + O(\mu^4) \tag{C.5}$$

in order to eliminate the μ term in the denominator. From (C.4) we can see that outside the surf zone, where the energy flux $E\,c_g$ is constant, we have

$$\hat{\zeta}_i \propto h_o^{-\frac{5}{2}} \tag{C.6}$$

REFERENCES

Abbott, M.B. (1979). *Computational hydraulics. Elements of the theory of free surface flow.* Pitman Publishing, London, 324 p.

Anderson, D.A., J.C. Tannehill and R.H. Pletcher (1984). *Computational fluid mechanics and heat transfer.* Hemisphere Publishing Corp., New York, 599 p.

Allender, J.H., J.D. Ditmars, W. Harrison and R.A. Paddock (1978). "Comparison of model and observed nearshore circulation." *Proc. of the 16th International Conference on Coastal Engineering*, pp. 810-827.

Atkinson, K.E. (1978). *An Introduction to numerical analysis.* J. Wiley & Sons, New York, 587 pp.

Battjes, J.A. (1974). "Surf similarity." *Proc. of the 14th International Conference on Coastal Engineering*, pp. 466-479.

Battjes, J.A. (1975). "Modelling of turbulence in the surf-zone." *Proc. of a Symposium on Modelling Techniques*, ASCE, San Francisco, pp. 1050-1061.

Baum, S.K. and D.R. Basco (1986). "A numerical investigation of the longshore current profile for multiple bar/trough beaches." *Proc. of the 16th International Conference on Coastal Engineering*, pp. 971-985.

Bender, C.M. and S.A. Orzag (1978). *Advanced mathematical methods for scientists and engineers.* McGraw-Hill, New York, 593 p.

Börekçi, O.S. (1982). "Distribution of wave-induced momentum fluxes over depth and application within the surf zone." Doctoral dissertation, Department of Civil Engineering, University of Delaware. 108 pp.

Bowen, A.J. (1969a). "The generation of longshore currents on a plane beach." *Journal of Marine Research, 27*, pp. 206-215.

Bowen, A.J. (1969b). "Rip currents. Part 1: Theoretical investigations." *Journal of Geophysical Research, 74*, pp. 5467-78.

Bowen, A.J. and R.T. Guza (1978). "Edge waves and surf beat." *Journal of Geophysical Research, 83*, pp. 1913-1920.

Bowen, A.J. and D.L. Inman (1974). "Nearshore mixing due to waves and wave induced currents." *Rapp. P.-v. Reun. Cons. Int., 167*, pp. 6-12.

Broeze, J. and E.F.G. Van Daalen (1992). "Radiation boundary conditions for the two-dimensional wave equation from a variational principle." *Math. Comp., vol. 58, no. 197*, pp. 73-82.

Brocchini, M., M. Drago and L. Iovenitti (1992). "The modeling of short waves in shallow waters. Comparison of numerical models based on Boussinesq and Serre equations." *Proc. of the 23rd International Conference on Coastal Engineering*, pp. 76-88.

Brocchini, M., and D.H. Peregrine (1996). "Integral flow properties of the swash zone and averaging." *J. of Fluid Mech., 317*, pp. 241-273.

Carrier, G.F. and H.P. Greenspan (1958). "Water waves of finite amplitude on a sloping beach." *J. Fluid Mech., 4, part 1*, pp. 97-109.

Church, J.C. and E.B. Thornton (1993). "Effects of breaking wave induced turbulence within a longshore current model." *Coastal Engineering, 20*, pp. 1-28.

Dally, W.R. and R.G. Dean (1984). "Suspended sediment transport and beach profile evaluation." *Journal of Waterway, Port, Coastal and Ocean Engineering, 110*, pp. 15-33.

Dally, W.R. and R.G. Dean (1986). "Discussion of 'Mass flux and undertow in a surf zone' by I.A. Svendsen." *Coastal Engineering, 10*, pp. 289-299.

Dalrymple, R.A. (1978). "Rip currents and their causes." *Proc. of the 16th International Conference on Coastal Engineering*, pp. 1414-1427.

Dalrymple, R.A. and C.J. Lozano (1978). "Wave-current interaction models for rip currents." *J. of Geophysical Res., 83*, pp. 6063-6071.

Deigaard, R. and J. Fredsøe (1989). "Shear stress distribution in dissipative water waves." *Coastal Engineering, 13*, pp. 357-378.

De Vriend, H.J. and M.J.F. Stive (1987). "Quasi-3D modelling of nearshore currents." *Coastal Engineering, 11*, pp. 565-601.

Dyhr-Nielsen, M. and T. Sörensen (1970). "Some sand transport phenomena on coasts with bars." *Proc. of the 12th International Conference on Coastal Engineering*, pp. 855-866.

Ebersole, B. and R.A. Dalrymple (1980). "Numerical modeling of nearshore circulation." *Proc. of the 17th International Conference on Coastal Engineering*, pp. 2710-2725.

Elder, J.W. (1959). "The dispersion of marked fluid in turbulent shear flow." *Journal of Fluid Mechanics, 5*, pp. 544-560.

Elgar, S., T.H.C. Herbers, M. Okihiro, J. Oltman-Shay and R. T. Guza (1992). "Observations of infragravity waves." *Journal of Geophysical Research, 97*, pp. 15,573-15,577.

Engquist, B. and A. Majda (1977). "Absorbing boundary conditions for the numerical simulation of waves." *Math. Comp., vol. 31, no. 139*, pp. 629-651.

Fischer, H.B. (1978). "On the tensor form of the bulk dispersion coefficient in a bounded skewed shear flow." *Journal of Geophysical Research, 83*, pp. 2373-2375.

Gallagher, B. (1971). "Generation of surf beat by non-linear wave interactions." *J. of Fluid Mechanics, 49*, pp. 1-20.

Givoli, D. (1991). "Non-reflective boundary conditions." *J. of Comp. Physics*, 94, pp. 1-29.

Guza, R.T. and A.J. Bowen (1975). "The resonant instabilities of long waves obliquely incident on a beach." *Journal of Geophysical Research, 80*, pp. 4529-4534.

Guza, R.T. and D.C. Chapman (1979). "Experimental study of the instabilities of waves obliquely incident on a beach." *J. of Fluid Mechanics, 95*, pp. 199-208.

Guza, R.T. and E.B. Thornton (1982). "Swash oscillations on a natural beach." *Journal of Geophysical Research, 87*, pp. 483-491.

Guza, R.T. and E.B. Thornton (1985). "Observations of surf beat." *Journal of Geophysical Research, 90, C2*, pp. 3161-3171.

Guza, R.T., E.B. Thornton and R.A. Holman (1984). "Swash on steep and shallow beaches." *Proc. of the 19th International Conference on Coastal Engineering*, pp. 708-723.

Herbers, T.H.C., S. Elgar and R.T. Guza (1995). "Generation and propagation of infragravity waves." *Journal of Geophysical Research, 100, C12*, pp. 24,863-24,872.

Hibberd, S. (1977). "Surf and run-up." Ph.D. dissertation, School of Mathematics, University of Bristol, 124 p.

Hibberd, S. and D.H. Peregrine (1979). "Surf and runup on a beach: a uniform bore." *J. of Fluid Mech., 95*, pp. 323-345.

Higdon, R.L. (1986). "Absorbing boundary conditions for difference approximations to the multi-dimensional wave equation." *Math. Comp, vol. 47, no. 176*, pp. 437-459.

Higdon, R.L. (1987). "Numerical Absorbing boundary conditions for the wave equation." *Math. Comp., vol. 49, no. 179*, pp. 65-90.

Holman, R.A. (1981). "Infragravity energy in the surfzone." *Journal of Geophysical Research, 86*, pp. 6442-6450.

Howd, P. A., J. Oltman-Shay and R.A. Holman (1991). "Wave variance partitioning in the trough of a barred beach." *Journal of Geophysical Research, 96*, pp. 12,781-12,795.

Huntley, D.A., R.T. Guza and E.B. Thornton (1981). "Field observations of surf beat, Part I: Progressive edge waves." *Journal of Geophysical Research, 86*, pp. 6451-6466.

Inman, D.L., R.J. Tait and C.E. Nordstrom (1971). "Mixing in the surf zone." *Journal of Geophysical Research, 76*, pp. 3493-3514.

Irribarren, C.R. and C. Nogales (1949). *Protection des ports.* XVIIth Int. Nav. Congress, Section II, Comm. 4, Lisbon, pp. 31-80.

Karambas, Th. and C. Koutitas (1992). "A breaking wave propagation model based on the Boussinesq equations." *Coastal Engineering, 18*, pp. 1-19.

Keys, R.G. (1985). "Absorbing boundary conditions for acoustic media." *Geophysics, vol. 50, no. 6*, pp. 892-902.

Kobayashi, N., G.S. De Silva and K.D. Watson (1989). "Wave transformation and swash oscillation on gentle and steep slopes." *Journal of Geophysical Research, 94*, pp. 951-966.

Kobayashi, N. and B. D. Johnson (1995). "Numerical model VBREAK for vertically two-dimensional breaking waves on impermeable slopes." *Research report CACR-95-06*, University of Delaware, 66 pp.

Kobayashi, N., A.K. Otta and I. Roy (1987). "Wave reflection and run-up on rough slopes." *Journal of Waterway, Port, Coastal and Ocean Engineering, 113, no. 3*, pp. 282-298.

Kobayashi, N. and A. Wurjanto (1992). "Irregular wave setup and runup on beaches." *Journal of Waterway, Port, Coastal and Ocean Engineering, 118*, pp. 368-386.

Kostense, J.K. (1984). "Measurements of surf beat and set-down beneath wave groups." *Proc. of the 19th International Conference on Coastal Engineering*, pp. 724-740.

Larson, M. and N. Kraus (1991). "Numerical model for longshore current for bar and trough beaches." *Journal of Waterway, Port, Coastal, and Ocean Engineering, 114*, pp. 326-347.

Liu, P.L.-F. (1989). "A note on long waves induced by short-wave groups over a shelf." *J. of Fluid Mech., 205*, pp. 163-170.

Liu, P.L.-F. and R.A. Dalrymple (1978). "Bottom frictional stresses and longshore currents due to waves with large angles of incidence." *Journal of Marine Research, 36*, pp. 357-375.

Longuet-Higgins, M.S. (1970). "Longshore currents generated by obliquely incident sea waves. Parts 1 and 2." *Journal of Geophysical Research, 75*, pp. 6778-6789 and pp. 6790-6801.

Longuet-Higgins, M.S. and E.D. Cokelet (1976). "The deformation of steep surface waves on water. I. A numerical method of computation." *Proc. Roy. Soc. Lond. A., 350*, pp. 1-26.

Longuet-Higgins, M.S. and R.W. Stewart (1962). "Radiation stress and mass transport in gravity waves with application to 'surf-beats'." *Journal of Fluid Mechanics, 8*, pp. 565-583.

Longuet-Higgins, M.S. and R.W. Stewart (1964). "Radiation stress in water waves, a physical discussion with applications." *Deep Sea Research, 11*, pp. 529-563.

Madsen, P.A., O.R. Sørensen and H.A. Schäffer (1994). "Time domain modelling of wave breaking, runup and surf beats." *Proc. 24th of the International Conference on Coastal Engineering*, pp. 399-411.

Mei, C.C. (1983). *The applied dynamics of ocean surface waves.* John Wiley and Sons, New York, 740 pp.

Mei, C.C. and C. Benmoussa (1984). "Long waves induced by short-wave groups over an uneven bottom." *J. of Fluid Mech., 139*, pp. 219-235.

Molin, B. (1982). "On the generation of long-period second order free waves due to changes in the bottom profile." *Rapp. IFP:30167, Inst. Français du Petrole.* [also published as *Ship Res. Inst. rep. 68*, Tokyo, Japan.] 23 p.

Munk, W.H. (1949). "Surf beats." *Transactions of the American Geophysical Union,30*, pp. 849-854.

Nadaoka, K. and T. Kondoh (1982). "Laboratory measurements of velocity field structure in the surf zone by LDV." *Coastal Engineering in Japan, 25*, pp. 125-145.

Noda, E.K. (1974). "Wave induced nearshore circulation." *J. of Geophys. Res., 79*, pp. 4097-4106.

Noda, E.K., C.J. Sonu, V.C. Rupert and J.I. Collins (1974). "Nearshore circulations under sea breeze conditions and wave-current interactions in the surf-zone." *Tetra Tech Rep. TC-149-4.*

Okayasu, A., T. Shibayama and K. Horikawa (1988). "Vertical variation of undertow in the surf-zone." *Proc. of the 21st International Conference on Coastal Engineering* , pp. 478-491.

Oltman-Shay, J. and R. T. Guza (1987). "Infragravity edge wave observations on two California beaches." *Journal of Physical Oceanography, 17*, pp. 644-663.

Özkan-Haller, H.T. and J.T. Kirby (1997). "A Fourier-Chebyshev collocation method for the shallow water equations including shoreline runup." *Applied Ocean Research*, in press.

Packwood, A. (1983). "The influence of beach porosity on wave uprush and backwash." *Coastal Engineering, 7*, pp. 29-40.

Packwood, A. and D.H. Peregrine (1980). "The propagation of solitary waves and bores over a porous bed." *Coastal Engineering, 3*, pp. 221-242.

Phillips, O.M. (1977). *The dynamics of the upper ocean.* Cambridge University Press, 336 pp.

Putrevu, U. and I.A. Svendsen (1991). "Wave induced nearshore currents: A study of the forcing, mixing and stability characteristics." *Research report CACR-91-11*, Department of Civil Engineering, University of Delaware.

Putrevu, U. and I.A. Svendsen (1992). "A mixing mechanism in the nearshore region." *Proc. of the 23rd International Conference on Coastal Engineering*, pp. 2758-2771.

Putrevu, U. and I.A. Svendsen (1993). "Vertical structure of the undertow outside the surf-zone." *Journal of Geophysical Research, 98, C12*, pp. 22,707-22,716.

Putrevu, U. and I.A. Svendsen (1995). "Infragravity velocity profiles in the surf-zone." *Journal of Geophysical Research, 100, C8*, pp. 16,131-16,142.

Putrevu, U. and I.A. Svendsen (1997). "Shear dispersion of momentum in the nearshore." Submitted to *J. of Fluid Mech.*

Reid, R.O. and B.R. Bodine (1968). "Numerical model for storm surges in Galveston Bay." *J. of the Waterways and Harbors Division, Proc. ASCE, 94, WW1*, pp. 33-57.

Reniers, A.J.H.M., E.B. Thornton and T.C. Lippmann (1995). "Longshore currents over barred beaches." *Proc. Coastal Dynamics*, pp. 413-424.

Rodi, W. (1980). *Turbulence models and their application in hydraulics.* Int'l Assoc. for Hydraulic Res., Delft, The Netherlands, 104 p.

Roelvink, J.A. (1993). "Surf beat and its effect on cross-shore profiles." Ph.D. Thesis, Delft University of Technology, 150 pp.

Roelvink, J.A. and M.J.F. Stive (1989). "Bar generating cross-shore flow mechanisms on a beach." *Journal of Geophysical Research, 94*, pp. 4785-4800.

Sánchez-Arcilla, A., F. Collado, C. Lemos and F. Rivero (1990). "Another quasi-3D model for surf-zone flows." *Proc. of the 22nd International Conference on Coastal Engineering*, pp. 316-329.

Sánchez-Arcilla, A., F. Collado and A. Rodriguez (1992). "Vertically varying velocity field in Q-3D nearshore circulation." *Proc. of the 23rd International Conference on Coastal Engineering* , pp. 2811-2824.

Sancho, F.E., I.A. Svendsen, A.R. Van Dongeren and U. Putrevu (1995). "Longshore nonuniformities of nearshore currents." *Proc. Coastal Dynamics*, pp. 425-436.

Schäffer, H.A. (1993). "Infragravity waves induced by short-wave groups." *J. Fluid Mech., 247*, pp. 551-588.

Schäffer, H.A. (1994). "Edge waves forced by short-wave groups." *J. Fluid Mech., 259*, pp. 125-148.

Schäffer, H.A., R. Deigaard and P.A. Madsen (1992). "A two-dimensional surf zone model based on the Boussinesq equations." *Proc. of the 23rd International Conference on Coastal Engineering*, pp. 576-589.

Schäffer, H.A., P.A. Madsen and R. Deigaard (1993). "A Boussinesq model for wave breaking in shallow water." *Coastal Engineering, 20*, pp. 185-202.

Schäffer, H.A. and I.A. Svendsen (1988). "Surf beat generation on a mild slope beach." *Proc. of the 21st International Conference on Coastal Engineering*, pp. 1058-1072.

Smith, J.M., M. Larson and N.C. Kraus (1993). "Longshore current on a barred beach: field measurements and calculation." *Journal of Geophysical Research, 98, C12*, pp. 22,717-22,731.

Smith, J.M. and I.A. Svendsen (1995). "Modelling time- and depth-varying currents at Supertank." *Proc. Coastal Dynamics*, pp. 245-256.

Smith, J.M. and I.A. Svendsen (1996). "Time- and depth-varying cross-shore currents: numerical modeling and laboratory measurements." *Research report No. CACR-96-04*, Center for Applied Coastal Research, University of Delaware, Newark, 208 p.

Sommerfeld, A. (1964). *Lectures on Theoretical Physics.* Academic Press, New York, N. Y.

Spielvogel, L.Q. (1976). "Single-wave run-up on sloping beaches." *J. Fluid Mech., 74, part 4*, pp. 685-694.

Stive, M.J.F. and H.J. de Vriend (1987). "Quasi-3D nearshore current modelling: Wave induced secondary currents." *Proc. of a special conference on coastal hydrodynamics*, ASCE, Newark, pp. 356-370.

Stive, M.J.F. and H.G. Wind (1982). "A study of radiation stress and set-up in the nearshore region." *Coastal Engineering, 6*, pp. 1-26.

Strikwerda, J.C. (1989). *Finite difference schemes and partial differential equations.* Wadsworth & Brooks/Cole Mathematical Series. Wadsworth, Belmont, CA.

Svendsen, I.A. (1974). "Cnoidal waves over a gently sloping bottom." *Series paper # 6*, Institute of Hydrodynamics and Hydraulic Engineering, Technical University of Denmark, 181 pp.

Svendsen, I.A. (1984a). "Wave heights and set-up in a surf-zone." *Coastal Engineering, 8*, pp. 303-329.

Svendsen, I.A. (1984b). "Mass flux and undertow in a surf-zone." *Coastal Engineering, 8*, pp. 347-365.

Svendsen, I.A. and J.B. Hansen (1988). "Cross-shore currents in surf-zone modelling." *Coastal Engineering , 12*, pp. 23-42.

Svendsen, I.A. and P. Justesen (1984). "Forces on slender cylinders from very high waves and spilling breakers." *Symposium on description and modelling of directional seas.*. Copenhagen 1984. Chapter D-7, 16 pp.

Svendsen, I.A. and R.S. Lorenz (1989). "Velocities in combined undertow and longshore currents." *Coastal Engineering, 13*, pp. 55-79.

Svendsen, I.A. and U. Putrevu (1990). "Nearshore circulation with 3-D profiles." *Proc. of the 22nd International Conference on Coastal Engineering*, pp. 241-254.

Svendsen, I.A. and U. Putrevu (1993). "Surf-zone wave parameters from experimental data." *Coastal Engineering, 19*, pp. 283-310.

Svendsen, I.A. and U. Putrevu (1994a). "Nearshore mixing and dispersion." *Proc. Roy. Soc. Lond. A., 445*, pp. 1-16.

Svendsen, I.A. and U. Putrevu (1994b). "Velocity structure in IG waves." *Proc. Int. Symp. on Waves - Physical and Numerical Modelling*, Vancouver, Aug. 21-24, (Isaacson and Quick, *Eds.*), pp. 346-355.

Svendsen, I.A. and U. Putrevu (1996). "Surf zone hydrodynamics." In *Advances in Coastal and Ocean Engineering*, Vol. 2, P.L.-F. Liu, *ed.*, World Scientific Publ., pp. 1-78.

Svendsen, I.A., H.A. Schäffer and J.B. Hansen (1987). "The interaction between the undertow and boundary layer flow on a beach." *Journal of Geophysical Research, 92*, pp. 11,845-11,856.

Symonds, G., D.A. Huntley and A.J. Bowen (1982). "Two dimensional surf-beat: Long wave generation by a time-varying break point." *Journal of Geophysical Research, 87, C1*, pp. 492-498.

Tang, E. and R.A. Dalrymple (1988). "Rip currents and wave groups." *In:* Nearshore Sediment Transport, R. J. Seymour, ed., Plenum Publishing Corporation, pp. 205-230.

Taylor, G.I. (1954). "The dispersion of matter in a turbulent flow through a pipe." *Proc. of the Royal Society of London. Series A*, 219, pp. 446-468.

Thornton, E.B. (1970). "Variation of longshore current across the surf zone." *Proc. of the 12th International Conference on Coastal Engineering*, pp. 291-308.

Thornton, E.B. and R.T. Guza (1986). "Surf-zone longshore currents and random waves: Field data and models." *Journal of Physical Oceanography, 16*, pp. 1165-1178.

Tucker, M.J. (1950). "Surf beats: sea waves of 1 to 5 minute period." *Proc. of the Royal Society of London, A, 202*, pp. 565-573.

Twizell, E.H. (1984). *Computational methods for partial differential equations.* Ellis Horwood Ltd., West Sussex, England, 276 p.

Van Dongeren, A.R., F.E. Sancho, I.A. Svendsen and U. Putrevu (1994). "SHORECIRC: A quasi 3-D nearshore model." *Proc. of the 24th International Conference on Coastal Engineering*, pp. 2741-2754.

Van Dongeren, A.R. and I.A. Svendsen (1997). "An absorbing-generating boundary condition for shallow water models." *Journal of Waterway, Port, Coastal and Ocean Engineering*, in press. Also: *Research report CACR-96-10*, Center for Applied Coastal Research, University of Delaware, Newark, 33 p.

Van Dongeren, A.R., I.A. Svendsen and F.E. Sancho (1995). "Application of the Q-3D SHORECIRC model to surfbeat." *Proc. Coastal Dynamics*, pp. 233-244.

Van Dongeren, A.R., I.A. Svendsen and F.E. Sancho (1996). "Generation of Infragravity Waves." *Proc. of the 25th International Conference on Coastal Engineering*, pp. 1335-1348.

Verboom, G.K and A. Slob (1984). "Weakly-reflective boundary conditions for two-dimensional shallow water flow problems." *Adv. Water Resources, vol. 7*, pp. 192-197.

Verboom, G.K., G.S. Stelling and M.J. Officier (1981). "Boundary conditions for the shallow water equations." *In:* Abbott, M.B. and J.A. Cung *Eds.*, *Engineering Applications of Computational Hydraulics*, vol. I, pp. 230-262.

Visser, P.J. (1984). "A mathematical model of uniform longshore currents and comparison with laboratory data." *Communications on Hydraulics. Report 84-2*, Department of Civil Engineering, Delft University of Technology, 151 pp.

Wei, G. (1997). "Simulation of water waves by Boussinesq models." Doctoral Dissertation, Dept. of Civil Eng., University of Delaware, 202 p.

Wind, H.G. and C.B. Vreugdenhil (1986). "Rip current generation near structures." *J. of Fluid Mechanics*, *171*, pp. 459-476.

Wright, L.D., J. Chappell, B.G. Thom, M.P. Bradshaw and P. Cowell (1979). "Morphodynamics of reflective and dissipative beaches and inshore systems: southeastern Australia." *Marine Geology*, *32*, 105.

Wright, L.D., R.T. Guza and A.D. Short (1982). "Dynamics of a high energy dissipative surf-zone." *Marine Geology*, *45*, pp. 41-62.

Wu, C.-S. and P. L-F. Liu (1985). "Finite element modeling of nonlinear coastal currents." *Journal of Waterway, Port, Coastal and Ocean Engineering*, *111*, *no. 2*, pp. 417-432.

Zelt, J.A. (1986). "Tsunamis: the response of harbours with sloping boundaries to long wave excitation." Doctoral dissertation, *Rep. No. KH-R-47*, W.M. Keck Laboratory of Hydraulics and Water Resources, Division of Engineering and Applied Science, California Institute of Technology, Pasadena, CA, 318 p.